Nuclear Resonances in X-ray Waveguides

Dissertation
zur Erlangung des
mathematisch-naturwissenschaftlichen Doktorgrades
“Doctor rerum naturalium” (Dr. rer. nat.)

der Georg-August-Universität Göttingen
im Promotionsstudiengang Physik
der Georg-August University School of Science (GAUSS)

vorgelegt von

Leon Merten Lohse
aus Ostercappeln

Göttingen, 2024

Betreuungsausschuss

Prof. Dr. Tim Salditt
Institut für Röntgenphysik
Georg-August-Universität Göttingen

Prof. Dr. Ralf Röhlsberger
Helmholtz-Institut Jena
und Friedrich-Schiller-Universität Jena

Prof. Dr. Claus Ropers
IV. Physikalisches Institut
Georg-August-Universität Göttingen
und Max-Planck-Institut für Multidisziplinäre Naturwissenschaften

Mitglieder der Prüfungskommission

Referent:
Prof. Dr. Tim Salditt
Institut für Röntgenphysik
Georg-August-Universität Göttingen

Koreferent:
Prof. Dr. Ralf Röhlsberger
Helmholtz-Institut Jena
und Friedrich-Schiller-Universität Jena

Prof. Dr. Claus Ropers
IV. Physikalisches Institut
Georg-August-Universität Göttingen
und Max-Planck-Institut für Multidisziplinäre Naturwissenschaften

Prof. Dr. Thorsten Hohage
Institut für Numerische und Angewandte Mathematik
Georg-August-Universität Göttingen
und Max-Planck-Institut für Sonnensystemforschung

Prof. Dr. Hans-Christian Hofsäss
II. Physikalisches Institut
Georg-August-Universität Göttingen

Prof. Dr. Matthias Krüger
Institut für Theoretische Physik
Georg-August-Universität Göttingen

Datum der mündlichen Prüfung: 14.06.2024

Contents

1. Introduction

1.1. Motivation

Atoms absorb and emit electromagnetic radiation at well-defined frequencies which are characteristic for each element. It has been one of the great successes of quantum mechanics to accurately explain these spectral lines as *transitions* of bound electrons between *discrete energy levels* in the attractive potential of the atomic nucleus (see for example Dirac [Dir10]). The occurring transition frequencies ω_0 (or photon energies $E = \hbar\omega_0$) span the entire electromagnetic spectrum. Prominent examples are the 21 cm hyperfine-line of hydrogen ($E \approx 6\,\mu\text{eV}$) in the radio frequency range, the 3.26 cm hyperfine-line of caesium-133 ($E = 38\,\mu\text{eV}$) in the microwave regime, the yellow 589.29 nm sodium D lines ($E = 2.1$ eV) in the visible light spectrum, and the tungsten Kα lines ($E \approx 59$ keV) in the hard x-ray regime. Other objects such as ions, molecules, quantum dots, atomic nuclei, and many more, have their own distinct spectral lines. Conceptually, we may consider all of them as abstract quantum systems with a discrete set of intrinsic quantum states and corresponding energy levels.

Atomic nuclei are rather extreme quantum systems. They are very small in size, in the order of 10^{-15} m and thereby 4 to 5 orders of magnitude smaller than atoms, which have radii in the order of the Bohr radius $a_0 = 5.29 \times 10^{-11}$ m. They are also highly symmetric so that their metastable quantum states are accurately described by eigenstates of the angular momentum operator, $|I\,m\rangle$, with nuclear spin I, magnetic quantum number m, and well-defined parity. Hyperfine-transitions between states with different m but identical I (the ground state) typically lie in the radio frequency range and are the basis of nuclear magnetic resonance (NMR) spectroscopy and magnetic resonance imaging (MRI). They do not concern us here. Transitions to metastable states with differing I, nuclear isomers, on the other hand typically lie between 1 keV to many MeV. The only isomers below 1 keV known to date are ^{229m}Th ($E \approx 8$ eV) and ^{235m}U ($E \approx 76$ eV) [Wen+16]. Nuclear states and their transitions have some favourable properties. Due to their size and symmetry, they interact only rather weakly with the environment. Bound in a solid, they do not experience collision broadening or Doppler broadening and can absorb and emit photons without recoil even at room temperature – the famous Mössbauer effect [Mös58]. The transition lines are well isolated, with often 100 keV between them. Finally, the natural lifetimes τ of isomers can be very long, in the order of 100 ns or even seconds in some cases, corresponding to ultra-narrow natural linewidths $\Gamma = 1/\tau$. Combined, this leads to extremely high quality factors, $Q = \omega_0/\Gamma$, such as 10^{12} for ^{57}Fe or 10^{19} for ^{45}Sc [Shv+23] – in the order of or even exceeding those of optical atomic clocks [Lud+15]. Since Mössbauer nuclei constitute exceptionally clean quantum systems, they are a cornerstone of the emerging field of x-ray quantum optics [Ada+13; RES20; RE21].

While radiative excitation of nuclear isomers is hampered by their extremely narrow linewidths and the limited spectral brightness of x-ray sources, many Mössbauer nuclei with $E \lesssim 100\,\mathrm{keV}$ can nowadays be resonantly driven by third- and fourth-generation synchrotron light sources [Röh05; RC21]. Modern x-ray free-electron laser (XFEL) sources extend this to even more isotopes with even narrower resonances (see for example Ref. [Shv+23]). Synchrotron (or XFEL) light sources generate broadband pulses with pulse lengths of about 100 ps (in the order of femtoseconds for XFELs), which is much shorter than the lifetimes of the driven nuclear isomers ($\tau = 141$ ns for ^{57}Fe). In this way, the ultra fine energy scale, way beyond the resolution of x-ray detectors or monochromators, is translated to a temporal response on a time scale that can be conveniently resolved by appropriate detection electronics. The nuclear resonant scattering contribution can, on resonance, far exceed the otherwise dominating electronic Thomson scattering. While the scattering amplitude for (electronic) Thomson scattering is $-Zr_\mathrm{e}$, where Z is the atomic number (electrons/atom) and $r_\mathrm{e} = 2.82 \times 10^{-15}$ m is the classical electron radius, the on-resonance scattering amplitude is (approximating the cross section with the natural dipole cross section) in the order of $\lambda/4\pi \sim 10^{-11}$ m (compare Ref. [HT99]). For the 14.4 keV-resonance of ^{57}Fe, the real part of the nuclear resonant scattering amplitude varies between $\approx \pm 220 r_\mathrm{e}$ around the resonance, illustrating how *on resonance* the nuclear interaction greatly dominates the weak non-resonant photon-matter interaction. Notably, the delayed temporal response is coherent on the order of the isomeric lifetime. This results in narrowband x-ray pulses with extreme longitudinal coherence lengths $l_\mathrm{c} \approx c\tau$, approximately 40 m for ^{57}Fe. Combined, these features enable some unique applications, which we classify into three categories.

(i) Sensing and metrology: Already in 1960, Pound and Rebka measured the gravitational red-shift – the "apparent weight of photons" – by observing the shift in photon energy due to the change in the gravitational potential over 22.5 m meters using the 14.41 keV-transition of ^{57}Fe [PR59; PR60]. Nowadays, the prospect of "nuclear clocks" promises to improve upon the precision of optical atomic clocks [WS20], which already corresponds to less than 1 s deviation in the estimated age of the universe [Lud+15]. This would, for example, enable new tests for fundamental physics [Pei+21]. The most promising candidate for such a nuclear clock is ^{229}Th [WS20; Thi+24; Tie+24]. Recently, also ^{45}Sc has been radiatively excited for the first time [Shv+23]. Its extremely high quality factor could enable measuring gravitational red-shifts on the millimeter scale [LA15; LAL25]. Aside from these prospects in metrology, nuclear transitions have been used for many decades in Mössbauer spectroscopy. There, the

effects of hyperfine interactions on the transition lines of Mössbauer nuclei, most prominently ^{57}Fe, are being used to obtain detailed information about samples with diverse applications in chemistry, earth sciences, biology, and materials science (see Refs. [YL13; YL21]).

(ii) Observing collective dynamics: Ensembles of nuclei that are coherently illuminated by short pulses exhibit collective temporal responses fundamentally different from those of the individual constituent nuclei. The photon emission originates from the spontaneous radiative decay of the *collective* many-body excitation of the nuclear ensemble and distinctly depends on the geometry and spatial distribution of the nuclei. A thick homogeneous foil illuminated in normal incidence exhibits clean dynamical (propagation) beats in its temporal response [Bür99; Smi+07]. Thin films of nuclei embedded in appropriately designed layer systems, illuminated in grazing incidence, can produce a wide variety of responses in the direction of specular reflection, such as superradiant speedup [Röh+05], a shifted resonance frequency [Röh+10], collective oscillations [Hab+17], or subluminal propagation [Hee+15].

(iii) Coherent control: The sensitivity of the resonance lines to (magnetic) hyperfine fields and Doppler shifts allows to dynamically control and shape the *coherent* temporal response either magnetically or optomechanically. This has been demonstrated with magnetic switching [Shv+96], transient magnons [Boc+21], piezo-induced motion [Hee+21], and acoustically induced transparency [Rad+20; Kha+21] – along with theoretical proposals [LPK12; KP16]. Moreover, the polarization-dependence of hyperfine-split resonance lines makes a sample with well-defined magnetization axis strongly birefringent [Smi99]. This can be exploited to separate the rotated nuclear response from the driving pulse using high-purity crossed polarizer-analyzer pairs (see for example Refs. [Hab+16; Hee+15]). In principle, such a sample could also function as a strongly dispersive waveplate for narrowband light.

All these experiments are realized with either bulk samples or translation-invariant thin-film systems, both being *macroscopic* and involving large numbers of nuclei. This bears the question: can we scale this down? In the optical regime (here referring to light with lower frequency), photonic components such as beam splitters, gratings, couplers, polarisers, interferometers, among others, can be connected with optical waveguides and integrated into microchips, forming photonic integrated chips (see the textbook Ref. [Lif05]). They are nowadays ubiquitous, for example in modern telecommunications infrastructure, in optical sensors, and are being developed also for quantum technologies [Pel+21]. Waveguides and nanofibers are used to controllably couple individual atoms that are precisely localized in lattices (see the reviews Ref. [She+23; Tür+19; Cha+18]) – a field of research becoming known as *waveguide quantum electrodynamics*. To what extent can any of this be realized in the x-ray regime?

Integrating Mössbauer nuclei into x-ray waveguides *could* have some promising applications. The gravitational red-shift could potentially be measured on the millimeter-scale [LAL25]. Tapered waveguides could funnel the available photons to a smaller spot and facilitate transient nuclear inversion [Che+22]. Some of the aforementioned coherent control schemes could be integrated on a chip, in particular by exploiting precisely controllable magnetic properties of thin films. This could enable on-chip devices for magnetic control of the temporal response, phase-shift, and polarization of narrowband x-ray pulses. Generally, the Mössbauer nuclei affect the temporal dimension, while waveguides primarily affect the spatial dimension.

Irrespective of such potential nanophotonic devices, Mössbauer nuclei coupled to x-ray waveguides are also an opportunity for basic physical research. Placing nanoscopic ensembles of Mössbauer nuclei in or close to x-ray waveguides potentially allows to couple the nuclei to one or a few propagating photon modes. The coupling strength can be controlled by engineering the waveguide geometry. One can study the *collective* evolution of the coupled many-body system consisting of nuclei and photons by observing the temporal response to impulsive excitation. The variety of temporal responses that can be realized already by reflection from translation-invariant thin-film systems (see Ref. [RE21]) highlights the potential of this approach. While the reflection-geometry has been restricted to samples with practically infinite extent, waveguides are bounded and break this translation invariance. They effectively have an additional spatial dimension. Finally, the waveguide boundaries can be used to couple light into and out of the waveguide, which enables to observe the transversal field distribution inside the waveguide through its angular emission patterns.

1.2. X-ray waveguides

Compared to the optical spectral range, x-ray waveguiding is much less prominent and common. As a result of the refractive index taking values $n = 1-\delta+i\beta$ (with $\delta, \beta \ll 1$), x-ray waveguiding is based on total *external* reflection and appears when a "core" of low electron density is surrounded by a "cladding" of high electron density. It seems to contradict the fact that x-ray wavelengths, $\lambda \sim 10^{-10}$ m, are at the scale of individual atoms and smaller than typical interatomic distances. However, while waveguiding in the optical regime emerges at length scales of or below the optical wavelength, for x-rays, the minimal mode confinement is about $l_0 \approx \sqrt{\pi/(4r_\mathrm{e}\Delta\rho_\mathrm{e})}$, where r_e is the classical electron radius and $\Delta\rho_\mathrm{e}$ is the contrast in electron number density between core and cladding [BKV03]. This length interestingly is independent of the photon energy and between about 7 nm for platinum and 20 nm for silicon cladding (assuming an air core). It expresses that x-ray waveguides are *weakly confining* (or weakly guiding), since $l_0 \gg \lambda$. X-ray waveguiding was first demonstrated five decades ago by Spiller and Segmüller [SS74], leading to further advancements of planar waveguides since the 1990s [Fen+93; Lag+97; Zwa+99; Bon+02; Fuh+04] and the development of channel waveguides since the early 2000s [Pfe+02; Jar+05].

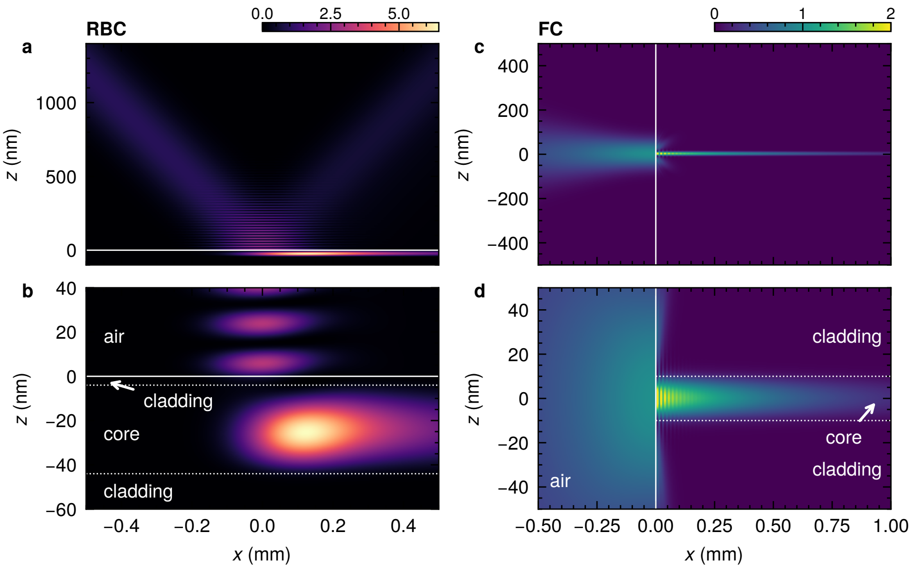

Figure 1.1.: Intensity in x-ray waveguides in the (**a** and **b**) resonant-beam-coupling (RBC) and (**c** and **d**) front-coupling (FC) geometries. **a** A collimated Gaussian beam from the left impinges in grazing incidence onto a thinned cladding and couples evanescently into leaky modes, while some of the beam is reflected. **c** A tightly focussed Gaussian beam from the left illuminates the front face of the waveguide and couples into guided modes, while the non-guided components are rapidly absorbed in the cladding. The lower panels show the waveguide of the respective upper panel in more detail. The color encodes the intensity relative to the illumination. Finite-difference frequency-domain simulations (2-dimensional) using the *Fresnel* library [Sol+21]. Parameters: 0.5 µm (RBC) and 0.1 µm (FC) beam waist diameter; 14.41 keV photon energy; Mo cladding, B_4C core.

Early (planar) x-ray waveguides were illuminated in grazing incidence so that the field could evanescently couple through a thin top cladding layer into the core – the so-called *resonant beam coupler* (RBC) geometry (see Fig. 1.1**a**) [Fen+93]. With the advancement of x-ray sub-micrometre focusing optics (see Ref. [SO20]), it became possible to couple into the front face of the waveguide – the *front-coupling* (FC) geometry (see Fig. 1.1**c**) [Fuh+04]. Nowadays, FC-waveguides are routinely used as optical elements to provide highly coherent and clean secondary sources of radiation ("coherence filters") for phase-contrast imaging and tomography (see for example Ref. [Sal+15b]). In the last two decades, x-ray waveguides have undergone some significant developments, mostly driven by the group of Tim Salditt in Göttingen, resulting in two main designs and fabrication methods: (i) Planar waveguides, fabricated by thin-film deposition [Sal+08; Krü+10; Krü+12] and (ii) air-core channel waveguides, fabricated by lithographic techniques [Jar+05; Neu+14; CHS15; Bar+15; HS16; Hof+16].

The channel waveguide design can not only generate clean wave fields but also allows flexible routing on the wafer. A number of layouts beyond straight channels have been demonstrated so far: off-axis holography with a double-waveguide device [FOS06], curved channels down to relatively small radii of curvature [Sal+15a], and beam splitters [HS16]. The main limitation of the design is its reliance on wafers as the single-material cladding. To date, silicon [Neu+14; Hof+16], germanium [HS16; Hof+16], silica (SiO_2) [Hof+16] (and to some extent tantalum [Sal+15a]) have been used. These materials lead to unfavourable performance for $E \gtrsim 10\,\mathrm{keV}$, however, either due to the low electron density of silicon, or the high absorption of germanium (and tantalum). Yet, moving to other materials is challenging because it requires the appropriate lithography protocols and adaption of the wafer bonding process.

Planar waveguides, on the other hand, are substantially simpler to fabricate and allow a much broader range of materials for better performance at higher photon energies. While they do not allow flexible routing, multiple planar waveguides can be stacked with precisely controllable layer thicknesses, which has for example been used to tailor the optical near field [Zho+17]. The layer structures can be freely designed from a broad range of materials.

X-ray waveguides distinctly alter the spatial modes of the electromagnetic field on the nanometer scale. On the one hand, the *incident* field in a waveguide under grazing-incidence illumination at a resonant angle is amplified (see Fig. 1.1**a**) and consequently also the fluorescence rate of embedded atoms [Jar+99; Sal+03]. On the other hand, the *emitted* fields are affected, too. In Ref. [Jia+20], directionally structured fluorescence from gold atoms inside a waveguide was observed. Similar observations were made with characteristic radiation due to irradiation with an electron beam [Jon+02]. Vassholz and Salditt even observed emission into resonant modes of a waveguide [VS21]. It has even been argued that an x-ray waveguide could significantly alter the density of photon states [Röh+05], leading to a Purcell-enhanced spontaneous emission rate [VS21]. (This is not the case, however, as we will clarify in this thesis.) To precisely control the coupling of emitters to the spatial field modes requires a theoretical model of the mode structure. This is challenging, because (i) the fields experience substantial material absorption (which can usually be neglected in the optical regime) and (ii) the weak confinement hampers numerical mode-finders.

1.3. Outline

In this thesis, we explore and investigate the physics of Mössbauer nuclei in planar x-ray waveguides. The principal structure of this thesis is a compilation of three journal articles (two of which are not yet published at the time of writing).

Chapter 2 presents the basic physical background and introduces the fundamental theories and experimental techniques that are used throughout this thesis. It is divided into three sections covering x-ray optics, Mössbauer nuclei, and collective excitation dynamics. A theoretical description of the coupled system of nuclei and electromagnetic fields in inhomogeneous materials based on classical electromagnetic Green's functions is introduced. It is kept on a rather general level without going into more specific geometries such as x-ray waveguides. The chapter is intended as a self-contained reference and can be considered a supplement to the cumulative dissertation.

Chapter 3 presents a *Nano-optical theory of planar x-ray waveguides* [LA24]. The theory in particular formalizes the notion of guided and resonant modes in absorbing waveguides. The most relevant results in the context of this thesis are (i) asymptotic expansions of the electromagnetic Green's functions for planar x-ray waveguides into resonant modes, together with (ii) a recipe to numerically compute all relevant coefficients for arbitrary layer structures. Based on these explicit expressions for the Green's functions, the theory also quantifies the emission rate from dipole emitters into the resonant modes, thereby clarifying that Purcell enhancement is negligible in x-ray waveguides.

Chapter 4, *Collective nuclear excitation dynamics in mono-modal x-ray waveguides* [Loh+24], reports on two experiments with Mössbauer nuclei in x-ray waveguides. They demonstrate for the first time (i) front-coupling into thin film x-ray waveguides with Mössbauer nuclei and (ii) detecting the delayed photons that leave the waveguide at its back end. The dynamical evolution of the collective nuclear excitation after impulsive illumination was investigated in the experiments. In the first experiment, the waveguides were illuminated in front-coupling geometry, in the second one in resonant-beam-coupling geometry (see Fig. 1.1). Depending on the geometry, two very distinct temporal emission characteristics were observed. These are explained by a unifying theoretical model, based on chapters 2.3 and 3, that also sheds new light on previous observations in reflection geometry.

In chapter 6, a *Direct measurement of resonant nuclear phase shift with a Young* *double-waveguide nano-interferometer* is being reported. While usually only the transmitted intensity can be measured and the phase shift is lost, here it was observed interferometrically. To that end, a nanoscopic double-waveguide interferometer, reminiscent of Young's double-slit experiment, was implemented. A Bayesian optimization approach was devised to quantitatively recover the phase shift from sparse interference pattern, each containing just a few photons. While chapter 4 considers impulsive broadband illumination and time-resolved measurements, here the waveguide is illuminated with highly monochromatic light and the measurements are energy-resolved.

Chapter 7 summarizes the results and gives an outlook.

References

[Ada+13] Bernhard W. Adams, Christian Buth, Stefano M. Cavaletto, Jörg Evers, Zoltán Harman, Christoph H. Keitel, Adriana Pálffy, Antonio Picón, Ralf Röhlsberger, Yuri Rostovtsev, and Kenji Tamasaku. "X-ray quantum optics." *Journal of Modern Optics* 60.1 (Jan. 2013), pp. 2–21. DOI: `10.1080/09500340.2012.752113`.

[Bar+15] M. Bartels, M. Krenkel, J. Haber, R. N. Wilke, and T. Salditt. "X-Ray Holographic Imaging of Hydrated Biological Cells in Solution." *Physical Review Letters* 114.4 (Jan. 2015), p. 048103. DOI: `10.1103/physrevlett.114.048103`.

[BKV03] C. Bergemann, H. Keymeulen, and J. F. van der Veen. "Focusing X-Ray Beams to Nanometer Dimensions." *Physical Review Letters* 91.20 (Nov. 2003), p. 204801. DOI: `10.1103/physrevlett.91.204801`.

[Boc+21] Lars Bocklage, Jakob Gollwitzer, Cornelius Strohm, Christian F. Adolff, Kai Schlage, Ilya Sergeev, Olaf Leupold, Hans-Christian Wille, Guido Meier, and Ralf Röhlsberger. "Coherent control of collective nuclear quantum states via transient magnons." *Science Advances* 7.5 (Jan. 2021). DOI: `10.1126/sciadv.abc3991`.

[Bon+02] J. H. H. Bongaerts, C. David, M. Drakopoulos, M. J. Zwanenburg, G. H. Wegdam, T. Lackner, H. Keymeulen, and J. F. van der Veen. "Propagation of a partially coherent focused X-ray beam within a planar X-ray waveguide." *Journal of Synchrotron Radiation* 9.6 (Nov. 2002), pp. 383–393. DOI: `10.1107/s0909049502016308`.

[Bür99] U. van Bürck. "Coherent pulse propagation through resonant media." *Hyperfine Interactions* 123–124.1–4 (Mar. 1999), pp. 483–509. DOI: `10.1023/a:1017080008712`.

[Cha+18] D. E. Chang, J. S. Douglas, A. González-Tudela, C.-L. Hung, and H. J. Kimble. "Colloquium: Quantum matter built from nanoscopic lattices of atoms and photons." *Reviews of Modern Physics* 90.3 (Aug. 2018), p. 031002. DOI: `10.1103/revmodphys.90.031002`.

[Che+22] Yu-Hsueh Chen, Po-Han Lin, Guan-Ying Wang, Adriana Pálffy, and Wen-Te Liao. "Transient nuclear inversion by x-ray free electron laser in a tapered x-ray waveguide." *Physical Review Research* 4.3 (July 2022), p. l032007. DOI: `10.1103/physrevresearch.4.l032007`.

[CHS15] H.-Y. Chen, S. Hoffmann, and T. Salditt. "X-ray beam compression by tapered waveguides." *Applied Physics Letters* 106.19 (May 2015), p. 194105. DOI: `10.1063/1.4921095`.

[Dir10] P. A. M. Dirac. *The principles of quantum mechanics*. 4th ed. International series of monographs on physics 27. Oxford [u.a.]: Clarendon Press, Oxford University Press, 2010. ISBN: 9780198520115.

[Fen+93] Y. P. Feng, S. K. Sinha, H. W. Deckman, J. B. Hastings, and D. P. Siddons. "X-ray flux enhancement in thin-film waveguides using resonant beam couplers." *Physical Review Letters* 71.4 (July 1993), pp. 537–540. DOI: 10.1103/physrevlett.71.537.

[FOS06] C. Fuhse, C. Ollinger, and T. Salditt. "Waveguide-Based Off-Axis Holography with Hard X Rays." *Physical Review Letters* 97.25 (Dec. 2006), p. 254801. DOI: 10.1103/physrevlett.97.254801.

[Fuh+04] Christian Fuhse, Ansgar Jarre, Christoph Ollinger, Jens Seeger, Tim Salditt, and Remi Tucoulou. "Front-coupling of a prefocused x-ray beam into a monomodal planar waveguide." *Applied Physics Letters* 85.11 (Sept. 2004), pp. 1907–1909. DOI: 10.1063/1.1791736.

[Hab+16] Johann Haber, Kai S. Schulze, Kai Schlage, Robert Loetzsch, Lars Bocklage, Tatiana Gurieva, Hendrik Bernhardt, Hans-Christian Wille, Rudolf Rüffer, Ingo Uschmann, Gerhard G. Paulus, and Ralf Röhlsberger. "Collective strong coupling of X-rays and nuclei in a nuclear optical lattice." *Nature Photonics* 10.7 (May 2016), pp. 445–449. DOI: 10.1038/nphoton.2016.77.

[Hab+17] Johann Haber, Xiangjin Kong, Cornelius Strohm, Svenja Willing, Jakob Gollwitzer, Lars Bocklage, Rudolf Rüffer, Adriana Pálffy, and Ralf Röhlsberger. "Rabi oscillations of X-ray radiation between two nuclear ensembles." *Nature Photonics* 11.11 (Oct. 2017), pp. 720–725. DOI: 10.1038/s41566-017-0013-3.

[Hee+15] Kilian P. Heeg, Johann Haber, Daniel Schumacher, Lars Bocklage, Hans-Christian Wille, Kai S. Schulze, Robert Loetzsch, Ingo Uschmann, Gerhard G. Paulus, Rudolf Rüffer, Ralf Röhlsberger, and Jörg Evers. "Tunable Subluminal Propagation of Narrow-band X-Ray Pulses." *Physical Review Letters* 114.20 (May 2015). DOI: 10.1103/physrevlett.114.203601.

[Hee+21] Kilian P. Heeg, Andreas Kaldun, Cornelius Strohm, Christian Ott, Rajagopalan Subramanian, Dominik Lentrodt, Johann Haber, Hans-Christian Wille, Stephan Goerttler, Rudolf Rüffer, Christoph H. Keitel, Ralf Röhlsberger, Thomas Pfeifer, and Jörg Evers. "Coherent X-ray-optical control of nuclear excitons." *Nature* 590.7846 (Feb. 2021), pp. 401–404. DOI: 10.1038/s41586-021-03276-x.

[Hof+16] Sarah Hoffmann-Urlaub, Philipp Höhne, Mike Kanbach, and Tim Salditt. "Advances in fabrication of X-ray waveguides." *Microelectronic Engineering* 164 (Oct. 2016), pp. 135–138. DOI: 10.1016/j.mee.2016.07.010.

[HS16] Sarah Hoffmann-Urlaub and Tim Salditt. "Miniaturized beamsplitters realized by X-ray waveguides." *Acta Crystallographica Section A* 72.5 (Aug. 2016), pp. 515–522. DOI: 10.1107/s205327331601144x.

[HT99] J. P. Hannon and G. T. Trammell. "Coherent γ-ray optics." *Hyperfine Interactions* 123–124.1–4 (Mar. 1999), pp. 127–274. DOI: 10.1023/a:1017011621007.

[Jar+05] A. Jarre, C. Fuhse, C. Ollinger, J. Seeger, R. Tucoulou, and T. Salditt. "Two-Dimensional Hard X-Ray Beam Compression by Combined Focusing and Waveguide Optics." *Physical Review Letters* 94.7 (Feb. 2005), p. 074801. DOI: 10.1103/physrevlett.94.074801.

[Jar+99] W. Jark, S. Di Fonzo, A. Cedola, and S. Lagomarsino. "The application of resonantly enhanced X-ray standing waves in fluorescence and waveguide experiments." *Spectrochimica Acta Part B: Atomic Spectroscopy* 54.10 (Oct. 1999), pp. 1487–1495. DOI: 10.1016/s0584-8547(99)00097-x.

[Jia+20] Zhang Jiang, Joseph W. Strzalka, Donald A. Walko, and Jin Wang. "Reconstruction of evolving nanostructures in ultrathin films with X-ray waveguide fluorescence holography." *Nature Communications* 11.1 (June 2020). DOI: 10.1038/s41467-020-16980-5.

[Jon+02] P. Jonnard, J.-M. Ândré, C. Bonnelle, F. Bridou, and B. Pardo. "Modulation of x-ray line intensity emitted by a periodic structure under electron excitation." *Applied Physics Letters* 81.8 (Aug. 2002), pp. 1524–1526. DOI: 10.1063/1.1502189.

[Kha+21] I. R. Khairulin, Y. V. Radeonychev, V. A. Antonov, and Olga Kocharovskaya. "Acoustically induced transparency for synchrotron hard x-ray photons." *Scientific Reports* 11.1 (Apr. 2021). DOI: 10.1038/s41598-021-86555-x.

[KP16] Xiangjin Kong and Adriana Pálffy. "Stopping Narrow-Band X-Ray Pulses in Nuclear Media." *Physical Review Letters* 116.19 (May 2016), p. 197402. DOI: 10.1103/physrevlett.116.197402.

[Krü+10] S. P. Krüger, K. Giewekemeyer, S. Kalbfleisch, M. Bartels, H. Neubauer, and T. Salditt. "Sub-15 nm beam confinement by two crossed x-ray waveguides." *Optics Express* 18.13 (June 2010), p. 13492. DOI: 10.1364/oe.18.013492.

[Krü+12] S. P. Krüger, H. Neubauer, M. Bartels, S. Kalbfleisch, K. Giewekemeyer, P. J. Wilbrandt, M. Sprung, and T. Salditt. "Sub-10nm beam confinement by X-ray waveguides: design, fabrication and characterization of optical properties." *Journal of Synchrotron Radiation* 19.2 (Jan. 2012), pp. 227–236. DOI: 10.1107/s0909049511051983.

[LA15] Wen-Te Liao and Sven Ahrens. "Gravitational and relativistic deflection of X-ray superradiance." *Nature Photonics* 9.3 (Feb. 2015), pp. 169–173. DOI: 10.1038/nphoton.2015.7.

[LA24] Leon M. Lohse and Petar Andrejić. "Nano-optical theory of planar x-ray waveguides." *Optics Express* 32.6 (Mar. 2024), p. 9518. DOI: 10.1364/oe.504206.

[Lag+97] S. Lagomarsino, A. Cedola, P. Cloetens, S. Di Fonzo, W. Jark, G. Soullié, and C. Riekel. "Phase contrast hard x-ray microscopy with submicron resolution." *Applied Physics Letters* 71.18 (Nov. 1997), pp. 2557–2559. DOI: 10.1063/1.119324.

[LAL25] Shin-Yu Lee, Sven Ahrens, and Wen-Te Liao. "Gravitationally sensitive structured x-ray optics using nuclear resonances." *Physical Review Research* 7.1 (Feb. 2025), p. 013158. DOI: 10.1103/physrevresearch.7.013158.

[Lif05] Ginés Lifante. *Integrated photonics. Fundamentals*. Chichester: Wiley, 2005. ISBN: 9780470848685.

[Loh+24] Leon M. Lohse, Petar Andrejić, Sven Velten, Malte Vassholz, Charlotte Neuhaus, Ankita Negi, Anjali Panchwanee, Ilya Sergeev, Adriana Pálffy, Tim Salditt, and Ralf Röhlsberger. *Collective nuclear excitation and pulse propagation in single-mode x-ray waveguides*. 2024. DOI: 10.48550/ARXIV.2403.06508.

[LPK12] Wen-Te Liao, Adriana Pálffy, and Christoph H. Keitel. "Coherent Storage and Phase Modulation of Single Hard-X-Ray Photons Using Nuclear Excitons." *Physical Review Letters* 109.19 (Nov. 2012), p. 197403. DOI: 10.1103/physrevlett.109.197403.

[Lud+15] Andrew D. Ludlow, Martin M. Boyd, Jun Ye, E. Peik, and P. O. Schmidt. "Optical atomic clocks." *Reviews of Modern Physics* 87.2 (June 2015), pp. 637–701. DOI: 10.1103/revmodphys.87.637.

[Mös58] Rudolf L. Mössbauer. "Kernresonanzfluoreszenz von Gammastrahlung in Ir^{191}." *Zeitschrift für Physik* 151.2 (Apr. 1958), pp. 124–143. DOI: 10.1007/bf01344210.

[Neu+14] H. Neubauer, S. Hoffmann, M. Kanbach, J. Haber, S. Kalbfleisch, S. P. Krüger, and T. Salditt. "High aspect ratio x-ray waveguide channels fabricated by e-beam lithography and wafer bonding." *Journal of Applied Physics* 115.21 (June 2014), p. 214305. DOI: 10.1063/1.4881495.

[Pei+21] E. Peik, T. Schumm, M. S. Safronova, A. Pálffy, J. Weitenberg, and P. G. Thirolf. "Nuclear clocks for testing fundamental physics." *Quantum Science and Technology* 6.3 (Apr. 2021), p. 034002. DOI: 10.1088/2058-9565/abe9c2.

[Pel+21] Emanuele Pelucchi, Giorgos Fagas, Igor Aharonovich, Dirk Englund, Eden Figueroa, Qihuang Gong, Hübel Hannes, Jin Liu, Chao-Yang Lu, Nobuyuki Matsuda, Jian-Wei Pan, Florian Schreck, Fabio Sciarrino, Christine Silberhorn, Jianwei Wang, and Klaus D. Jöns. "The potential and global outlook of integrated photonics for quantum technologies." *Nature Reviews Physics* 4.3 (Dec. 2021), pp. 194–208. DOI: 10.1038/s42254-021-00398-z.

[Pfe+02] F. Pfeiffer, C. David, M. Burghammer, C. Riekel, and T. Salditt. "Two-Dimensional X-ray Waveguides and Point Sources." *Science* 297.5579 (July 2002), pp. 230–234. DOI: 10.1126/science.1071994.

[PR59] R. V. Pound and G. A. Rebka. "Gravitational Red-Shift in Nuclear Resonance." *Physical Review Letters* 3.9 (Nov. 1959), pp. 439–441. DOI: 10.1103/physrevlett.3.439.

[PR60] R. V. Pound and G. A. Rebka. "Apparent Weight of Photons." *Physical Review Letters* 4.7 (Apr. 1960), pp. 337–341. DOI: 10.1103/physrevlett.4.337.

[Rad+20] Y. V. Radeonychev, I. R. Khairulin, F. G. Vagizov, Marlan Scully, and Olga Kocharovskaya. "Observation of Acoustically Induced Transparency for γ-Ray Photons." *Physical Review Letters* 124.16 (Apr. 2020), p. 163602. DOI: 10.1103/physrevlett.124.163602.

[RC21] Rudolf Rüffer and Aleksandr I. Chumakov. "Historical Developments and Future Perspectives in Nuclear Resonance Scattering." In: *Modern Mössbauer Spectroscopy*. Ed. by Yutaka Yoshida and Guido Langouche. Topics in Applied Physics. Springer Singapore, 2021, pp. 1–55. ISBN: 9789811594229. DOI: 10.1007/978-981-15-9422-9_1.

[RE21] Ralf Röhlsberger and Jörg Evers. "Quantum Optical Phenomena in Nuclear Resonant Scattering." In: *Modern Mössbauer Spectroscopy*. Ed. by Yutaka Yoshida and Guido Langouche. Topics in Applied Physics. Springer Singapore, 2021, pp. 105–171. DOI: 10.1007/978-981-15-9422-9_3.

[RES20] Ralf Röhlsberger, Jörg Evers, and Sharon Shwartz. "Quantum and Nonlinear Optics with Hard X-Rays." In: *Synchrotron Light Sources and Free-Electron Lasers*. Ed. by Eberhard J. Jaeschke, Shaukat Khan, Jochen R. Schneider, and Jerome B. Hastings. Springer International Publishing, 2020, pp. 1399–1431. DOI: 10.1007/978-3-030-23201-6_32.

[Röh+05] R. Röhlsberger, K. Schlage, T. Klein, and O. Leupold. "Accelerating the Spontaneous Emission of X Rays from Atoms in a Cavity." *Physical Review Letters* 95.9 (Aug. 2005). DOI: 10.1103/physrevlett.95.097601.

[Röh+10] R. Röhlsberger, K. Schlage, B. Sahoo, S. Couet, and R. Rüffer. "Collective Lamb Shift in Single-Photon Superradiance." *Science* 328.5983 (May 2010), pp. 1248–1251. DOI: 10.1126/science.1187770.

[Röh05] Ralf Röhlsberger. *Nuclear Condensed Matter Physics with Synchrotron Radiation*. Springer Tracts in Modern Physics. Springer Berlin Heidelberg, 2005. ISBN: 9783540446996. DOI: 10.1007/b86125.

[Sal+03] T. Salditt, F. Pfeiffer, H. Perzl, A. Vix, U. Mennicke, A. Jarre, A. Mazuelas, and T. H. Metzger. "X-ray waveguides and thin macromolecular films." *Physica B: Condensed Matter* 336.1–2 (Aug. 2003), pp. 181–192. DOI: 10.1016/s0921-4526(03)00288-6.

[Sal+08] T. Salditt, S. P. Krüger, C. Fuhse, and C. Bähtz. "High-Transmission Planar X-Ray Waveguides." *Physical Review Letters* 100.18 (May 2008), p. 184801. DOI: 10.1103/physrevlett.100.184801.

[Sal+15a] T. Salditt, S. Hoffmann, M. Vassholz, J. Haber, M. Osterhoff, and J. Hilhorst. “X-Ray Optics on a Chip: Guiding X Rays in Curved Channels.” *Physical Review Letters* 115.20 (Nov. 2015), p. 203902. DOI: 10.1103/physrevlett.115.203902.

[Sal+15b] Tim Salditt, Markus Osterhoff, Martin Krenkel, Robin N. Wilke, Marius Priebe, Matthias Bartels, Sebastian Kalbfleisch, and Michael Sprung. “Compound focusing mirror and X-ray waveguide optics for coherent imaging and nano-diffraction.” *Journal of Synchrotron Radiation* 22.4 (June 2015), pp. 867–878. DOI: 10.1107/s1600577515007742.

[She+23] Alexandra S. Sheremet, Mihail I. Petrov, Ivan V. Iorsh, Alexander V. Poshakinskiy, and Alexander N. Poddubny. “Waveguide quantum electrodynamics: Collective radiance and photon-photon correlations.” *Reviews of Modern Physics* 95.1 (Mar. 2023), p. 015002. DOI: 10.1103/revmodphys.95.015002.

[Shv+23] Yuri Shvyd’ko et al. “Resonant X-ray excitation of the nuclear clock isomer ^{45}Sc.” *Nature* 622.7983 (Sept. 2023), pp. 471–475. DOI: 10.1038/s41586-023-06491-w.

[Shv+96] Yu. V. Shvyd’ko, T. Hertrich, U. van Bürck, E. Gerdau, O. Leupold, J. Metge, H. D. Rüter, S. Schwendy, G. V. Smirnov, W. Potzel, and P. Schindelmann. “Storage of Nuclear Excitation Energy through Magnetic Switching.” *Physical Review Letters* 77.15 (Oct. 1996), pp. 3232–3235. DOI: 10.1103/physrevlett.77.3232.

[Smi+07] G. V. Smirnov, U. van Bürck, J. Arthur, G. S. Brown, A. I. Chumakov, A. Q. R. Baron, W. Petry, and S. L. Ruby. “Currents and fields reveal the propagation of nuclear polaritons through a resonant target.” *Physical Review A* 76.4 (Oct. 2007), p. 043811. DOI: 10.1103/physreva.76.043811.

[Smi99] G. V. Smirnov. “General properties of nuclear resonant scattering.” *Hyperfine Interactions* 123–124.1–4 (Mar. 1999), pp. 31–77. DOI: 10.1023/a:1017007520099.

[SO20] Tim Salditt and Markus Osterhoff. “X-ray Focusing and Optics.” In: *Nanoscale Photonic Imaging*. Ed. by Tim Salditt, Alexander Egner, and D. Russell Luke. Topics in Applied Physics. Cham: Springer International Publishing, 2020, pp. 71–124. ISBN: 9783030344139. DOI: 10.1007/978-3-030-34413-9_3.

[Sol+21] Jakob Soltau, Leon Merten Lohse, Markus Osterhoff, and Tim Salditt. “Finite-difference propagation for the simulation of x-ray multilayer optics.” *Optics Express* 29.25 (Dec. 2021), p. 41932. DOI: 10.1364/oe.445300.

[SS74] Eberhard Spiller and Armin Segmüller. “Propagation of x rays in waveguides.” *Applied Physics Letters* 24.2 (Jan. 1974), pp. 60–61. DOI: 10.1063/1.1655093.

[Thi+24] Peter G. Thirolf, Sandro Kraemer, Daniel Moritz, and Kevin Scharl. “The thorium isomer ^{229m}Th: review of status and perspectives after more than 50 years of research.” *The European Physical Journal Special Topics* (Jan. 2024). DOI: 10.1140/epjs/s11734-024-01098-2.

[Tie+24] J. Tiedau, M. V. Okhapkin, K. Zhang, J. Thielking, G. Zitzer, E. Peik, F. Schaden, T. Pronebner, I. Morawetz, L. Toscani De Col, F. Schneider, A. Leitner, M. Pressler, G. A. Kazakov, K. Beeks, T. Sikorsky, and T. Schumm. “Laser Excitation of the Th-229 Nucleus.” *Physical Review Letters* 132.18 (Apr. 2024), p. 182501. DOI: 10.1103/physrevlett.132.182501.

[Tür+19] Pierre Türschmann, Hanna Le Jeannic, Signe F. Simonsen, Harald R. Haakh, Stephan Götzinger, Vahid Sandoghdar, Peter Lodahl, and Nir Rotenberg. “Coherent nonlinear optics of quantum emitters in nanophotonic waveguides.” *Nanophotonics* 8.10 (Aug. 2019), pp. 1641–1657. DOI: 10.1515/nanoph-2019-0126.

[VS21] Malte Vassholz and Tim Salditt. “Observation of electron-induced characteristic x-ray and bremsstrahlung radiation from a waveguide cavity.” *Science Advances* 7.4 (Jan. 2021). DOI: 10.1126/sciadv.abd5677.

[Wen+16] Lars von der Wense, Benedict Seiferle, Mustapha Laatiaoui, Jürgen B. Neumayr, Hans-Jörg Maier, Hans-Friedrich Wirth, Christoph Mokry, Jörg Runke, Klaus Eberhardt, Christoph E. Düllmann, Norbert G. Trautmann, and Peter G. Thirolf. “Direct detection of the ^{229}Th nuclear clock transition.” *Nature* 533.7601 (May 2016), pp. 47–51. DOI: 10.1038/nature17669.

[WS20] Lars von der Wense and Benedict Seiferle. “The ^{229}Th isomer: prospects for a nuclear optical clock.” *The European Physical Journal A* 56.11 (Nov. 2020). DOI: 10.1140/epja/s10050-020-00263-0.

[YL13] Yutaka Yoshida and Guido Langouche, eds. *Mössbauer Spectroscopy: Tutorial Book*. Springer Berlin Heidelberg, 2013. ISBN: 9783642322204. DOI: 10.1007/978-3-642-32220-4.

[YL21] Yutaka Yoshida and Guido Langouche, eds. *Modern Mössbauer Spectroscopy: New Challenges Based on Cutting-Edge Techniques*. Vol. 137. Topics in Applied Physics. Springer Singapore, 2021. ISBN: 9789811594229. DOI: 10.1007/978-981-15-9422-9.

[Zho+17] Q. Zhong, M. Osterhoff, M. W. Wen, Z. S. Wang, and T. Salditt. “X-ray waveguide arrays: tailored near fields by multi-beam interference.” *X-Ray Spectrometry* 46.2 (Jan. 2017), pp. 107–115. DOI: 10.1002/xrs.2740.

[Zwa+99] M. J. Zwanenburg, J. F. Peters, J. H. H. Bongaerts, S. A. de Vries, D. L. Abernathy, and J. F. van der Veen. “Coherent Propagation of X Rays in a Planar Waveguide with a Tunable Air Gap.” *Physical Review Letters* 82.8 (Feb. 1999), pp. 1696–1699. DOI: 10.1103/physrevlett.82.1696.

2. Background and fundamentals

This chapter lays out the physical background and introduces the fundamental theories and experimental techniques that are used throughout the thesis. In section 2.1, we introduce some aspects of x-ray optics, in particular the scattering problem in inhomogeneous media (without nuclear resonances). In section 2.2, we first give an overview of Mössbauer nuclei and experimental techniques, then derive a theoretical description of nuclear resonances in inhomogeneous media, and finally discuss some collective resonant phenomena that arise in nuclear resonant scattering. Finally in section 2.3, we analyze how the nuclear excitation amplitude of an extended sample evolves in time and space in a nuclear forward scattering experiment and discuss its relation to certain quantum-theories of collective spontaneous decay and single-photon superradiance.

2.1. X-ray optics

2.1.1. General aspects

X-rays are electromagnetic radiation like visible light, just with shorter wavelengths $\lambda \sim 0.1\,\mathrm{nm}$. As a form of light, they adhere to the same physical principles and are commonly described by Maxwell's equations (see for example Ref. [Jac09]). Prominent differences to the visible spectrum arise in the interaction of x-rays with matter. With wavelengths shorter than interatomic distances and comparable to the radius of the hydrogen atom ($a_0 = 0.05\,\mathrm{nm}$), the internal structure of matter becomes relevant and gives rise to diffraction peaks in coherent x-ray scattering. Moreover, the energy of an individual x-ray photon, $\hbar\omega \sim 10\,\mathrm{keV}$, is in the order of the binding energy of atomic inner-shell electrons so that even weak x-ray beams can ionize atoms.

Compared to visible light, the interaction of x-rays with matter is weak so that lighter elements appear to be transparent to x-rays. In the hard x-ray regime (here: $\hbar\omega \gtrsim 5\,\mathrm{keV}$), refractive indices are typically expressed as

$$n = 1 - \delta + i\beta, \tag{2.1}$$

where $\delta, \beta \ll 1$ due to the weak interaction strength (see Fig. 2.1). Since the x-ray energies are higher than typical material resonance energies, the real part of the

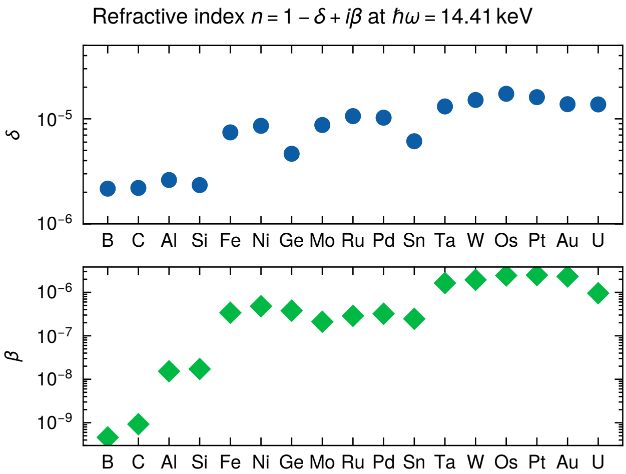

Figure 2.1.: Refractive indices of some elements at a photon energy of 14.41 keV, using densities of solid at 20 °C (data from Ref. [HGD93]).

refractive index is less than unity. While the weak interaction and the corresponding high penetration power of x-rays is a blessing for many applications, it comes with a cost and makes focussing of x-rays very challenging [SO20]. The best focus that can theoretically be achieved (disregarding near-field optics) is given by Abbe's diffraction limit $l \gtrsim \lambda/(2\,\mathrm{NA})$, where the numerical aperture (NA) is essentially equal to half the opening angle of the converging beam. While the x-ray wavelength λ is favourably small, it is difficult to produce strongly focusing large-diameter x-ray optics, so that the numerical aperture limits the focus in practice. Notwithstanding these difficulties, several groups have demonstrated extreme x-ray focusing below 10 nm using various approaches, from parabolic total-external reflection mirrors, over Fresnel zone plates, to multilayer zone plates and multilayer Laue lenses [Dre+24] (see Ref. [SO20] for an overview). So-called compound refractive lenses (CRL) [Sni+96] routinely provide moderate focusing down to below 100 nm [Sei+18].

X-rays make it seem particularly obvious that light is quantized – a single 10 keV photon produces about 2.8×10^3 electron-hole pairs upon absorption in a silicon sensor (3.6 eV electron-hole pair creation energy at room temperature), which can easily be registered and discriminated from thermal noise. The vast majority of experiments, however, involve purely *classical light* in the sense that the measured photon statistics can be accurately described by classical (statistical) optics and photodetection theory (see for example Ref. [MW95]). This can be explained by the fact that the already weak *linear* interactions in the x-ray regime imply even weaker non-linear interactions, making the generation of entangled photons pairs very inefficient. Yet, facilitated by the availability of x-ray free-electron lasers, the field of x-ray quantum optics is rapidly emerging (see the reviews [Ada+13] and [RES20]).

For a modern introduction to x-ray physics, refer to Als-Nielsen [Als17]. Paganin derives coherent x-ray optics in a refractive index formulation [Pag06]. X-ray diffraction is presented by Authier [Aut02] and in the classical textbook by James [Jam62].

2.1.2. X-ray interaction with matter

We briefly recall the theory of x-ray interaction with matter in the framework of classical electrodynamics, losely following Authier [Aut02] but in a slightly more general way to accommodate for the optical anisotropy and magnetic nature of nuclear resonant scattering. Throughout this chapter, we consider complex Fourier components of all involved signals at frequency ω, so that the time dependence has the form $\exp(-i\omega t)$. Note that this is the usual convention in modern optics but differs from the classical x-ray optics literature, where typically $\exp(i\omega t)$ is assumed.

Susceptibilities

Matter is described by its electric *polarization* $\mathbf{P}(\omega)$ and magnetic *magnetization* $\mathbf{M}(\omega)$. We assume a linear and causal response to applied fields $\mathbf{E}$ and $\mathbf{H}$ via [Jac09]

$$\mathbf{P}(\omega) = \epsilon_0 \underline{\chi}_{\mathrm{e}}(\omega) \cdot \mathbf{E}(\omega), \qquad \mathbf{M}(\omega) = \underline{\chi}_{\mathrm{m}}(\omega) \cdot \mathbf{H}(\omega). \tag{2.2}$$

The coefficients are the usual electric and magnetic *susceptibility* tensors $\underline{\chi}_{\mathrm{e}}(\omega)$ and $\underline{\chi}_{\mathrm{m}}(\omega)$. The fundamental electric and magnetic fields $\mathbf{E}$ and $\mathbf{B}$ are related to the auxiliary fields $\mathbf{D}$ and $\mathbf{H}$ via $\mathbf{D} = \epsilon_0\mathbf{E} + \mathbf{P}$ and $\mathbf{H} = \mathbf{B}/\mu_0 - \mathbf{M}$. Here ϵ_0 is the vacuum permittivity and μ_0 the vacuum permeability. Inserting (2.2) yields the constitutive relations

$$\mathbf{D}(\omega) = \epsilon_0\mathbf{E}(\omega) + \mathbf{P}(\omega) = \epsilon_0 \left[1 + \underline{\chi}_{\mathrm{e}}(\omega)\right] \cdot \mathbf{E}(\omega), \tag{2.3}$$

$$\mathbf{B}(\omega) = \mu_0\mathbf{H}(\omega) + \mu_0\mathbf{M}(\omega) = \mu_0 \left[1 + \underline{\chi}_{\mathrm{m}}(\omega)\right] \cdot \mathbf{H}(\omega). \tag{2.4}$$

The terms in brackets are the relative permittivities and permeabilities (tensors) $\underline{\epsilon} = 1 + \underline{\chi}_{\mathrm{e}}$ and $\underline{\mu} = 1 + \underline{\chi}_{\mathrm{m}}$. Most materials are isotropic, such that the susceptibility tensors simplify to scalars. Moreover, magnetic interactions are typically much weaker than electric interactions (at least with the atomic electrons) and typically neglected by setting $\chi_{\mathrm{m}} \approx 0$.

The vector wave equations

The fields are related by Maxwell's equations [Jac09]

$$\nabla \times \mathbf{E}(\mathbf{r},\omega) = i\omega \mathbf{B}(\mathbf{r},\omega), \qquad \nabla \times \mathbf{H}(\mathbf{r},\omega) = -i\omega \mathbf{D}(\mathbf{r},\omega). \tag{2.5}$$

These are often referred to as the *macroscopic* formulation, because they involve the auxiliary fields. Note, however, that von Laue's dynamical theory of x-ray diffraction in crystals – which is clearly *not* macroscopic – is based on (2.5), assuming a continuous (periodic) distribution of electric dipoles (see the discussion in Ref. [Aut02]). Taking the curl and inserting (2.3) and (2.4) yields the *vector wave equations* (see Ref. [Che99])

$$\nabla \times \underline{\mu}(\mathbf{r})^{-1} \nabla \times \mathbf{E}(\mathbf{r}) - \frac{\omega^2}{c^2} \underline{\epsilon}(\mathbf{r}) \cdot \mathbf{E}(\mathbf{r}) = 0, \tag{2.6a}$$

$$\nabla \times \underline{\epsilon}(\mathbf{r})^{-1} \nabla \times \mathbf{H}(\mathbf{r}) - \frac{\omega^2}{c^2} \underline{\mu}(\mathbf{r}) \cdot \mathbf{H}(\mathbf{r}) = 0. \tag{2.6b}$$

For isotropic media, multiplying both sides with μ and ϵ, respectively yields

$$\mu \nabla \times \mu(\mathbf{r})^{-1} \nabla \times \mathbf{E}(\mathbf{r}) - \frac{\omega^2}{c^2} n(\mathbf{r})^2 \cdot \mathbf{E}(\mathbf{r}) = 0, \tag{2.7a}$$

$$\epsilon \nabla \times \epsilon(\mathbf{r})^{-1} \nabla \times \mathbf{H}(\mathbf{r}) - \frac{\omega^2}{c^2} n(\mathbf{r})^2 \cdot \mathbf{H}(\mathbf{r}) = 0. \tag{2.7b}$$

where

$$n^2 \approx 1 + \chi_\mathrm{e} + \chi_\mathrm{m} \tag{2.8}$$

defines the refractive index and $c = 1/\sqrt{\epsilon_0 \mu_0}$ is the speed of light. Here, we have used that the susceptibilities are small compared to unity and neglected the second-order contribution in the refractive index. It immediately follows that

$$n \approx [1 + \chi_\mathrm{e} + \chi_\mathrm{m}]^{\frac{1}{2}} \approx 1 + \frac{1}{2}\chi_\mathrm{e} + \frac{1}{2}\chi_\mathrm{m} \tag{2.9}$$

The vector wave equations are rarely needed in their full generality in x-ray optics and we will simplify them, shortly.

Dyadic Green's functions

While the vector wave equations model free fields in the absence of source terms, fields produced by sources can be expressed in terms of dyadic Green's functions (see for example Refs. [Che99; NH12; Buh13]), solutions of

$$\mu(\mathbf{r})\nabla \times \mu(\mathbf{r})^{-1}\nabla \times \underline{\mathbf{G}}_{\mathrm{e}}(\mathbf{r},\mathbf{r}') - \frac{\omega^2}{c^2}n(\mathbf{r})^2\underline{\mathbf{G}}_{\mathrm{e}}(\mathbf{r},\mathbf{r}') = \mu(\mathbf{r})\delta(\mathbf{r}-\mathbf{r}')\underline{\mathbf{1}}, \tag{2.10a}$$

$$\epsilon(\mathbf{r})\nabla \times \epsilon(\mathbf{r})^{-1}\nabla \times \underline{\mathbf{G}}_{\mathrm{m}}(\mathbf{r},\mathbf{r}') - \frac{\omega^2}{c^2}n(\mathbf{r})^2\underline{\mathbf{G}}_{\mathrm{m}}(\mathbf{r},\mathbf{r}') = \epsilon(\mathbf{r})\delta(\mathbf{r}-\mathbf{r}')\underline{\mathbf{1}}, \tag{2.10b}$$

together with boundary conditions. We follow Buhmann's convention [Buh13] but other authors use slightly different ones. The magnetic Green's function is much less prevalent in the literature but is useful for magnetic dipoles. It is related to the electric Green's function through a duality transformation [Buh13]. The fields due to an oscillating dipole at $\mathbf{r}_0$ can be compactly written as

$$\mathbf{E}(\mathbf{r},\omega) = \frac{1}{\epsilon_0}\frac{\omega^2}{c^2}\underline{\mathbf{G}}_{\mathrm{e}}(\mathbf{r},\mathbf{r}_0,\omega)\cdot\mathbf{p}(\omega) \tag{2.11}$$

for an electric dipole moment $\mathbf{p}(\omega)$ or

$$\mathbf{H}(\mathbf{r},\omega) = \frac{\omega^2}{c^2}\underline{\mathbf{G}}_{\mathrm{m}}(\mathbf{r},\mathbf{r}_0,\omega)\cdot\mu(\mathbf{r}_0)\mathbf{m}(\omega) \tag{2.12}$$

for a magnetic dipole moment $\mathbf{m}(\omega)$ (see Ref. [Buh13]). Here we assume $\mathbf{r} \neq \mathbf{r}_0$. The Green's functions have singularities at the diagonal ($\mathbf{r} = \mathbf{r}'$) that demand special treatment [Che99]. The equations (2.10a) and (2.10b) can be greatly simplified in the macroscopic approximation, similar to the vector wave equations as we will discuss shortly.

Atomic scattering amplitudes

The photon interaction with matter is contained in the susceptibilities in the formalism discussed here. Their exact values and frequency-dependence can be relatively complicated, because electrons bound to an atomic potential are a rather complex many-body quantum system, in particular close to electronic transitions or binding energies. Refractive index and electric susceptibility are typically obtained from the *atomic scattering amplitude* f, which relates an incoming plane wave with amplitude A_0, wavevector $\mathbf{k}_0$, and polarization vector $\hat{\epsilon}_0$ to an outgoing wave, via

$$A_{\mathrm{f}} = f(\mathbf{k}_{\mathrm{f}},\hat{\epsilon}_{\mathrm{f}};\mathbf{k}_0,\hat{\epsilon}_0;\omega)\frac{e^{ikr}}{r}A_0, \tag{2.13}$$

where r is the distance from the atom. In general, f depends on polarization and wavevectors of incoming and scattered field. The polarization-dependence can in many cases be simplified to the factor $\hat{\epsilon}_{\mathrm{f}}^* \cdot \hat{\epsilon}_0$. The scattering amplitude has the dimension of length. The refractive index depends only on the *forward-scattering* amplitude with $\mathbf{k}_0 \approx \mathbf{k}_\mathrm{f}$, which we simply write as $f(\omega)$. The susceptibility becomes

$$\chi_\mathrm{e}(\omega) = 4\pi \frac{c^2}{\omega^2} \rho f(\omega), \tag{2.14}$$

where ρ the atomic number density (assuming a single species). The atomic scattering factor is usually written as

$$f(\omega) = f^0 + f'(\omega) + i f''(\omega), \tag{2.15}$$

where f^0 corresponds to Thomson scattering from free electrons and $f'(\omega) + i f''(\omega)$ are known as *dispersion corrections*. The (electronic) Thomson scattering amplitude is $f^0 = -r_\mathrm{e} Z$, where Z is the atomic number (= electrons/atom). This result can also be obtained by taking the high frequency limit $\omega \gg \omega_0$ in the classical forced-oscillator model for the atomic susceptibility (the Lorentz model) [Jac09].

Photon-matter interaction is mostly dominated by interactions with the atomic electrons, while *nuclear* Thomson scattering is extremely weak and typically neglected [HT99]. The electronic Thomson scattering amplitude can be written as $-Zr_\mathrm{e} = -Ze^2/(4\pi\epsilon_0 c^2 m_e)$. Thus, nuclear Thomson scattering is about $m_\mathrm{p}/m_\mathrm{e} \approx 1836$ times weaker, corresponding to the ratio between the proton mass m_p and the electron mass m_e (see Ref. [HT99]). Close to nuclear *resonances* however, nuclear *resonant* scattering can be very strong, since it does not depend on the mass. We will discuss this in detail in section 2.2.

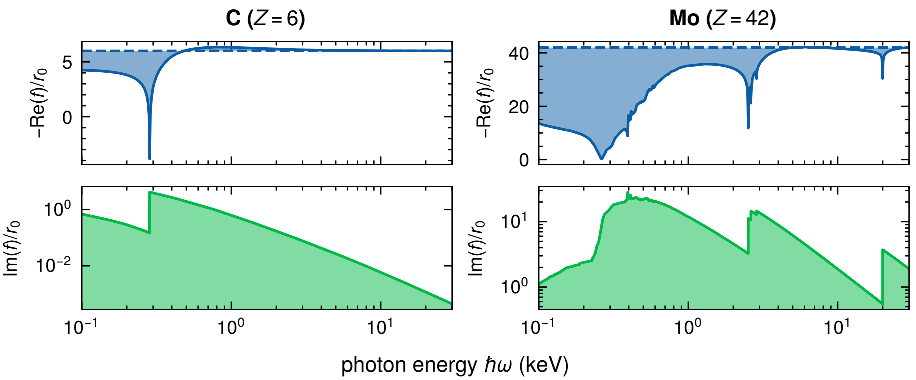

Figure 2.2.: Atomic scattering amplitudes for the elements carbon and molybdenum. The shaded area indicates the "dispersion correction" to the Thomson form factor. Steps in the imaginary part and cusps in the real part are clearly visible, which correspond to the inner-shell electron binding energies. (Data from Ref. [HGD93])

The dispersion corrections to the atomic scattering factor can be computed numerically and generally do not take a simple analytical form. A theoretical introduction within non-relativistic (Coulomb-gauge) quantum electrodynamics is given in Ref. [San08]. Experimental methods to measure the dispersion corrections are discussed in Ref. [Aut02]. In practice, one can use systematic tables of scattering factors for all relevant energy ranges and elements, based on numerical simulations [CL70; Cha95; Kis00] and experimental absorption spectra [HGD93], and also in the form of data libraries using multiple sources [CHK97]. Figure 2.2 shows exemplary values of $f(\omega)$. Measuring (or computing) $f'(\omega)$ *directly* is challenging, nevertheless, so that its value is often evaluated indirectly from tabulated values of the imaginary part $f''(\omega)$, which can be much easier obtained from attenuation measurements or simulated absorption cross sections.

Causality and Kramers-Kronig relations

The real and imaginary parts of the susceptibility depend on each other, simply because it describes a *causal* response of the medium to an input field. This is formalized in the Kramers-Kronig relations (see Ref. [Ste23] for a detailed derivation),

$$\mathrm{Re}\{\chi(\omega)\} = \frac{2}{\pi}\mathrm{P.V.}\int_0^\infty \mathrm{d}\omega' \frac{\omega' \,\mathrm{Im}\{\chi(\omega')\}}{\omega'^2 - \omega^2}. \tag{2.16}$$

The integral is meant as a Cauchy principal value. An identical relation can be derived for the dispersion corrections under certain assumptions [Jam62; Als17; HGD93],

$$f'(\omega) = \frac{2}{\pi}\mathrm{P.V.}\int_0^\infty \mathrm{d}\omega' \frac{\omega' f''(\omega')}{\omega'^2 - \omega^2}. \tag{2.17}$$

It is sometimes called “dispersion formula” [Jam62].

2.1.3. Macroscopic refractive optics

We will now go into a macroscopic picture, assuming that any changes of the susceptibilities occur on length scales much larger than the x-ray wavelength. For a detailed presentation, refer to Paganin [Pag06].

The scalar Helmholtz equation

The vector wave equations (2.6a) and (2.6b) are somewhat cumbersome, since they each involve three cartesian components of the fields, which are even coupled. Luckily, we can drastically simplify them in the x-ray regime. Applying a series of vector calculus identities and assuming that ϵ and μ vary slowly with respect to the wavelength yields

$$\mu\nabla \times \mu^{-1}\nabla \times \mathbf{E} \approx -\nabla^2\mathbf{E}, \tag{2.18}$$

so that (2.7a) simplifies to the scalar *Helmholtz equation*

$$\left\{\nabla^2 + k^2n^2(\mathbf{r},\omega)\right\} U(\mathbf{r},\omega) = 0, \tag{2.19}$$

with $k = \omega/c$, for each of the 6 cartesian components U of the fields (E_j, H_j for $j \in \{x, y, z\}$). Since the components decouple and all obey the very same differential equation, one can transition to a scalar theory.

The paraxial regime and numerical solutions

Assuming that the field can be written as a slowly varying perturbation (again, with respect to the wavelength) of a propagating plane wave permits further simplifications. We express the field as a plane-wave factor and an envelope,

$$U(\mathbf{r},\omega) = e^{ikx}u(\mathbf{r},\omega). \tag{2.20}$$

Inserting (2.20) into (2.19), and invoking the "slowly-varying-envelope approximation" $|\partial_x^2 u| \ll |k\partial_x u|$ yields

$$\left\{2ik\frac{\partial}{\partial x} + \nabla_\perp^2 + k^2(n^2-1)\right\}u = 0, \tag{2.21}$$

where $\nabla_\perp^2 = \partial_y^2 + \partial_z^2$ denotes the transverse Laplacian.

This paraxial wave equation is ideally suited to describe forward-propagating beams but it does not permit counter-propagating solutions [$\propto \exp(-ikx)$] and thereby fails to model back-reflection and standing waves. In the optical regime, it is hence of limited use in the analysis of scattering problems and mainly used to model beams in homogeneous media or the propagation in dielectric waveguides. In the x-ray regime, however, back-reflection is virtually non-existent (except for Bragg), inhomogeneous material distributions only weakly perturb an incident field, and this approximation hence has far greater applicability.

It is particularly well suited for numerical simulations of scattering problems. Equation (2.21) is of first order in the propagation direction, in contrast to (2.19), which is of second order. This allows to compute the entire field $u(\mathbf{r})$ from only the value of the complex wavefront $u_0(y,z)$ given in some plane, $u|_{x=x_0} = u_0$. Based on this, we have developed a software library, named "Fresnel", for the numerical propagation of x-ray beams through arbitrary spatial distributions of complex refractive indices, using a finite-difference frequency-domain approach. The name is motivated by the fact that (2.21) corresponds to the Fresnel diffraction regime and the Fresnel propagator formally describes an exact solution in vacuum. The simulation framework is detailed and benchmarked in Ref. [Sol+21], where we have applied it to numerically investigate x-ray multilayer optics for nanometer focussing.

2.2. Mössbauer nuclei

2.2.1. General aspects

Certain isotopes exhibit rather *long-lived* nuclear states (isomers) that are relatively *low-lying* above the nuclear ground state. Low-lying here means excitation energies from a few keV to 100 keV – much lower than the typical nuclear transition energies in the MeV regime. Long-lived means lifetimes in the order of a few ns, corresponding to linewidths in the order of neV. The 14.41 keV-level of ^{57}Fe, for example, has a linewidth of $\hbar\Gamma = 4.7\,\mathrm{neV}$, corresponding to a lifetime of $\tau = 141\,\mathrm{ns}$. An extreme example is ^{45}Sc with a transition energy of $E_0 = 12.39\,\mathrm{keV}$ but a linewidth of only $\hbar\Gamma = 1.4\,\mathrm{feV}$ [Shv+23]. A tabulated list of Mössbauer isotopes can be found in Ref. [Röh05]. Note that *electronic* transitions in the hard x-ray regime typically have linewidths in the order of 1 eV. This drastic difference is commonly attributed to a size effect by the following argument from Ref. [HT99]. The radiative decay rate Γ_{rad} of an electric dipole (E1) transition is proportional to the square of the electric transition dipole moment, which is roughly proportional to the radius of the charge distribution. With nuclear and atomic radii being different by a factor of about 10^4, nuclear transition lines must be about a factor of 10^8 sharper than electronic ones [HT99]. This reasoning is persuasive but fails to explain the lifetime for the very common magnetic dipole (M1) transitions. Those do not depend on the nuclear size and scale with the magnetic transition dipole moment, which is in the order of the nuclear magneton $\mu_{\mathrm{N}} = \hbar e/(2m_{\mathrm{p}})$ with proton mass m_{p} (see for example appendix B in Ref. [RS04]). Comparing E1-allowed and E1-forbidden transitions shows that the interaction matrix elements are often in the same order magnitude for similar transition energies [PEK08], unlike the electronic case.

The ultrasharp lines can be observed due to the recoil-free absorption and emission of photons interacting with nuclei that are bound in a solid – the *Mössbauer effect*, named after Rudolf Mössbauer, who discovered it in 1958 during experiments with cooled ^{191}Ir [Mös58a; Mös58b]. An unbound atom in a gas experiences a recoil upon absorption or emission of a photon due to momentum conservation, $|\Delta\mathbf{p}_{\mathrm{atom}}| =$

$|\mathbf{p}_{\text{ph}}| = E_0/c$, which leads to a shift of the photon energy,

$$\Delta E_{\text{recoil}} = \frac{|\Delta \mathbf{p}_{\text{atom}}|^2}{2m_{\text{a}}} = \frac{E_0^2}{2m_{\text{a}}c^2}, \tag{2.22}$$

where m_{a} is the atomic mass. For ^{57}Fe, this recoil energy is $E_{\text{recoil}} = 1.9\,\text{meV}$, roughly 10^6 times larger than the natural transition linewidth. If the atom is bound in a solid on the other hand, the recoil can be absorbed by the entire solid so that m_{a} in (2.22) is replaced by the mass of the solid and the recoil energy becomes negligible. However, the photon can still couple to vibrational modes of the solid – *phonons*. The probability of a recoil-free event, the zero-phonon probability, is called the *Lamb-Mössbauer factor* f_{LM} and can be defined as

$$f_{\text{LM}} = \exp\left\{-k^2 \left\langle x^2 \right\rangle\right\}, \tag{2.23}$$

where $k = E_0/(\hbar c) = 2\pi/\lambda_0$ is the resonance wave number and x the vibrational amplitude in the photon propagation direction [HT68; Mös76]. The notation $\langle\cdot\rangle$ indicates an ensemble average. Equation (2.23) illustrates that recoilless events rapidly become less probable with increasing photon energy and temperature. For this reason, only nuclei with nuclear levels below 100 keV are candidates for *Mössbauer isotopes* [RC21]. The 14.41 keV-resonance of ^{57}Fe exhibits the rather large value of $f_{\text{LM}} \approx 0.8$ in the solid matrix of bcc-iron at room temperature.

The radiative decay competes with non-radiative decay via internal conversion (IC), where an orbital inner-shell electron interacts with the nucleus, absorbs the excess energy and is emitted. The electronic core hole subsequently relaxes accompanied by emission of a fluorescence photon or an Auger electron. The ratio of the two decay channels is tabulated as the *branching ratio* (also *internal conversion coefficient* or *electron conversion coefficient*) $\alpha = \Gamma_{\text{IC}}/\Gamma_{\text{rad}}$. The total decay rate is $\Gamma \equiv \Gamma_{\text{IC}} + \Gamma_{\text{rad}}$, so that $\Gamma_{\text{rad}} = \Gamma/(1+\alpha)$. Internal conversion typically dominates substantially and α can be very large. For ^{57}Fe, it takes the relatively small value $\alpha = 8.56$ [Bha98], while for ^{45}Sc it becomes as large as $\alpha = 424$ [Shv+23] (other sources give $\alpha = 632$ [Bur08]).

The nuclear transitions have well-defined *multipolarity*. Most Mössbauer transitions are electric dipole-forbidden (with some exceptions, such as ^{181}Ta) because ground and excited state have the same parity. Consequently, the transition is either a magnetic dipole (M1), electric quadrupole (E2), magnetic quadrupole (M2), or in some cases a combination of two (M1+E2) transitions. The ^{57}Fe transition is tabulated as M1+E2 but commonly considered as a simple M1 transition, since the E2-contribution is negligibly small (mixing ratio $\delta = 2 \times 10^{-3}$ [Bha98]). We discuss the transitions in more detail in section 2.2.3.

The nucleus is a highly complex many-body quantum system (see for example Ref. [RS04]). In the absence of external (to the nucleus) fields, however, the nuclear energy levels can be characterized by a small number of quantities: energy E_0, nuclear spin

I, parity π, magnetic dipole moment μ, and electric quadrupole moment Q. Each energy level is further split into $2I + 1$ quantum states distinguished by the magnetic quantum number m. The energy degeneracy of these states is lifted through *hyperfine interactions* of the nucleus with external *hyperfine fields* – via magnetic Zeeman splitting and electric field gradients (EFG). In the presence of such hyperfine fields, the single transition line is split into a multiplet structure. Precise measurements of this multiplet structure are used in Mössbauer spectroscopy to extract the strength and orientation of the hyperfine fields and thereby obtain information about the magnetic and chemical environment of the nucleus (see for example Ref. [GG71]).

2.2.2. Experimental techniques

The ultra-narrow width of Mössbauer transition lines, many orders of magnitude sharper than anything else at these photon energies, are arguably their greatest strength, but also pose significant practical challenges [RC21]. The only source of such highly monochromatic radiation are the nuclei themselves. An alternative method to probe these extreme energy scales is based on broadband excitation with short pulses of synchrotron radiation, causing a temporal response on the time-scale that corresponds to the linewidth, the lifetime $\tau = \hbar/\Gamma$ (141 ns for ^{57}Fe), which can be resolved rather conveniently.

Energy-domain techniques

Conventional Mössbauer experiments utilize a radioactive parent isotope that decays to the Mössbauer isomer, which subsequently decays to the stable ground state by emission of the desired γ quant. For ^{57}Fe, a convenient parent isotope is ^{57}Co (see Fig. 2.3a). The photon energy can be tuned by controlled application of the Doppler effect. To that end, the source (or the sample) is mounted on a highly stabilized velocity transducer (the "Mössbauer drive") that is undergoing periodic motion with typical peak speed in the order of $v_{\mathrm{max}} \sim 10\,\mathrm{mm\,s^{-1}}$. This results in shifts of the photon energy of $\Delta E_{\mathrm{D}}(t) = E_0 v(t)/c$ that can be conveniently registered by synchronizing the photon detection events with the instantaneous speed of the velocity transducer (see Fig. 2.3b). The natural linewidth corresponds to $\Gamma \sim 0.1\,\mathrm{mm\,s^{-1}}$ for $E_0 = 14.4\,\mathrm{keV}$. A rather contemporary introduction to classical Mössbauer spectroscopy can be found in Ref. [YL13]. A modern perspective is given in Ref. [YL21]. The γ-ray source is typically used to illuminate a sample and measurements are taken as a function of "detuning" $\Delta = \omega - \omega_{\mathrm{ref}}$ (with respect to the resonance ω_{ref} of some reference absorber such as α-iron). Different channels can be detected:

- Transmission spectroscopy, measuring the transmitted γ-photons (see Fig. 2.3c).

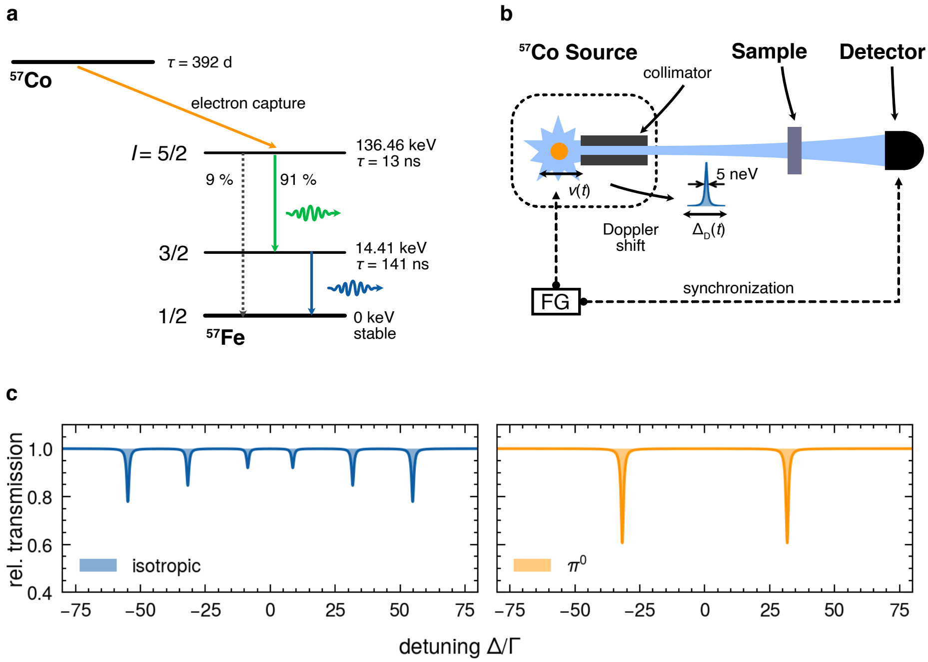

Figure 2.3.: Principle of conventional Mössbauer spectroscopy, at the example of ^{57}Fe. **a** The parent isotope decays via electron capture to the short-lived 136.5 keV-level of ^{57}Fe. Subsequently, it decays to the 14.4 keV isomer through emission of a 122 keV photon. This finally results in isotropic emission of 14.4 keV γ-rays with energy bandwidth of the natural linewidth Γ (if the source is sufficiently clean). **b** The radioactive source is mounted on a velocity transducer to shift the photon energy via the Doppler effect. A setup in transmission geometry is shown. **c** Absorption spectrum of α-iron, magnetically split by the ferromagnetic hyperfine field of 33 T. The left panel shows the spectrum for unpolarized light. The right panel shows the *hypothetical* spectrum corresponding to well-defined γ-ray polarization and hyperfine field magnetization axis (π^0-configuration).

- Conversion electron Mössbauer spectroscopy (CEMS), measuring the electrons ejected by internal conversion.
- Fluorescence spectrosopy, measuring for example the fluorescence photons radiated by the relaxation of core-hole states produced by internal conversion.

A useful side-effect of the cascaded decay is that the second γ-photon emission (14.4 keV) can be heralded by detection of the preceding γ-photon (122 keV) [Vag+14; HHW71].

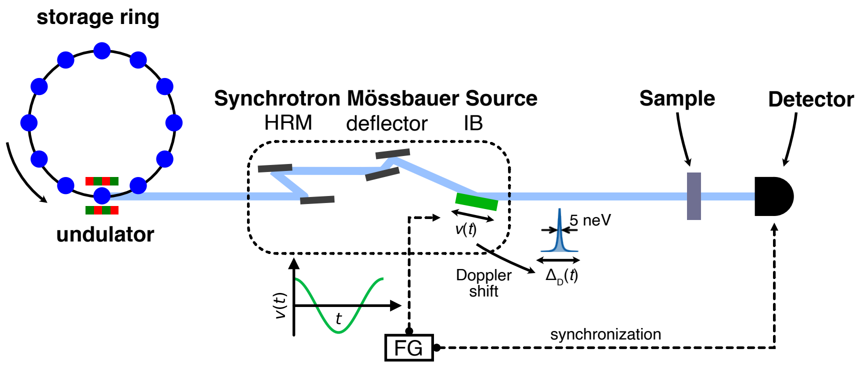

Figure 2.4.: Sketch (simplified) of the Synchrotron Mössbauer Source at the Nuclear Resonance beamline ID18 (now ID14) at ESRF [Pot+12]. It consists of a high-resolution ($\sim$ 10 meV bandwidth) monochromator (HRM), a deflector, and the iron borate (IB) crystal (isotopically enriched in ^{57}Fe), which filters the broadband synchrotron radiation to the natural linewidth.

The radioactive sources need to be rather large (millimeters) to produce sufficiently high count rates, making it very challenging to efficiently focus the radiation to the micrometer scale [Yos+08] or below, due to the low transversal coherence. This limitation was overcome by so-called *Synchrotron Mössbauer Sources*, which have been implemented at a few synchrotron beamlines [Mit+09; Pot+12]. Instead of a radioisotope, they use a nuclear monochromator based on a so-called pure nuclear crystal reflection (electronically forbidden but nuclearly allowed; see for example [Smi+11]) to filter a beam of synchrotron radiation down to a bandwidth in the order of the natural linewidth (see Fig. 2.4). Iron borate ($^{57}FeBO_3$, isotopically enriched in ^{57}Fe) single crystals are the current state of the art. Synchrotron Mössbauer sources produce highly monochromatic and collimated x-ray beams with practically zero background, which can be reliably focused to spot sizes below 0.5 μm (see chapter 5). A contemporary perspective on the technique is presented in Ref. [RC21].

Nuclear forward scattering

Short pulses of synchrotron radiation, provided by modern synchrotron storage rings, enable a complementary experimental method to probe Mössbauer resonances: nuclear forward scattering [Has+91; Bür+92] (see Ref. [Röh05] for a comprehensive introduction). The method harnesses that (i) nuclear lifetimes are in the order of 100 ns, which can be conveniently resolved by dedicated x-ray detectors and electronics, and (ii) present-day synchrotron light sources are pulsed with pulse durations in the order of 100 ps and repetition periods longer than the nuclear lifetime (for certain filling patterns of the electron storage ring). The principle can be readily explained in terms of a *response function* (see Ref. [Smi99]). The sample corresponds to a dispersive complex transmission function $K(\omega)$, which alters an incoming field by

$$E_{\text{out}}(\omega) = K(\omega)E_{\text{in}}(\omega). \tag{2.24}$$

The synchrotron pulse has a bandwidth in the order of 1 meV minimum, which is 10^5 times wider than Γ, but 10^3 times narrower than the scale of variations in the electronic refractive index. In the time-domain, this corresponds to a response function

$$E_{\text{out}}(t) \approx \int_{-\infty}^{\infty} K(t-t')E_{\text{in}}(t')\mathrm{d}t', \qquad K(t) = \int_{-\infty}^{\infty} K(\omega)e^{-i\omega t}\frac{\mathrm{d}\omega}{2\pi}, \tag{2.25}$$

where the response kernel can be written as

$$K(t) = K_0\delta(t) + K_{\text{res}}(t)\Theta(t). \tag{2.26}$$

The first term describes a non-resonant (constant within the pulse bandwidth) contribution and the second term the resonant one. As the response must be causal, the resonant response function contains the unit step function $\Theta(t)$. Equation (2.26) illustrates how the illuminating x-ray pulse is split into an instantaneous *prompt* response and a *delayed* response, which is caused by the nuclear resonances.

The prompt response is many orders of magnitude more intense than the delayed one, proportional to the ratio of illumination bandwidth to resonant bandwidth $\Delta E_{\text{in}}/(\hbar\Gamma)$. Typical monochromators that are installed at synchrotron beamlines have an energy resolution of $\Delta E/E \sim 10^{-4}$, providing a bandwidth in the order of 1 eV at 14.4 keV photon energy. For nuclear forward scattering, however, special *high-resolution monochromators* (HRM) are employed [Röh05], which filter the radiation down to a bandwidth of less than 1 meV and thereby reduce the prompt intensity by a factor of 10^3. Such a highly monochromatic 1 meV-pulse typically contains about 10^3 photons (assuming $5 \times 10^9\,\mathrm{s}^{-1}$ average photon flux and a pulse spacing of 192 ns), which corresponds to an average of 5×10^{-3} photons within the natural linewidth Γ of ^{57}Fe in each pulse. This, in combination with fast silicon *avalanche photo diode* (APD) detectors (see Ref. [Bar00]) and dedicated timing electronics, ultimately makes it possible to measure the delayed response with high temporal precision (sub-ns resolution) and very low noise (below $0.1\,\mathrm{s}^{-1}$). As an alternative to APDs, time-resolving pixel detectors based on the Timepix4 chip [Llo+22] are currently being developed and tested [Cor+24], which provide spatial (55 μm pixel pitch) in addition to the temporal resolution.

Another perspective onto the underlying physics of nuclear forward scattering is provided by the *nuclear exciton* picture. Since the timescale of the exciting pulse is significantly shorter than the lifetime of the isomer, excitation and relaxation can be considered as separate processes. Thus, the short synchrotron pulse coherently prepares a delocalized excited state of the nuclear ensemble – the *nuclear exciton* (see Ref. [Smi96] for a historical perspective). After the impulsive excitation, the nuclear ensemble collectively evolves, free of external driving, and subsequently undergoes spontaneous decay. The delayed photons thus result from the collaborative spontaneous emission of the nuclear exciton. This is discussed in more detail in section 2.3. This excited state is commonly expressed as [HT99; Röh05; Smi+07]

$$|\psi(\mathbf{k}_0)\rangle = \frac{1}{\sqrt{N}} \sum_{j=1}^{N} e^{i\mathbf{k}_0 \cdot \mathbf{r}_j} \left|g_1 g_2 \cdots g_{j-1} e_j g_{j+1} \cdots g_N\right\rangle, \tag{2.27}$$

where $\mathbf{k}_0$ is the wave vector of the excitation pulse, $\mathbf{r}_j$ the position of the jth nucleus and

$$\left|g_1 g_2 \cdots g_{j-1} e_j g_{j+1} \cdots g_N\right\rangle \tag{2.28}$$

denotes the state where the jth nucleus is excited and all other nuclei are in the ground state. Equation (2.27) is misleading, however, since it does *not* describe the state of a nuclear ensemble after excitation by a synchrotron radiation pulse [Ada09; Scu07] (also see section 2.3). It describes a dipole-moment-free non-classical state, as it might be prepared by a single photon source (see for example Ref. [Scu07]). Synchrotron pulses, on the other hand, should be considered classical fields and can be described as thermal light (see for example Ref. [Kun+97]). This issue will be discussed in more detail in section 2.3.

2.2.3. Basic theory

A theoretical model for the interaction of x-rays with Mössbauer nuclei requires two components. First, a description of the nuclear quantum states and energy levels under the influence of hyperfine fields, and second, a description of the coherent interaction of incident photons with a spatial ensemble of nuclei. The former problem is at the very heart of Mössbauer resonant absorption spectroscopy and thoroughly discussed in textbooks [GG71]. A compact and self-contained derivation can be found in Ref. [VR06]. The latter problem is of less relevance for classical Mössbauer absorption spectroscopy but vital for experiments with coherent synchrotron light, where it accounts for a rich variety of phenoma that are unique to Mössbauer optics. We will come back to both after a brief historical account.

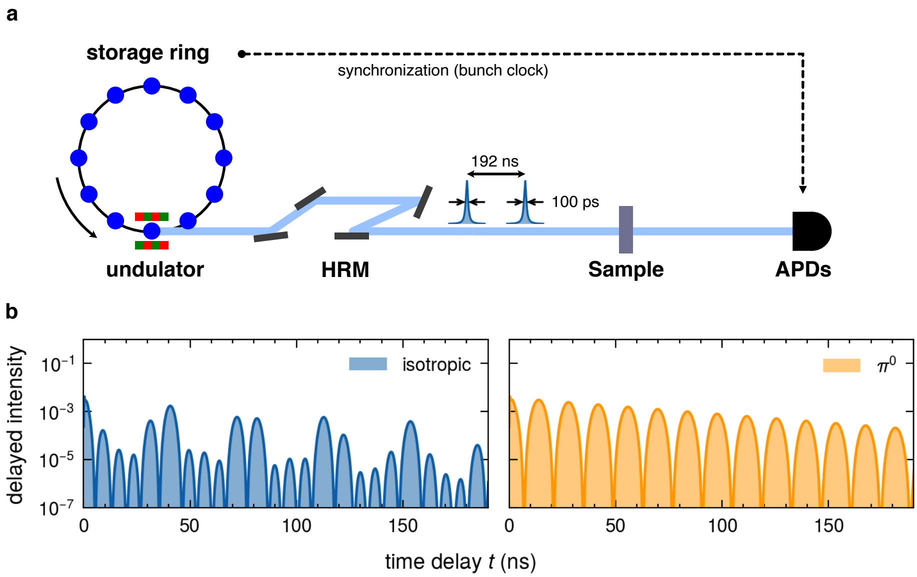

Figure 2.5.: Experimental principle of nuclear forward scattering. **a** Simplified setup, consisting of high-resolution monochromator (HRM), sample, and APD detectors. The time structure corresponds to the 40-bunch mode of PETRA III (DESY, Hamburg). **b** "Time-spectra" – delayed intensity $|K_{\mathrm{res}}(t)|^2$ for an α-iron foil with isotropic (left) and aligned (right) magnetization.

Historical account

The first theories for Mössbauer diffraction have been developed in the 1960s by Afanas'ev and Kagan [AK64; AK65; KAK79; Kag99] and by Hannon and Trammell [HT68; HT69]. In the latter papers, the single-photon scattering problem is rigorously solved within the framework of (Lorenz-gauge) relativistic quantum electrodynamics, first for a single atom, an ensemble of atoms, and all the way to dynamical diffraction from crystals [HCT74a; HCT74b]. A comprehensive review is given in Ref. [HT99]. In principle, the coherent elastic scattering amplitude,

$$f(\mathbf{e}_{\mathrm{f}}, \mathbf{k}_{\mathrm{f}}; \mathbf{e}_0, \mathbf{k}_0; \omega) = f_{\mathrm{e}} + f_{\mathrm{n}}, \tag{2.29}$$

for scattering from the electronic shell (f_{e}) and the nucleus (f_{n}) is derived. Importantly, the basic optical equations for coherent x-ray and γ-ray optics in the theory of Hannon and Trammell are "identical in form to the semiclassical equations used to develop the dynamical theory of x-ray diffraction" [HT99], but are in fact the exact single-photon coherent scattering equations from a collection of scatterers.

This microscopic scattering picture is readily translated to a *macroscopic* refractive optical model (see for example Refs. [BK68; Stu04]). Building on this, the reflectivity from stratified media containing Mössbauer nuclei under grazing incidence illumination has been derived [Röh99; Röh05]. The theories of Hannon and Trammell were implemented in the software package "CONUSS" [SG94; Stu00] and, more recently, in "Nexus" [Boc23]. The formalism accounts for electronic scattering, the relevant nuclear multipolar scattering terms, as well as interference between electronic and nuclear contributions. The "time-and-space picture", developed by Shvyd'ko [Shv99; Shv00], gives a time-domain formalism and allows to model time-dependent changes of the sample, such as magnetic switching or velocity variations on the same time scale as the nuclear lifetime. Theories for *incoherent* scattering have been developed in parallel (see for example Refs. [SK99; Stu04] and the references therein). These theories combined provide a comprehensive account of nuclear resonant scattering processes [Stu04] and have been employed to describe a plethora of experiments with highest accuracy (see for example Ref. [Röh05]). Nevertheless, the scattering formalism has some limitations. First, it does not explicitly account for the nuclear excitations – the intermediate state in the scattering picture – so that modeling the nuclear excitation dynamics requires a different approach (see for example Refs. [SK95; Smi+07]). Second, it is conceptionally limited to single-photon scattering and a rigorous generalization to the multi-photon case is impractical.

A number of quantum-optical theories have recently been developed [Len+20; KCP20], which overcome these limitations, in particular for cavity-like thin-film systems probed in reflection geometry (see Ref. [Len21] for a comprehensive overview). One particularly promising approach is based on the Gruner-Welsch quantization of the macroscopic formulation of Maxwell's equations [GW96], also known as *macroscopic quantum electrodynamics* (MQED) (see Refs. [SB08; Buh13]). The central object in these quantum-optical theories is the excitation state of the nuclear ensemble. Interactions between individual nuclei are modeled as dipole-dipole interactions (see Ref. [DKW02]), which are quantified by the classical electromagnetic Green's functions of the (absorbing) cavity-like dielectric environment.

While the underlying formalism is rather general, the particular theories are formulated in a "spin-wave" basis using the full translation invariance of dielectric environment, fields, and collective excitation states, as it is approximately realized in thin-film systems illuminated by a plane wave in reflection geometry. As a consequence, however, the theories are not applicable for propagation problems such as "forward-scattering" from a foil, and also not for resonant propagation in waveguides. To address this, Andrejić recently developed a theory [ALP24; And23] to model propagation problems, specifically in x-ray waveguides. The theory is derived ab initio from the Gruner-Welsch quantization [GW96] but explicitly models the field operators throughout, instead of eliminating them in favor of dipole-dipole interactions between the nuclei. It utilizes asymptotic expansions of the waveguide Green's function in terms of its spatial coordinates as derived in Ref. [LA24] (chapter 3 of this work) to obtain analytic solutions of the resonant propagation problem.

In the following, we present yet another theory that can be considered a semi-classical version of Ref. [ALP24]. We first solve the single-nucleus problem in a quantum-optical formalism and then consider the classical many-body problem (with classical fields and neglecting quantum correlations between the nuclei).

Nuclear Hamiltonian and hyperfine splitting

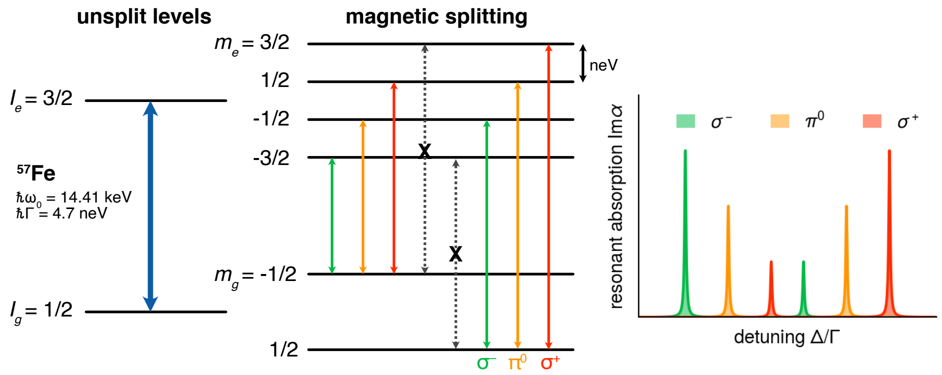

Figure 2.6.: Nuclear energy levels of the Mössbauer isotope ^{57}Fe and selection rules for M1 transitions. (left) Unsplit levels in the absence of hyperfine fields. (center) The levels are split by an static magnetic field. The M1-allowed transitions are also shown. (right) Absorption spectrum as a function of detuning $\Delta = \omega - \omega_0$. The color indicates the 3 possible polarizations corresponding to the change in magnetic quantum number.

The quantum many-body problem of the atomic nucleus is rather complex [RS04]. Luckily, the excitation states of the nucleus are highly rotationally symmetric and hence well described by their nuclear spin I, which corresponds to eigenstates of an angular momentum operator (see Ref. [Ros95]). We consider a ground level g and an excited level e with transition energy $\hbar\omega_0$ and nuclear spins I_g and I_e, respectively. Each level corresponds to a degenerate multiplet that differs in their respective magnetic quantum numbers m_g and m_e. The nuclear states are $|I_g\ m_g\rangle$ where $m_g \in \{-I_g, -I_g+1, \ldots, I_g\}$ and $|I_e\ m_e\rangle$ where $m_e \in \{-I_e, -I_e+1, \ldots, I_e\}$, denoting states in the angular momentum basis. The unperturbed nuclear Hamiltonian, in the absence of hyperfine fields, can then be written as

$$\hat{H}^0_{\text{nuc}} = \sum_{m_e=-I_e}^{I_e} \hbar\omega_0 \,|I_e\, m_e\rangle\langle I_e\, m_e| \,. \tag{2.30}$$

The nuclear states are generally perturbed by *hyperfine interactions*. Because of the rotational symmetry of the nucleus, the hyperfine interactions can be expanded in a multipole series and only the first 3 terms are kept: the *hyperfine fields* are then quantified as an electric monopole δ_{hf}, a magnetic hyperfine field $\mathbf{B}_{\text{hf}}$, and the electric field gradient $\underline{\mathbf{V}}_{\text{hf}}$. The perturbed nuclear Hamiltonian can be written as [GG71]

$$\hat{H}_{\text{nuc}} = \hat{H}^0_{\text{nuc}} + \hat{H}_{\text{hf}}(\delta_{\text{hf}}, \mathbf{B}_{\text{hf}}, \underline{\mathbf{V}}_{\text{hf}}). \tag{2.31}$$

A detailed discussion of the hyperfine Hamiltonian is out of scope here but can be found in Refs. [GG71; YL13]. Figure 2.6 exemplifies the nuclear energy levels under a magnetic hyperfine field. Importantly, the hyperfine Hamiltonian can be readily expressed in the angular momentum basis, $\langle I\, m|\hat{H}_{\text{nuc}}|I\, m'\rangle$, and the perturbation acts separately on the ground and excited states so that it does not introduce coupling between the two. As a result, the perturbed nuclear Hamiltonian $\hat{H}_{\text{nuc}}$ is no longer diagonal in the angular momentum basis. The new eigenstates, however, can be readily obtained by diagonalizing the perturbed Hamiltonian. This can be done separately in the subspaces of the ground and excited states. From this procedure, we obtain the perturbed eigenstates, which we denote by latin letters, $|j\rangle$, for the ground states and greek letters, $|\mu\rangle$, for the excited states. In this new basis, the perturbed Hamiltonian becomes

$$\hat{H}_{\text{nuc}} = \sum_{\mu} \hbar(\omega_0 + \Delta_\mu)\,|\mu\rangle\langle\mu| + \sum_{j} \hbar\Delta_j\,|j\rangle\langle j| \,, \tag{2.32}$$

with the transition matrix

$$|\mu\rangle = \sum_{m_e} |I_e\, m_e\rangle\,\langle I_e\, m_e|\mu\rangle \tag{2.33}$$

and accordingly for the ground states. The Δ_μ and Δ_j denote the hyperfine shifts of the nuclear levels.

The magnetic dipole operator

Having established the nuclear Hamiltonian, we now turn our attention to radiative transitions. Without hyperfine interactions, this becomes a textbook problem making heavy use of rotational symmetry (see Refs. [Ste23; Ros95]).

We consider a magnetic dipole interaction Hamiltonian,

$$\hat{H}_{\text{int}} = -\hat{\mathbf{m}} \cdot \mathbf{B}, \tag{2.34}$$

corresponding to, for example, the M1 transition of ^{57}Fe. Here $\hat{\mathbf{m}}$ denotes the magnetic moment operator and $\mathbf{B}$ the rapidly oscillating magnetic field (it is irrelevant whether the field is classical or quantized). Importantly, both operators are vectors (spherical tensors of first order). First, we separate the magnetic moment operator into the different transition terms. To that end, we define the projection operators

$$P_g = \sum_j |j\rangle\langle j|, \qquad P_e = \sum_\mu |\mu\rangle\langle\mu|, \tag{2.35}$$

which project onto the ground and excited subspaces, respectively. Then, we write

$$\begin{aligned}\hat{\mathbf{m}} &= (P_g + P_e)\hat{\mathbf{m}}(P_g + P_e)\\ &= P_g\hat{\mathbf{m}}P_g + P_e\hat{\mathbf{m}}P_e + P_g\hat{\mathbf{m}}P_e + P_e\hat{\mathbf{m}}P_g\\ &= \hat{\mathbf{m}}_{gg} + \hat{\mathbf{m}}_{ee} + \hat{\mathbf{m}}^+ + \hat{\mathbf{m}}^-.\end{aligned} \tag{2.36}$$

The diagonal elements do not vanish here because we are dealing with the *magnetic* dipole operator, which couples states with equal parity. The diagonal elements describe static magnetic moments and radiofrequency hyperfine transitions, which we are not interested in. In the following, we will be concerned with the operator mediating the coupling between ground an excited state, $\hat{\mathbf{m}}^+ = P_g\hat{\mathbf{m}}P_e$.

By virtue of the Wigner-Eckart theorem it follows that (the details are worked out in Appendix B.1)

$$\hat{\mathbf{m}}^+ = m_0 \sum_{\mu,j} |j\rangle\langle\mu|\, \mathbf{d}_{j\mu}, \tag{2.37}$$

with some yet to be specified dipole amplitude m_0 and normalized dipole moments

$$\mathbf{d}_{j\mu} = \sqrt{3}\sum_q C(1q, j \leftarrow \mu)\hat{\boldsymbol{\xi}}_q^*, \tag{2.38}$$

where

$$C(1q, j \leftarrow \mu) = \sum_{m_g,m_e} \langle I_e\, m_e|\mu\rangle \langle j|I_g\, m_g\rangle (-1)^{-m_g} \begin{pmatrix} I_e & I_g & 1\\ m_e & -m_g & q\end{pmatrix} \tag{2.39}$$

and $\hat{\boldsymbol{\xi}}_q$ are the spherical basis vectors, $\hat{\boldsymbol{\xi}}_0 = \hat{\mathbf{z}}$ and $\hat{\boldsymbol{\xi}}_{\pm1} = \mp(\hat{\mathbf{x}} \pm i\hat{\mathbf{y}})/\sqrt{2}$ [Ste23]. The term in parentheses denotes Wigner's 3j symbols. In the absence of hyperfine splitting, the coefficients reduce to

$$C(1q, m_g \leftarrow m_e) = (-1)^{-m_g} \begin{pmatrix} I_e & I_g & 1 \\ m_e & -m_g & q \end{pmatrix}, \tag{2.40}$$

which mathematically describes the selection rules (see Fig. 2.6).

The definition of $\mathbf{d}_{j\mu}$ in (2.38) ensures normalization so that

$$\sum_{j,\mu} |\mathbf{d}_{j\mu}|^2 = 3, \tag{2.41}$$

$$\sum_{j,\mu} \mathbf{d}_{j\mu} \otimes \mathbf{d}^*_{j\mu} = \underline{\mathbf{1}}, \tag{2.42}$$

as shown in Appendix B.1. The symbol "$\otimes$" denotes the dyadic product (or tensor product) of the two vectors and $\underline{\mathbf{1}} = \hat{\mathbf{x}} \otimes \hat{\mathbf{x}} + \hat{\mathbf{y}} \otimes \hat{\mathbf{y}} + \hat{\mathbf{z}} \otimes \hat{\mathbf{z}}$ the unit dyad (identity matrix in a matrix representation). Taking the orientational average yields

$$\langle \mathbf{d}_{j\mu} \otimes \mathbf{d}^*_{j\mu} \rangle = \frac{1}{3} |\mathbf{d}_{j\mu}|^2 \underline{\mathbf{1}}. \tag{2.43}$$

For vanishing hyperfine splitting, this can be further evaluated to

$$\frac{1}{3} |\mathbf{d}_{j\mu}|^2 = \sum_q \left\{ \begin{pmatrix} I_e & I_g & 1 \\ \mu & -j & q \end{pmatrix} \right\}^2, \tag{2.44}$$

giving values listed in Tab. 2.1.

Table 2.1.: Relative dipole moments $|\mathbf{d}_{j\mu}|^2/3$ for vanishing hyperfine fields, $j \equiv m_g$, $\mu \equiv m_e$ ($I_g = 1/2, I_e = 3/2$) . Only 6 out of the 8 possible transitions are realized as a result of the selection rules for M1 transitions.

$m_g \setminus m_e$	-3/2	-1/2	1/2	3/2
-1/2	1/4	1/6	1/12	0
1/2	0	1/12	1/6	1/4

Note how we have obtained an explicit expression for the transition dipole moment operator $\hat{\mathbf{m}}^+$ in (2.37) only from symmetry considerations – without having to integrate over any charge or current densities within the nucleus. Importantly, the nucleus "looks" like a set of dipoles to the electromagnetic field, the orientations $\mathbf{d}_{j\mu}$ of which we can readily compute via (2.38) for arbitrary hyperfine fields. The only undetermined quantity is the dipole amplitude m_0. In principle, it is tabulated in terms of so-called "reduced transition probabilities" for various nuclear transitions, but we can readily translate it to the lifetime.

Decay rates and dipole amplitude

The dipole amplitude is related to the spontaneous emission rate. As we have just established, each individual transition between an excited and a ground state is nothing more than a simple magnetic dipole transition – which is a solved problem. For a specific decay, the spontaneous emission rate is [Ste23]

$$\Gamma_{\mu\to j} = \frac{\mu_0 k_0^3}{3\pi\hbar} |\langle\mu|\hat{\mathbf{m}}|j\rangle|^2. \tag{2.45}$$

To get the total decay rate, we average over initial and sum over final states, resulting in

$$\begin{aligned}\Gamma_{\text{rad}} &= \frac{1}{2I_e+1}\sum_{\mu,j}\Gamma_{\mu\to j}\\ &= \frac{\mu_0 k_0^3}{3\pi\hbar}\frac{1}{2I_e+1}\sum_{\mu,j}|\langle\mu|\hat{\mathbf{m}}|j\rangle|^2\\ &= \frac{\mu_0 k_0^3}{\pi\hbar}\frac{1}{2I_e+1}|m_0|^2.\end{aligned} \tag{2.46}$$

Here we have used the normalization of $\mathbf{d}_{j\mu}$. The transition dipole amplitude is thus [using $\Gamma_{\text{rad}} = \Gamma/(1+\alpha)$]

$$|m_0|^2 = \frac{\Gamma}{1+\alpha}\frac{\pi\hbar}{\mu_0 k_0^3}(2I_e+1) = \frac{\Gamma/2}{1+\alpha}\frac{\sigma_0\hbar}{\mu_0 k}(2I_e+1) \tag{2.47}$$

with the natural dipole scattering cross-section (see for example Ref. [Ste23])

$$\sigma_0 = \frac{2\pi}{k_0^2} = \frac{2\pi c^2}{\omega_0^2}. \tag{2.48}$$

In the nuclear resonant scattering literature one often finds the effective radiative cross section

$$\sigma_{\text{rad}} = \frac{\sigma_0}{1+\alpha}\frac{2I_e+1}{2I_g+1}, \tag{2.49}$$

in terms of which the dipole amplitude becomes

$$|m_0|^2 = \frac{\sigma_{\text{rad}}\hbar}{\mu_0 k_0}\frac{\Gamma}{2}(2I_g+1). \tag{2.50}$$

As usual, the phase can be chosen arbitrarily, so we define m_0 to be real.

We amend these definitions to phenomenologically take into account the non-zero probability of inelastic scattering. The value of the radiative decay rate Γ_{rad} on the left hand side of (2.46) corresponds to its value at cryogenic temperatures, where $f_{\mathrm{LM}} \approx 1$. In general, the observed (elastic) decay rate would be smaller by $f_{\mathrm{LM}} < 1$, since some of the spontaneous decay events involve phonon creation or annihilation and do not contribute. Substituting $\Gamma_{\mathrm{rad}} \to f_{\mathrm{LM}}\Gamma_{\mathrm{rad}}$ accounts for this and yields the correct expressions. As a consequence, the dipole amplitude will be redfined as $m_0^2 \to f_{\mathrm{LM}} m_0^2$. For brevity, we absorb this factor into the cross section, so that it becomes

$$\tilde{\sigma}_{\mathrm{rad}} = f_{\mathrm{LM}} \frac{\sigma_0}{1+\alpha} \frac{2I_e + 1}{2I_g + 1}. \tag{2.51}$$

In the following we will drop the tilde but keep the definition (2.51) in mind.

Nuclear excitation amplitudes

We model the nuclear excitation using *nuclear transition operators* $\hat{\sigma}_{j\mu} = |j\rangle\langle\mu|$ in the Heisenberg representation. This rather abstract object corresponds to a physical quantity. From (2.37) we have

$$\hat{\mathbf{m}}^{+} = m_0 \sum_{\mu,j} \hat{\sigma}_{j\mu} \mathbf{d}_{j\mu}. \tag{2.52}$$

The expectation value of the transition operator thus corresponds to the (magnetic) transition dipole moment,

$$\langle\psi_0|\hat{\mathbf{m}}^{+}|\psi_0\rangle = m_0 \sum_{\mu,j} \langle\psi_0|\hat{\sigma}_{j\mu}|\psi_0\rangle\, \mathbf{d}_{j\mu}, \tag{2.53}$$

where $|\psi_0\rangle$ describes a state of the nuclear ensemble. For a single two-level system, consider the weakly excited state $|\epsilon\rangle = \sqrt{1-\epsilon^2}\,|g\rangle + \epsilon\,|e\rangle$. In this state, the expectation value of the transition operator evaluates to

$$\langle\epsilon|\hat{\sigma}_{ge}|\epsilon\rangle = \epsilon + \mathcal{O}(\epsilon^2). \tag{2.54}$$

The expectation value thus corresponds to the excitation amplitude ϵ.

Excitation and nuclear Bloch equations

To describe how the nuclear states evolve under x-ray illumination, we consider an x-ray field $\mathbf{B}(t)$ tuned close to the resonance energy $\hbar\omega_0$ of the nuclei. Separating the positive and negative frequencies, we write

$$\mathbf{B}(t) = \mathbf{B}^{+}(t)e^{-i\omega_0 t} + \mathbf{B}^{-}(t)e^{i\omega_0 t}. \tag{2.55}$$

In the rotating frame of the nuclear transition frequency (factoring out the $e^{-i\omega_0 t}$ oscillation of $\hat{\sigma}_{j\mu}$) and under the rotating wave approximation, the transition operators obey the optical Bloch equations [ALP24]

$$\frac{\mathrm{d}}{\mathrm{d}t}\hat{\sigma}_{j\mu}(t) = \left[i(\Delta_j - \Delta_\mu) - \frac{\Gamma}{2}\right]\hat{\sigma}_{j\mu}(t) - \frac{im_0}{\hbar}\left[\sum_\nu \hat{\sigma}_{\nu\mu}(t)\mathbf{d}^*_{j\nu} - \sum_k \hat{\sigma}_{jk}\mathbf{d}^*_{k\mu}\right]\cdot \mathbf{B}^{+}(t). \tag{2.56}$$

The ground state $\hat{\sigma}_{jk}$ and excited state $\hat{\sigma}_{\nu\mu}$ operators follow similar equations. Here, (2.56) assumes a *classical* field, which is sufficient for our purposes. The equations for field operators are formally identical and can be found in any quantum optics textbook for the case of a single transition (for example Ref. [Ste23]). Refs. [ALP24; And23] contain a detailed derivation of (2.56) within macroscopic quantum electrodynamics, all the way from the nuclear many-body and field Hamiltonians. For the current discussion it suffices to consider the expectation values, $\sigma_{j\mu} = \langle\hat{\sigma}_{j\mu}\rangle$, $\sigma_{\mu\nu} = \langle\hat{\sigma}_{\mu\nu}\rangle$, and $\sigma_{jk} = \langle\hat{\sigma}_{jk}\rangle$.

Weak excitation approximation

The nuclear resonances are so narrow that synchrotron pulses are too weak to excite them with appreciable probability, even under ideal focussing. In the weak excitation regime, we can approximate $\hat{\sigma}_{\mu\nu} \approx 0$ and $\hat{\sigma}_{jk} \approx \delta_{jk}/(2I_g + 1)$ in the right hand side of (2.56), resulting in the linearized Bloch equation

$$\frac{\mathrm{d}}{\mathrm{d}t}\sigma_{j\mu}(t) \approx \left[i(\Delta_j - \Delta_\mu) - \frac{\Gamma}{2}\right]\sigma_{j\mu}(t) + \frac{im_0}{\hbar(2I_g+1)}\mathbf{d}^*_{j\mu}\cdot \mathbf{B}^{+}(t). \tag{2.57}$$

This *weak-excitation approximation* is conceptually very different from the single-photon assumption that underlies the scattering theories [HT99]. In fact, equation (2.56) does not include any notion of photons. The relevant quantity is the pulse area (see for example Ref. [AE87]), which can be defined as

$$A = \frac{m_0}{\hbar(2I_g+1)}\int \mathbf{d}^*_{j\mu}\cdot \mathbf{B}^{+}(t)\mathrm{d}t, \tag{2.58}$$

where the integral goes over one pulse. The approximation is justified as long as $A \ll 1$. For a tightly focussed synchrotron beam, we estimate $A \sim 1{\times}10^{-6}$ (see Appendix A for a derivation). A few theoretical studies have been published, laying out experiments with the aim to excite a sizeable fraction of nuclei [Che+22] using x-ray free electron laser pulses as well as methods to detect signatures of the weakly nonlinear regime [WE23; HKE16]. Nonlinear optics with two-level system in general is also well-known in the literature (see for example the textbooks by Allen and Eberly [AE87] or Boyd [Boy20]). However, no *experimental* signatures of nonlinear effects with Mössbauer nuclei have been reported to date. It is even unclear to what degree (2.56) remains applicable in the nonlinear regime, because the extremely high intensities necessary to excite the nuclei will rapidly ionize the atoms, alter the hyperfine fields, and might have other side effects that are not captured by this simple model. That said, the weak-excitation approximation is very well justified for the present discussion.

Comparison to classical damped oscillator

The semi-classical optical Bloch equation (2.57) is closely related to a classical damped harmonic oscillator – the Lorentz model (see for example Refs. [Jac09; Ste23]). Let $\tilde{\mathbf{x}}(t) = \hat{\mathbf{e}}\tilde{x}(t)$ be the position of an electron bound to the nucleus by a linear spring and $\tilde{\mathbf{p}}(t) = -e\tilde{\mathbf{x}}(t)$ the atomic dipole moment. Separating the positive and negative frequency components, we have

$$\frac{\mathrm{d}^2}{\mathrm{d}t^2}\tilde{p}^+(t) + \Gamma\frac{\mathrm{d}}{\mathrm{d}t}\tilde{p}^+(t) + \omega_0^2\tilde{p}^+(t) = \frac{e^2}{m}\hat{\mathbf{e}}^* \cdot \tilde{\mathbf{E}}^+(t). \tag{2.59}$$

Factoring out the rapid oscillation of the resonance frequency (going to the rotating frame) via $\tilde{E}^+(t) = E^+(t)e^{-i\omega_0 t}$ and $\tilde{p}^+(t) = p^+(t)e^{-i\omega_0 t}$ and making the slowly-varying envelope approximation yields

$$\frac{\mathrm{d}}{\mathrm{d}t}p^+(t) = -\frac{\Gamma}{2}p^+(t) + i\frac{e^2}{2\omega_0 m}\hat{\mathbf{e}}^* \cdot \mathbf{E}^+(t), \tag{2.60}$$

which has the same form as (2.57). This illustrates that the quantum two-level system, governed by (2.57) in the linear regime, is formally identical to the fully classical Lorentz model (as discussed for example in Ref. [AE87]).

Magnetic polarizability

Equation (2.57) can be readily solved in the frequency domain. Fourier-transforming both sides yields

$$\sigma_{j\mu}(\omega) = -\frac{1}{\omega - (\Delta_\mu - \Delta_j) + i\Gamma/2}\frac{m_0}{\hbar(2I_g + 1)}\mathbf{d}_{j\mu}^* \cdot \mathbf{B}^+(\omega), \tag{2.61}$$

showing that $\sigma_{j\mu}$ is proportional to the magnetic field. Since $\sigma_{j\mu}$ is related to the magnetic dipole moment through (2.52), we can express the proportionality constant as the *magnetic polarizability* $\underline{\boldsymbol{\alpha}}_{\mathrm{m}}$,

$$\mathbf{m}(\omega) = \underline{\boldsymbol{\alpha}}_{\mathrm{m}}(\omega) \cdot \mathbf{B}^{+}(\omega), \tag{2.62}$$

which becomes

$$\begin{aligned}\underline{\boldsymbol{\alpha}}_{\mathrm{m}}(\omega) &= -\frac{m_0^2}{\hbar(2I_g+1)} \sum_{\mu,j} \frac{\mathbf{d}_{j\mu} \otimes \mathbf{d}_{j\mu}^{*}}{\omega - \Delta_\mu + \Delta_j + i\Gamma/2} \\ &= -\frac{\sigma_{\mathrm{rad}}}{\mu_0 k_0} \frac{\Gamma}{2} \sum_{\mu,j} \frac{\mathbf{d}_{j\mu} \otimes \mathbf{d}_{j\mu}^{*}}{\omega - \Delta_\mu + \Delta_j + i\Gamma/2}.\end{aligned} \tag{2.63}$$

Magnetization and susceptibility

In a homogeneous medium with nuclear number density ρ, the microscopic quantities are readily translated to the macroscopic magnetization

$$\mathbf{M}^{+} \equiv \rho \mathbf{m}^{+} \tag{2.64}$$

and the (macroscopic) magnetic susceptibility

$$\underline{\chi}_{\mathrm{m}}(\omega) = \rho \mu_0 \underline{\boldsymbol{\alpha}}_{\mathrm{m}}(\omega). \tag{2.65}$$

Note that we assume a simple linear relation between polarizability and susceptibility. Lorentz-Lorenz corrections (see for example chapter 2.3 in Ref. [BW19]) can safely be neglected because of the small value of α_{m}. The magnetic susceptibility relates the magnetization to the magnetic field via

$$\mathbf{M}^{+}(\omega) = \underline{\chi}_{\mathrm{m}}(\omega)\mathbf{H}^{+}(\omega) = \frac{1}{\mu_0}\underline{\chi}_{\mathrm{m}}(\omega)\mathbf{B}^{+}(\omega), \tag{2.66}$$

where we have used $\mathbf{H}^{+} = \mathbf{B}^{+}/\mu_0$, assuming an (otherwise) non-magnetic environment. The susceptibility then becomes

$$\underline{\chi}_{\mathrm{m}}(\omega) = -\frac{\rho\sigma_{\mathrm{rad}}}{k_0} \frac{\Gamma}{2} \sum_{\mu,j} \frac{\mathbf{d}_{j\mu} \otimes \mathbf{d}_{j\mu}^{*}}{\omega - \Delta_\mu + \Delta_j + i\Gamma/2}, \tag{2.67}$$

which simplifies to

$$\underline{\chi}_{\mathrm{m}}(\omega) = -\frac{\rho\sigma_{\mathrm{rad}}}{k_0} \frac{\Gamma/2}{\omega + i\Gamma/2} \underline{\mathbf{1}} \tag{2.68}$$

in the absence of hyperfine splitting [see (2.42)]. While (2.68) is diagonal, hyperfine fields can turn the nuclei optically active, which is expressed in the tensorial form of the susceptibility in (2.67).

We have obtained an optical model of nuclear resonant media in terms of a (magnetic) susceptibility, which can be plugged into the Helmholtz equations or the vector wave equations (2.6a) and (2.6b) to solve, for example, transmission through resonant media as outlined in Ref. [Stu04]. In the isotropic case, the magnetic susceptibility can readily be absorbed into the complex refractive index of the non-resonant environment n, so that

$$n_{\mathrm{res}}(\omega) = n(\omega_0)\sqrt{1 + \chi_{\mathrm{m}}(\omega)} \approx n(\omega_0) + \frac{1}{2}\chi_{\mathrm{m}}(\omega). \tag{2.69}$$

This result is identical to the refractive index [Stu04] obtained from QED-derivations of the nuclear scattering amplitude [SG94]. We were able to avoid the QED-formalism entirely, because the resonant interaction with the nuclei are very accurately described as simple magnetic dipole transitions, for which the interaction can be modeled with optical Bloch equations.

In principle, this provides a complete theoretical foundation to model a wide range of nuclear resonant forward scattering problems, including reflection from stratified media in a matrix formalism [Röh99], as well as propagation through general inhomogeneous media using the finite-difference frequency-domain approach mentioned in section 2.1.3 (see Ref. [Sol+21]).

2.2.4. A Green's function perspective

There are good reasons *not* to absorb the nuclear resonance into a strongly dispersive refractive index, but to separate resonant and non-resonant solutions. First, the nuclear resonance linewidth is many orders of magnitude narrower than any changes in the electronic refractive index. This suggests to solve the non-resonant scattering problem once and then model the resonant response separately. Second, the refractive-index formulation obscures the nuclear excitation state.

Both can be addressed by a Green's function approach. The general idea is to find the classical electromagnetic Green's function of the non-resonant dielectric environment and use it to describe the fields emitted by the nuclei. Finding the Green's function is equivalent to solving the non-resonant scattering problem.

Emitted field

Suppose that we have solved the non-resonant scattering problem and have found $\underline{\mathbf{G}}_{\mathrm{m}}(\mathbf{r}, \mathbf{r}', \omega)$, the magnetic Green's function of the (dielectric) environment *without* the nuclear resonances as defined in (2.10b). The field that is emitted by the nuclei through their magnetic transition dipole moments can be written as [see (2.12)]

$$\mathbf{B}^+_{\text{nuc}}(\mathbf{r},\omega) = \mu_0 k^2 \sum_i \underline{\mathbf{G}}_{\text{m}}(\mathbf{r},\mathbf{r}_i,\omega+\omega_0)\cdot \mathbf{m}^+_i(\omega), \tag{2.70}$$

where $k = (\omega+\omega_0)/c$. Interestingly, (2.70) can be derived consistently within macroscopic quantum electrodynamics, so that $\mathbf{B}^+$ and $\mathbf{m}^+$ can be replaced by their corresponding operators [ALP24; And23]. A general solution for the magnetic field can then be written as

$$\mathbf{B}^+ = \mathbf{B}^+_0 + \mathbf{B}^+_{\text{nuc}}, \tag{2.71}$$

where $\mathbf{B}^+_0$ denotes a *free* (unaffected by the nuclei) solution of the vector wave equations or the Helmholtz equation, which is subject to boundary conditions.

The resonant scattering problem

Equation (2.70) provides an alternative formulation of the resonant scattering problem. Substituting the polarizability (2.62) into (2.70) yields the Lippmann-Schwinger-type equation

$$\mathbf{B}^+(\mathbf{r},\omega) = \mathbf{B}^+_0(\mathbf{r},\omega) + \mu_0 k \sum_i \underline{\mathbf{G}}_{\text{m}}(\mathbf{r},\mathbf{r}_i,\omega+\omega_0)\cdot \underline{\boldsymbol{\alpha}}_{\text{m}}(\omega)\cdot \mathbf{B}^+(\mathbf{r}_i,\omega). \tag{2.72}$$

It is particularly useful when the geometry allows an analytical solution (or approximation) of the Green's function.

To illustrate the approach, consider a homogeneous slab of isotropic resonant material, which is illuminated by a plane wave as sketched in Fig. 2.7. Assuming an average nuclear number density of ρ, we can describe the ensemble as a continuum, so that

$$\begin{aligned}\mathbf{B}^+_{\text{nuc}}(\mathbf{r},\omega) &= \mu_0 \rho k^2\, \text{P.V.}\int \mathrm{d}\mathbf{r}'\, \underline{\mathbf{G}}_{\text{m}}(\mathbf{r},\mathbf{r}',\omega+\omega_0)\cdot \underline{\boldsymbol{\alpha}}_{\text{m}}(\omega)\cdot \mathbf{B}^+(\mathbf{r}',\omega)\\ &= k^2 \int_0^L \mathrm{d}x'\, \underline{\mathbf{G}}^{\text{ps}}_{\text{m}}(x,x',\omega+\omega_0)\cdot \underline{\chi}_{\text{m}}(\omega)\cdot \mathbf{B}^+(x',\omega).\end{aligned} \tag{2.73}$$

where (see Appendix B.2.1)

$$\underline{\mathbf{G}}^{\text{ps}}_{\text{m}}(x,x',\omega+\omega_0) = \int \mathrm{d}y'\mathrm{d}z' \underline{\mathbf{G}}_{\text{m}}(\mathbf{r},\mathbf{r}',\omega+\omega_0) = \frac{in}{2k} e^{ikn|x-x'|}\underline{\mathbf{1}}_{\perp}, \tag{2.74}$$

which is the Green's function of a planar source at x', extending coherently over y and z. The symbol $\underline{\mathbf{1}}_{\perp} = \hat{\mathbf{y}}\otimes\hat{\mathbf{y}} + \hat{\mathbf{z}}\otimes\hat{\mathbf{z}}$ denotes the transversal unit dyad. Crucially, we can use the *bulk* Green's function here (for a medium stretching to infinity) because reflection at the interfaces ($x = 0$ and $x = L$) is practically non-existent in the x-ray regime. Assuming an isotropic resonance yields

$$B^+_{\mathrm{nuc}}(x,\omega) = \frac{ikn\chi_{\mathrm{m}}(\omega)}{2}\int_0^L \mathrm{d}x'\, e^{ikn|x-x'|}B^+(x',\omega). \tag{2.75}$$

The field at depth x in (2.75) contains upstream ($0 \le x' \le x$) and downstream ($x \le x' \le L$) contributions. We make the *forward-scattering* approximation to neglect the downstream contributions (see Ref. [And23]). Consequently,

$$e^{-iknx}B^+_{\mathrm{nuc}}(x,\omega) = \frac{ikn\chi_{\mathrm{m}}(\omega)}{2}\int_0^x \mathrm{d}x'\, e^{-iknx'}B^+(x',\omega). \tag{2.76}$$

Inserting the free solution $B^+_0(x,\omega) = B_{\mathrm{in}}(\omega)e^{iknx}$ and recalling that $B^+ = B^+_0 + B^+_{\mathrm{nuc}}$, we obtain

$$e^{-iknx}B^+(x,\omega) = B_{\mathrm{in}}(\omega) + \frac{ikn\chi_{\mathrm{m}}(\omega)}{2}\int_0^x \mathrm{d}x'\, e^{-iknx'}B^+(x',\omega), \tag{2.77}$$

which is solved by

$$B^+(x,\omega) = B_{\mathrm{in}}(\omega)e^{iknx}\exp\left[\frac{ikn\chi_{\mathrm{m}}(\omega)x}{2}\right]. \tag{2.78}$$

Equation (2.78) is identical to the solution one obtains by assuming the resonant refractive index $n_{\mathrm{res}}(\omega) = n[1+\chi_{\mathrm{m}}(\omega)/2]$. This Green's-function approach, however, is readily generalized to more complicated dielectric environments, such as waveguides [ALP24].

Nuclear excitation dynamics

Instead of solving for the field, one can consider the nuclear excitations σ_{ge} and eliminate the field into dipole-dipole coupling terms. To present the essential features of this approach, we neglect the magnetic states and consider a single transition between g and e (thus, a spin-1/2 system). We again split the field into nuclear and free components [see (2.71)]. Fourier-transforming (2.57) and inserting (2.70) yields

$$\begin{aligned} -i\omega\sigma^i_{ge}(\omega) &\approx -\frac{\Gamma}{2}\sigma^i_{ge}(\omega) + \frac{im_0}{\hbar}\mathbf{d}^*\cdot\mathbf{B}^+(\omega) \\ &= -\frac{\Gamma}{2}\sigma_{ge}(\omega) + i\Omega(\mathbf{r}_i,\omega) + i\sum_j g_{ij}(\omega)\sigma^j_{ge}(\omega) \end{aligned} \tag{2.79}$$

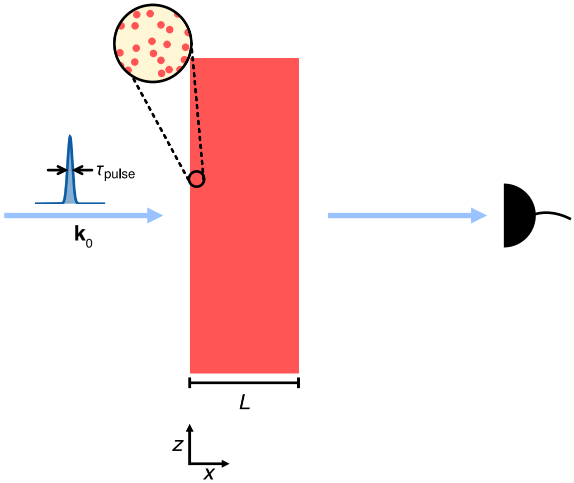

Figure 2.7.: A homogeneous slab of resonant material is illuminated by a short pulse of plane waves in normal incidence (resonant forward scattering).

with dipole-dipole coupling terms

$$
\begin{aligned}
g_{ij}(\omega) &= \frac{\mu_0 m_0^2}{\hbar} k^2 \mathbf{d}^* \cdot \underline{\mathbf{G}}_{\mathrm{m}}(\mathbf{r}, \mathbf{r}_i, \omega + \omega_0) \cdot \mathbf{d} \\
&= \sigma_{\mathrm{rad}} k \frac{\Gamma}{2} \mathbf{d}^* \cdot \underline{\mathbf{G}}_{\mathrm{m}}(\mathbf{r}, \mathbf{r}_i, \omega + \omega_0) \cdot \mathbf{d}
\end{aligned}
\tag{2.80}
$$

and the free (driving) field is expressed as a Rabi frequency $\Omega(\mathbf{r}_i, t) = (m_0/\hbar)\mathbf{d}^* \cdot \mathbf{B}_0^+(\mathbf{r}_i, t)$. The free field is a solution for the non-resonant medium.

This perspective is particularly well suited for nuclear resonant scattering with short synchrotron pulses, because the driving field can be approximated by a delta-like pulse so that Ω vanishes for $t > 0$ and (2.79) effectively governs the free dynamics. We are going to develop this further in section 2.3.

The dynamical equation (2.79) can be derived [Ase+17] from an effective atom-atom Hamiltonian in a quantum many-body theory using the field-quantization scheme of Welsch and colleagues [GW96; DKW02; Buh13]. It has been used to describe atom-light interactions in waveguides [Ase+17] but also underlies the quantum optical theories developed for Mössbauer nuclei in cavity-like systems in reflection geometry [KCP20; Len+20]. This quantum-optical approach goes beyond (2.79) and can provide insights also into the spectrum and dynamics of strongly coupled atoms [DKW02].

For the present purpose, however, the semi-classical dynamical equation suffices.

2.2.5. Collective resonant phenomena

Ensembles of resonant atoms can exhibit peculiar collective phenomena upon coherent interaction with light. The propagation of coherent light pulses through resonant media is for example discussed in the textbook by Allen and Eberly [AE87], yet mainly focused on strong pulses. Mössbauer nuclei, in particular in combination with short pulses of synchrotron radiation, allow experiments in a rather unique parameter range: Negligible inhomogeneous line-broadening, coherent excitation with bandwidths many orders of magnitude broader than the linewidth (corresponding to almost instantaneous excitation) on the one hand, but restricted to extremely weak small-area pulses on the other hand. Here we discuss non-crystalline ensembles in the continuous approximation. Coherent phenomena in resonant crystals are extensively discussed in Ref. [HT99].

Dynamical beats

A short pulse propagating through resonant media induces beat patterns in its temporal response – so-called *dynamical beats*. The phenomenon is ubiquitous in nuclear forward scattering experiments. A detailed review is given by van Bürck [Bür99]. Such dynamical beats (also called propagation beats) have also been observed in other physical systems (see the historical references in [Bür99]), and recently in an optical nanofiber coupled to an ensemble of ^{133}Cs atoms [Su+23].

The phenomenon is readily explained using the resonant susceptibility defined in (2.68). Here we assume an unsplit resonance. References [SB99; Shv+98] discuss dynamical beats for hyperfine-split resonances. Consider a homogeneous slab of material of thickness L and an incident pulse $B_{\mathrm{in}}(x=0,t) = B_0\Pi(t)$, where $\Pi(t)$ is the normalized pulse envelope with $\int \Pi(t)\mathrm{d}t = 1$. The linear energy-domain response (in the weak excitation regime) can then be written as

$$\begin{aligned} B(L,\omega) &= B_0\Pi(\omega)e^{iknL}\exp\left[\frac{ik\chi_m(\omega)L}{2}\right] \\ &= B_0\Pi(\omega)e^{iknL}\exp\left[-i\frac{L}{2\Lambda_{\mathrm{res}}}\frac{\Gamma/2}{\omega+i\Gamma/2}\right], \end{aligned} \tag{2.81}$$

where $\Lambda_{\mathrm{res}} = 1/(\rho\sigma_{\mathrm{rad}})$ is the on-resonance attenuation length and $\Pi(\omega)$ the Fourier-transform of $\Pi(t)$. The temporal response is obtained via Fourier-transform,

$$\begin{aligned} B(L,t) &= \int \frac{\mathrm{d}\omega}{2\pi} B(L,\omega) e^{-i\omega t} \\ &= B_0 e^{iknL} \left[\Pi(t) - \Gamma\tau_{\text{pulse}} \frac{T}{4} e^{-\Gamma t/2} \frac{2J_1\left(\sqrt{\Gamma t T}\right)}{\sqrt{\Gamma t T}} \right], \end{aligned} \tag{2.82}$$

where $T = L/\Lambda_{\text{res}} = L\rho\sigma_{\text{rad}}$ is the on-resonance optical depth (known as "effective thickness" in the nuclear resonant scattering community) and $\tau_{\text{pulse}} = \Pi(\omega = 0)$ is the duration of the incident pulse. This was derived in similar form by Kagan, Afanas'ev, and Kohn [KAK79]. The integral can be computed by series-expansion of the exponential function, contour-integration of the individual terms, and identifying the resulting series with the Bessel function of first kind $J_1(x)$. Equation (2.82) displays the two contributions, the prompt and delayed pulse that were introduced in (2.26). Figure 2.8 shows the delayed pulse for different optical depths T.

The last term in (2.82) is normalized so that

$$\frac{2J_1\left(\sqrt{x}\right)}{\sqrt{x}} \approx 1 - \frac{x}{8} + \mathcal{O}\left(x^{\frac{3}{2}}\right). \tag{2.83}$$

For optically thin samples ($T \ll 1$), the oscillations are not observable in a finite observation window, because they would only set in long after the natural lifetime $1/\Gamma$ (see Fig. 2.8a). For short time delay, the oscillating term can be approximated as $\sim \exp(-\Gamma t T/4)$, leading to an apparent initial decay $\propto \exp[-(1 + T/2)\Gamma t/2]$ – a collective *initial speedup* of the decay rate $(1 + T/2)\Gamma$.

Several physical interpretations of the dynamical beats have been discussed, from interference of two polariton branches [Bür99], interference of bright and dark radiative eigenmodes [RE21], repeated absorption and reemission of the resonant photon [Smi+07], to emissions from a so-called nuclear exciton-polariton [Smi+07]. Some quantitative insight is provided by the microscopic theory. The expectation value of the nuclear transition operator at depth x and time t can be written as (ignoring time retardation)

$$\sigma_{ge}(x,t) = iAe^{iknx} e^{-\Gamma t/2} J_0\left(\sqrt{\Gamma t T}\right), \tag{2.84}$$

where $A = m_0 B_0 \tau_{\text{pulse}}/\hbar \ll 1$ is the pulse area, as we are going to show in section 2.3. It has been derived in similar form by Smirnov [Smi+07]. The rather abstract quantity is proportional to a magnetization $M = \rho m_0 \sigma_{ge}$. Figure 2.8b shows the envelope of this magnetization without the rapidly oscillating term e^{iknx} . The synchrotron pulse intially excites the entire sample homogeneously, but the excitation amplitude then develops a depth-dependency and slow spatio-temporal oscillations. This can be

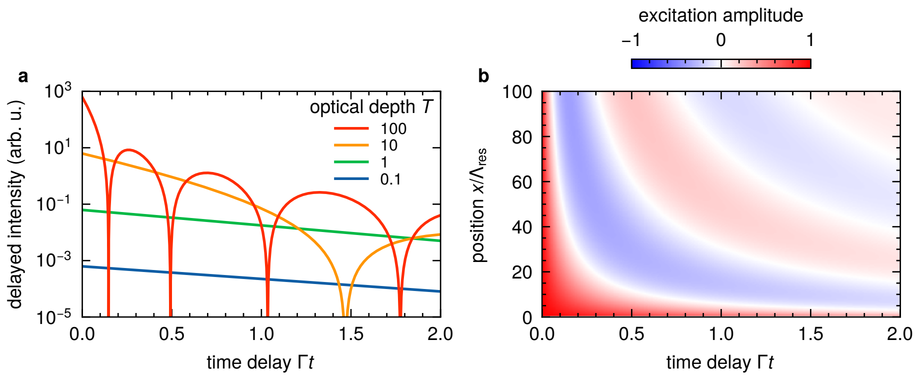

Figure 2.8.: Dynamical beats in nuclear forward scattering. **a** Dynamical beats in the delayed emissions following impulsive excitation of slab/foil samples with different on-resonance optical depths $T = L/\Lambda_{\text{res}}$. **b** Envelope of the local magnetization M (excitation amplitude) as a function of time and sample depth (relative to its maximum). In both panels, off-resonant absorption is neglected.

interpreted as a boundary effect: Every nucleus experiences the field produced by all other nuclei upstream of its position. Since the boundary at $x = 0$ breaks translational symmetry, the field at each depth is different, causing the oscillations.

Thin-film structures

More complex geometries give rise to a wider variety of phenomena. Thin film structures and multilayers, probed in θ-2θ reflection geometry (see Fig. 2.9), have proven particularly fruitful. This geometry is still rather simple because it is to a good approximation fully translation invariant in 2 dimensions and can be thought of as an effective Fabry-Pérot cavity (see Fig. 2.9b). Ref. [RE21] gives a comprehensive review.

Röhlsberger and coworkers demonstrated a speedup of the decay rate *without* dynamical beats from a thin layer of ^{57}Fe embedded in a planar waveguide structure [Röh+05]. The speedup is tuneable by changing the incidence angle. They went on to demonstrate a corresponding shift of the resonance frequency in a similar sample [Röh+10]. Two thin layer of resonant material can be placed in such a way that the reflectivity spectrum $R(\omega)$ exhibits a narrow dip [Röh+12]. This can be related to the concept of electromagnetically induced transparency, if the excitation states of the two nuclear layers are interpreted as states of an effective three-level atom. This concept is further discussed in Refs. [HE15; RE21; Len+20]. In a similar sample consisting of two stacked waveguide layers with a thin resonant layer each, a collective *harmonic* oscillation between the two layers was demonstrated [Hab+16].

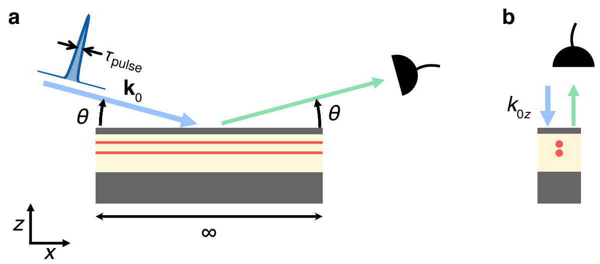

Figure 2.9.: Schema of a resonant thin-film “cavity” probed in reflection geometry. **a** The layer system contains one or more thin films of resonant nuclei (red). It is illuminated at an incidence angle of θ with a short pulse of synchrotron radiation and the delayed emission into the direction of specular reflection is observed. **b** Due to translation invariance, the system can be considered as a 1-dimensional Fabry-Pérot cavity. Each film of nuclei can be considered as a single atom and the cavity is illuminated with wave vector $k_{0z} = |\mathbf{k}_0| \cos\theta$.

2.3. Excitation dynamics

2.3.1. Nuclear excitation in forward scattering

We analyze the nuclear excitation dynamics – the time-evolution of the nuclear excitation amplitude $\sigma_{eg}(x,t)$ – in nuclear forward scattering from a simple slab. We employ the formalism of (2.79) to familiarize ourselves with the approach, again in the simplified model of a (spin-1/2) two-level system. Similar considerations were made by Smirnov and coworkers [Smi+07] (see also Ref. [Smi+05]).

Consider once again the simplest conceivable geometry, the homogeneous slab illuminated by a plane wave (Fig. 2.7). The (free) synchrotron pulse $\mathbf{B}_0^+(\mathbf{r},t)$ propagates through the slab as dictated by the (non-dispersive) complex refractive index n. We express this excitation pulse in terms of the Rabi frequency $[\Omega(\mathbf{r},t) = m_0 \mathbf{d} \cdot \mathbf{B}_0^+(\mathbf{r},t)/\hbar]$

$$\Omega(x,t) = \Omega_0 \Pi(t_{\text{ret}}) e^{ik_0 n x}, \tag{2.85}$$

where $\Pi(t)$ is some dimensionless pulse envelope and $t_{\text{ret}} = t - nx/c$ the retarded time. We assume that the pulse $\Pi(t)$ is temporally supported on $t \in [0, t_0]$ and is considerably shorter than the natural lifetime, $t_0 \ll 1/\Gamma$.

The continuous one-dimensional equation

Going to continuous variables and integrating (2.79) over y and z yields

$$-i\omega\sigma_{ge}(x,\omega) = -\frac{\Gamma}{2}\sigma_{ge}(x,\omega) + i\Omega(x,\omega) + i\rho\int_0^L \mathrm{d}x g(x-x',\omega+\omega_0)\sigma_{ge}(x',\omega) \quad (2.86)$$

with

$$\begin{aligned} g(x-x',\omega+\omega_0) &= \sigma_{\mathrm{rad}} k\frac{\Gamma}{2}\mathbf{d}^* \cdot \underline{\mathbf{G}}^{\mathrm{ps}}_{\mathrm{m}}(x-x',\omega+\omega_0)\cdot\mathbf{d} \\ &= \frac{in\sigma_{\mathrm{rad}}}{2}\frac{\Gamma}{2}e^{ikn|x-x'|}. \end{aligned} \quad (2.87)$$

Substituting the coupling term in (2.86) leads to

$$-i\omega\sigma_{ge}(x,\omega) = -\frac{\Gamma}{2}\sigma_{ge}(x,\omega) + i\Omega(x,\omega) - \frac{n\Gamma}{4\Lambda_{\mathrm{res}}}\int_0^L \mathrm{d}x e^{ikn|x-x'|}\sigma_{ge}(x',\omega). \quad (2.88)$$

Fourier-transforming (2.88) finally yields

$$\frac{\mathrm{d}}{\mathrm{d}t}\sigma_{ge}(x,t) = -\frac{\Gamma}{2}\sigma_{ge}(x,t) + i\Omega(x,t) - \frac{n\Gamma}{4\Lambda_{\mathrm{res}}}\int_0^L \mathrm{d}x e^{ik_0n|x-x'|}\sigma_{ge}\left(x', t-n\frac{|x-x'|}{c}\right). \quad (2.89)$$

We have obtained a one-dimensional integro-differential equation that describes the nuclear excitation amplitude after interaction with a pulse of synchrotron radiation. A three-dimensional version (with $1/|\mathbf{r}-\mathbf{r}'|$ dependence) is discussed for example in Ref. [SZS15] in the context of single-photon superradiance. Equation (2.89) appears a bit cumbersome because of the time-retardation in the coupling term. For certain initial conditions, the retardation, in fact, produces interesting non-local dynamics [Svi12]. In the present case, however, the time-retardation can be effectively eliminated, which considerably simplifies the dynamics, as we will see in the following.

Impulsive excitation and the nuclear exciton

The excitation pulse depends on the retarded time. We therefore define $\tilde{\sigma}_{ge}(x,t) = \sigma_{ge}[x, t_{\mathrm{adv}}(x)]$, with the advanced time $t_{\mathrm{adv}}(x) = t + nx/c$. The nuclear excitation immediately after the synchrotron pulse can then be written as

$$\tilde{\sigma}_{ge}(x,t_0) = i\left[\Omega_0\int_0^{\tau_{\mathrm{pulse}}}\Pi(t)\mathrm{d}t\right]e^{ik_0nx} = iAe^{ik_0nx}, \quad (2.90)$$

so that A is the pulse area. Equation (2.90) describes the *nuclear exciton* in terms of the transition-operator. After the synchrotron pulse has passed ($t \geq t_0$), the dynamical equation (2.89) simplifies to

$$\frac{\mathrm{d}}{\mathrm{d}t}\tilde{\sigma}_{ge}(x,t) = -\frac{\Gamma}{2}\tilde{\sigma}_{ge}(x,t) - \frac{n\Gamma}{4\Lambda_{\mathrm{res}}}\int_0^L \mathrm{d}x e^{ik_0 n|x-x'|}\tilde{\sigma}_{ge}\left(x', t - n\frac{|x-x'|}{c} - n\frac{x'-x}{c}\right). \tag{2.91}$$

The forward-scattering approximation

We can effectively neglect the downstream-contribution ($x \leq x' \leq L$) in the integral. To that end, consider only the integral term

$$\begin{aligned}&\int_0^L \mathrm{d}x e^{ik_0 n|x-x'|}\tilde{\sigma}_{ge}\left(x', t - \frac{|x-x'|}{c} - n\frac{x'-x}{c}\right)\\ &\quad = \int_0^x \mathrm{d}x e^{ik_0 n(x-x')}\tilde{\sigma}_{ge}\left(x',t\right) + \int_x^L \mathrm{d}x e^{ik_0 n(x'-x)}\tilde{\sigma}_{ge}\left(x', t - 2n\frac{x'-x}{c}\right).\end{aligned} \tag{2.92}$$

Initially, $\tilde{\sigma}(x, t_0)$ is prepared with the spatial frequency of the excitation pulse, so that $\tilde{\sigma}(x) \propto \exp(ik_0 nx)$. Consequently, the second integral in (2.92) is rapidly oscillating with twice the spatial frequency, whereas the first integral fully cancels these high-frequency oscillations. Thus, similar to the rotating wave approximation, we neglect the second integral. Since this amounts to neglecting the downstream-contributions we call this the *forward-scattering approximation* (see Ref. [And23]).

Initial value problem

Making this forward-scattering approximation yields the following initial value problem for the nuclear excitation dynamics,

$$\frac{\mathrm{d}}{\mathrm{d}t}\tilde{\sigma}_{ge}(x,t) = -\frac{\Gamma}{2}\tilde{\sigma}_{ge}(x,t) - \frac{n\Gamma}{4\Lambda_{\mathrm{res}}}\int_0^x \mathrm{d}x e^{ik_0 n(x-x')}\tilde{\sigma}_{ge}\left(x',t\right), \tag{2.93a}$$

$$\tilde{\sigma}_{ge}(x,t_0) = iAe^{ik_0 nx}. \tag{2.93b}$$

This problem is not only significantly simpler than (2.89) but also structurally very different. Neglecting time-retardation, (2.89) is essentially a Fredholm integral equation (with respect to the spatial variable). This particular equation is commonly approached as an eigenvalue problem, to find the *radiative eigenmodes* of the atomic ensemble (see Refs. [SC08; SCS10; FM08b; RE21]). Equation (2.93a) however, is a Volterra integral equation. As such, it does not have any eigenvalues and the concept of radiative eigenmodes therefore no longer applies. Instead, (2.93a) has a rather simple analytical solution:

$$\tilde{\sigma}_{ge}(x,t) = iAe^{ik_0 nx}e^{-\Gamma t/2}J_0\left(\sqrt{\Gamma t x/\Lambda_{\mathrm{res}}}\right), \tag{2.94}$$

where J_0 is a Bessel function of first kind. We have already discussed (2.94) in the context of dynamical beats.

2.3.2. Collective spontaneous emission

The cooperative decay of excited Mössbauer nuclei is closely related to the concept of *superradiance* (see for example Refs. [Ada09; Röh+10; Chu+17]). The details of this relation, however, are subtle and have been vividly debated [Scu07]. The concept of superradiance was introduced by Dicke in 1954 [Dic54] and concerns the collective spontaneous emission from an ensemble of excited atoms. It has been the subject of a plethora of experimental and theoretical investigations since then. A comprehensive review was presented already four decades ago by Gross and Haroche [GH82] but there are still new aspects to it (see for example Ref. [MA22]).

Dipole moments

Before diving in, let us briefly consider the dipole moment associated with a two-level system with ground state $|g\rangle$ and excited state $|e\rangle$. The dipole operator can be defined in this basis as [Ste23]

$$\hat{\mathbf{d}} = \langle g|\hat{\mathbf{d}}|e\rangle\left(|g\rangle\langle e| + |e\rangle\langle g|\right) = \mathbf{d}_{ge}\left(\hat{\sigma}_{ge} + \hat{\sigma}_{ge}^{\dagger}\right), \tag{2.95}$$

where $\mathbf{d}_{ge}$ is a real vector. Importantly, in the fully excited state $|e\rangle$, the dipole moment vanishes, since

$$\langle e|\hat{\mathbf{d}}|e\rangle = 0. \tag{2.96}$$

On the other hand, in the weakly excited state $|\epsilon\rangle := \sqrt{1-\epsilon^2}\,|g\rangle + \epsilon\,|e\rangle$, which is a superposition of ground and excited state, the transition dipole moment is

$$\langle\epsilon|\hat{\mathbf{d}}|\epsilon\rangle \approx 2\mathbf{d}_{ge}\,\mathrm{Re}\{\epsilon\}, \tag{2.97}$$

for $|\epsilon| \ll 1$. Classically, this weakly excited state corresponds to an oscillating dipole, since the charge density oscillates between the two states with the transition frequency ω_0 (corresponding to the energy difference of the two states). The fully excited state, on the other hand, has no such dipole moment and does not correspond to a classical oscillating dipole.

Superradiance and single-photon superradiance

Perhaps the simplest case of superradiance corresponds to a cloud of N atoms, prepared so that all of the atoms are initially in their excited state. This state of full population inversion but no optical dipole moment is highly non-classical. When the atoms decay spontaneously, the collective decay rate can scale as N^2 – much faster than the scaling of N that would be expected from *independently* decaying atoms. Note that the radiation from N *coherently* oscillating classical dipoles also scales as N^2. The significance of superradiance hence lies in the fact that the independent (supposedly *incoherent*) spontaneous emission undergoes spontaneous "phase-locking" throughout the medium [GH82].

Yet, what is *super* about superradiance is a matter of perspective. In an article titled "The Super of Superradiance", Scully and Svidzinsky argue "the greatest radiation anomaly" to be an enhanced single-photon emission rate [SS09a]. They consider the following. An ensemble of N atoms is excited by a single photon, so that exactly one atom is excited but it is unknown which one. The decay rate is then N times the single-atom decay rate even though only a single atom is excited [Dic54]. The initial state again has no dipole moment and is highly non-classical. That aside, however, the decay rate is exactly what to expect from N classical oscillating dipoles [Ebe06]. Distributing a single excitation coherently over N atoms would allocate a dipole moment of $1/\sqrt{N}$ to each atom. The total dipole moment is then $\sqrt{N}$ and the decay rate $\propto N$.

This *single-photon superradiance* has received considerable interest in the early 2000s [Ebe06; Scu+06; FM08b; SCS08]. In particular, the evolution of the so-called *timed Dicke state* [Scu07] of an atomic ensemble after absorption of a single photon with wave vector $\mathbf{k}_0$ has been investigated. It is defined as

$$|\psi(\mathbf{k}_0)\rangle = \frac{1}{\sqrt{N}} \sum_{j=1}^{N} e^{i\mathbf{k}_0\cdot\mathbf{r}_j} \left|g_1 g_2 \cdots g_{j-1} e_j g_{j+1} \cdots g_N\right\rangle \tag{2.98}$$

where $\left|g_1 g_2 \cdots g_{j-1} e_j g_{j+1} \cdots g_N\right\rangle$ denotes the state where the jth atom is in its excited state and all other atoms are in their ground states and the field is assumed to be in its vacuum state (no photons). In contrast to the situation considered by Dicke [Dic54], here the atoms can be spatially separated by more than the wavelength. The state exhibits directed spontaneous emission [Scu+06; Ebe06] and a *collective Lamb shift* of the transition energy [Scu09]. Moreover, for spatially extended atomic ensembles, *collective Rabi oscillations*, harmonic absorption-emission oscillations of the coupled atom-radiation system, were predicted [SCS08]. This was argued to be "a new kind of cavity QED" [SS09a].

Quantum states in nuclear resonant scattering

The timed Dicke state (2.98) is formally identical to the nuclear exciton state (2.27), which is commonly employed in the theory of nuclear resonant scattering of synchrotron radiation pulses [HT99; Smi+07; RE21]. However, as pointed out earlier, equation (2.27) does not at all describe the state of the nuclear ensemble after interaction with a synchtrotron pulse. A better (but still oversimplified) description is

$$\begin{aligned} |\psi_\epsilon(\mathbf{k}_0)\rangle &= \prod_{j=1}^{N}\left(\sqrt{1-\epsilon^2}\,|g_j\rangle + \frac{\epsilon}{\sqrt{N}}e^{i\mathbf{k}_0\cdot\mathbf{r}_j}\,|e_j\rangle\right) \\ &\approx |\mathrm{gnd}\rangle + \frac{\epsilon}{\sqrt{N}}\sum_{j=1}^{N} e^{i\mathbf{k}_0\cdot\mathbf{r}_j}\,|g_1g_2\cdots g_{j-1}e_jg_{j+1}\cdots g_N\rangle + \mathcal{O}(\epsilon^2), \end{aligned} \tag{2.99}$$

where $|\mathrm{gnd}\rangle$ denotes the state where all atoms are in their ground states. For the lack of better words, we call (2.99) a *timed dipole state*. It *has* an associated dipole moment and is *conceptually* very different from the timed Dicke state (2.98). Consequently, it was pointed out [Scu07; Ada09] that nuclear resonant scattering of synchrotron radiation does *not* implement the situation considered in single-photon superradiance.

That said, the two states (2.98) and (2.99) radiate identical intensities for $N \gg 1$ (disregarding difference in photon statistics) [Ebe06]. Moreover, the quantum-mechanical treatment of spontaneous emission in weakly excited atomic ensembles is *analogous* to the emission of ensembles of classical harmonic oscillators [SCS10; SZS15] and obeys identical dynamical equations. Therefore, from a *practical* perspective and leaving the subtle conceptual differences aside, it should be possible to reproduce the theoretical predictions experimentally with nuclear resonant scattering. The correspondence between the transition-operator formalism employed here and the state equations of the single-photon superradiance literature are further explored in Appendix B.3.

Indeed, some theoretical predictions have been reproduced experimentally in this way. Röhlsberger and coworkers observed collective shifts of the resonance energy as well as a collective speed-up of the temporal response from a thin ensemble of ^{57}Fe embedded in a cavity-like environment in reflection geometry [Röh+10] – corresponding to the collective Lamb shift and single-photon superradiance predicted by Scully [Scu09]. Note that the so-called collective Lamb shift is a shift in the frequency of the radiative eigenmodes of the atomic ensemble (see Refs. [SC08; FM08a; FM08b; FM10; SCS10]) and, despite the name, an effect that identically emerges in ensembles of classical oscillators. Oscillations in the temporal response are also well known as dynamical beats in nuclear resonant scattering. While Ref. [SCS08] incorrectly states a linear time-dependence of the oscillations, this was later amended in Ref. [SS09b] (see also Refs. [SC08; FM08a; FM08b; FM08c; SCS10]). The amended time-dependence matches (2.94) and the experimentally observed behaviour.

We conclude that the discussion about "single-photon superradiance" being intuitive [Ebe06] or not [SS09a] revolves around the conceptual differences between the the quantum states (2.98) and (2.99). In nuclear resonant scattering, we do not control the exact quantum state of the nuclear ensemble and currently do not have the means to prepare the timed Dicke state (2.98). Thus, for the purpose of modeling the nuclear exciton dynamics in nuclear resonant scattering, we have chosen a description based on expectation values of single-atom transition operators [see (2.79)] that is manifestly independent of the many-body quantum state because we have neglected quantum correlations in the linear approximation. It entirely circumvents the subtleties that arise in the discussion of collaborative spontaneous emission due to the interpretation of quantum states. Finally, while originating from a fully quantized formalism, the linear dynamical equations and our observables exclusively depend on the *expectation values* and are thus equally applicable to mixed states.

References

[Ada+13] Bernhard W. Adams, Christian Buth, Stefano M. Cavaletto, Jörg Evers, Zoltán Harman, Christoph H. Keitel, Adriana Pálffy, Antonio Picón, Ralf Röhlsberger, Yuri Rostovtsev, and Kenji Tamasaku. "X-ray quantum optics." *Journal of Modern Optics* 60.1 (Jan. 2013), pp. 2–21. DOI: 10.1080/09500340.2012.752113.

[Ada09] B. W. Adams. "Nuclear γ-ray superradiance." *Journal of Modern Optics* 56.18-19 (Oct. 2009), pp. 1974–1984. DOI: 10.1080/09500340903199921.

[AE87] Leslie Allen and Joseph H. Eberly. *Optical resonance and two-level atoms*. unabridged and corr. ed. New York, NY: Dover, 1987. ISBN: 9780486655338.

[AK64] A. M. Afanas'ev and Yu. Kagan. "Theory of Hyperfine Structure of the Mössbauer Line in Paramagnetic Substances." *Journal of Experimental and Theoretical Physics* 14.4 (Apr. 1964), p. 1660.

[AK65] A. M. Afanas'ev and Yu. Kagan. "Suppression of Inelastic Channels in Resonant Nuclear Scattering in Crystals." *Journal of Experimental and Theoretical Physics* 21.1 (July 1965), p. 215.

[ALP24] Petar Andrejić, Leon Merten Lohse, and Adriana Pálffy. "Waveguide QED with Mössbauer nuclei." *Physical Review A* 109.6 (June 2024), p. 063702. DOI: 10.1103/physreva.109.063702.

[Als17] Jens Als-Nielsen. *Elements of modern X-ray physics*. Ed. by Des McMorrow. Second edition, reprinted with revisions and corrections. Chichester, West Sussex: John Wiley & Sons, Ltd, 2017. ISBN: 9780470973950.

[And23] Petar Andrejić. "Control of high frequency electromagnetic radiation." PhD thesis. Ruprecht-Karls-Universität Heidelberg, 2023.

[Ase+17] A. Asenjo-Garcia, J. D. Hood, D. E. Chang, and H. J. Kimble. "Atom-light interactions in quasi-one-dimensional nanostructures: A Green's-function perspective." *Physical Review A* 95.3 (Mar. 2017), p. 033818. DOI: 10.1103/physreva.95.033818.

[Aut02] André Authier. *Dynamical theory of X-ray diffraction*. Reprint. Monographs on crystallography 11. Oxford [u.a.]: Oxford Univ. Pr., 2002. ISBN: 0198559607.

[Bar00] Alfred Q. R. Baron. "Detectors for nuclear resonant scattering experiments." *Hyperfine Interactions* 125.1–4 (Mar. 2000), pp. 29–42. DOI: `10.1023/a:1012625418707`.

[Bha98] M. R. Bhat. "Nuclear Data Sheets for A = 57." *Nuclear Data Sheets* 85.3 (Nov. 1998), pp. 415–536. DOI: `10.1006/ndsh.1998.0021`.

[BK68] M. Blume and O. C. Kistner. "Resonant Absorption in the Presence of Faraday Rotation." *Physical Review* 171.2 (July 1968), pp. 417–425. DOI: `10.1103/physrev.171.417`.

[Boc23] Lars Bocklage. *Nexus - Nuclear Elastic X-ray scattering Universal Software*. en. 2023. DOI: `10.5281/ZENODO.10074447`.

[Boy20] Robert W. Boyd. *Nonlinear optics*. Fourth edition. London: Elsevier, AP Academic Press, 2020. ISBN: 9780128110034.

[Buh13] Stefan Yoshi Buhmann. *Dispersion Forces I*. Springer Tracts in Modern Physics 247. Berlin, Heidelberg: Springer Berlin Heidelberg, 2013. ISBN: 9783642324840.

[Bür+92] U. van Bürck, D. P. Siddons, J. B. Hastings, U. Bergmann, and R. Hollatz. "Nuclear forward scattering of synchrotron radiation." *Physical Review B* 46.10 (Sept. 1992), pp. 6207–6211. DOI: `10.1103/physrevb.46.6207`.

[Bur08] T. W. Burrows. "Nuclear Data Sheets for A = 45." *Nuclear Data Sheets* 109.1 (Jan. 2008), pp. 171–296. DOI: `10.1016/j.nds.2007.12.002`.

[Bür99] U. van Bürck. "Coherent pulse propagation through resonant media." *Hyperfine Interactions* 123–124.1–4 (Mar. 1999), pp. 483–509. DOI: `10.1023/a:1017080008712`.

[BW19] Max Born and Emil Wolf. *Principles of optics*. Seventh anniversary edition, 60th anniversary of first edition, 20th anniversary of seventh edition. Cambridge: Cambridge University Press, 2019. ISBN: 9781108769914.

[Cha95] C. T. Chantler. "Theoretical Form Factor, Attenuation, and Scattering Tabulation for Z=1–92 from E=1–10 eV to E=0.4–1.0 MeV." *Journal of Physical and Chemical Reference Data* 24.1 (Jan. 1995), pp. 71–643. DOI: `10.1063/1.555974`.

[Che+22] Yu-Hsueh Chen, Po-Han Lin, Guan-Ying Wang, Adriana Pálffy, and Wen-Te Liao. "Transient nuclear inversion by x-ray free electron laser in a tapered x-ray waveguide." *Physical Review Research* 4.3 (July 2022), p. l032007. DOI: `10.1103/physrevresearch.4.l032007`.

[Che99] Weng Cho Chew. *Waves and Fields in Inhomogenous Media*. IEEE Press Series on Electromagnetic Wave Theory. Wiley-IEEE Press, 1999. ISBN: 9780780347496.

[CHK97] D. E. Cullen, J. H. Hubbell, and L. Kissel. *EPDL97: the evaluated photo data library '97 version*. Sept. 1997. DOI: `10.2172/295438`.

[Chu+17] Aleksandr I. Chumakov, Alfred Q. R. Baron, Ilya Sergueev, Cornelius Strohm, Olaf Leupold, Yuri Shvyd'ko, Gennadi V. Smirnov, Rudolf Rüffer, Yuichi Inubushi, Makina Yabashi, Kensuke Tono, Togo Kudo, and Tetsuya Ishikawa. "Superradiance of an ensemble of nuclei excited by a free electron laser." *Nature Physics* 14.3 (Nov. 2017), pp. 261–264. DOI: `10.1038/s41567-017-0001-z`.

[CL70] Don T. Cromer and David Liberman. "Relativistic Calculation of Anomalous Scattering Factors for X Rays." *The Journal of Chemical Physics* 53.5 (Sept. 1970), pp. 1891–1898. DOI: `10.1063/1.1674266`.

[Cor+24] Jonathan Correa, Alexandr Ignatenko, David Pennicard, Sabine Lange, Sergei Fridman, Sebastian Karl, Leon Lohse, Björn Senfftleben, Ilya Sergeev, Sven Velten, Deepak Prajapat, Lars Bocklage, Hubertus Bromberger, Andrey Samartsev, Aleksandr Chumakov, Rudolf Rüffer, Joachim von Zanthier, Ralf Röhlsberger, and Heinz Graafsma. "TEMPUS, a Timepix4-based system for the event-based detection of X-rays." *Journal of Synchrotron Radiation* 31.5 (July 2024). DOI: 10.1107/s1600577524005319.

[Dic54] R. H. Dicke. "Coherence in Spontaneous Radiation Processes." *Physical Review* 93.1 (Jan. 1954), pp. 99–110. DOI: 10.1103/physrev.93.99.

[DKW02] Ho Trung Dung, Ludwig Knöll, and Dirk-Gunnar Welsch. "Resonant dipole-dipole interaction in the presence of dispersing and absorbing surroundings." *Physical Review A* 66.6 (Dec. 2002), p. 063810. DOI: 10.1103/physreva.66.063810.

[Dre+24] J. Lukas Dresselhaus, Margarita Zakharova, Nikolay Ivanov, Holger Fleckenstein, Mauro Prasciolu, Oleksandr Yefanov, Chufeng Li, Wenhui Zhang, Philipp Middendorf, Dmitry Egorov, Ivan De Gennaro Aquino, Henry N. Chapman, and Saša Bajt. "X-ray focusing below 3 nm with aberration-corrected multilayer Laue lenses." *Optics Express* 32.9 (Apr. 2024), p. 16004. DOI: 10.1364/oe.518964.

[Ebe06] J. H. Eberly. "Emission of one photon in an electric dipole transition of one among N atoms." *Journal of Physics B: Atomic, Molecular and Optical Physics* 39.15 (July 2006), S599–S604. DOI: 10.1088/0953-4075/39/15/s07.

[FM08a] Richard Friedberg and Jamal T. Manassah. "Effects of including the counterrotating term and virtual photons on the eigenfunctions and eigenvalues of a scalar photon collective emission theory." *Physics Letters A* 372.14 (Mar. 2008), pp. 2514–2521. DOI: 10.1016/j.physleta.2007.11.064.

[FM08b] Richard Friedberg and Jamal T. Manassah. "Eigenfunctions and eigenvalues in superradiance with x-y translational symmetry." *Physics Letters A* 372.16 (Apr. 2008), pp. 2787–2801. DOI: 10.1016/j.physleta.2007.12.056.

[FM08c] Richard Friedberg and Jamal T. Manassah. "Reply to: "Comment on: 'Effects of including the counterrotating term and virtual photons on the eigenfunctions and eigenvalues of a scalar photon collective emission theory' [Phys. Lett. A 372 (2008) 2514]" [Phys. Lett. A 372 (2008) 5732]." *Physics Letters A* 372.35 (Aug. 2008), pp. 5734–5740. DOI: 10.1016/j.physleta.2008.06.057.

[FM10] Richard Friedberg and Jamal T. Manassah. "Analytic expressions for the initial Cooperative Decay Rate and Cooperative Lamb Shift for a spherical sample of two-level atoms." *Physics Letters A* 374.15-16 (Apr. 2010), pp. 1648–1659. DOI: 10.1016/j.physleta.2010.02.012.

[GG71] N. N. Greenwood and T. C. Gibb. *Mössbauer Spectroscopy*. Springer Netherlands, 1971. ISBN: 9789400956971. DOI: 10.1007/978-94-009-5697-1.

[GH82] M. Gross and S. Haroche. "Superradiance: An essay on the theory of collective spontaneous emission." *Physics Reports* 93.5 (Dec. 1982), pp. 301–396. DOI: 10.1016/0370-1573(82)90102-8.

[GW96] T. Gruner and D.-G. Welsch. "Green-function approach to the radiation-field quantization for homogeneous and inhomogeneous Kramers-Kronig dielectrics." *Physical Review A* 53.3 (Mar. 1996), pp. 1818–1829. DOI: 10.1103/physreva.53.1818.

[Hab+16] Johann Haber, Kai S. Schulze, Kai Schlage, Robert Loetzsch, Lars Bocklage, Tatiana Gurieva, Hendrik Bernhardt, Hans-Christian Wille, Rudolf Rüffer, Ingo Uschmann, Gerhard G. Paulus, and Ralf Röhlsberger. "Collective strong coupling of X-rays and nuclei in a nuclear optical lattice." *Nature Photonics* 10.7 (May 2016), pp. 445–449. DOI: 10.1038/nphoton.2016.77.

[Has+91] J. B. Hastings, D. P. Siddons, U. van Bürck, R. Hollatz, and U. Bergmann. "Mössbauer spectroscopy using synchrotron radiation." *Physical Review Letters* 66.6 (Feb. 1991), pp. 770–773. DOI: 10.1103/physrevlett.66.770.

[HCT74a] J. P. Hannon, N. J. Carron, and G. T. Trammell. "Mössbauer diffraction. III. Emission of Mössbauer γ-rays from crystals. A. General theory." *Physical Review B* 9.7 (Apr. 1974), pp. 2791–2809. DOI: 10.1103/physrevb.9.2791.

[HCT74b] J. P. Hannon, N. J. Carron, and G. T. Trammell. "Mössbauer diffraction. III. Emission of Mössbauer γ-rays from crystals. B. Dynamical solutions." *Physical Review B* 9.7 (Apr. 1974), pp. 2810–2831. DOI: 10.1103/physrevb.9.2810.

[HE15] Kilian P. Heeg and Jörg Evers. "Collective effects between multiple nuclear ensembles in an x-ray cavity-QED setup." *Physical Review A* 91.6 (June 2015), p. 063803. DOI: 10.1103/physreva.91.063803.

[HGD93] B. L. Henke, E. M. Gullikson, and J. C. Davis. "X-Ray Interactions: Photoabsorption, Scattering, Transmission, and Reflection at E = 50-30,000 eV, Z = 1-92." *Atomic Data and Nuclear Data Tables* 54.2 (July 1993), pp. 181–342. DOI: 10.1006/adnd.1993.1013.

[HHW71] Gilbert R. Hoy, Dennis W. Hamill, and Peter P. Wintersteiner. "Coincidence Mössbauer Spectroscopy." In: *Proceedings of the Sixth Symposium on Mössbauer Effect Methodology New York City, January 25, 1970*. Ed. by Irwin J. Gruverman. Springer US, 1971, pp. 109–121. ISBN: 9781468431599. DOI: 10.1007/978-1-4684-3159-9_9.

[HKE16] K. P. Heeg, C. H. Keitel, and J. Evers. *Inducing and detecting collective population inversions of Mössbauer nuclei*. 2016. DOI: 10.48550/ARXIV.1607.04116.

[HT68] J. P. Hannon and G. T. Trammell. "Mössbauer Diffraction. I. Quantum Theory of Gamma-Ray and X-Ray Optics." *Physical Review* 169.2 (May 1968), pp. 315–329. DOI: 10.1103/physrev.169.315.

[HT69] J. P. Hannon and G. T. Trammell. "Mössbauer Diffraction. II. Dynamical Theory of Mössbauer Optics." *Physical Review* 186.2 (Oct. 1969), pp. 306–325. DOI: 10.1103/physrev.186.306.

[HT99] J. P. Hannon and G. T. Trammell. "Coherent γ-ray optics." *Hyperfine Interactions* 123–124.1–4 (Mar. 1999), pp. 127–274. DOI: 10.1023/a:1017011621007.

[Jac09] John David Jackson. *Classical electrodynamics*. 3rd ed. Hoboken, NY: Wiley, 2009. ISBN: 9780471309321.

[Jam62] Reginald William James. *The optical principles of the diffraction of X-Rays*. Ed. by Lawrence Bragg. Vol. 2. The Crystalline State. London: G. Bell and Sons Ltd, 1962.

[Kag99] Yu. Kagan. "Theory of coherent phenomena and fundamentals in nuclear resonant scattering." *Hyperfine Interactions* 123–124.1–4 (Mar. 1999), pp. 83–126. DOI: 10.1023/a:1017059504169.

[KAK79] Yu Kagan, A. M. Afanas'ev, and V. G. Kohn. "On excitation of isomeric nuclear states in a crystal by synchrotron radiation." *Journal of Physics C: Solid State Physics* 12.3 (Feb. 1979), pp. 615–631. DOI: 10.1088/0022-3719/12/3/027.

[KCP20] Xiangjin Kong, Darrick E. Chang, and Adriana Pálffy. "Green's-function formalism for resonant interaction of x rays with nuclei in structured media." *Physical Review A* 102.3 (Sept. 2020), p. 033710. DOI: 10.1103/physreva.102.033710.

[Kis00] Lynn Kissel. "RTAB: the Rayleigh scattering database." *Radiation Physics and Chemistry* 59.2 (Aug. 2000), pp. 185–200. DOI: 10.1016/s0969-806x(00)00290-5.

[Kun+97] Y. Kunimune, Y. Yoda, K. Izumi, M. Yabashi, X.-W. Zhang, T. Harami, M. Ando, and S. Kikuta. "Two-Photon Correlations in X-rays from a Synchrotron Radiation Source." *Journal of Synchrotron Radiation* 4.4 (July 1997), pp. 199–203. DOI: 10.1107/s0909049597006912.

[LA24] Leon M. Lohse and Petar Andrejić. "Nano-optical theory of planar x-ray waveguides." *Optics Express* 32.6 (Mar. 2024), p. 9518. DOI: 10.1364/oe.504206.

[Len+20] Dominik Lentrodt, Kilian P. Heeg, Christoph H. Keitel, and Jörg Evers. "Ab initio quantum models for thin-film x-ray cavity QED." *Physical Review Research* 2.2 (June 2020), p. 023396. DOI: 10.1103/physrevresearch.2.023396.

[Len21] Dominik Lentrodt. "Ab initio approaches to x-ray cavity QED - From multi-mode theory to nonlinear dynamics of Mössbauer nuclei." PhD thesis. Universität Heidelberg, 2021. DOI: 10.11588/HEIDOK.00030671.

[Llo+22] X. Llopart, J. Alozy, R. Ballabriga, M. Campbell, R. Casanova, V. Gromov, E. H. M. Heijne, T. Poikela, E. Santin, V. Sriskaran, L. Tlustos, and A. Vitkovskiy. "Timepix4, a large area pixel detector readout chip which can be tiled on 4 sides providing sub-200 ps timestamp binning." *Journal of Instrumentation* 17.01 (Jan. 2022), p. C01044. DOI: 10.1088/1748-0221/17/01/c01044.

[MA22] Stuart J. Masson and Ana Asenjo-Garcia. "Universality of Dicke superradiance in arrays of quantum emitters." *Nature Communications* 13.1 (Apr. 2022). DOI: 10.1038/s41467-022-29805-4.

[Mit+09] Takaya Mitsui, Naohisa Hirao, Yasuo Ohishi, Ryo Masuda, Yumiko Nakamura, Hirotoshi Enoki, Kouji Sakaki, and Makoto Seto. "Development of an energy-domain ^{57}Fe-Mössbauer spectrometer using synchrotron radiation and its application to ultrahigh-pressure studies with a diamond anvil cell." *Journal of Synchrotron Radiation* 16.6 (Sept. 2009), pp. 723–729. DOI: 10.1107/s0909049509033615.

[Mös58a] Rudolf L. Mössbauer. "Kernresonanzabsorption von Gammastrahlung in Ir^{191}." *Die Naturwissenschaften* 45.22 (1958), pp. 538–539. DOI: 10.1007/bf00632050.

[Mös58b] Rudolf L. Mössbauer. "Kernresonanzfluoreszenz von Gammastrahlung in Ir^{191}." *Zeitschrift für Physik* 151.2 (Apr. 1958), pp. 124–143. DOI: 10.1007/bf01344210.

[Mös76] R. L. Mössbauer. "Debye Waller factors and Lamb factors in the scattering of X-rays, γ-rays and thermal neutrons." *Le Journal de Physique Colloques* 37.C6 (Dec. 1976), pp. C6-11-C6–13. DOI: 10.1051/jphyscol:1976602.

[MW95] Leonard Mandel and Emil Wolf. *Optical Coherence and Quantum Optics*. Cambridge University Press, Sept. 1995. ISBN: 9781139644105. DOI: 10.1017/cbo9781139644105.

[NH12] Lukas Novotny and Bert Hecht. *Principles of Nano-Optics*. Cambridge University Press, 2012. ISBN: 9780511794193.

[Pag06] David M. Paganin. *Coherent x-ray optics*. Oxford series on synchrotron radiation no. 6. Oxford: Oxford University Press, 2006. ISBN: 0191717967.

[PEK08] Adriana Pálffy, Jörg Evers, and Christoph H. Keitel. "Electric-dipole-forbidden nuclear transitions driven by super-intense laser fields." *Physical Review C* 77.4 (Apr. 2008), p. 044602. DOI: 10.1103/physrevc.77.044602.

[Pot+12] Vasily Potapkin, Aleksandr I. Chumakov, Gennadii V. Smirnov, Jean-Philippe Celse, Rudolf Rüffer, Catherine McCammon, and Leonid Dubrovinsky. "The ^{57}Fe Synchrotron Mössbauer Source at the ESRF." *Journal of Synchrotron Radiation* 19.4 (May 2012), pp. 559–569. DOI: 10.1107/s0909049512015579.

[RC21] Rudolf Rüffer and Aleksandr I. Chumakov. “Historical Developments and Future Perspectives in Nuclear Resonance Scattering.” In: *Modern Mössbauer Spectroscopy*. Ed. by Yutaka Yoshida and Guido Langouche. Topics in Applied Physics. Springer Singapore, 2021, pp. 1–55. ISBN: 9789811594229. DOI: `10.1007/978-981-15-9422-9_1`.

[RE21] Ralf Röhlsberger and Jörg Evers. “Quantum Optical Phenomena in Nuclear Resonant Scattering.” In: *Modern Mössbauer Spectroscopy*. Ed. by Yutaka Yoshida and Guido Langouche. Topics in Applied Physics. Springer Singapore, 2021, pp. 105–171. DOI: `10.1007/978-981-15-9422-9_3`.

[RES20] Ralf Röhlsberger, Jörg Evers, and Sharon Shwartz. “Quantum and Nonlinear Optics with Hard X-Rays.” In: *Synchrotron Light Sources and Free-Electron Lasers*. Ed. by Eberhard J. Jaeschke, Shaukat Khan, Jochen R. Schneider, and Jerome B. Hastings. Springer International Publishing, 2020, pp. 1399–1431. DOI: `10.1007/978-3-030-23201-6_32`.

[Röh+05] R. Röhlsberger, K. Schlage, T. Klein, and O. Leupold. “Accelerating the Spontaneous Emission of X Rays from Atoms in a Cavity.” *Physical Review Letters* 95.9 (Aug. 2005). DOI: `10.1103/physrevlett.95.097601`.

[Röh+10] R. Röhlsberger, K. Schlage, B. Sahoo, S. Couet, and R. Rüffer. “Collective Lamb Shift in Single-Photon Superradiance.” *Science* 328.5983 (May 2010), pp. 1248–1251. DOI: `10.1126/science.1187770`.

[Röh+12] Ralf Röhlsberger, Hans-Christian Wille, Kai Schlage, and Balaram Sahoo. “Electromagnetically induced transparency with resonant nuclei in a cavity.” *Nature* 482.7384 (Feb. 2012), pp. 199–203. DOI: `10.1038/nature10741`.

[Röh05] Ralf Röhlsberger. *Nuclear Condensed Matter Physics with Synchrotron Radiation*. Springer Tracts in Modern Physics. Springer Berlin Heidelberg, 2005. ISBN: 9783540446996. DOI: `10.1007/b86125`.

[Röh99] R. Röhlsberger. “Theory of X-ray grazing incidence reflection in the presence of nuclear resonance excitation.” *Hyperfine Interactions* 123–124.1–4 (Mar. 1999), pp. 301–325. DOI: `10.1023/a:1017063605078`.

[Ros95] Morris Edgar Rose. *Elementary theory of angular momentum*. New York: Dover Publications, Inc., 1995. ISBN: 0486684806.

[RS04] Peter Ring and Peter Schuck. *The nuclear many body problem*. Texts and monographs in physics. Berlin: Springer, 2004. ISBN: 9783540212065.

[San08] Robin Santra. “Concepts in x-ray physics.” *Journal of Physics B: Atomic, Molecular and Optical Physics* 42.2 (Dec. 2008), p. 023001. DOI: `10.1088/0953-4075/42/2/023001`.

[SB08] Stefan Scheel and Stefan Yoshi Buhmann. “Macroscopic Quantum Electrodynamics - Concepts and Applications.” *Acta Physica Slovaca* 58.5 (Oct. 2008), pp. 675–809. DOI: `10.48550/arxiv.0902.3586`. arXiv: `0902.3586 [quant-ph]`.

[SB99] Yu. V. Shvyd’ko and U. van Bürck. “Hybrid forms of beat phenomena in nuclear forward scattering of synchrotron radiation.” *Hyperfine Interactions* 123–124.1–4 (Mar. 1999), pp. 511–527. DOI: `10.1023/a:1017084209621`.

[SC08] Anatoly Svidzinsky and Jun-Tao Chang. “Cooperative spontaneous emission as a many-body eigenvalue problem.” *Physical Review A* 77.4 (Apr. 2008), p. 043833. DOI: `10.1103/physreva.77.043833`.

[SCS08] Anatoly A. Svidzinsky, Jun-Tao Chang, and Marlan O. Scully. “Dynamical Evolution of Correlated Spontaneous Emission of a Single Photon from a Uniformly Excited Cloud of N Atoms.” *Physical Review Letters* 100.16 (Apr. 2008), p. 160504. DOI: `10.1103/physrevlett.100.160504`.

[SCS10] Anatoly A. Svidzinsky, Jun-Tao Chang, and Marlan O. Scully. “Cooperative spontaneous emission of N atoms: Many-body eigenstates, the effect of virtual Lamb shift processes, and analogy with radiation of N classical oscillators.” *Physical Review A* 81.5 (May 2010), p. 053821. DOI: 10.1103/physreva.81.053821.

[Scu+06] Marlan O. Scully, Edward S. Fry, C. H. Raymond Ooi, and Krzysztof Wódkiewicz. “Directed Spontaneous Emission from an Extended Ensemble of N Atoms: Timing Is Everything.” *Physical Review Letters* 96.1 (Jan. 2006), p. 010501. DOI: 10.1103/physrevlett.96.010501.

[Scu07] M. O. Scully. “Correlated spontaneous emission on the Volga.” *Laser Physics* 17.5 (May 2007), pp. 635–646. DOI: 10.1134/s1054660x07050064.

[Scu09] Marlan O. Scully. “Collective Lamb Shift in Single Photon Dicke Superradiance.” *Physical Review Letters* 102.14 (Apr. 2009), p. 143601. DOI: 10.1103/physrevlett.102.143601.

[Sei+18] Frank Seiboth, Felix Wittwer, Maria Scholz, Maik Kahnt, Martin Seyrich, Andreas Schropp, Ulrich Wagner, Christoph Rau, Jan Garrevoet, Gerald Falkenberg, and Christian G. Schroer. “Nanofocusing with aberration-corrected rotationally parabolic refractive X-ray lenses.” *Journal of Synchrotron Radiation* 25.1 (Jan. 2018), pp. 108–115. DOI: 10.1107/s1600577517015272.

[SG94] W. Sturhahn and E. Gerdau. “Evaluation of time-differential measurements of nuclear-resonance scattering of x rays.” *Physical Review B* 49.14 (Apr. 1994), pp. 9285–9294. DOI: 10.1103/physrevb.49.9285.

[Shv+23] Yuri Shvyd’ko et al. “Resonant X-ray excitation of the nuclear clock isomer ^{45}Sc.” *Nature* 622.7983 (Sept. 2023), pp. 471–475. DOI: 10.1038/s41586-023-06491-w.

[Shv+98] Yu. V. Shvyd’ko, U. van Bürck, W. Potzel, P. Schindelmann, E. Gerdau, O. Leupold, J. Metge, H. D. Rüter, and G. V. Smirnov. “Hybrid beat in nuclear forward scattering of synchrotron radiation.” *Physical Review B* 57.6 (Feb. 1998), pp. 3552–3561. DOI: 10.1103/physrevb.57.3552.

[Shv00] Yuri V. Shvyd’ko. “MOTIF: Evaluation of time spectra for nuclear forward scattering.” *Hyperfine Interactions* 125.1–4 (Mar. 2000), pp. 173–188. DOI: 10.1023/a:1012633620524.

[Shv99] Yuri V. Shvyd’ko. “Nuclear resonant forward scattering of x rays: Time and space picture.” *Physical Review B* 59.14 (Apr. 1999), pp. 9132–9143. DOI: 10.1103/physrevb.59.9132.

[SK95] G. V. Smirnov and V. G. Kohn. “Theory of nuclear resonant scattering of synchrotron radiation in the presence of diffusive motion of nuclei.” *Physical Review B* 52.5 (Aug. 1995), pp. 3356–3365. DOI: 10.1103/physrevb.52.3356.

[SK99] W. Sturhahn and V. G. Kohn. “Theoretical aspects of incoherent nuclear resonant scattering.” *Hyperfine Interactions* 123–124.1–4 (Mar. 1999), pp. 367–399. DOI: 10.1023/a:1017071806895.

[Smi+05] G. V. Smirnov, U. van Bürck, W. Potzel, P. Schindelmann, S. L. Popov, E. Gerdau, Yu. V. Shvyd’ko, H. D. Rüter, and O. Leupold. “Propagation of nuclear polaritons through a two-target system: Effect of inversion of targets.” *Physical Review A* 71.2 (Feb. 2005), p. 023804. DOI: 10.1103/physreva.71.023804.

[Smi+07] G. V. Smirnov, U. van Bürck, J. Arthur, G. S. Brown, A. I. Chumakov, A. Q. R. Baron, W. Petry, and S. L. Ruby. “Currents and fields reveal the propagation of nuclear polaritons through a resonant target.” *Physical Review A* 76.4 (Oct. 2007), p. 043811. DOI: 10.1103/physreva.76.043811.

[Smi+11] G. V. Smirnov, A. I. Chumakov, V. B. Potapkin, R. Rüffer, and S. L. Popov. “Multispace quantum interference in a ^{57}Fe synchrotron Mössbauer source.” *Physical Review A* 84.5 (Nov. 2011), p. 053851. DOI: 10.1103/physreva.84.053851.

[Smi96] G. V. Smirnov. “Nuclear resonant scattering of synchrotron radiation.” *Hyperfine Interactions* 97-98.1 (Dec. 1996), pp. 551–588. DOI: 10.1007/bf02150198.

[Smi99] G. V. Smirnov. “General properties of nuclear resonant scattering.” *Hyperfine Interactions* 123–124.1–4 (Mar. 1999), pp. 31–77. DOI: 10.1023/a:1017007520099.

[Sni+96] A. Snigirev, V. Kohn, I. Snigireva, and B. Lengeler. “A compound refractive lens for focusing high-energy X-rays.” *Nature* 384.6604 (Nov. 1996), pp. 49–51. DOI: 10.1038/384049a0.

[SO20] Tim Salditt and Markus Osterhoff. “X-ray Focusing and Optics.” In: *Nanoscale Photonic Imaging*. Ed. by Tim Salditt, Alexander Egner, and D. Russell Luke. Topics in Applied Physics. Cham: Springer International Publishing, 2020, pp. 71–124. ISBN: 9783030344139. DOI: 10.1007/978-3-030-34413-9_3.

[Sol+21] Jakob Soltau, Leon Merten Lohse, Markus Osterhoff, and Tim Salditt. “Finite-difference propagation for the simulation of x-ray multilayer optics.” *Optics Express* 29.25 (Dec. 2021), p. 41932. DOI: 10.1364/oe.445300.

[SS09a] Marlan O. Scully and Anatoly A. Svidzinsky. “The Super of Superradiance.” *Science* 325.5947 (Sept. 2009), pp. 1510–1511. DOI: 10.1126/science.1176695.

[SS09b] Anatoly A. Svidzinsky and Marlan O. Scully. “Evolution of collective N atom states in single photon superradiance: Effect of virtual Lamb shift processes.” *Optics Communications* 282.14 (July 2009), pp. 2894–2897. DOI: 10.1016/j.optcom.2009.04.011.

[Ste23] Daniel A. Steck. *Quantum and Atom Optics*. available online at http://steck.us/teaching. Aug. 2023. URL: http://steck.us/teaching.

[Stu00] W. Sturhahn. “CONUSS and PHOENIX: Evaluation of nuclear resonant scattering data.” *Hyperfine Interactions* 125.1–4 (Mar. 2000), pp. 149–172. DOI: 10.1023/a:1012681503686.

[Stu04] Wolfgang Sturhahn. “Nuclear resonant spectroscopy.” *Journal of Physics: Condensed Matter* 16.5 (Jan. 2004), S497–S530. DOI: 10.1088/0953-8984/16/5/009.

[Su+23] Dianqiang Su, Yuan Jiang, Silvia Cardenas-Lopez, Ana Asenjo-Garcia, Pablo Solano, Luis A. Orozco, and Yanting Zhao. “Dynamical beats of short pulses in waveguide QED.” *Physical Review Research* 5.4 (Dec. 2023), p. l042041. DOI: 10.1103/physrevresearch.5.l042041.

[Svi12] Anatoly A. Svidzinsky. “Nonlocal effects in single-photon superradiance.” *Physical Review A* 85.1 (Jan. 2012), p. 013821. DOI: 10.1103/physreva.85.013821.

[SZS15] Anatoly A. Svidzinsky, Xiwen Zhang, and Marlan O. Scully. “Quantum versus semiclassical description of light interaction with atomic ensembles: Revision of the Maxwell-Bloch equations and single-photon superradiance.” *Physical Review A* 92.1 (July 2015), p. 013801. DOI: 10.1103/physreva.92.013801.

[Vag+14] Farit Vagizov, Vladimir Antonov, Y. V. Radeonychev, R. N. Shakhmuratov, and Olga Kocharovskaya. “Coherent control of the waveforms of recoilless γ-ray photons.” *Nature* 508.7494 (Mar. 2014), pp. 80–83. DOI: 10.1038/nature13018.

[VR06] C. J. Voyer and D. H. Ryan. “A complete solution to the Mössbauer problem, all in one place.” *Hyperfine Interactions* 170.1–3 (June 2006), pp. 91–104. DOI: 10.1007/s10751-006-9467-2.

[WE23] Lukas Wolff and Jörg Evers. "Characterization and detection method for x-ray excitation of Mössbauer nuclei beyond the low-excitation regime." *Physical Review A* 108.4 (Oct. 2023), p. 043714. DOI: 10.1103/physreva.108.043714.

[YL13] Yutaka Yoshida and Guido Langouche, eds. *Mössbauer Spectroscopy: Tutorial Book*. Springer Berlin Heidelberg, 2013. ISBN: 9783642322204. DOI: 10.1007/978-3-642-32220-4.

[YL21] Yutaka Yoshida and Guido Langouche, eds. *Modern Mössbauer Spectroscopy: New Challenges Based on Cutting-Edge Techniques*. Vol. 137. Topics in Applied Physics. Springer Singapore, 2021. ISBN: 9789811594229. DOI: 10.1007/978-981-15-9422-9.

[Yos+08] Yutaka Yoshida, Kunifumi Suzuki, Kazuo Hayakawa, Kenichi Yukihira, and Hiroyoshi Soejima. "Mössbauer spectroscopic microscope." *Hyperfine Interactions* 188.1–3 (Oct. 2008), pp. 121–126. DOI: 10.1007/978-3-540-78697-9_188.

3. Nano-optical theory of planar x-ray waveguides

This chapter is recompiled[1] under the terms of the *Optica Open Access Publishing Agreement* from the published article:

Leon M. Lohse and Petar Andrejić. "Nano-optical theory of planar x-ray waveguides." *Optics Express* 32.6 (Mar. 2024), p. 9518. DOI: `10.1364/oe.504206`

Author Contributions

Both authors developed the theory. LML wrote the manuscript with significant contributions from PA.

Abstract

X-ray waveguides are routinely used at synchrotron light sources in imaging setups and as a platform for experiments with quantum emitters, providing nanometer-sized confinement – even x-ray optics on a chip has been showcased. X-ray waveguides are weakly guiding and experience significant material absorption, such that the established waveguide theory is not immediately applicable. Here, a general self-contained nano-optical theory of planar waveguides is derived, which is appropriate for hard x-ray energies. Solutions of the electromagnetic fields and its Green's functions are derived in detail. Asymptotic expansions into resonant and non-resonant modes are derived, which are particularly useful in the presence of strong material absorption. A method to reliably find the resonant modes of x-ray waveguide structures is presented. Based on the general theory, certain common experimental geometries, namely evanescent coupling in grazing-incidence, front-coupling in forward-incidence and radiation from buried emitters, are discussed in more detail. Complementing the analytic discussion, numerical tools are provided and applied to quantitatively extract the main figures of merit. The theory provides an analytic foundation for the interpretation of past and future experiments and, combined with the numerical tools, will facilitate the computer-aided design of x-ray waveguides.

[1]Subject to slight adjustments of the notation and minor corrections.

3.1. Introduction

Half a century after the first demonstration of x-ray waveguiding [SS74], x-ray waveguides have been advanced [Fen+93; Zwa+99; Pfe+02] to the point that they can now be routinely used as optical elements for imaging [Gie+10; Sal+15b]. They can bend, split and recombine x-rays on chips [HS16; Sal+15a], and they are employed as cavity resonators for quantum-optical experiments [Röh+10; Hab+19; Ma+22; RE21]. And soon, due to the increasing availability of x-ray free electron lasers, new kinds of phenomena that require extremely high intensities facilitated by x-ray waveguides, such as transient nuclear inversion [Che+22], might come into reach.

X-ray waveguides and cavities have enabled a multitude of experiments in different fields. For phase-contrast imaging and tomography, x-ray waveguides provide highly coherent [Bon+02; Sal+08; OS11; PP14; SO20] nanometer-sized secondary point-sources [Car+08; Gie+10; Sal+15b; Zho+17]. These are used to acquire 3d images with resolutions well below 100 nm for research ranging from medicine, biology to chemical catalysis. Recently, Vassholz and Salditt have demonstrated the effective generation of x-rays inside a multilayer waveguide [VS21] which could lead to more brilliant x-ray sources for the laboratory. For fundamental quantum-mechanics, x-ray waveguides provide one-dimensional confinement and enhanced coupling to atoms embedded into the waveguide, thereby forming a cavity resonator. Exploiting this, Röhlsberger and coworkers embedded Mössbauer nuclei into a waveguide and reported the first observation of the collective Lamb shift [Röh+10]. This paved the way for many more demonstrations of quantum-optical phenomena in the hard x-ray regime with Mössbauer nuclei (see the review [RE21]) and atomic resonances, including on artificial two-level systems and demonstrating spectral control of inner-shell resonances [Hab+19; Ma+22]. In front coupling, Lee, Ahrens and Liao [LAL25] have proposed using the longitudinal Rabi oscillations between two modes coupled to Mössbauer nuclei as a sensitive measure of the gravitational red-shift, while we have proposed using a similar setup as a platform for implementing geometry-dependent super-radiance in Mössbauer nuclei [ALP24].

Ongoing developments promise to reach new regimes with the help of x-ray waveguides. X-ray free electron lasers are much brighter than synchrotron sources so that multi-photon phenomena with resonant nuclei [RE21] or non-linear phenomena with resonant inner-shell electrons [Che+22] become feasible. Moreover, beam-splitters and curved waveguides [Sal+15a; Pel16] combined with resonant nuclei could lead to more complex quantum-optical experiments on millimeter-sized chips.

A sound theoretical foundation facilitates interpretation of results and the design of new experiments. Diffraction of hard x-rays, electromagnetic waves with wavelengths in the order of 10^{-10} m, largely follow the same principles as light in the visible and infrared wavelengths and can be well described in terms of refractive indices n. Theory for dielectric waveguides, mainly focussing on optical wavelengths, has been extensively studied already in the 1960s (see for example [Mar74]). Nowadays, also due to their important applications in telecommunication, dielectric waveguides are well-understood by the optics and electrical engineering communities.

However, x-ray waveguides have important differences to their longer-wavelength counterparts, because the refractive indices, typically written as

$$n = 1 - \delta + i\beta, \quad \delta, \beta \lesssim 10^{-5}, \tag{3.1}$$

in the x-ray regime, are generally very close to unity. As a first consequence, the index *contrast* is tiny so that x-ray waveguides are generally only *weakly guiding* resulting in the extent of guided modes being many times larger than the wavelength. Second, *absorption* due to photoionization is appreciably large, $\mathrm{Im}\{n\} = \beta > 0$, and the mean free path of photons typically ranges from a mere micrometers in heavy materials up to a few millimeters in lighter materials.

For longer wavelengths, absorption is mostly of little concern because other losses dominate. As a result, the theory of optical waveguides has largely been formulated for *real* refractive indices and losses are considered separately – notable exeptions are [Vas79; Bur70; Che99; SHB97]. The restriction to real indices has tremendous advantages because the theory can now be formulated in terms of *self-adjoint* Sturm-Liouville theory, closely related to potential scattering theory in quantum mechanics. For x-ray waveguides, the existing theory of waveguides with real indices has also been the method of choice and absorption has been included ad hoc [Bon+02; JD04; Pel+06; Lag+08; OS11; Buk+13a]. In addition, semi-analytical calculations [OS11] and numerical finite-differences propagation have been performed [FS05; FS06; Pel+07; Sol+21] to accurately simulate the performance of waveguides. Notably, semi-analytical calculations based on the full complex refractive indices have also been reported [TPP13]. The design and optimization of parameters for x-ray waveguides has also been studied from the perspective of applied mathematics [Sch11]. In that work, important theorems about the existence of resonances and their dependence on the refractive index profile have been rigorously proven. Several other papers covering specific theoretical aspects of x-ray waveguides have been published, including dispersion in 3-layer waveguides [Pel+06] and wave-field formation in front-coupling geometry [Buk+06].

Waveguiding is closely linked to a material structure supporting guided modes, so one of the main tasks has been to find those guided modes for given parameters. For simple 3-layer waveguides and negligible material absorption, the modes can readily be written down analytically [Mar74]. This becomes unfeasible for more complicated layer structures and is no longer possible when absorption is included. For optical wavelengths, various analytical approaches and numerical techniques have been developed that can reliably find and characterize the modes both for 1d (planar) and 2d confinement (see for example [Che+00]) for (in principle) arbitrary layer structures.

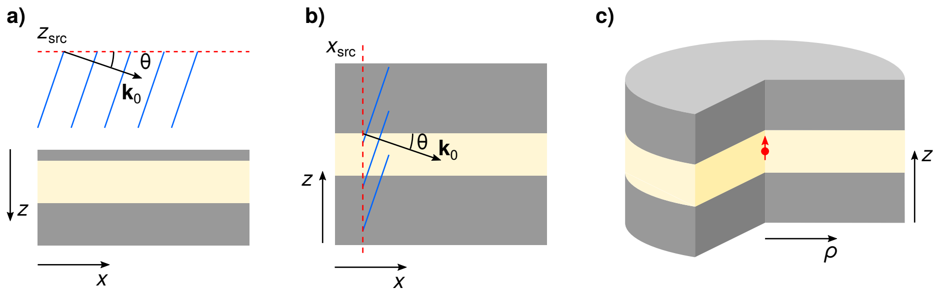

Figure 3.1.: (a) Evanescent coupling in grazing incidence. (b) Front-coupling in forward-incidence. (c) Emission from a dipole within the waveguide.

In the x-ray regime, however, the aforementioned weak guiding and finite absorption poses its own challenge and the established techniques can not trivially been applied. Here, the guided modes have been characterized with finite-difference propagation simulations [FS05; Buk+13b] and with Numerov's method [OS09].

Planar waveguides that are probed in grazing incidence, historically referred to as resonant beam couplers, are much simpler to describe because, assuming that the incoming fields are plane waves, fields and refractive indices are translationally invariant and the problem becomes effectively one-dimensional. The field profiles and reflected intensities for arbitrary complex layer structures can then be readily computed with transfer matrix calculations [Abe50]. Based on this method, a number of software packages have been developed to cater the popularity of x-ray reflectivity measurements (see for example [Tol99]).

When classical or quantum scatterers that are not modeled macroscopically by the complex indices are embedded in a waveguide, the system can no longer be described purely in terms of the fields resulting from the index profile. However, these scattering problems can be formulated [Len+20; AP21; KCP20] in terms of the *classical* electromagnetic Green's function (see for example [Buh13]), which is fully determined by the refractive indices. This is also being used in the emerging field of waveguide quantum electrodynamics (see for example [Ase+17]). Several authors have derived algorithms to compute the Green's function for arbitrary complex index profiles [Tom95; Joh11; Buh13].

Notably, the importance of the characteristic Green's function of waveguides has already been discussed in the electrical engineering literature (see for example Vassallo [Vas79], Chew [Che99], van Stralen [SHB97], and the references therein). In fact, the mode structure of the fields in a waveguide naturally emerges from poles and branch cuts of the in-plane spatial Fourier transform of its time-harmonic Green's functions. The Green's function is thus closely connected to the source-free solutions of the electromagnetic field equations.

While waveguide theory has been extensively studied in the past, the focus has been on longer wavelengths and the results applicable to – or relevant for – x-ray waveguides are sparsely scattered throughout the literature. On the other hand, the unavoidable material absorption prevalent in x-ray waveguides means that the usual Hermitian mode expansions and orthogonality that are commonly used in the non-absorbing case do not apply, and the non-Hermitian generalisations of these mode expansions have received little attention so far.

In this paper, we give a revised self-contained presentation of the nano-optical theory of planar x-ray waveguides. To that end, we present the theory from the ground up, giving derivations where appropriate and also translate some key results from the electrical engineering literature with application to the hard x-ray spectrum. The basic theory is universally applicable to short and longer wavelengths with the most notable features that it consistently assumes complex permittivities and arbitrary layer structures. We derive asymptotic expansions of the electromagnetic Green's functions in terms of resonant modes using a novel generalised bi-orthogonality relation, which is particularly useful in the presence of strong material absorption. We then apply this general theory and discuss three common experimental geometries for x-ray waveguides (see figure 3.1), namely front-coupling in forward-incidence, evanescent coupling in grazing indicence, and emission from buried dipoles. Using the mode expansions yields compact expressions for some key quantities, such as absorption length, wavelength, and coupling coefficients. In addition to the analytical discussion, we also present numerical code to find resonant waveguide modes and the corresponding coefficients as well as to compute the full Green's functions in stratified media. The code is made publicly available under the GPLv3 license [LA23].

After this introduction, the paper is structured as follows. Section 3.2 introduces the vector wave equations and Green's functions in inhomogeneous media. In section 3.3, we derive solutions to the vector wave equations in the absence of sources and discuss their classification into resonant and non-resonant modes. In section 3.4 we derive and discuss the fields caused by line sources. Point sources are considered in section 3.5. In section 3.6, we discuss a matrix formalism and our numerical approach that can be used to compute the fields and Green's functions in layered media. In section 3.7, these general results are then applied. For three important geometries corresponding to prototypical experiments with x-ray waveguides, we derive analytical expressions and present numerical calculations. We conclude the paper in section 3.8.

3.2. Equations for the electromagnetic fields

Starting from Maxwell's equations, we remind ourselves of the derivation of the time harmonic vector wave equations and their solutions in terms of electromagnetic Green's functions within macroscopic electrodynamics. We then discuss transverse solutions in translationally invariant stratified media.

3.2.1. Vector wave equations

Consider linear, isotropic, and possibly lossy materials characterized by their position-dependent complex relative permittivity $\epsilon(\mathbf{r})$ and permeability $\mu(\mathbf{r})$. For electromagnetic fields with harmonic time dependence $e^{-i\omega t}$, the macroscopic Maxwell equations read

$$\nabla \times \mathbf{E} = -\mathbf{J}_{\mathrm{m}} + i\omega\mathbf{B}, \tag{3.2}$$

$$\nabla \times \mathbf{H} = \mathbf{J}_{\mathrm{e}} - i\omega\mathbf{D}. \tag{3.3}$$

Here, $\mathbf{J}_{\mathrm{e}}$ is the electric and $\mathbf{J}_{\mathrm{m}}$ the magnetic current density. The latter is commonly introduced to make the equations symmetric from a mathematical viewpoint (see for example [Che99] or [HY02]). Even though there are no microscopic magnetic charges or true magnetic currents, magnetic dipoles due to microscopic electric current loops or atomic or nuclear transitions can be described by this magnetic current density.

In linear and isotropic media, we have the constitutive relations $\mathbf{D} = \epsilon_0\epsilon\mathbf{E}$ and $\mathbf{B} = \mu_0\mu\mathbf{H}$. Substituting the constitutive relations into the Maxwell equations and taking the curl gives inhomogeneous equations for the electric and magnetic fields, the *vector wave equations*

$$\left\{\mu\nabla \times \frac{1}{\mu}\nabla \times -k^2n^2\right\}\mathbf{E} = i\omega\mu_0\mu\mathbf{J}_{\mathrm{e}} - \mu\nabla \times \frac{\mathbf{J}_{\mathrm{m}}}{\mu}, \tag{3.4a}$$

$$\left\{\epsilon\nabla \times \frac{1}{\epsilon}\nabla \times -k^2n^2\right\}\mathbf{H} = i\omega\epsilon_0\epsilon\mathbf{J}_{\mathrm{m}} + \epsilon\nabla \times \frac{\mathbf{J}_{\mathrm{e}}}{\epsilon}, \tag{3.4b}$$

where $k = \omega/c = \omega\sqrt{\mu_0\epsilon_0}$ and $n^2 = \epsilon\mu$ is the complex refractive index. Noting the symmetry of (3.4a) and (3.4b), a manifestation of the duality principle of electric and magnetic fields, we write

$$\left\{s_a\nabla \times \frac{1}{s_a}\nabla \times -k^2n^2\right\}\mathbf{U}_a = s_a\mathbf{F}_a, \tag{3.5}$$

with fields $\mathbf{U}_\mathrm{e} = \mathbf{E}$, $\mathbf{U}_\mathrm{m} = H$, source terms

$$\mathbf{F}_\mathrm{e} = i\omega\mu_0\mathbf{J}_\mathrm{e} - \nabla\times\mu^{-1}\mathbf{J}_\mathrm{m}, \tag{3.6a}$$

$$\mathbf{F}_\mathrm{m} = i\omega\epsilon_0\mathbf{J}_\mathrm{m} + \nabla\times\epsilon^{-1}\mathbf{J}_\mathrm{e}, \tag{3.6b}$$

and $s_\mathrm{e} = \mu$ and $s_\mathrm{m} = \epsilon$. In the following we omit the field index a whenever the meaning is clear.

3.2.2. Green's functions

The field produced by a source $\mathbf{F}$ can be solved in terms of the dyadic Green's functions,

$$\mathbf{U}_a(\mathbf{r}) = \int \mathrm{d}^3\mathbf{r}'\underline{\mathbf{G}}_a(\mathbf{r},\mathbf{r}')\cdot\mathbf{F}_a(\mathbf{r}') \tag{3.7}$$

with the Green's function being a solution of the vector wave equations for a point source,

$$\left\{s_a(\mathbf{r})\nabla\times\frac{1}{s_a(\mathbf{r})}\nabla\times -k^2n(\mathbf{r})^2\right\}\underline{\mathbf{G}}_a(\mathbf{r},\mathbf{r}') = s_a(\mathbf{r})\delta(\mathbf{r}-\mathbf{r}')\underline{\mathbf{1}}, \tag{3.8}$$

where $a = \mathrm{e,m}$. The Green's functions are unique when boundary conditions are specified. In an unbounded and absorbing medium, the solutions must vanish at infinity. The validity of (3.7) can be easily verified by inserting (3.7) into (3.5) and using (3.8). Note that (3.7) is only valid for $\mathbf{r}$ not lying in the support of the source term $\mathbf{F}$, because the Green's function has a singularity at $\mathbf{r} = \mathbf{r}'$ that requires special treatment [HY02; Che99]. To simplify the discussion, we assume here and in the following that the observation point lies outside the source region.

The dyadic Green's functions for the electric and magnetic field are not independent, but are related by

$$\underline{\mathbf{G}}_\mathrm{e}(\mathbf{r},\mathbf{r}') = -\frac{1}{\epsilon(\mathbf{r})k^2}\delta^3(\mathbf{r}-\mathbf{r}') - \frac{1}{\epsilon(\mathbf{r})k}\nabla\times\underline{\mathbf{G}}_\mathrm{m}\times\overleftarrow{\nabla}'\frac{1}{\epsilon(\mathbf{r}')k} \tag{3.9a}$$

$$\underline{\mathbf{G}}_\mathrm{m}(\mathbf{r},\mathbf{r}') = -\frac{1}{\mu(\mathbf{r})k^2}\delta^3(\mathbf{r}-\mathbf{r}') - \frac{1}{\mu(\mathbf{r})k}\nabla\times\underline{\mathbf{G}}_\mathrm{e}\times\overleftarrow{\nabla}'\frac{1}{\mu(\mathbf{r}')k} \tag{3.9b}$$

(compare [Buh13], eq. 2.204). While many authors focus on the electric Green's function for that reason, both have their use in the present discussion.

The fields can be expressed in terms of the electric and magnetic currents. Here, we consider the electric field caused by an electric source current. The general case is derived in appendix 3.D. Substituting $\mathbf{F}$ in (3.7), assuming a purely electric source current, yields

$$\mathbf{E}(\mathbf{r}) = \frac{i\omega\epsilon_0}{c^2}\int \mathrm{d}^3\mathbf{r}'\underline{\mathbf{G}}_{\mathrm{e}}(\mathbf{r},\mathbf{r}')\cdot\mathbf{J}_{\mathrm{e}}(\mathbf{r}'). \tag{3.10}$$

This allows to directly compute the electric and magnetic field caused by oscillating dipoles, such as $\mathbf{J}_{\mathrm{e}}(\mathbf{r}) = -i\omega\mathbf{p}\delta^3(\mathbf{r}-\mathbf{r}_0)$.

3.2.3. Transverse solutions in stratified media

The equations simplify significantly in stratified media, and even further for fields that are constant along y.

Consider a stratified medium in a coordinate system where the relative permeability ϵ and relative permeability μ depend on z only. Further, assume that the fields are constant along y. In this case, the term in curly braces in (3.5) and (3.8) becomes

$$\left\{\begin{pmatrix} -s\partial_z s^{-1}\partial_z & 0 & s\partial_z s^{-1}\partial_x \\ 0 & -\partial_x^2 - s\partial_z s^{-1}\partial_z & 0 \\ \partial_x\partial_z & 0 & -\partial_x^2 \end{pmatrix} - k^2n^2\right\} \tag{3.11}$$

so that the y-component decouples from the x and y components. In source-free regions, since the fields are coupled by (3.2) and (3.3), only 2 out of the 6 components of $\mathbf{E}$ and $\mathbf{H}$ are independent. A solution for H_y and E_y fully specifies the solution for the remaining components. Solutions with $H_y = 0$ and E_y are often called *transverse electric* (TE) and *transverse magnetic* (TM), respectively. The derivatives for the two polarizations are summarized in Tab. 3.1. Since the two polarizations decouple, we can analyze them independently.

Table 3.1.: Transverse field components and their derivatives.

polarization	U	$\partial_x U$	$\partial_z U$
TE	E_y	$ik\mu Z_0 H_z$	$-ik\mu Z_0 H_x$
TM	H_y	$-ik\epsilon Z_0^{-1}E_z$	$ik\epsilon Z_0^{-1}E_x$

3.2.4. Power flow

Power flow is given by the real value of the Poynting vector, which is defined as

$$\mathbf{S} = \frac{1}{2}\mathbf{E}\times\overline{\mathbf{H}} = \frac{-i}{2\omega\mu_0\bar{\mu}}\mathbf{E}\times(\nabla\times\overline{\mathbf{E}}). \tag{3.12}$$

For fields with $\partial_y \mathbf{E} = 0$, it separates into TE and TM contributions like

$$\mathbf{S}^{\mathrm{TE}} = \frac{-i}{2\omega\mu_0\bar{\mu}} \left\{ E_y \partial_x \bar{E}_y \hat{\mathbf{x}} + E_y \partial_z \bar{E}_y \hat{\mathbf{z}} \right\} \tag{3.13}$$

$$\mathbf{S}^{\mathrm{TM}} = \frac{-i}{2\omega\mu_0\bar{\mu}} \left\{ E_z(\partial_x \bar{E}_z - \partial_z \bar{E}_x)\hat{\mathbf{x}} - E_x(\partial_x \bar{E}_z - \partial_z \bar{E}_x)\hat{\mathbf{z}} \right\}. \tag{3.14}$$

They can be expressed in terms of U_y using Tab. 3.1.

3.3. Free fields in stratified media

We discuss the structure of solutions for the source-free case of the vector wave equations (3.5). Suppose that permittivity and permeability independent of x and y and take constant values ϵ_-, μ_- and ϵ_+, μ_+ when $z < z_-$ and $z > z_+$, respectively, for some positions z_-, z_+ in bottom and top half-space.

3.3.1. Separating the dimensions

The TE- and TM-polarized components of (3.5) decouple as in (3.11), so that the y-component simplifies to

$$\left\{ s\partial_z s^{-1}(z)\partial_z + \partial_x^2 + k^2 n^2(z) \right\} U_y = 0. \tag{3.15}$$

The components E_y and H_y as well as E_x and H_x are continuous across interfaces, which implies that U_y and $s^{-1}\partial_z U_y$ with $U_y = E_y$ (TE) and $U_y = H_y$ (TM) are continuous.

We use separation of variables on (3.15) and write $U_y(x, z) = u_x(x)u_z(z)$, obtaining a pair of eigenvalue problems for each polarization,

$$-\partial_x^2 u_x(x) = k^2\nu^2 u_x(x), \tag{3.16a}$$

$$\left\{ s\partial_z s^{-1}\partial_z + k^2 n^2(z) \right\} u_z(z) = k^2\nu^2 u_z(z), \tag{3.16b}$$

such that u_x, $(u_x)'$, u_z, as well as $s^{-1}(u_z)'$ are continuous, complex-valued functions. The unit-less quantity $\nu \in \mathbb{C}$ is known as the *effective (refractive) index* and the wavenumber $q = k\nu$ as the *propagation constant* in the context of waveguides. The general solution for u_x is easily found to be a superposition of forward-propagating $\exp(ik\nu x)$ and backward-propagating $\exp(-ik\nu x)$ components. The transversal equation will occupy us in the following section.

3.3.2. The transversal eigenvalue problem

While the longitudinal eigenvalue problem (3.16a) has a continuous spectrum, the transversal eigenvalue problem (3.16b) is of Sturm-Liouville form and generally has a discrete and a continuous spectrum of eigenvalues [HY02]. The discrete spectrum of proper solutions correspond to the *guided* (or surface-wave) modes, whereas the continuous spectrum of improper solutions correspond to the *radiative* modes in the context of classical waveguide theory.

It is worthwhile to take a closer look at the operator on the left-hand side of (3.16b),

$$L = s\partial_z s^{-1}\partial_z + k^2 n^2. \tag{3.17}$$

Importantly, L is generally *not* self-adjoint because the refractive index n is complex-valued. While self-adjoint Sturm-Liouville operators were extensively studied in the literature, among other things due to their manifold applications in quantum mechanics, the non-self-adjoint theory is much less developed (see for example [Zet12]). In particular, analagous to the situation occuring in the eigensystems of non-symmetric matrices, many tools of self-adjoint operator theory such as the L^2-orthogonality of eigenfunctions cannot be applied. Nevertheless, we can find similar relations in many cases.

Analagous to non-symmetric matrices having distinct left and right eigenvectors, the eigenfunctions and adjoint eigenfunctions of L are distinct. In the case that the following integrals converge, integration by parts gives

$$\left\langle \overline{s^{-1}u}, Lv\right\rangle = \left\langle \overline{s^{-1}v}, Lu\right\rangle + \left[s^{-1}(uv' - u'v)\right]_{-\infty}^{\infty}, \tag{3.18}$$

where $\langle f, g\rangle$ denotes the usual L^2 inner product with complex conjugation in the first argument. If v and its derivative vanish sufficiently rapidly compared with u and its derivative, and/or vice versa, the boundary term vanishes. Thus, for for a given eigenfunction u with eigenvalue λ, the corresponding adjoint eigenfunction is $\overline{s^{-1}u}$, in the sense that for any sufficiently rapidly decaying test function ψ we have

$$\langle \overline{s^{-1}u}, L\psi\rangle = \langle \overline{s^{-1}\psi}, Lu\rangle = \lambda\langle \overline{s^{-1}\psi}, u\rangle = \lambda\langle \overline{s^{-1}u}, \psi\rangle. \tag{3.19}$$

In particular, taking u, v in (3.18) to be two normalizable eigenfunctions u_i, u_j with eigenvalues λ_i, λ_j we can show the following relation,

$$(\lambda_i - \lambda_j)\langle \overline{s^{-1}u_n}, u_m\rangle = 0. \tag{3.20}$$

Thus, (normalizable) eigenfunctions are orthogonal to adjoint eigenfunctions corresponding to distinct eigenvalues, and we will choose to normalize these eigenfunctions such that

$$\langle\overline{s^{-1}u_n}, u_m\rangle = \delta_{nm}. \tag{3.21}$$

This *biorthogonality* replaces the usual orthogonality of the eigenfunctions. It should be noted, that this fact is well-established, also in optics (see for example [Sie79]), yet not relevant for non-absorbing waveguides. An alternative way to formalize (3.21) is the introduction of 2-form such that the eigenfunctions are orthogonal with respect to this form [LLY94].

In general, not all (generalized) eigenfunctions are L^2-normalizable, and the integrals may fail to converge. Nevertheless, we will demonstrate that a suitable generalization of (3.21) exists that allows to normalize certain non-normalizable eigenfunctions.

3.3.3. Resonant modes

Any formal solution to $(L - k^2\nu^2)u = 0$ can be written for $z < z_-$ and $z > z_+$, for some points $z_\pm$ in the bottom and top layer respectively, as

$$u(z) = a_\pm e^{ikp_\pm(z-z_\pm)} + b_\pm e^{-ikp_\pm(z-z_\pm)}, \tag{3.22}$$

where $p_\pm^2 = n_\pm^2 - \nu^2$. The coefficients $a_\pm, b_\pm \in \mathbb{C}$ depend on the boundary conditions. An important class of solutions are those that can be written as a single exponential function in both of the regions, so that $a_- = 0$ and $b_+ = 0$. Equivalently, for some points z_- and z_+ in the bottom and top layer, respectively,

$$u'(z) = -ikp_- u(z), \text{ for all } z < z_-, \tag{3.23a}$$
$$u'(z) = ikp_+ u(z), \text{ for all } z \geq z_+. \tag{3.23b}$$

We call the solutions satisfying both (3.23a) and (3.23b) *resonant modes*. They are equivalent to the ”resonances” that have been studied by Schenk [Sch11].

Note that, since $p_\pm$ are complex numbers with arbitrary sign, the resonant modes are not necessarily bounded at infinity, and not all resonant modes are normalizable.

3.3.4. Modified inner product

We can modify the inner product to be applicable to functions belonging to the solution class of resonant modes and to avoid the divergences at infinity. Inspired by a similar definition for quasi-normal modes [LLY94], we define

$$\langle u, v\rangle_\partial := \int_{z_-}^{z_+} \overline{u(z)} v(z) \mathrm{d}z - \left[\frac{\bar{u}v}{\bar{u}'/\bar{u} + v'/v}\right]_{z_-}^{z_+}. \tag{3.24}$$

More generally, (3.24) merely requires the functions u and v to satisfy (3.23a) and (3.23b) and not necessarily requires them to be solutions of (3.16b). For convenience, we will refer to (3.24) as the modified *inner product*, although we emphasize that it is not, strictly, an inner product. Equation (3.24) naturally emerges in the semi-spectral representation of the Green's function in section 3.4.5 and appendix 3.C. Given (3.23a) and (3.23b), this definition does not depend on the choice of $z_\pm$ as long as they are points in the bottom and top layer. Moreover, if both u and v decay for $|z| \to \infty$, definition (3.24) reduces to the standard L^2 inner product, as the boundary terms correspond to the integrals from $z_\pm$ to $\pm\infty$.

In appendix 3.A we show for any functions u, v which can be written as an exponential function in the top and bottom layers, the following integration by parts identity holds,

$$\langle u', v\rangle_\partial + \langle u, v'\rangle_\partial = 0. \tag{3.25}$$

Thus, the adjoint of L is well defined with respect to the modified inner product, and in particular every resonant mode has a corresponding adjoint eigenfunction with respect to the modified inner product,

$$\left\langle \overline{s^{-1}u_i}, Lv\right\rangle_\partial = \lambda_i \left\langle \overline{s^{-1}u_i}, v\right\rangle_\partial . \tag{3.26}$$

This in turn shows that even for divergent resonant modes, we have the following bi-symmetry relation

$$\left\langle \overline{s^{-1}u_m}, Lu_n\right\rangle_\partial = \left\langle \overline{s^{-1}u_n}, Lu_m\right\rangle_\partial . \tag{3.27}$$

The bi-symmetry relation guarantees that resonant modes, even diverging ones, are bi-orthogonal with respect to (3.24), and thus we can normalize all resonant modes to obey

$$\left\langle \overline{s^{-1}u_n}, u_m\right\rangle_\partial = \delta_{m,n}. \tag{3.28}$$

3.3.5. The Wronskian resonance condition

Next, we present a practical method to classify whether a given complex number $\nu \in \mathbb{C}$ admits a resonant-mode solution with that eigenvalue ν. To that end, we use a relatively general method (see [GG01], Ch IV.6) to relate the resonance condition (3.23a) and (3.23b) to a condition about the solutions of a regular Sturm-Liouville initial value problem on the compact interval (z_-, z_+). It leads to a one-to-one correspondence of the complex roots of a holormorphic function, and the set of resonant modes.

There are at most a discrete set of resonant modes, and possibly none at all [Sch11, Thm. 2.12]. Certainly, it is clear that (3.23a) and (3.23b) can only simultaneously be fulfilled for special values of ν. However, since the initial value problem on the interval (z_-, z_+) has a solution for all possible initial values and this solution is unique [Zet12], we can always find unique solutions up to a global scale that satisfy *either* (3.23a) or (3.23b). We construct solutions $u_+(z;\nu)$ and $u_-(z;\nu)$ by setting

$$\begin{cases} u_\pm(z_\pm;\nu) = 1 \\ \partial_z u_\pm(z_\pm;\nu) = \pm ikp_\pm(\nu). \end{cases} \tag{3.29}$$

These solutions are resonant modes if and only if they are linearly dependent, that is, if their Wronskian vanishes,

$$\operatorname{Wron}\{u_-(z), u_+(z)\} = u_-(z)\frac{\partial u_+(z)}{\partial_z} - \frac{\partial u_-(z)}{\partial_z}u_+(z) = 0. \tag{3.30}$$

Here, the identically vanishing Wronskian implies linear dependence because the solutions are different from zero throughout the interval (z_-, z_+) (see [Bôc01]). Instead of the bare Wronskian, it is useful to work with the weighted Wronskian defined as

$$W(\nu) = \frac{1}{s}\left(u_-(\nu)\frac{\partial u_+(\nu)}{\partial_z} - \frac{\partial u_-(\nu)}{\partial_z}u_+(\nu)\right), \tag{3.31}$$

which is independent of z, as can be easily shown by inserting (3.16b).

We thus have a one-to-one correspondence between the set of resonant modes and the complex roots of the weighted Wronskian $W(\nu)$.

The weighted Wronskian takes particularly simple forms at z_- or z_+,

$$\begin{aligned} W &= s^{-1}(z_+)ikp_+u_-(z_+) - s^{-1}(z_+)\partial_z u_-(z_+) \\ &= s^{-1}(z_-)ikp_-u_+(z_-) + s^{-1}(z_-)\partial_z u_+(z_-). \end{aligned} \tag{3.32}$$

We will see in section 3.6 how it can be readily computed in the transfer matrix formalism.

A resonant mode $u_\pm$ for fixed ν_m, with $W(\nu_m) = 0$, is unique up to a global prefactor. We normalize the solutions by setting

$$u_m(z) := \frac{u_\pm(z)}{\sqrt{\left\langle s^{-1}u_\pm, u_\pm\right\rangle_\partial}}. \tag{3.33}$$

Note that (3.33) may give a different overall sign for u_+ and u_-, so a choice has to be made for consistency.

3.3.6. Riemann sheets and branch cuts

The choice of sign in the mappings $\nu \mapsto p_\pm(\nu)$ that solve $n_\pm^2 - \nu^2 = p_\pm^2$ for the resonance condition (3.23a) and (3.23b) dictates the asymptotic behavior of the corresponding modes and thereby what kind of modes are found when solving $W(\nu) = 0$. Each of the two quadratic expressions has a 2-valued solution set for every complex number ν, the Riemann surface of the complex square root. In the same way, $W(\nu)$ can be seen as a 4-valued Riemann surface, discriminated by the two signs for $p_+(\nu)$ and $p_-(\nu)$. As a consequence, the complex function $W(\nu)$ has 4 algebraic branch points where the mode index coincides with the material index of the bottom or top layer, $\nu \in \{\pm n(z_-), \pm n(z_+)\}$. In general, resonant modes can be located on all 4 sheets of the Riemann surface. A single-valued function W is obtained by choosing a single-valued complex square root, which introduces 4 branch cuts, as shown in Fig. 3.2.

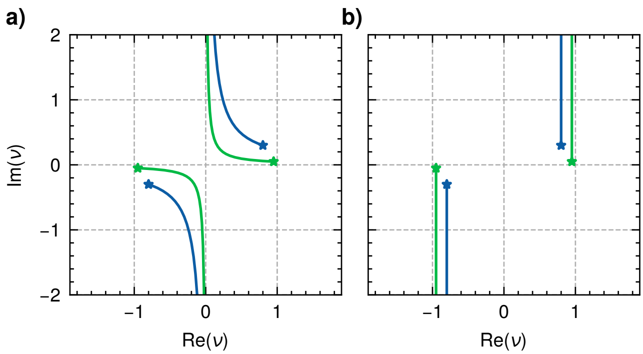

Figure 3.2.: Sketch of branch points (stars) and branch cuts (lines) for non-degenerate outer layer indices. (a) Natural branch cuts for bounded solutions. (b) Vertical branch cuts. The branch points, which are the refractive indices of the outer layers, would be indistinguishable from 1 at this scale for hard x-rays.

Clearly, a resonant mode is normalizable if and only if $\mathrm{Im}\{p_-\} > 0$ and $\mathrm{Im}\{p_+\} > 0$. Setting $p_\pm = p_{\mathrm{dec}}(\nu; n_\pm)$, where

$$p_{\mathrm{dec}}(\nu; n) = i\sqrt{\nu^2 - n^2} \tag{3.34}$$

with the principal complex square root, ensures that $\mathrm{Im}\{p_\pm\} \geq 0$.

Each single-valued mapping $\nu \mapsto W(\nu)$ is a holomorphic function in the entire complex plane $\mathbb{C}$ except for the two branch cuts. This is guaranteed because solutions of the regular Sturm-Liouville initial value problem are complex differentiable everywhere as a function of their data and initial values [Zet12]. The branch cuts enter through the initial values in (3.29).

In addition to the *decaying* choice of branch cut made in (3.34), there are other useful choices.

$$p_{\mathrm{out}}(\nu) := \sqrt{n^2 - \nu^2} \tag{3.35}$$

with the standard choice of complex square root guarantees $\mathrm{Re}\{p\} \geq 0$, so that the corresponding modes are outwards-propagating. It is easy to see that for absorbing materials, $\mathrm{Im}\{\nu\} > 0$, both definitions coincide on the real axis so that $p_{\mathrm{out}}(\nu) = p_{\mathrm{dec}}(\nu)$ for $\mathrm{Im}\{\nu\} = 0$.

Neither definitions, (3.34) and (3.35), are ideal for numerical purposes, because they define branch cuts which are curved in the complex ν plane. The inverse Fourier integral along the branch cut involves a plane-wave factor of the form $e^{ik\nu x}$, and a curved branch cut will result in a rapdily oscillating integral, which is challenging to numerically evaluate.

Setting

$$p_{\mathrm{vert}}(\nu) := i\sqrt{-i(n-\nu)}\sqrt{-i(n+\nu)} \tag{3.36}$$

results in branch cuts that are parallel to the imaginary axis. Along such a branch cut, the real part of ν is constant, and thus the plane wave factor $e^{ik\nu x}$ in the inverse Fourier integral will be purely exponentially decaying, and the integral will rapidly converge.

Finally, the Riemann surface can be unfolded to eliminate the branch points using conformal mappings [SFH93; BAG97]. Setting

$$p_{\pm}(\xi) = \xi \pm \frac{n_+^2 - n_-^2}{4\xi}, \tag{3.37}$$

eliminates the branch cuts [SFH93] for $W(\xi) = W(\nu(\xi))$. The other quantities then become

$$p(\xi) = i\sqrt{-p_+^2(\xi) - (n^2 - n_+^2)}, \qquad \nu(\xi) = \sqrt{n_+^2 - p_+^2(\xi)}. \tag{3.38}$$

Using the mapped coordinates, $W(\xi) = 0$ will be solved by all resonant modes.

3.3.7. Guided and leaky modes

In the literature, the resonant modes are classified into *guided* and *leaky* modes (see for example [HM09] for a recent discussion). Guided modes are the *normalizable* resonant modes. In contrast to guided modes, leaky modes are diverging for either $z \to -\infty$ (bottom-leaky), $z \to \infty$ (top-leaky), or both (double-leaky).

Depending on the choice of branch cuts, the complex roots of $W(\nu)$ correspond to different types of resonant modes. For the "natural" choice defined in (3.34) [see

Fig. 3.2(a)], the transversal solutions are bounded and the roots hence only correspond to guided modes. For other branch cuts, such as (3.36) (see Fig. 3.2(b)), on the other hand, the solution set in general consists of both guided and leaky modes.

3.3.8. Radiative modes

The non-nomalizable but bounded improper solutions of $(L - k^2\nu^2)u = 0$ form the set of radiative (or radiation) modes. As discussed by Vassallo [Vas79], they can be divided into two groups that are either radiative in the top or bottom layer. The groups become degenerate when top and bottom materials are identical, which can be avoided by changing one of the indices by an infinitesimal imaginary amount.

A solution is radiative in the top or bottom layer, if $\mathrm{Im}\{p_+\} = 0$ or $\mathrm{Im}\{p_-\} = 0$, respectively. Setting $p_+ = p_{\mathrm{out}}(\nu)$ ensures that $\mathrm{Im}\{p_+\} = 0$ when

$$\nu \in \left\{\nu : \mathrm{Im}\{\nu^2\} = \mathrm{Im}\{n_+^2\}, |\mathrm{Re}\{\nu\}| \leq \mathrm{Re}\{n_+\}\right\},$$

and p_- accordingly. The mode indices ν of radiative modes have

$$\mathrm{Im}\{\nu\} = \mathrm{Re}\{\nu\}\,\mathrm{Im}\{n_\pm\}/\,\mathrm{Re}\{n_\pm\}.$$

For any such ν, the radiative modes are simply given by $u_\pm$ as defined in (3.29), and using (3.34) for the non-radiative layer. If $n_+ \neq n_-$, no solution can be radiative in the top and bottom layer simultaneously.

3.3.9. Mode dispersion

So far we have looked at the strictly monochromatic case only. X-ray light sources such as synchrotrons and x-ray free electron lasers, however, produce pulsed light, which has a finite bandwidth, typically in the order of 1 eV. When discussing pulses, it is important to know how the mode indices depend on the angular frequency ω. The group velocity is approximated to first order by

$$v_{\mathrm{g}} = \frac{c}{\mathrm{Re}\left\{\nu_m + \omega\frac{\partial \nu_m}{\partial \omega}\right\}} \approx \frac{c}{\mathrm{Re}\{\nu_m\}}. \tag{3.39}$$

In appendix 3.B, we show that

$$\nu_m \frac{\partial \nu_m}{\partial \omega} = \frac{1}{2}\left\langle \frac{\partial \ln(s)}{\partial \omega}(\nu_m^2 - n^2)\right\rangle_{u_m} + \frac{c^2}{2\omega^2}\left\langle \frac{\partial \ln(s)}{\partial \omega}\right\rangle_{\partial_z u_m} + \left\langle \frac{n^2 - \nu_m^2}{\omega}\right\rangle_{u_m} + \left\langle n\frac{\partial n}{\partial \omega}\right\rangle_{u_m}, \quad (3.40)$$

for any resonant mode with index $\nu_m(\omega)$. Here, the 'expectation value' is defined as $\langle A\rangle_u = \langle \overline{s^{-1}u}, Au\rangle_\partial$. For TE-modes, we have $s \equiv \mu \equiv 1$ so that the first 2 terms vanish. Using $\nu_m \approx n \approx 1$, this can be well approximated by

$$\frac{\partial \nu_m(\omega)}{\partial \omega} \approx \int \left\{\frac{2(n-\nu)}{\omega} + \frac{\partial n(z,\omega)}{\partial \omega}\right\} \frac{u_m(z,\omega)^2}{s(z,\omega)} \mathrm{d}z. \quad (3.41)$$

As a consequence, the mode dispersion is on the scale of the material dispersion and hence small in the absence of absorption edges or other resonances. Corrections to the group velocity can be computed using (3.41).

It should be noted that the decomposition into guided and leaky modes is only valid *locally* in the frequency spectrum. For broad-band pulses, or in the vicinity of strong material resonances, the mode classification is no longer unique [SHB97].

3.4. Line sources

The fields in the presence of sources can be conveniently solved in terms of the dyadic Green's functions, defined in (3.8). An important special case are line sources, which extend homogeneously along one dimension, here y. This case was previously discussed in [Vas79].

3.4.1. The two-dimensional Green's function

When the source terms are constant over y, the integral over y in (3.7) can be performed and the Green's function for line sources can be defined as

$$\underline{\mathbf{G}}^{\mathrm{ls}}(x-x', z, z') = \int \mathrm{d}y' \underline{\mathbf{G}}(x-x', y-y', z, z'). \quad (3.42)$$

While the 3-dimensional Green's functions have the dimension of inverse length, these 2-dimensional Green's functions are dimensionless. By integrating both sides of

(3.8) over y and using the fact that the functions vanish at infinity, it follows that

$$\left\{D(z) - k^2 n(\mathbf{r})^2\right\} \underline{\mathbf{G}}_a^{\mathrm{ls}}(\mathbf{r}, \mathbf{r}') = s_a(\mathbf{r})\delta(x - x')\delta(z - z')\underline{\mathbf{1}}, \tag{3.43}$$

with

$$D(z) = \begin{pmatrix} -s\partial_z s^{-1}\partial_z & 0 & s\partial_z s^{-1}\partial_x \\ 0 & -\partial_x^2 - s\partial_z s^{-1}\partial_z & 0 \\ \partial_x \partial_z & 0 & -\partial_x^2 \end{pmatrix}. \tag{3.44}$$

Consequently, the yy-components decouple as in (3.11) and we can analyze the two *scalar* yy-components independently. Defining $g_a = \underline{\mathbf{G}}^{\mathrm{ls}}_{a,yy}$, we obtain

$$\left\{\partial_x^2 + s\partial_z s_a^{-1}\partial_z + k^2 n^2(z)\right\} g_a(x - x', z, z') = -s_a(z)\delta(z - z')\delta(x - x'). \tag{3.45}$$

This shows that the yy-components of the Green's function for line sources are simply the two-dimensional Green's functions of the medium. In the following, we will discuss solutions of (3.45). We will drop the index a for convenience and keep in mind that the expressions are valid for both electric and magnetic Green's functions.

3.4.2. Homogeneous Green's function

We start by deriving the two-dimensional Green's function for homogeneous media $g^{(0)}(x - x', z - z')$. Writing the Green's function as a Fourier transform and exploiting its rotational symmetry, we obtain

$$\begin{aligned} g^{(0)}(\boldsymbol{\rho}) &= \int \frac{\mathrm{d}^2 q}{(2\pi)^2} e^{i\mathbf{q}\cdot\boldsymbol{\rho}} g^{(0)}(q) \\ &= \int_0^\infty \frac{\mathrm{d}q}{2\pi} J_0(q\rho) q g^{(0)}(q), \end{aligned} \tag{3.46}$$

where J_0 is the Bessel function of first kind. Inserting (3.46) into (3.45) and using that s and n are constants, we immediately obtain the spectral representation

$$g^{(0)}(q) = \frac{s}{q^2 - k^2 n^2}. \tag{3.47}$$

Inserting (3.47) into (3.46) yields

$$g^{(0)}(\boldsymbol{\rho}) = \frac{is}{4} H_0^{(1)}(nk\rho), \tag{3.48}$$

where $H_0^{(1)}$ is the Hankel function of first kind.

3.4.3. Semi-spectral representation

The general stratified medium can be solved similarly using Fourier transforms. While the solution is well known, we briefly remind ourselves of its construction. Taking the one-dimensional Fourier transform of (3.45) with respect to $x - x'$ yields

$$\left\{s\partial_z s^{-1}\partial_z + k^2n^2(z) - q^2\right\} g(q,z,z') = -s(z)\delta(z-z'), \tag{3.49}$$

where $g(q,z,z')$ is a continuous function of z. Identifying q^2 with $k^2\nu^2$, equation (3.49) becomes identical to the source-free eigenvalue problem (3.16b), except for the δ-contribution at $z = z'$. As a consequence, we can construct a bounded solution piece-wise for $z < z'$ and $z > z'$,

$$g(q,z,z') = a_-u_-(z;q)\Theta(z'-z) + a_+u_+(z;q)\Theta(z-z'), \tag{3.50}$$

where we have inserted the solutions defined in (3.29). The symbol $\Theta(z)$ denotes the unit step function. It remains to find the two coefficients $a_\pm$. In the following the q-dependence is not displayed. Integrating (3.49) from $z' - 0$ to $z' + 0$ and using that $g(q,z)$ is continuous yields

$$\partial_z g(q,z'+0,z') - \partial_z g(q,z'-0,z') = -s(z'), \tag{3.51}$$

which, using (3.50), becomes

$$a_+\partial_z u_+(z') - a_-\partial_z u_-(z') = -s(z'). \tag{3.52}$$

Moreover, we have from continuity that $a_-u_-(z') = a_+u_+(z')$, so that

$$\frac{-a_-a_+}{s(z')}\left(u_-(z')\partial_z u_+(z') - u_+(z')\partial_z u_-(z')\right) = a_+u_+(z') = a_-u_-(z'). \tag{3.53}$$

We obtain $a_\pm = -u_\mp(z')/W$, where we have inserted W as defined in (3.31), which is independent of z. Inserting the coefficients into (3.50) finally gives

$$g(q,z,z') = -\frac{1}{W}\left\{u_+(z')u_-(z)\Theta(z'-z) + u_-(z')u_+(z)\Theta(z-z')\right\}, \tag{3.54}$$

which we call the *semi-spectral representation*.

As an example, consider a homogeneous environment with refractive index n. Equation (3.54) then yields

$$g^{(0)}(q,z,z') = \frac{is}{2kp}e^{ikp|z-z'|}, \tag{3.55}$$

the Fourier-transform of (3.48).

3.4.4. Derivation of real-space solutions

The real-space form of the Green's function can be written as

$$g(x-x',z,z') = \int_{-\infty}^{\infty} \frac{\mathrm{d}q}{2\pi} e^{iq(x-x')} g(q,z,z'). \tag{3.56}$$

Numerical integration is difficult due to the rapidly oscillating integrand. We can however extend the integral over a closed contour and exploit the structure of $g(q,z,z')$. The Fourier-space Green's function is given as a rational function (3.54), where the numerator $u_+(q)u_-(q)$ is holomorphic everywhere and the denominator $W(q)$ is holomorphic everywhere except at its 4 algebraic branch points. Since $W(q)$ is the denominator, its complex roots produce poles in $g(q)$.

For $x > x'$ ($x < x'$), we close the contour in the upper half (lower half) of the complex q plane (see Fig. 3.2) such that that arc portion of the integral vanishes due to the exponential decay of $\exp(iq(x-x'))$. We must, however, be careful to choose the contours in a way to avoid the poles and branch cuts of the integrand.

Note, however, that the branch cuts can be chosen (compare Section 3.3.6) and its choice influences which poles are exposed. The branch cut corresponding to decaying solutions is curved and only exposes the poles corresponding to guided modes, a finite number N_{guided}. We deform the contour so that it runs next to the branch cut from infinity to the branch point and back to infinity on the other side (see Fig. 3.2). We obtain

$$\begin{aligned} g(x-x',z,z') = i &\sum_{m=1}^{N_{\text{guided}}} \operatorname{Res}\{g; q = k\nu_m\} e^{ik\nu_m|x-x'|} \\ &+ r_{\text{top}}(x-x',z,z') + r_{\text{bot}}(x-x',z,z'). \end{aligned} \tag{3.57}$$

The non-resonant terms r_{top} and r_{bot} correspond to the parts of the contour wrapping around the branch cuts caused by the top and bottom layer, respectively. Since the branch cuts coincide with the radiation modes, these terms can be understood as contribution by radiation modes. Performing the integrals for these non-resonant terms is non-trivial, because the branch cuts run almost parallel to the real axis, causing rapid oscillations. However, in many cases the guided modes alone provides good asymptotic approximations of the Green's function.

But not all systems even support guided modes. To obtain asymptotic expressions for those systems, we deform the branch cuts to be parallel to the imaginary axis. This does not change the value of the integral, because it leaves the real axis unaffected. It changes, however, the non-resonant contributions to the integral and exposes the poles corresponding to leaky modes, if they exist. We obtain

$$\begin{aligned} g(x-x',z,z') = i\sum_m \operatorname{Res}\{g; q = k\nu_m\} e^{ik\nu_m|x-x'|} \\ + \tilde{r}_{\text{top}}(x-x',z,z') + \tilde{r}_{\text{bot}}(x-x',z,z'), \end{aligned} \tag{3.58}$$

where now m runs over the (possibly infinite) number of exposed guided and leaky modes. The non-resonant terms $\tilde{r}_{\text{top}}$ and $\tilde{r}_{\text{bot}}$ now correspond to the contour integrals following the *deformed* vertical branch cuts, which makes them easier to compute numerically. Due to the change of branch cut, these non-resonant modes are diverging for $|z| \to \infty$. We call them *diverging radiation modes*. Given that the total Green's function decays at infinity and the deformation of the branch cuts does not change the value of the integral (3.56), the leaky modes and diverging radiation modes must interfere destructively outside the central layers in such a way that the total Green's function does not diverge [HM09].

3.4.5. Computation of the residues

The residues in (3.58) can be expressed in a more useful way. From (3.54) and using that numerator and denominator are holomorphic functions of q, we can read off

$$\operatorname{Res}\{g; q = k\nu_m\} = -\frac{u_+(z')u_-(z)}{\partial_q W(q = k\nu_m)}, \tag{3.59}$$

where we used that $u_+ \propto u_-$ for zeros of W. As derived in appendix 3.C, we obtain

$$\partial_q W(\nu_m) = -2\nu_m k \left\langle \overline{s^{-1}u_-}, u_+ \right\rangle_\partial , \tag{3.60}$$

where $\langle \cdot, \cdot \rangle_\partial$ is the modified inner product as defined in (3.24). It then follows that

$$\operatorname{Res}\{g; q = k\nu_m\} = \frac{u_+(z')u_-(z)}{2\nu_m k \left\langle \overline{s^{-1}u_-}, u_+ \right\rangle_\partial}. \tag{3.61}$$

Using $u_+ \propto u_-$, we can insert the normalized modes to obtain

$$\operatorname{Res}\{g; q = k\nu_m\} = \frac{u_m(z')u_m(z)}{2\nu_m k}. \tag{3.62}$$

Inserting (3.62) into (3.58) or (3.57), we have

$$g(x-x',z,z') = i\sum_m \frac{u_m(z')u_m(z)}{2\nu_m k} e^{ik\nu_m|x-x'|} + \text{non-resonant}, \tag{3.63}$$

where the sum goes either over the guided modes or all the resonant modes and the non-resonant part changes accordingly. Knowing the resonant terms, the semi-spectral representation of (3.63) is easily seen to be

$$g(q,z,z') = \sum_m \frac{u_m(z')u_m(z)}{q^2-(\nu_m k)^2} + \text{non-resonant}, \tag{3.64}$$

where the non-resonant terms are the Fourier-transforms of the non-resonant terms in (3.63). Note that due to its branch points, $g(q,z,z')$ is not meromorphic as a function of q so that Mittag-Leffler's theorem is not applicable and the non-resonant terms are in general not holomorphic.

3.4.6. The dyadic Green's functions for line sources

From (3.43) it follows that the dyadic Green's function for line sources has 5 non-vanishing components,

$$\underline{\mathbf{G}}_a^{\text{ls}} = \begin{pmatrix} G_{a,xx}^{\text{ls}} & 0 & G_{a,xz}^{\text{ls}} \\ 0 & G_{a,yy}^{\text{ls}} & 0 \\ G_{a,zx}^{\text{ls}} & 0 & G_{a,zz}^{\text{ls}} \end{pmatrix}. \tag{3.65}$$

The index a indicates the electric ($a=\text{e}$) and magnetic ($a=\text{m}$) Green's functions.

While we have derived the yy-component in the previous section, $G_{a,yy}^{\text{ls}} \equiv g_a$, we can express the remaining components of (3.65) in terms of g_a. Integrating both sides of (3.9a) over y and inserting $\underline{\mathbf{G}}_{\text{m}}^{\text{ls}} = \text{g}_{\text{m}}\hat{\mathbf{y}}\hat{\mathbf{y}}$, we obtain, neglecting the deltas,

$$G_{\text{e},xx}^{\text{ls}}(x-x',z,z') = \frac{\partial_z\partial_{z'}\text{g}_{\text{m}}(x-x',z,z')}{k^2\epsilon(z)\epsilon(z')} \tag{3.66a}$$

$$G_{\text{e},xz}^{\text{ls}}(x-x',z,z') = -\frac{\partial_z\partial_{x'}\text{g}_{\text{m}}(x-x',z,z')}{k^2\epsilon(z)\epsilon(z')} \tag{3.66b}$$

$$G_{\text{e},zx}^{\text{ls}}(x-x',z,z') = -\frac{\partial_x\partial_{z'}\text{g}_{\text{m}}(x-x',z,z')}{k^2\epsilon(z)\epsilon(z')} \tag{3.66c}$$

$$G_{\text{e},zz}^{\text{ls}}(x-x',z,z') = \frac{\partial_x\partial_{x'}\text{g}_{\text{m}}(x-x',z,z')}{k^2\epsilon(z)\epsilon(z')}, \tag{3.66d}$$

and accordingly for $\underline{\mathbf{G}}_{\text{m}}^{\text{ls}}$.

Taking the Fourier-transform with respect to $x-x'$ yields, separating the TE and

TM components,

$$\underline{\mathbf{G}}_{\mathrm{e}}^{\mathrm{TE}}(q) = g_{\mathrm{e}}(q)\hat{\mathbf{y}}\hat{\mathbf{y}} \tag{3.67}$$

$$\underline{\mathbf{G}}_{\mathrm{e}}^{\mathrm{TM}}(q) = \frac{1}{k^2\epsilon(z)\epsilon(z')}\left\{\partial_z\partial_{z'}\hat{\mathbf{x}}\hat{\mathbf{x}} + iq\partial_z\hat{\mathbf{x}}\hat{\mathbf{z}} - iq\partial_{z'}\hat{\mathbf{z}}\hat{\mathbf{x}} + q^2\hat{\mathbf{z}}\hat{\mathbf{z}}\right\}g_{\mathrm{m}}(q). \tag{3.68}$$

We can read off the residues of the remaining components, complementing (3.62), at the resonances $q = k\nu_m^{\mu}$,

$$\mathrm{Res}\{G^{\mathrm{ls}}_{\mathrm{e},xx}; q = k\nu_{\mathrm{m},m}\} = \frac{1}{k^2\epsilon(z)\epsilon(z')}\frac{\partial_{z'}u_{\mathrm{m},m}(z')\partial_z u_{\mathrm{m},m}(z)}{2\nu_{\mathrm{m},m}k} \tag{3.69a}$$

$$\mathrm{Res}\{G^{\mathrm{ls}}_{\mathrm{e},xz}; q = k\nu_{\mathrm{m},m}\} = \frac{i}{k^2\epsilon(z)\epsilon(z')}\frac{u_{\mathrm{m},m}(z')\partial_z u_{\mathrm{m},m}(z)}{2} \tag{3.69b}$$

$$\mathrm{Res}\{G^{\mathrm{ls}}_{\mathrm{e},zx}; q = k\nu_{\mathrm{m},m}\} = -\frac{i}{k^2\epsilon(z)\epsilon(z')}\frac{\partial_{z'}u_{\mathrm{m},m}(z')u_{\mathrm{m},m}(z)}{2} \tag{3.69c}$$

$$\mathrm{Res}\{G^{\mathrm{ls}}_{\mathrm{e},zz}; q = k\nu_{\mathrm{m},m}\} = \frac{k\nu_m^H}{k^2\epsilon(z)\epsilon(z')}\frac{u_{\mathrm{m},m}(z')u_{\mathrm{m},m}(z)}{2}, \tag{3.69d}$$

and accordingly for $\underline{\mathbf{G}}^{\mathrm{ls}}_{\mathrm{m}}$.

To compute the semi-spectral representation of the full dyadic Green's function, one can first compute $G_{\mathrm{m},yy}(q)$ and $G_{\mathrm{e},yy}(q)$ and insert them into (3.67) and (3.68). To compute asymptotic expansions for the real-space Green's functions, the following strategy can be used. First, find the complex roots of $W_a(\nu)$ corresponding to the guided modes and as many of the leaky modes as needed for both E and H. Second, compute the corresponding residues for the 5 non-vanishing components. Finally, substitute the residues into (3.58).

3.5. Point sources

The Green's functions for line sources is useful to describe 2-dimensional problems. We now discuss the 3-dimensional Green's function, the solution of (3.8), which describes the fields due to a point source. It can be computed from the 2-dimensional one by exploiting the cylindrical symmetry [Joh11]. Similar to the 2-dimensional Green's function, we start with the semi-spectral representation and proceed with asymptotic expansions of the real-space function.

3.5.1. Symmetry considerations

The 3-dimensional Green's function takes the form $\underline{\mathbf{G}}(\mathbf{r}, \mathbf{r}') = \underline{\mathbf{G}}(\mathbf{r}_\parallel - \mathbf{r}'_\parallel, z, z')$ because of the in-plane symmetry. Writing the in-plane difference vector $\mathbf{r}_\parallel - \mathbf{r}'_\parallel$ in polar coordinates (ρ, ϕ), we obtain

$$\underline{\mathbf{G}}(\rho, \phi, z, z') = R_z(\phi)\underline{\mathbf{G}}(\rho, \phi = 0, z, z')R_z(\phi)^t, \tag{3.70}$$

with rotation matrix

$$R_z(\phi) = \begin{pmatrix} \cos\phi & -\sin\phi & 0 \\ \sin\phi & \cos\phi & 0 \\ 0 & 0 & 1 \end{pmatrix}. \tag{3.71}$$

We write the Green's function as a Fourier transform with respect to $\mathbf{r}_\parallel - \mathbf{r}'_\parallel$, assuming it exists,

$$\begin{aligned} \underline{\mathbf{G}}(\rho, 0, z, z') &= \int \frac{\mathrm{d}^2 q}{(2\pi)^2} e^{i\mathbf{q}\cdot(\mathbf{r}_\parallel - \mathbf{r}'_\parallel)} \underline{\mathbf{G}}(q, \phi_q, z, z') \\ &= \int_0^\infty \frac{\mathrm{d}q}{2\pi} q \int_0^{2\pi} \frac{\mathrm{d}\phi_q}{2\pi} e^{iq\rho\cos\phi_q} \underline{\mathbf{G}}(q, \phi_q, z, z'). \end{aligned} \tag{3.72}$$

Substituting (3.72) into (3.8) yields

$$\left\{R_z(\phi_q)D(q)R_z(\phi_q)^t - k^2 n^2(z)\right\} \underline{\mathbf{G}}(q, \phi_q, z, z') = s(z)\delta(z - z'), \tag{3.73}$$

with

$$D(q) = \begin{pmatrix} -s\partial_z s^{-1}\partial_z & 0 & s\partial_z s^{-1} iq \\ 0 & q^2 - s\partial_z s^{-1}\partial_z & 0 \\ iq\partial_z & 0 & q^2 \end{pmatrix} \tag{3.74}$$

being the Fourier transform of (3.11). Applying the rotation matrix to both sides of the equation, we obtain

$$\left\{D(q) - k^2 n^2(z)\right\} \underline{\mathbf{G}}(q, \phi_q = 0, z, z') = s(z)\delta(z - z'). \tag{3.75}$$

So the rotated Fourier-space equation is just the equation for the line source (3.43), and consequently $\underline{\mathbf{G}}(q, \phi_q = 0, z, z') \equiv \underline{\mathbf{G}}^{\mathrm{ls}}(q, z, z')$.

3.5.2. Derivation of the 3d real-space Green's function

We can thus insert the known expressions for the 2-dimensional Green's function into (3.72) and perform the integral. The Fourier-space Green's functions have 5 non-vanishing components (3.65). Computing the matrix-product and performing the angular integrals in (3.72) yields [Joh11]

$$G_{xx}(\rho,z,z') = \int_0^\infty \frac{\mathrm{d}q}{2\pi}\left\{\left[qJ_0(q\rho) - \frac{J_1(q\rho)}{\rho}\right] G^{\mathrm{ls}}_{xx}(q,z,z') + \frac{J_1(q\rho)}{\rho} G^{\mathrm{ls}}_{yy}(q,z,z')\right\} \tag{3.76}$$

$$G_{xz}(\rho,z,z') = i\int_0^\infty \frac{\mathrm{d}q}{2\pi} qJ_1(q\rho) G^{\mathrm{ls}}_{xz}(q,z,z') \tag{3.77}$$

$$G_{zz}(\rho,z,z') = \int_0^\infty \frac{\mathrm{d}q}{2\pi} qJ_0(q\rho) G^{\mathrm{ls}}_{zz}(q,z,z'). \tag{3.78}$$

The remaining components can be obtained by replacing x with y in the indices.

Computing the integrals involving the Bessel functions is difficult due to their rapid oscillations and the divergence of the Bessel functions for complex q complicates contour integration. This can be avoided by splitting the Bessel function into Hankel functions [Joh11]. Using

$$J_n(z) = \frac{1}{2}\left\{H_n^{(1)}(z) + H_n^{(2)}(z)\right\}, \tag{3.79}$$

the reflection formula, $H_n^{(2)}(ze^{-i\pi i}) = -e^{in\pi i}H_n^{(1)}(z)$, and the symmetry and anti-symmetry with respect to q of the diagonal and non-diagonal elements of the Green's tensor, respectively, we obtain

$$G_{xx}(\rho,z,z') = \frac{1}{2}\int_{-\infty}^\infty \frac{\mathrm{d}q}{2\pi}\left\{\left[qH_0^{(1)}(q\rho) - \frac{H_1^{(1)}(q\rho)}{\rho}\right] G^{\mathrm{ls}}_{xx}(q,z,z') + \frac{H_1^{(1)}(q\rho)}{\rho} G^{\mathrm{ls}}_{yy}(q,z,z')\right\} \tag{3.80}$$

$$G_{xz}(\rho,z,z') = \frac{i}{2}\int_{-\infty}^\infty \frac{\mathrm{d}q}{2\pi} qH_1^{(1)}(q\rho) G^{\mathrm{ls}}_{xz}(q,z,z') \tag{3.81}$$

$$G_{zz}(\rho,z,z') = \frac{1}{2}\int_{-\infty}^\infty \frac{\mathrm{d}q}{2\pi} qH_0^{(1)}(q\rho) G^{\mathrm{ls}}_{zz}(q,z,z'). \tag{3.82}$$

The path of integration adopted by Sommerfeld runs slightly above the negative, and slightly below the positive real axis.

Even though the expressions look relatively complicated, the trace takes a much simpler form,

$$\operatorname{tr}\underline{\mathbf{G}} = \sum_{j=x,y,z} \int_{-\infty}^{\infty} \frac{\mathrm{d}q}{2\pi} q H_0^{(1)}(q\rho) G_{jj}^{\mathrm{ls}}(q,z,z'). \tag{3.83}$$

Moreover, two of the three terms of the xx and yy-components decay with $1/\rho$ and can be neglected in many cases.

Similarly to the 2-dimensional case, we use contour integration to expand the integrals in terms of their residues. Here we give the derivation for the zz-component. Closing the contour in (3.82), the integral has two contributions: due to the poles and due to the branch cuts. We obtain

$$\begin{aligned} G_{zz}(\rho,z,z') = \frac{i}{2} \sum_m k\nu_m H_0^{(1)}(k\nu_m\rho) \operatorname{Res}\{G_{zz}^{\mathrm{ls}}; q = k\nu_m\} \\ + \frac{1}{2}\tilde{r}_{\mathrm{bot}}(\rho) + \frac{1}{2}\tilde{r}_{\mathrm{top}}(\rho) \end{aligned} \tag{3.84}$$

where $\tilde{r}_{\mathrm{bot}}$ are the contributions due to the branch cuts. Inserting the residues for the electric Green's function, we are left with

$$\begin{aligned} G_{\mathrm{e},zz}(\rho,z,z') = \frac{i}{4\epsilon(z)\epsilon(z')} \sum_m \nu_{\mathrm{m},m}^2 H_0^{(1)}(k\nu_{\mathrm{m},m}\rho) u_{\mathrm{m},m}(z') u_{\mathrm{m},m}(z) \\ + \frac{1}{2}\tilde{r}_{\mathrm{bot}}(\rho) + \frac{1}{2}\tilde{r}_{\mathrm{top}}(\rho). \end{aligned} \tag{3.85}$$

The other integrals can be expanded similarly.

3.6. Transfer matrix formalism for layered media

For piece-wise continuous media, the solutions of (3.16b) can be conveniently formulated in a transfer matrix formalism closely related to the Abelès formalism for reflectivity [Abe50]. Here we follow the convention of Chilwell and Hodgkinson [CH84].

3.6.1. A single layer

First, we bring the second-order equation $(L - k^2\nu^2)u = 0$ into first-order form, setting

$$V = \begin{pmatrix} u \\ k^{-1}s^{-1}u' \end{pmatrix} \tag{3.86}$$

so that

$$V' = QV = \begin{pmatrix} 0 & ks \\ -ks^{-1}(n^2 - \nu^2) & 0 \end{pmatrix} V. \tag{3.87}$$

Note that $V(z)$ is manifestly continuous. Diagonalizing Q gives

$$Q(z) = A(z) \begin{pmatrix} ikp(z) & 0 \\ 0 & -ikp(z) \end{pmatrix} A^{-1}(z), \quad A = \begin{pmatrix} 1 & 1 \\ \frac{ip}{s} & \frac{-ip}{s} \end{pmatrix}, \tag{3.88}$$

where $p^2 = (n^2 - \nu^2)$. The sign of p is arbitrary, as long as it is consistent in all 3 matrices. For constant n and s, we read off that

$$V(z+d) = A(z+d) \begin{pmatrix} e^{ikpd} & 0 \\ 0 & e^{-ikpd} \end{pmatrix} A^{-1}(z) V(z). \tag{3.89}$$

This immediately generalizes to piece-wise constant media as follows.

3.6.2. Multiple layers

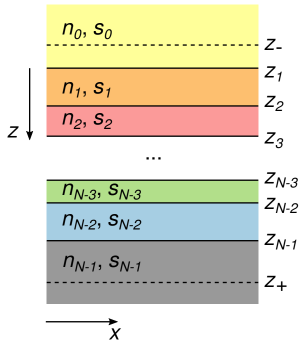

Figure 3.3.: We consider a layer system with piece-wise constant refractive indices n_l and relative permeabilities and permittivities s_l indicated by the colors. Outside the interval (z_-, z_+), the quantities are constant.

Let $N \geq 2$ be the number of layers and let $\underline{n} \in \mathbb{C}^N$ and $\underline{s} \in \mathbb{C}^N$ denote values of n_l and s_l in each layer. Moreover, let $\underline{z} = (z_0, z_1, z_2, \dots, z_N) \in \mathbb{R}^{N-1}$ denote the interface positions as shown in Fig. 3.3. Then

$$V(z_{l+1}) = M_l(z_{l+1} - z_l) V(z_l), \tag{3.90}$$

where, with $A_l = A(z_l)$,

$$M_l(d) = A_l \begin{pmatrix} e^{ip_l d} & 0 \\ 0 & e^{-ip_l d} \end{pmatrix} A_l^{-1} = \begin{pmatrix} \cos(p_l kd) & \frac{s_l}{p_l}\sin(p_l kd) \\ -\frac{p_l}{s_l}\sin(p_l kd) & \cos(p_l kd) \end{pmatrix}. \tag{3.91}$$

The transfer matrix from z_n to $z_m > z_n$ can be seen to be the matrix product

$$M(z_m, z_n) = M_{m-1}(z_m, z_{m-1}) \cdots M_n(z_{n+1}, z_n), \tag{3.92}$$

as well as $M(z_n, z_m) = M^{-1}(z_m, z_n)$. Note that when allowing arbitrary position arguments, $M(z, z')$, for fixed z', is a fundamental matrix of (3.87), since its two columns are linearly independent solutions.

The two decaying solutions (3.29) can be computed as

$$\begin{pmatrix} u_\pm(z) \\ k^{-1}s^{-1}(z)u'_\pm(z) \end{pmatrix} = M(z, z_\pm)V_\pm, \quad V_\pm = \begin{pmatrix} 1 \\ \pm ip_\pm s^{-1}(z_\pm)) \end{pmatrix}. \tag{3.93}$$

The Wronskian function can be computed via

$$\begin{aligned} W &= k\left(is^{-1}(z_+)p_+, \quad -1\right)M(z_+, z_-)V_- \\ &= k\left(is^{-1}(z_-)p_-, \quad 1\right)M(z_-, z_+)V_+. \end{aligned} \tag{3.94}$$

3.6.3. Numerical solutions

Having formulated matrix expressions for the solutions $u_\pm(z;\nu)$ and the Wronskian $W(\nu)$, it is straightforward to numerically compute the semi-spectral representation of the Green's functions $\underline{\mathbf{G}}(q, z, z')$. For the asymptotic expansions of the real-space Green's functions and to find the resonant modes, we need the complex roots of the Wronskian.

Since $W(\nu)$ is holomorphic up to 4 algebraic and possibly degenerate branch points, Cauchy's argument principle can be employed to count and localize the complex roots. This approach, commonly known as Cauchy's integration method or the argument principle method, has been used in numerical waveguide mode finders for many years (see [Che+00] and the references therein).

Since $W(\nu)$ continuously depends on the parameters of the layer system such as layer thickness, refractive indices, and wavenumber, the location of the roots of $W(\nu)$ does, too. As a consequence, the roots can be conveniently tracked. This has been formally proven for this particular problem [Sch11]. A root $\nu_m \in \mathbb{C}$ that is known for a certain configuration can be easily found by local root-searching methods such as Newton's method for a slightly changed configuration.

We have implemented the transfer matrices in C++ with bindings to the Python language to efficiently compute the semi-spectral Green's functions as well as the Wronskian function. We use the open source software package *cxroots* [Par18] to find all roots within a given complex contour. These are then used to compute the transversal mode profiles as well as the asymptotic expansions of the Green's functions. The code is available at Ref. [LA23].

3.7. Applications

3.7.1. Grazing incidence

We discuss the scattering of a plane wave illuminating a layer system in grazing incidence. The geometry is translationally symmetric and as such reduces to a one-dimensional problem. By convention, we chose the coordinate system so that z is pointing "down" and the "top" layer extends to $z \to -\infty$ (see Fig. 3.1a). We derive the fields generated by a horizontal sheet of source currents embedded into the top layer, which would produce a plane wave in a homogeneous environment. The fields can be expressed in terms of the semi-spectral representation of the two-dimensional Green's function evaluated on the real axis. Resonant modes manifest as damped resonances.

Consider an electrical current distribution generating a y-polarized plane wave incoming under the angle $\theta \in (0, \pi/2)$ with respect to the x-axis,

$$\mathbf{J}_{\mathrm{e}}(x,z) = \delta(z - z_{\mathrm{src}}) e^{in_- k \cos\theta x} J_{\mathrm{e},0}(\theta)\hat{\mathbf{y}}, \tag{3.95}$$

where n_- is the refractive index in the top layer. This current generates the electric field

$$\begin{aligned}\mathbf{E}(x,z) &= i\omega\mu_0 \int \underline{\mathbf{G}}_{\mathrm{e}}^{\mathrm{ls}}(x-x', z, z')\mathbf{J}_{\mathrm{e}}(x',z')\mathrm{d}x'\mathrm{d}z' \\ &= i\omega\mu_0 J_{\mathrm{e},0}(\theta) \int g(x-x', z, z_{\mathrm{src}}) e^{in_- k\cos\theta x'}\mathrm{d}x'\hat{\mathbf{y}}.\end{aligned} \tag{3.96}$$

The integral takes the form of a Fourier transform and can be rewritten as

$$\mathbf{E}(x,z) = \frac{i2kp_- E_0}{\mu_-} e^{in_- k\cos\theta x} g(q = n_- k\cos\theta, z, z_{\mathrm{src}})\hat{\mathbf{y}}, \tag{3.97}$$

where $E_0 = -\mu_0\mu_- J_{\mathrm{e},0} c/(2p_-)$, $p_- = n_-|\sin\theta|$, and μ_- is the permeability of the top layer.

In a homogeneous medium we obtain, using (3.55),

$$\mathbf{E}_{\text{inc}}(x, z) = E_0 e^{in_- k(x\cos\theta + (z - z_{\text{src}})\sin\theta)} \hat{\mathbf{y}}, \tag{3.98}$$

which is a plane wave propagating in $\hat{\mathbf{k}} = \cos\theta\hat{\mathbf{x}} + \sin\theta\hat{\mathbf{z}}$. An arbitrary layer system can be readily computed by using (3.54) to compute g in (3.97). Substituting (3.54) and using (3.32), we bring (3.97) into a more explicit form,

$$\mathbf{E}(x, z) = i2kp_- E_0 e^{in_- k\cos\theta x} \left. \frac{u_-(z_{\text{src}}; q) u_+(z; q)}{ikp_- u_+(z_-; q) + u'_+(z_-; q)} \right|_{q = n_- k\cos\theta} \hat{\mathbf{y}}, \tag{3.99}$$

where we have assumed that $z > z_{\text{src}}$. For points z in the top layer, we can further simplify the expression. Rewriting $u_+(z)$ using (3.89), we obtain

$$\mathbf{E}(x, z) = \mathbf{E}_{\text{inc}}(x, z)\left\{1 + re^{-2in_- k\sin\theta(z - z_-)}\right\}. \tag{3.100}$$

with

$$r = \left. \frac{ikp_- u_+(z_-; q) - u'_+(z_-; q)}{ikp_- u_+(z_-; q) + u'_+(z_-; q)} \right|_{q = n_- k\cos\theta}. \tag{3.101}$$

The second term in (3.100) represents the reflected part of the field. For completeness, let us remark that the amplitude reflection coefficient r can be readily computed using the transfer matrix formalism,

$$r = \frac{C_2}{C_1}, \quad \begin{pmatrix} C_1 \\ C_2 \end{pmatrix} = A^{-1}(z_-) M(z_-, z_+) V_+, \tag{3.102}$$

using the definitions from section 3.6. This is equivalent to the popular matrix method proposed by Abelès [Abe50].

Figure 3.4 shows the mode structure and electric field amplitude in an air/-Pt(2.6 nm)/C(16 nm)/Fe(0.6 nm)/C(16 nm)/Pt layer system at a photon energy of 14.4 keV. The photon energy $\mathcal{E}$ is converted to the vacuum wavenumber via $k = \mathcal{E}/(c\hbar)$. The layer structure corresponds to a cavity used in an experiment reported in [Röh+10]. Here, we are interested in non-resonant scattering applications, and ignore the resonant nuclear contribution of the Mössbauer isotope ^{57}Fe to the refractive index. The refractive indices were taken from [Sch+11]. Since the refractive index of carbon is lower than that of air, the system does not permit guided modes but only negative and double leaky modes, as can be seen in panel (a). In panel (b), the squared modulus of the 2d Green's function is plotted as a function of $\nu = q/k$ on the real axis, which corresponds to the incidence angle via $\nu = \cos\theta$. The Green's function $|g(k\nu)|^2$ is proportional to the local intensity $|E|^2$ based on (3.97). It shows pronounced resonances around the real values of the resonant mode indices, $\nu \sim \text{Re}\{\nu_m\}$. The vertical

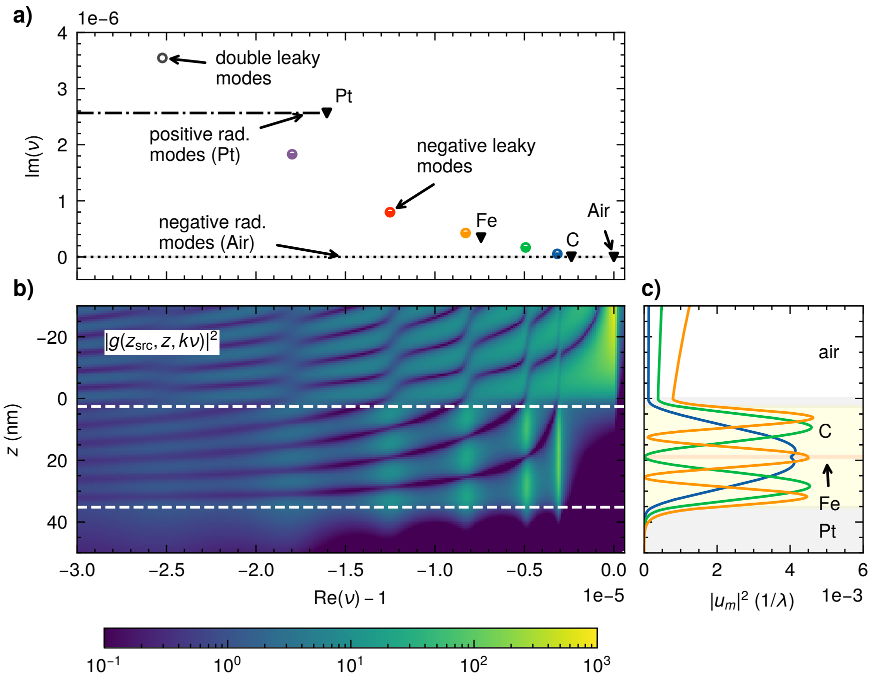

Figure 3.4.: Mode structure and field amplitude of the layer system shown in (c) at 14.4 keV photon energy. (a) Mode indices in the complex plane. (b) Squared modulus of the 2d Green's function, which corresponds to the electric field as a function of height and incidence angle $\nu = \cos\theta$. The dashed lines indicate the interfaces between platinum and carbon. (c) Layer system and transversal profiles of the negative leaky modes (squared modulus). The profiles in (c) correspond to the mode indices in (a) of matching colors.

profiles in b) for real $\nu \sim \mathrm{Re}\{\nu_m\}$, closely resemble the vertical profiles at the complex resonances ν_m, shown in panel (c), up to the divergence for $z < 0$. Hence, one can get a good understanding of field within the waveguide from just the resonant modes.

3.7.2. Waveguide propagation

Let us now discuss the propagation of x-rays in a waveguide layer system. To that end, we derive the fields generated by a vertical sheet of source currents that would generate a plane wave in a homogeneous medium. This situation closely corresponds to a plane wave that is coupled into the front face of a waveguide, as long as back-reflection can be neglected. Having a plane of origin perpendicular to the layer interfaces breaks the translational symmetry and makes this problem inherently two-dimensional. The fields in the waveguide can be computed using the two-dimensional Green's function, and we will see that the resonant modes emerge as an asymptotic approximation for longer propagation distances.

Consider a vertical sheet of electric currents at $x = x_{\mathrm{src}}$ with a linear phase shift,

$$\mathbf{J}_\mathrm{e}(x, z) = \delta(x - x_{\mathrm{src}}) e^{in_0 \sin\theta z} J_{\mathrm{e},0}(\theta)\hat{\mathbf{y}}. \tag{3.103}$$

This current generates the electric field

$$\begin{aligned}\mathbf{E}(x, z) &= i\omega\mu_0 \int \underline{\mathbf{G}}_\mathrm{e}^{\mathrm{ls}}(x - x', z, z')\mathbf{J}_\mathrm{e}(x', z')\mathrm{d}z'\mathrm{d}z' \\ &= i\omega\mu_0 J_{\mathrm{e},0}(\theta) \int \mathrm{g}(x - x_{\mathrm{src}}, z, z_{\mathrm{src}}) e^{in_0 \sin\theta z'} \mathrm{d}x'\hat{\mathbf{y}}.\end{aligned} \tag{3.104}$$

For brevity, we set $x_{\mathrm{src}} = 0$.

In a homogeneous medium with refractive index n_{hom}, we get

$$\mathbf{E}_{\mathrm{inc}}(x, z) = E_0 e^{in_{\mathrm{hom}}k\hat{\mathbf{k}}\cdot\mathbf{r}} \tag{3.105}$$

with $\hat{\mathbf{k}} = \cos\theta\hat{\mathbf{x}} + \sin\theta\hat{\mathbf{z}}$ and $E_0 = -\mu_0 J_{\mathrm{e},0}\omega/(2kn_{\mathrm{hom}}\cos\theta)$. For stratified media, we use (3.63) to obtain

$$\mathbf{E}(x, z) = E_0 \sum_m C_m e^{ik\nu_m x} u_m(z)\hat{\mathbf{y}} + \text{non-resonant}, \tag{3.106}$$

where

$$C_m = \int \mathrm{d}z' u_m(z') e^{in_0 z' \sin\theta} \frac{n_{\mathrm{hom}} \cos\theta}{\nu_m} \tag{3.107}$$

is a complex coefficient that quantifies how the incoming field couples into the modes. The sum goes over all guided modes and the non-resonant part is the integral over the radiative modes. Note that for this infinitely extended source sheet, leaky modes are of little use due to their divergence. The coupling coefficients (3.107) are determined by the integral over the mode profile u_m.

All relevant information is contained in the mode indices ν_m and the mode profiles $u_m(z)$. A single mode decays like

$$|\mathbf{E}(x,z)_m|^2 = |E_0|^2 |C_m|^2 |u_m(z)|^2 e^{-2k\,\mathrm{Im}\{\nu_m\}x}, \tag{3.108}$$

so that the $1/e$-length is given by $\lambda/(4\pi\,\mathrm{Im}\{\nu_m\})$. Two or more contributing modes interfere with period $\lambda/\,\mathrm{Re}\{\nu_m - \nu_{m'}\}$.

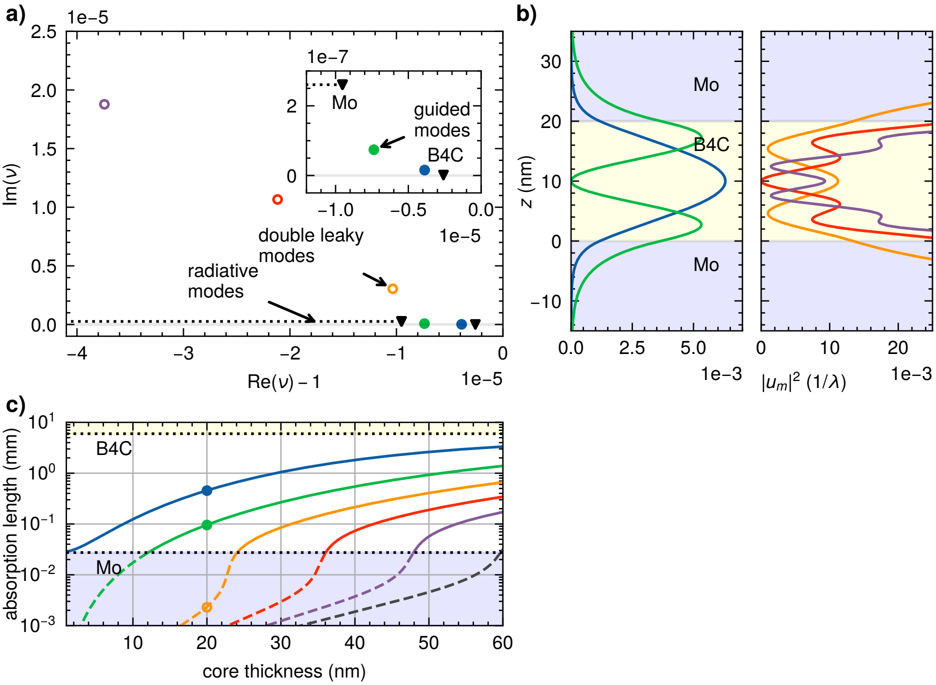

Figure 3.5.: Mode structure and mode transmission of a Mo/B_4C/Mo waveguide at 13.8 keV photon energy. (a) Mode and material indices, including guided modes (filled circles), double leaky modes (empty circles) and radiative modes (dotted line). (b) Transversal mode profiles (squared modulus) corresponding to the mode indices in a. (c) Mode attenuation lengths ($1/e$) for the waveguide as a function of the B_4C guiding layer thickness. The drawn through and dashed lines correspond to guided and double leaky modes, respectively.

Figure 3.5(a) shows the mode indices for a Mo/B_4C(20 nm)/Mo waveguide and a photon energy of 13.8 keV, (b) shows the corresponding transversal mode profiles of the 2 guided modes and the first 3 double leaky modes. Here, the leaky mode indices have significantly larger imaginary parts compared to the guided and radiative modes, where the guided mode indices have the smallest imaginary parts because of the weak absorption of B_4C compared to molybdenum.

Figure 3.5(c) shows the attenuation lengths of the resonant modes as a function of the B_4C core layer thickness. It demonstrates that the number of resonant modes stays invariant, while leaky modes turn into guided modes for increasing thickness.

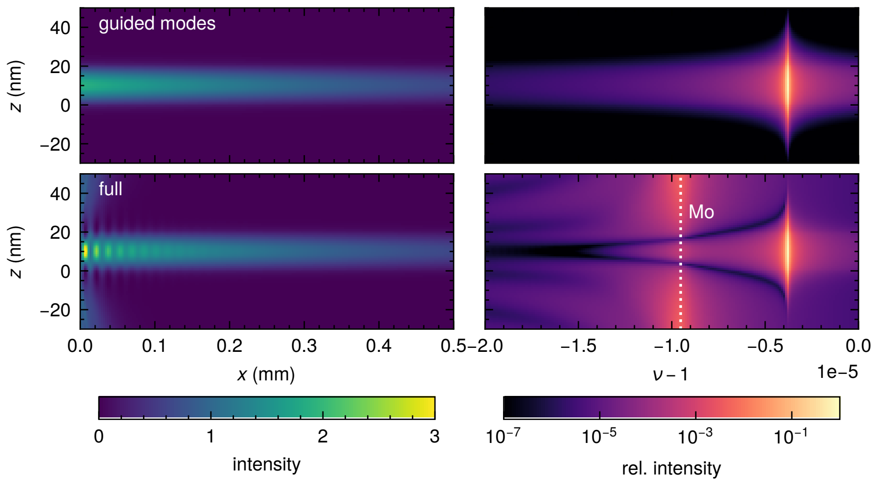

Figure 3.6.: Electric field in the waveguide for an incoming plane wave at 0° incidence angle computed from only the guided modes (top) and the full field (bottom), as a function of spatial coordinates (left) and Fourier-transformed with respect to x (right).

Figure 3.6 shows the electric field modulus inside the same waveguide, irradiated by a y-polarized plane wave under normal incidence. The top row shows only the guided mode contributions computed with (3.106) while the bottom row shows the full solution, obtained in a finite-difference simulation of the paraxial Helmholtz equation (see [Sol+21] for details). Due to the normal incidence and symmetry, only the first guided mode contributes. The full field shows some interference in the first few 100 μm, which is caused by the radiative modes interfering with the guided modes (compare [Buk+06]). This is more evident in the Fourier-transformed fields. The full numerical solution (bottom right) shows background contributions that peak around the refractive index of the cladding material, molybdenum, in addition to the resonance of the guided mode (top right). Evidently, the non-resonant contributions decay on significantly shorter length scales, so that the field after ∼

300 μm is accurately described by only the guided modes. This highlights the validity of the guided-mode approximation as an asymptotic expansion of the field for large propagation distances, which is possible because of the large material absorption.

So far we have considered strictly time-harmonic fields. X-ray free electron lasers produce pulses of a few femtoseconds, so the questions arises if waveguides introduce dispersion. The bandwidth of hard x-rays produced by synchrotron or x-ray free electron laser sources is generally in the order of 1 eV. The change of refractive indices in this energy bandwidth is generally negligible, as long as the photon energy is far from absorption edges and resonances. We can thus approximate the refractive index to be independent of frequency. The wavenumber $k = \omega/c$, however, enters $W(\nu)$ and in principle causes a frequency-dependence of the mode indices $\nu_m \equiv \nu_m(\omega)$ and $u_m(z) \equiv u_m(z, \omega)$. Consequently, there is in principle intra-mode dispersion due to the frequency-dependence of $\nu_m(\omega)$ as well as inter-mode dispersion due to the difference in ν_m. Since k only changes on the order of the relative bandwidth, which is typically 1×10^{-4}, the change in u_m and ν_m (compare (3.41)), and thus also intra-mode dispersion, are typically negligible. Neglecting the time-dependence of u_m and ν_m and splitting the real and imaginary part of ν_m, (3.106) becomes

$$\mathbf{E}(x, z, t) \approx \hat{\mathbf{y}} \sum_m E_0(t - \mathrm{Re}\{\nu_m\}x/c) C_m e^{-2k_0 \,\mathrm{Im}\{\nu_m\}x} u_m(z), \tag{3.109}$$

where $k_0 = \omega_0/c$ is the central wave number. Pulses of length Δt thus separate on length scales of $\Delta t c / \mathrm{Re}\{\nu_m - \nu_{m'}\}$. For $\Delta t = 1$ fs and $\mathrm{Re}\{\nu_m - \nu_{m'}\} \sim 10^{-5}$ this dispersion length is 3 cm. Conversely, for longer pulses or shorter waveguides, dispersion can be neglected (compare [Pel+06]).

3.7.3. Dipole emission into waveguide modes

Finally, we discuss the fields produced by a single dipole buried in a waveguide layer structure. This corresponds to, for example, fluorescence or characteristic x-ray emission into a waveguide, as it was experimentally observed recently [VS21]. The fields can be described using the three-dimensional Green's function, which asymptotically reduces to its guided modes.

For simplicity, consider a vertically oriented dipole, $\mathbf{p} = |p|\hat{\mathbf{z}}$, so that the problem is rotationally symmetric. Using (3.10), the electric field produced by the dipole can be written in cylindrical coordinates as

$$\mathbf{E}(\rho, \phi, z) = \omega^2 \mu_0 \underline{\mathbf{G}}_{\mathrm{e}}(\rho, \phi, z, z') \cdot \mathbf{p}. \tag{3.110}$$

The field is then TM-like in the sense that the electric field is oriented in the $\hat{\boldsymbol{\rho}}$-$\hat{\mathbf{z}}$ plane with $E_\rho = \omega^2 \mu \mu_0 G_{xz}(\rho, 0, z, z')|p|$ and $E_z = \omega^2 \mu \mu_0 G_{zz}(\rho, 0, z, z')|p|$. Using (3.85) and neglecting the non-resonant contributions, we have

$$E_\rho(\rho,z) = \frac{\mu_0\omega^2|p|}{4\epsilon(z)\epsilon(z')k}\sum_m \nu_{\mathrm{m},m}H_1^{(1)}(k\nu_{\mathrm{m},m}\rho)u_{\mathrm{m},m}(z')\partial_z u_{\mathrm{m},m}(z) \tag{3.111}$$

$$E_z(\rho,z) = i\frac{\mu_0\omega^2|p|}{4\epsilon(z)\epsilon(z')}\sum_m \nu_{\mathrm{m},m}^2 H_0^{(1)}(k\nu_{\mathrm{m},m}\rho)u_{\mathrm{m},m}(z')u_{\mathrm{m},m}(z). \tag{3.112}$$

Note that ρ only appears in the Hankel functions. They have the asymptotic expressions

$$H_n^{(1)}(\xi) \sim \sqrt{\frac{2}{\pi\xi}}e^{-i(1+2n)\pi/4}e^{i\xi} \tag{3.113}$$

for $|\xi| \to \infty$. Although both field components decay similarly, the global magnitude of the radial component is generally a lot smaller. For $k\rho \gg 1$, the absolute square of an individual mode becomes

$$|E_{z,m}(\rho,z)|^2 \approx \frac{\mu_0\omega^4|p|^2}{8\pi}\frac{|u_m(z)|^2}{|\epsilon(z)|^2}\frac{|u_m(z')|^2}{|\epsilon(z')|^2}\frac{\exp\{-2k\rho\,\mathrm{Im}\{\nu_m\}\}}{k\rho}, \tag{3.114}$$

where we have approximated $\nu_m \approx 1$.

We can read off several characteristics. The absolute square decays hyperbolically due to the planar geometry and exponentially due to material absorption, which is quantified by the complex effective index. The coupling into the mode scales with the mode function $|u_m(z')|^2$. If more than one mode is populated, the fields interfere on the length scale $\rho \sim \lambda/\,\mathrm{Re}\{\nu_m - \nu_{m'}\}$.

Let us now compute the total power flow into a given mode m. The radial component of the pointing vector is given by

$$\hat{\boldsymbol{\rho}}\cdot\mathbf{S}(\rho,z) = \frac{-i}{2\omega\mu_0\bar{\mu}}E_z(\partial_\rho\bar{E}_z - \partial_z\bar{E}_\rho). \tag{3.115}$$

Inserting (3.112) and neglecting the second term, we obtain

$$\frac{\omega^3|p|^2\mu_0\mu(z)}{32}|\nu_m|^4 k\bar{\nu}_m\left|H_0^{(1)}(k\nu_m\rho)\right|^2\frac{|u_m(z')|^2}{|\epsilon(z')|^2}\frac{|u_m(z)|^2}{|\epsilon(z)|^2}. \tag{3.116}$$

Integrating over the cylinder surface and inserting (3.113) gives

$$P_m(\rho) \approx \frac{\omega^3|p|^2\mu_0}{8}|\nu_m|^3\bar{\nu}_m\exp\{-2k\rho\,\mathrm{Im}\{\nu_m\}\}\frac{|u_m(z')|^2}{|\epsilon(z')|^2}\int_{-\infty}^{\infty}\frac{|u_m(z)|^2\mu(z)}{|\epsilon(z)|^2}\mathrm{d}z \tag{3.117}$$

The remaining integral evaluates to a number close to unity. We obtain the estimate for the total radiated power

$$P_m(\rho) \sim \frac{\omega|p|^2k^3}{4\pi\epsilon_0} \exp\{-2k\rho \operatorname{Im}\{\nu_m\}\} \frac{\lambda|u_m(z')|^2}{4}. \tag{3.118}$$

Compared to the total radiated power of a dipole in vacuum [NH12],

$$P_{\text{hom}} = \frac{\omega|p|^2k^3}{12\pi\epsilon_0}, \tag{3.119}$$

we notice the scaling with the coupling coefficient $|u_m(z')|^2\lambda$. Since u_m is bi-normalized, it takes values in the order of the reciprocal mode width l. We obtain the simple result that the radiated power scales effectively with the geometric factor $\sim \lambda/l$. For hard x-rays, l is typically at least 2 orders of magnitude larger than the wavelength, so that the coupling efficiency is in the order of 0.01.

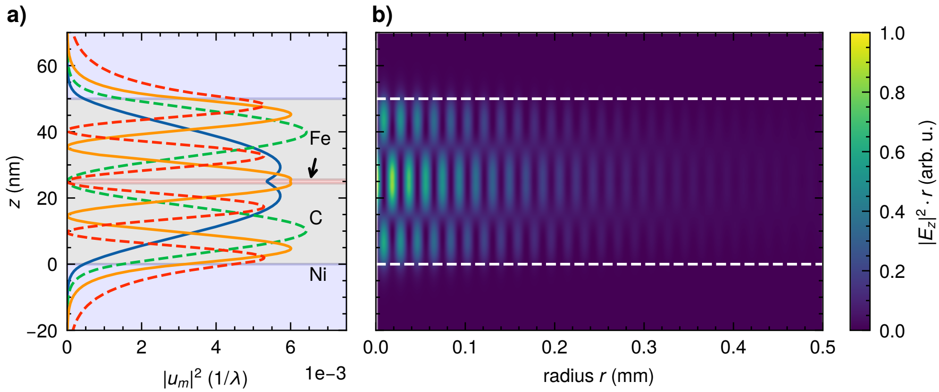

Figure 3.7.: Fields produced by an electric dipole buried in a waveguide at the iron Kα fluorescence energy 6.4 keV. (a) Layer structure and transversal profiles (squared modulus) of the guided modes. A dipole in the central layer couples to the 1st and 3rd (solid lines) but not to the 2nd and 4th (dashed lines) guided modes. (b) Electric field amplitude produced by an iron atom in the central layer, considering only the two contributing guided modes.

As a numerical example, consider a Ni/C(24.5 nm)/Fe(1 nm)/C(24.5 nm)/Ni layer system, in which one of the iron atoms in the central layer undergoes a radiative decay, emitting a 6.4 keV Kα fluorescence photon. This structure corresponds to a sample used in experiments by Vassholz and Salditt [VS21]. We model the steady-state case by a classical electric dipole. Figure 3.7(a) shows the transversal guided mode profiles in the layer structure. The system admits 4 guided modes but only two of them couple to the dipole. Panel (b) shows the transversal field computed with (3.112) up to a global scaling and compensated by the geometrical $1/\rho$-decay. It shows pronounced interference between the two contributing modes as well as an overall attenuation due to photoelectric absorption. This interference has been experimentally observed by Vassholz and Salditt (see Fig. 4 in [VS21]). In their original interpretation, however, the oscillations would be caused by a change of the emission process itself due to the position of the emitter within the waveguide. Our theory clearly indicates that the oscillations can be caused by the interference of the two populated guided modes alone, without assuming a modification of the emission process such as the Purcell effect.

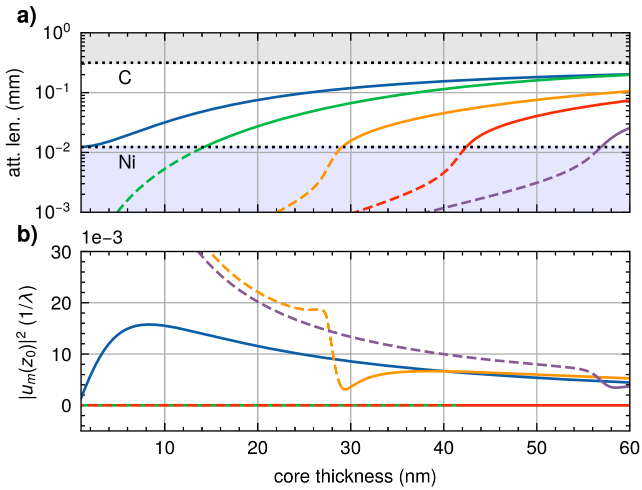

Figure 3.8.: Attenuation length (a) and mode coupling coefficient (b) as a function of waveguide thickness for an electric dipole buried in a waveguide at the iron Kα fluorescence energy 6.4 keV. The layer structure is Ni/C(x)/Fe(1 nm)/C(x)/Ni and the core thickness $2x + 1$ nm is varied.

Next, we analyze how the waveguide thickness affects some emission characteristics. Figure 3.8 shows the $1/e$ attenuation length and coupling coefficient of the guided modes as a function of overall waveguide thickness. Increasing the thickness converts more leaky modes into guided modes and increases the attenuation length of each individual mode. Less desirably, increasing the thickness also decreases the coupling strength of each individual mode slightly on a linear scale. The first guided mode has a pronounced optimum between 5 nm to 10 nm, below which the coupling coefficient rapidly drops to 0. Since the coupling coefficients are approximately inversely proportional to the square root of the mode spread, the optimum coupling corresponds to the minimum mode spread. Smaller waveguides cannot effectively contain the modes due to the weak index contrast.

3.8. Conclusions

In summary, we have presented a self-contained nano-optical theory of planar x-ray waveguides combined with numerical code, that allows for the modelling of fields in arbitrary layer structures while fully including material absorption. As one of the main results, we have use a novel generalised bi-orthogonality relation to obtain asymptotic expansions into resonant modes that are particularly useful for x-ray wavelengths due to the presence of significant material absorption. Our theory allows to model, in a unified framework, both the ”classical” geometries of x-ray waveguides, front-coupling and evanescent coupling geometries with their main figures of merit, as well as atom-light interactions with buried dipoles. In addition, we have discussed how interference patterns emerge in the fields caused by buried emitters, offering new interpretations of recently published experiments.

In more technical terms, we have shown how the solutions of the frequency-space vector wave equations (3.5) of lossy stratified media, which are describing the electromagnetic fields in x-ray waveguides, can be decomposed into resonant and non-resonant modes, solutions of the transversal eigenvalue problem, and we have derived asymptotic expansions of the corresponding dyadic Green’s functions in terms of the resonant modes. The modes of the free solution naturally reappear in the semi-spectral representation of the Green’s function, where the resonant modes manifest as pole singularities.

The presence of material losses makes the underlying equations inherently non-hermitian and causes the resonant modes to violate the usual orthogonality property, which is replaced by a bi-orthogonality property (3.28). Due to the dielectric boundary layers, the mode cut-off is soft, and in general an infinite number of modes are supported. However, material losses in many cases rapidly attenuate all but the lowest order resonant modes so that the asymptotic mode expansions give accurate results on relevant length scales.

The resonant mode expansion is similar to but distinct from so-called quasi normal mode expansions (see for example [KH13; LLY94]). While quasi-normal modes usually refer to complex-frequency resonances of the time-dependent solution, the resonant modes discussed in this paper correspond resonances of the monochromatic frequency-space solution with respect to the complex longitudinal wavenumber q. In particular, we note that the 3-dimensional vector wave equations for stratified media, as they were discussed here, do not have resonant frequencies, because the system is translationally invariant.

We have applied the theory to important experimental geometries, including irradiation by a plane wave in grazing incidence, propagation of a plane wave inside a waveguide, and emission into waveguide modes from a dipole embedded inside the waveguide. The unified theory highlights the similarities in the underlying mode structure of the 3 geometries but also elucidates important differences due to the different dimensionalities, symmetries, and boundary conditions.

The results presented in this paper have further applications. First, the theory together with our numerical solvers allows us to efficiently optimize layer designs for specific experimental needs. Important figures of merit such as attenuation length and coupling efficiencies are immediately obtainable from the the mode indices and profiles. This facilitates the computer-aided design of x-ray waveguides for imaging, where previously one mainly relied on finite-difference propagation simulations, which are relatively complex and provide little structural insight. Another example is the design and optimization of structured multilayer x-ray sources as proposed in ref. [VS21].

Second, the dyadic Green's functions and their asymptotic mode expansions can be used for quantum theories of, for example, coupled quantum systems in x-ray waveguides, since the classical Green's function enters the quantization of the electromagnetic field in the framework of macroscopic quantum electrodynamics [Len+20; AP21; KCP20; Buh13]. Our analytic theory, in particular the resonant mode expansion, will help to clarify the structure of the electromagnetic fields in x-ray waveguides. In addition, our numerical tools will complement current efforts [DLE22] to design waveguide structures for quantum-optical experiments.

3.A. Integration by parts for the modified inner product

We will demonstrate that for the class of function that are of the form

$$u(z) = u_0 e^{ik_\pm z} \tag{3.120}$$

in the top (+) and bottom (-) layer, that our modified inner product obeys the following integration by parts law,

$$\langle u', v\rangle_\partial + \langle u, v'\rangle_\partial = 0. \tag{3.121}$$

Using the definition (3.24), we have

$$\langle u', v\rangle_\partial + \langle u, v'\rangle_\partial = \int_{z_-}^{z_+} \bar{u}'(z)v(z) + \bar{u}(z)v'(z)\,\mathrm{d}z - \left[\frac{\bar{u}'v + \bar{u}v'}{\bar{u}'/u + v'/v}\right]_{z_-}^{z_+}, \tag{3.122}$$

where we have used the property that evaluated at $z_\pm$ we have

$$u''/u' = u'/u, \quad v''/v' = v'/v. \tag{3.123}$$

We may use ordinary integration by parts to evaluate the integral, giving

$$\langle u', v\rangle_\partial + \langle u, v'\rangle_\partial = \left[\bar{u}v - \frac{\bar{u}'v + \bar{u}v'}{\bar{u}'/\bar{u} + v'/v}\right]_{z_-}^{z_+} = 0, \tag{3.124}$$

since the right hand term can be simplified to

$$\frac{\bar{u}'v + \bar{u}v'}{\bar{u}'/\bar{u} + v'/v} = \bar{u}v\frac{\bar{u}'/\bar{u} + v'/v}{\bar{u}'/\bar{u} + v'/v} = \bar{u}v. \tag{3.125}$$

3.B. Derivation of mode dispersion

We derive identity (3.41) for the resonant modes.

Beginning with the eigenvalue equation

$$Lu = \lambda u, \tag{3.126}$$

we take a frequency derivative to obtain

$$\frac{\partial L}{\partial \omega}u + L\frac{\partial u}{\partial \omega} = \frac{\partial \lambda}{\partial \omega}u + \lambda\frac{\partial u}{\partial \omega}. \tag{3.127}$$

As u can be written as an exponential function in the top and bottom layers, so can $\frac{\partial L}{\partial \omega}u$ and $\frac{\partial u}{\partial \omega}$, and our modified inner product remains valid to use. Thus, we project onto the adjoint eigenfunction $\overline{s^{-1}u}$ with the modified inner product, to obtain

$$\left\langle \overline{s^{-1}u}, \frac{\partial L}{\partial \omega}u \right\rangle_\partial + \left\langle \overline{s^{-1}u}, L\frac{\partial u}{\partial \omega} \right\rangle_\partial = \frac{\partial \lambda}{\partial \omega} + \lambda \left\langle \overline{s^{-1}u}, \frac{\partial u}{\partial \omega} \right\rangle_\partial. \tag{3.128}$$

We can then note that as we have the differentiation by parts identity (3.25), $\overline{s^{-1}u}$ acts an adjoint eigenfunction with respect to our modified inner product, and thus we have

$$\left\langle \overline{s^{-1}u}, L\frac{\partial u}{\partial \omega} \right\rangle_\partial = \lambda \left\langle \overline{s^{-1}u}, \frac{\partial u}{\partial \omega} \right\rangle_\partial. \tag{3.129}$$

We obtain the result

$$\frac{\partial \lambda}{\partial \omega} = \left\langle \frac{\partial L}{\partial \omega} \right\rangle_u, \tag{3.130}$$

where for an operator A we denote the 'expectation value' with respect to u as

$$\langle A \rangle_u \equiv \left\langle \overline{s^{-1}u}, Au \right\rangle_\partial . \tag{3.131}$$

Evaluating the frequency derivative of L, we have

$$\frac{\partial L}{\partial \omega} = \frac{\partial s}{\partial \omega}\partial_z s^{-1}\partial_z - s\partial_z s^{-2}\frac{\partial s}{\partial \omega}\partial_z + \frac{2\omega^2}{c^2}\left(\frac{n^2}{\omega} + \frac{n}{\omega}\frac{\partial n}{\partial \omega}\right). \tag{3.132}$$

The rightmost terms of (3.132) are straightforward to compute with respect to the expectation value, but care must be taken when evaluating the first two terms. Taking an expecation value with respect to u gives for the first term

$$\left\langle \frac{\partial s}{\partial \omega}\partial_z s^{-1}\partial_z \right\rangle_u = \left\langle s^{-1}\frac{\partial s}{\partial \omega}(L - \frac{\omega^2}{c^2}n^2) \right\rangle_u = \left\langle s^{-1}\frac{\partial s}{\partial \omega}(\lambda - \frac{\omega^2}{c^2}n^2) \right\rangle_u . \tag{3.133}$$

For the second term we have

$$\left\langle s\partial_z s^{-2}\frac{\partial s}{\partial \omega}\partial_z \right\rangle_u = \left\langle \overline{s^{-1}u}, s\partial_z s^{-2}\frac{\partial s}{\partial \omega}\partial_z u \right\rangle_\partial = \left\langle \overline{u}, \partial_z s^{-2}\frac{\partial s}{\partial \omega}\partial_z u \right\rangle_\partial , \tag{3.134}$$

where we have used the antilinearity of the inner product. We can then use integration by parts to obtain

$$\left\langle s\partial_z s^{-2}\frac{\partial s}{\partial \omega}\partial_z \right\rangle_u = -\left\langle \overline{s^{-1}\partial_z u}, s^{-1}\frac{\partial s}{\partial \omega}\partial_z u \right\rangle_\partial = -\left\langle s^{-1}\frac{\partial s}{\partial \omega} \right\rangle_{\partial_z u} . \tag{3.135}$$

Putting it all together, we have

$$\frac{\partial \lambda}{\partial \omega} = \left\langle s^{-1}\frac{\partial s}{\partial \omega}(\lambda - \frac{\omega^2}{c^2}n^2) \right\rangle_u + \left\langle s^{-1}\frac{\partial s}{\partial \omega} \right\rangle_{\partial_z u} + \frac{2\omega^2}{c^2}\left(\left\langle \frac{n^2}{\omega} \right\rangle_u + \left\langle n\frac{\partial n}{\partial \omega} \right\rangle_u\right). \tag{3.136}$$

Finally, we have

$$\lambda = \frac{\omega^2}{c^2}\nu^2, \tag{3.137}$$

$$\frac{\partial \lambda}{\partial \omega} = \frac{2\omega^2}{c^2}\left(\frac{\nu^2}{\omega} + \nu\frac{\partial \nu}{\partial \omega}\right), \tag{3.138}$$

giving us for the mode dispersion

$$\nu\frac{\partial \nu}{\partial \omega} = \frac{1}{2}\left\langle \frac{\partial \ln(s)}{\partial \omega}(\nu^2 - n^2) \right\rangle_u + \frac{c^2}{2\omega^2}\left\langle \frac{\partial \ln(s)}{\partial \omega} \right\rangle_{\partial_z u} + \left\langle \frac{n^2 - \nu^2}{\omega} \right\rangle_u + \left\langle n\frac{\partial n}{\partial \omega} \right\rangle_u . \tag{3.139}$$

3.C. Derivation of the Wronskian derivative

We derive the identity (3.60). The derivation is inspired by a similar derivation for quasi-normal modes of the vector wave equations [LLY94]. We have, using (3.15), that

$$k^2(\nu^2 - \nu_j^2) \int_{z_-}^{z_+} s^{-1} u_-(\nu_j) u_+(\nu) \mathrm{d}z = \left[s^{-1} \left(u_-(\nu_j) u_+'(\nu) - u_-'(\nu_j) u_+(\nu) \right) \right]_{z=z_-}^{z_+} . \quad (3.140)$$

Using that $u_-'(\nu, z_-) = -ikp_-(\nu) u_-(\nu, z_-)$ and $u_+'(\nu, z_+) = ikp_+(\nu) u_+(\nu, z_+)$, as well as $u_-(\nu_j, z) \propto u_+(\nu_j, z)$, the right-hand side of (3.140) becomes

$$\begin{aligned} &ik \left[s^{-1} \left(p_+(\nu) - p_+(\nu_j) \right) u_-(\nu_j) u_+(\nu) \right]_{z=z_+} \\ &\qquad - \left[s^{-1} \left(u_-(\nu_j) u_+'(\nu) - u_-'(\nu_j) u_+(\nu) \right) \right]_{z=z_-} \end{aligned} \quad (3.141)$$

Taking the derivative with respect to ν at $\nu = \nu_j$, the left-hand side of (3.140) becomes

$$2\nu_j k^2 \int_{z_-}^{z_+} s^{-1} u_-(\nu_j) u_+(\nu_j) \mathrm{d}z \quad (3.142)$$

and (3.141) evaluates to

$$ik \left[s^{-1} \frac{\partial p_+}{\partial \nu} u_- u_+ \right]_{z_+} - \partial_\nu W(\nu_j) - \left[s^{-1} \left(\frac{\partial u_-'}{\partial \nu} u_+ - \frac{\partial u_-}{\partial \nu} u_+' \right) \right]_{z_-} , \quad (3.143)$$

where we have substituted the expression for the Wronskian function (3.31). To simplify the last term in (3.143), we use that $u_-(z_-) \equiv 1$ and $u_-'(z_-) = -ikp_- u_-(z_-')$, which implies

$$\left[s^{-1} \left(\frac{\partial u_-'}{\partial \nu} u_+ - \frac{\partial u_-}{\partial \nu} u_+' \right) \right]_{z_-} = -ik \left[s^{-1} \frac{\partial p_-}{\partial \nu} u_- u_+ \right]_{z_-} \quad (3.144)$$

Solving for the Wronskian function yields

$$\begin{aligned} \partial_\nu W(\nu_j) = -2\nu_j k^2 &\int_{z_-}^{z_+} s^{-1} u_- u_+ \mathrm{d}z \\ &+ ik \left[s^{-1} \frac{\partial p_+}{\partial \nu} u_- u_+ \right]_{z_+} + ik \left[s^{-1} \frac{\partial p_-}{\partial \nu} u_- u_+ \right]_{z_-} . \end{aligned} \quad (3.145)$$

Finally, for both the decaying choice of branch cut, $p = p_{\mathrm{dec}}$, and the vertical choice of branch cut, $p = p_{\mathrm{vert}}$, we get $\partial_\nu p_\pm = -\nu/p_\pm$, so that

$$\begin{aligned}\partial_q W(\nu_j) &= -2\nu_j k \int_{z_-}^{z_+} s^{-1} u_- u_+ \mathrm{d}z - i\nu_j \left[\frac{u_- u_+}{s p_+}\right]_{z_+} - i\nu_j \left[\frac{u_- u_+}{s p_-}\right]_{z_-} \\ &= -2\nu_j k \left\langle \overline{s^{-1} u_-}, u_+ \right\rangle_\partial .\end{aligned} \tag{3.146}$$

3.D. Computing the scattered field

A common problem is to evaluate the total field in the wave-guide given the specification of an incident beam in free space. This can be done using virtual sources.

The fields can be expressed in terms of the electric and magnetic currents. Substituting $\vec{F}$ in (3.7) and integrating by parts yields for the electric field,

$$\vec{E}(\vec{r}) = \frac{i\omega\epsilon_0}{c^2} \int \mathrm{d}^3\vec{r}' \underline{\mathbf{G}}_{\mathrm{e}}(\vec{r},\vec{r}') \cdot \vec{J}_{\mathrm{e}}(\vec{r}') - \int \mathrm{d}^3\vec{r}' \underline{\mathbf{G}}_{\mathrm{e}}(\vec{r},\vec{r}') \times \overleftarrow{\nabla} \cdot \mu^{-1}(\vec{r}')\vec{J}_{\mathrm{m}}(\vec{r}'), \tag{3.147}$$

where we have assumed the boundary terms to vanish. Taking the curl of (3.9b) and inserting (3.8), it follows that

$$\underline{\mathbf{G}}_{\mathrm{e}}(\vec{r},\vec{r}') \times \overleftarrow{\nabla}' \mu(\vec{r}')^{-1} = \epsilon(\vec{r})^{-1} \nabla \times \underline{\mathbf{G}}_{\mathrm{m}}(\vec{r},\vec{r}'). \tag{3.148}$$

Equation (3.147) then becomes

$$\vec{E}(\vec{r}) = \frac{i\omega\epsilon_0}{c^2} \int \mathrm{d}^3\vec{r}' \underline{\mathbf{G}}_{\mathrm{e}}(\vec{r},\vec{r}') \cdot \vec{J}_{\mathrm{e}}(\vec{r}') - \frac{1}{\epsilon(\vec{r})} \nabla \times \int \mathrm{d}^3\vec{r}' \underline{\mathbf{G}}_{\mathrm{m}}(\vec{r},\vec{r}') \cdot \vec{J}_{\mathrm{m}}(\vec{r}'). \tag{3.149}$$

A similar relation can be derived for the magnetic field.

Let us suppose that the free-space incident beam $\vec{E}_0$ is specified within some connected volume V with boundary ∂V. We may then use Stratton-Chu equations to relate the electric field at a point $\vec{r}$ in the interior of V to the electric and magnetic fields on the boundary via (see [Che99], ch. 1.4)

$$\vec{E}_0(\vec{r}) = \int_{\partial V} \mathrm{d}^2 s \Big(\frac{i\omega\epsilon_0}{c^2} \underline{\mathbf{G}}^{(0)}(\vec{r},\vec{s}) \cdot \vec{H}_0(\vec{s}) \times \hat{n}(\vec{s}) - \underline{\mathbf{G}}^{(0)}(\vec{r},\vec{s}) \cdot \vec{E}_0(\vec{s}) \times \hat{n}(\vec{s}) \Big), \tag{3.150}$$

where $\underline{\mathbf{G}}^{(0)}$ denotes a free-space Green's function. Comparing with (3.149), we can see that this is equivalent to the field emitted by virtual electric and magnetic currents given by

$$\vec{J}_{\mathrm{e},0}(\vec{r}) = \vec{H}_0(\vec{r}) \times \hat{S}(\vec{r}) \tag{3.151}$$

$$\vec{J}_{\mathrm{m},0}(\vec{r}) = \vec{E}_0(\vec{r}) \times \hat{S}(\vec{r}), \tag{3.152}$$

where $\vec{S}$ is the surface normal distribution for ∂V, equal to the product of the indicator distribution and the field of normal vectors of ∂V.

This can be used to obtain the scattered field as follows: suppose V completely encloses all scatterers, and that the Green's function taking into account the scatterers is known. Then the scattered field can be determined in terms of the incident field by treating the free-space field values along ∂V as virtual sources via (3.151) and (3.152), and propagating their field using the full Green's function, including the effects of scattering. Using (3.149), it is then straightforward to show that the total field $\vec{E}$, including the scattered field, is given in terms of the incident field $\vec{E}_0$, $\vec{B}_0$ by

$$\begin{aligned}\vec{E}(\vec{r},\omega) = \frac{i\omega\epsilon_0}{c^2}\int_{\partial V} \mathrm{d}^2 s \underline{\mathbf{G}}^E(\vec{r},\vec{s},\omega)\cdot\vec{H}_0(\vec{s},\omega)\times\hat{n}(\vec{s})\\ -\frac{1}{\epsilon(\vec{r})}\nabla\times\int_{\partial V}\mathrm{d}^2 s\underline{\mathbf{G}}^H(\vec{r},\vec{s},\omega)\cdot\vec{E}_0(\vec{s},\omega)\times\hat{n}(\vec{s}),\end{aligned} \tag{3.153}$$

where $\underline{\mathbf{G}}$ refers to the full Green's function.

Funding
Max Planck School of Photonics; Deutsche Forschungsgemeinschaft (432680300 SFB 1456/C03, 429529648 TRR 306/C04)

Acknowledgements
The authors have had fruitful discussions with Tim Salditt, Ralf Röhlsberger, Markus Osterhoff, and Adriana Pálffy during the preparation of this manuscript and are very grateful for their support.

Disclosures
The authors declare no conflict of interest.

Data Availability
Data underlying the results presented in this paper are available in Ref. [LA23].

References

[Abe50] Florin Abelès. “Recherches sur la propagation des ondes électromagnétiques sinusoïdales dans les milieux stratifiés.” *Annales de Physique* 12.5 (1950), pp. 596–640. DOI: 10.1051/anphys/195012050596.

[ALP24] Petar Andrejić, Leon Merten Lohse, and Adriana Pálffy. “Waveguide QED with Mössbauer nuclei.” *Physical Review A* 109.6 (June 2024), p. 063702. DOI: 10.1103/physreva.109.063702.

[AP21] Petar Andrejić and Adriana Pálffy. “Superradiance and anomalous hyperfine splitting in inhomogeneous ensembles.” *Physical Review A* 104.3 (Sept. 2021), p. 033702. DOI: 10.1103/physreva.104.033702.

[Ase+17] A. Asenjo-Garcia, J. D. Hood, D. E. Chang, and H. J. Kimble. “Atom-light interactions in quasi-one-dimensional nanostructures: A Green’s-function perspective.” *Physical Review A* 95.3 (Mar. 2017), p. 033818. DOI: 10.1103/physreva.95.033818.

[BAG97] A. Bakhtazad, H. Abiri, and R. Ghayour. “A general transform for regularizing planar open waveguide dispersion relation.” *Journal of Lightwave Technology* 15.2 (1997), pp. 383–390. DOI: 10.1109/50.554392.

[Bôc01] Maxime Bôcher. “Certain cases in which the vanishing of the Wronskian is a sufficient condition for linear dependence.” *Transactions of the American Mathematical Society* 2.2 (1901), pp. 139–149. DOI: 10.1090/s0002-9947-1901-1500560-5.

[Bon+02] J. H. H. Bongaerts, C. David, M. Drakopoulos, M. J. Zwanenburg, G. H. Wegdam, T. Lackner, H. Keymeulen, and J. F. van der Veen. “Propagation of a partially coherent focused X-ray beam within a planar X-ray waveguide.” *Journal of Synchrotron Radiation* 9.6 (Nov. 2002), pp. 383–393. DOI: 10.1107/s0909049502016308.

[Buh13] Stefan Yoshi Buhmann. *Dispersion Forces I*. Springer Tracts in Modern Physics 247. Berlin, Heidelberg: Springer Berlin Heidelberg, 2013. ISBN: 9783642324840.

[Buk+06] I. Bukreeva, A. Popov, D. Pelliccia, A. Cedola, S. B. Dabagov, and S. Lagomarsino. “Wave-Field Formation in a Hollow X-Ray Waveguide.” *Physical Review Letters* 97.18 (Oct. 2006), p. 184801. DOI: 10.1103/physrevlett.97.184801.

[Buk+13a] Inna Bukreeva, Alessia Cedola, Daniele Pellicia, Werner Jark, and Stefano Lagomarsino. “X-ray Waveguides.” In: *The X-Ray Standing Wave Technique*. Ed. by Jörg Zegenhagen and Alexander Kazimirov. Vol. 7. Series on Synchrotron Radiation Techniques and Applications. World Scientific, Mar. 2013, pp. 143–162. DOI: 10.1142/9789812779014_0009.

[Buk+13b] Inna Bukreeva, Andrea Sorrentino, Alessia Cedola, Ennio Giovine, Ana Diaz, Fernando Scarinci, Werner Jark, Leonid Ognev, and Stefano Lagomarsino. “Periodically structured X-ray waveguides.” *Journal of Synchrotron Radiation* 20.5 (July 2013), pp. 691–697. DOI: 10.1107/s0909049513018657.

[Bur70] J. J. Burke. “Propagation Constants of Resonant Waves on Homogeneous, Isotropic Slab Waveguides.” *Applied Optics* 9.11 (Nov. 1970), p. 2444. DOI: 10.1364/ao.9.002444.

[Car+08] L. De Caro, C. Giannini, D. Pelliccia, C. Mocuta, T. H. Metzger, A. Guagliardi, A. Cedola, I. Burkeeva, and S. Lagomarsino. “In-line holography and coherent diffractive imaging with x-ray waveguides.” *Physical Review B* 77.8 (Feb. 2008), p. 081408. DOI: 10.1103/physrevb.77.081408.

[CH84] John Chilwell and Ian Hodgkinson. “Thin-films field-transfer matrix theory of planar multilayer waveguides and reflection from prism-loaded waveguides.” *Journal of the Optical Society of America A* 1.7 (July 1984), p. 742. DOI: 10.1364/josaa.1.000742.

[Che+00] Chengkun Chen, Pierre Berini, Dazeng Feng, Stoyan Tanev, and Velko Tzolov. "Efficient and accurate numerical analysis of multilayer planar optical waveguides in lossy anisotropic media." *Optics Express* 7.8 (Oct. 2000), p. 260. DOI: `10.1364/oe.7.000260`.

[Che+22] Yu-Hsueh Chen, Po-Han Lin, Guan-Ying Wang, Adriana Pálffy, and Wen-Te Liao. "Transient nuclear inversion by x-ray free electron laser in a tapered x-ray waveguide." *Physical Review Research* 4.3 (July 2022), p. l032007. DOI: `10.1103/physrevresearch.4.l032007`.

[Che99] Weng Cho Chew. *Waves and Fields in Inhomogenous Media*. IEEE Press Series on Electromagnetic Wave Theory. Wiley-IEEE Press, 1999. ISBN: 9780780347496.

[DLE22] Oliver Diekmann, Dominik Lentrodt, and Jörg Evers. "Inverse design approach to x-ray quantum optics with Mössbauer nuclei in thin-film cavities." *Physical Review A* 105.1 (Jan. 2022), p. 013715. DOI: `10.1103/physreva.105.013715`.

[Fen+93] Y. P. Feng, S. K. Sinha, H. W. Deckman, J. B. Hastings, and D. P. Siddons. "X-ray flux enhancement in thin-film waveguides using resonant beam couplers." *Physical Review Letters* 71.4 (July 1993), pp. 537–540. DOI: `10.1103/physrevlett.71.537`.

[FS05] Christian Fuhse and Tim Salditt. "Finite-difference field calculations for one-dimensionally confined X-ray waveguides." *Physica B: Condensed Matter* 357.1-2 (Feb. 2005), pp. 57–60. DOI: `10.1016/j.physb.2004.11.019`.

[FS06] Christian Fuhse and Tim Salditt. "Finite-difference field calculations for two-dimensionally confined x-ray waveguides." *Applied Optics* 45.19 (July 2006), p. 4603. DOI: `10.1364/ao.45.004603`.

[GG01] Israel Gohberg and Seymour Goldberg. "Spectral Theory of Integral Operators." In: *Basic Operator Theory*. Birkhäuser Boston, 2001, pp. 131–151. ISBN: 9781461259855. DOI: `10.1007/978-1-4612-5985-5_4`.

[Gie+10] K. Giewekemeyer, H. Neubauer, S. Kalbfleisch, S. P. Krüger, and T. Salditt. "Holographic and diffractive x-ray imaging using waveguides as quasi-point sources." *New Journal of Physics* 12.3 (Mar. 2010), p. 035008. DOI: `10.1088/1367-2630/12/3/035008`.

[Hab+19] Johann Haber, Jakob Gollwitzer, Sonia Francoual, Martin Tolkiehn, Jörg Strempfer, and Ralf Röhlsberger. "Spectral Control of an X-Ray L-Edge Transition via a Thin-Film Cavity." *Physical Review Letters* 122.12 (Mar. 2019), p. 123608. DOI: `10.1103/physrevlett.122.123608`.

[HM09] Jonathan Hu and Curtis R. Menyuk. "Understanding leaky modes: slab waveguide revisited." *Advances in Optics and Photonics* 1.1 (Jan. 2009), pp. 58–106. DOI: `10.1364/AOP.1.000058`.

[HS16] Sarah Hoffmann-Urlaub and Tim Salditt. "Miniaturized beamsplitters realized by X-ray waveguides." *Acta Crystallographica Section A* 72.5 (Aug. 2016), pp. 515–522. DOI: `10.1107/s205327331601144x`.

[HY02] George W. Hanson and Alexander B. Yakovlev. *Operator Theory for Electromagnetics. An Introduction*. New York, NY: Springer, 2002. ISBN: 9781475736793. DOI: `10.1007/978-1-4757-3679-3`.

[JD04] Werner H. Jark and Silvia Di Fonzo. "Transmission calculations for one- and two-dimensional x-ray waveguides." In: *Design and Microfabrication of Novel X-Ray Optics II*. Ed. by Anatoly A. Snigirev and Derrick C. Mancini. Vol. 5539. SPIE, Nov. 2004. DOI: `10.1117/12.556661`.

[Joh11] Peter Johansson. "Electromagnetic Green's function for layered systems: Applications to nanohole interactions in thin metal films." *Physical Review B* 83.19 (May 2011), p. 195408. DOI: `10.1103/physrevb.83.195408`.

[KCP20] Xiangjin Kong, Darrick E. Chang, and Adriana Pálffy. "Green's-function formalism for resonant interaction of x rays with nuclei in structured media." *Physical Review A* 102.3 (Sept. 2020), p. 033710. DOI: 10.1103/physreva.102.033710.

[KH13] Philip Trøst Kristensen and Stephen Hughes. "Modes and Mode Volumes of Leaky Optical Cavities and Plasmonic Nanoresonators." *ACS Photonics* 1.1 (Dec. 2013), pp. 2–10. DOI: 10.1021/ph400114e.

[LA23] Leon M. Lohse and Petar Andrejić. *xwglib – a library for the simulation of x-ray waveguides*. 2023. URL: https://gitlab.gwdg.de/irp/xwglib.

[Lag+08] Stefano Lagomarsino, Inna Bukreeva, Alessia Cedola, Daniele Pelliccia, and Werner Jark. "Theoretical Analysis of X-Ray Waveguides." In: *Modern Developments in X-Ray and Neutron Optics*. Ed. by Alexei Erko, Mourad Idir, Thomas Krist, and Alan G. Michette. Springer Series in Optical Sciences. Springer Berlin Heidelberg, 2008, pp. 91–111. ISBN: 9783540745617. DOI: 10.1007/978-3-540-74561-7_6.

[LAL25] Shin-Yu Lee, Sven Ahrens, and Wen-Te Liao. "Gravitationally sensitive structured x-ray optics using nuclear resonances." *Physical Review Research* 7.1 (Feb. 2025), p. 013158. DOI: 10.1103/physrevresearch.7.013158.

[Len+20] Dominik Lentrodt, Kilian P. Heeg, Christoph H. Keitel, and Jörg Evers. "Ab initio quantum models for thin-film x-ray cavity QED." *Physical Review Research* 2.2 (June 2020), p. 023396. DOI: 10.1103/physrevresearch.2.023396.

[LLY94] P. T. Leung, S. Y. Liu, and K. Young. "Completeness and orthogonality of quasinormal modes in leaky optical cavities." *Physical Review A* 49.4 (Apr. 1994), pp. 3057–3067. DOI: 10.1103/physreva.49.3057.

[Ma+22] Zi-Ru Ma, Xin-Chao Huang, Tian-Jun Li, Hong-Chang Wang, Gen-Chang Liu, Zhan-Shan Wang, Bo Li, Wen-Bin Li, and Lin-Fan Zhu. "First Observation of New Flat Line Fano Profile via an X-Ray Planar Cavity." *Physical Review Letters* 129.21 (Nov. 2022), p. 213602. DOI: 10.1103/physrevlett.129.213602.

[Mar74] Dietrich Marcuse. *Theory of dielectric optical waveguides*. Quantum electronics - principles and applications. New York: Academic Press, 1974. ISBN: 0-12-470950-8.

[NH12] Lukas Novotny and Bert Hecht. *Principles of Nano-Optics*. Cambridge University Press, 2012. ISBN: 9780511794193.

[OS09] Markus Osterhoff and Tim Salditt. "Real structure effects in X-ray waveguide optics: The influence of interfacial roughness and refractive index profile on the near-field and far-field distribution." *Optics Communications* 282.16 (Aug. 2009), pp. 3250–3256. DOI: 10.1016/j.optcom.2009.05.008.

[OS11] Markus Osterhoff and Tim Salditt. "Coherence filtering of x-ray waveguides: analytical and numerical approach." *New Journal of Physics* 13.10 (Oct. 2011), p. 103026. DOI: 10.1088/1367-2630/13/10/103026.

[Par18] Robert Parini. *cxroots: A Python module to find all the roots of a complex analytic function within a given contour*. 2018. URL: https://github.com/rparini/cxroots.

[Pel+06] D. Pelliccia, I. Bukreeva, A. Cedola, and S. Lagomarsino. "Dispersion properties of x-ray waveguides." *Applied Optics* 45.12 (Apr. 2006), p. 2821. DOI: 10.1364/ao.45.002821.

[Pel+07] D. Pelliccia, I. Bukreeva, M. Ilie, W. Jark, A. Cedola, F. Scarinci, and S. Lagomarsino. "Computer simulations and experimental results on air-gap X-ray waveguides." *Spectrochimica Acta Part B: Atomic Spectroscopy* 62.6-7 (July 2007), pp. 615–621. DOI: 10.1016/j.sab.2007.02.018.

[Pel16] Daniele Pelliccia. “Bending X-rays with nanochannels.” *Nature Photonics* 10.2 (Jan. 2016), pp. 75–77. DOI: 10.1038/nphoton.2015.275.

[Pfe+02] F. Pfeiffer, C. David, M. Burghammer, C. Riekel, and T. Salditt. “Two-Dimensional X-ray Waveguides and Point Sources.” *Science* 297.5579 (July 2002), pp. 230–234. DOI: 10.1126/science.1071994.

[PP14] Daniele Pelliccia and David M. Paganin. “Coherence filtering and revivals in x-ray waveguides: a communication-modes approach.” *Journal of the Optical Society of America A* 31.8 (July 2014), p. 1754. DOI: 10.1364/josaa.31.001754.

[RE21] Ralf Röhlsberger and Jörg Evers. “Quantum Optical Phenomena in Nuclear Resonant Scattering.” In: *Modern Mössbauer Spectroscopy*. Ed. by Yutaka Yoshida and Guido Langouche. Topics in Applied Physics. Springer Singapore, 2021, pp. 105–171. DOI: 10.1007/978-981-15-9422-9_3.

[Röh+10] R. Röhlsberger, K. Schlage, B. Sahoo, S. Couet, and R. Rüffer. “Collective Lamb Shift in Single-Photon Superradiance.” *Science* 328.5983 (May 2010), pp. 1248–1251. DOI: 10.1126/science.1187770.

[Sal+08] T. Salditt, S. P. Krüger, C. Fuhse, and C. Bähtz. “High-Transmission Planar X-Ray Waveguides.” *Physical Review Letters* 100.18 (May 2008), p. 184801. DOI: 10.1103/physrevlett.100.184801.

[Sal+15a] T. Salditt, S. Hoffmann, M. Vassholz, J. Haber, M. Osterhoff, and J. Hilhorst. “X-Ray Optics on a Chip: Guiding X Rays in Curved Channels.” *Physical Review Letters* 115.20 (Nov. 2015), p. 203902. DOI: 10.1103/physrevlett.115.203902.

[Sal+15b] Tim Salditt, Markus Osterhoff, Martin Krenkel, Robin N. Wilke, Marius Priebe, Matthias Bartels, Sebastian Kalbfleisch, and Michael Sprung. “Compound focusing mirror and X-ray waveguide optics for coherent imaging and nano-diffraction.” *Journal of Synchrotron Radiation* 22.4 (June 2015), pp. 867–878. DOI: 10.1107/s1600577515007742.

[Sch+11] Tom Schoonjans, Antonio Brunetti, Bruno Golosio, Manuel Sanchez del Rio, Vicente Armando Solé, Claudio Ferrero, and Laszlo Vincze. “The xraylib library for X-ray–matter interactions. Recent developments.” *Spectrochimica Acta Part B: Atomic Spectroscopy* 66.11-12 (Nov. 2011), pp. 776–784. DOI: 10.1016/j.sab.2011.09.011.

[Sch11] Felix Schenk. *Optimization of resonances for multilayer x-ray resonators*. Ed. by Tim Salditt. Vol. 3. Göttingen series in x-ray physics. Göttingen: Universitätsverlag Göttingen, 2011. ISBN: 9783863950088.

[SFH93] R. E. Smith, G. W. Forbes, and S. N. Houde-Walter. “Unfolding the multivalued planar waveguide dispersion relation.” *IEEE Journal of Quantum Electronics* 29.4 (Apr. 1993), pp. 1031–1034. DOI: 10.1109/3.214486.

[SHB97] M. J. N. van Stralen, K. F. I. Haak, and H. Blok. “On the classification of discrete modes in lossy planar waveguides: the modal analysis revisited.” *Optical and Quantum Electronics* 29.2 (1997), pp. 243–262. DOI: 10.1023/a:1018562307611.

[Sie79] A. E. Siegman. “Orthogonality properties of optical resonator eigenmodes.” *Optics Communications* 31.3 (Dec. 1979), pp. 369–373. DOI: 10.1016/0030-4018(79)90217-7.

[SO20] Tim Salditt and Markus Osterhoff. “X-ray Focusing and Optics.” In: *Nanoscale Photonic Imaging*. Ed. by Tim Salditt, Alexander Egner, and D. Russell Luke. Topics in Applied Physics. Cham: Springer International Publishing, 2020, pp. 71–124. ISBN: 9783030344139. DOI: 10.1007/978-3-030-34413-9_3.

[Sol+21] Jakob Soltau, Leon Merten Lohse, Markus Osterhoff, and Tim Salditt. "Finite-difference propagation for the simulation of x-ray multilayer optics." *Optics Express* 29.25 (Dec. 2021), p. 41932. DOI: 10.1364/oe.445300.

[SS74] Eberhard Spiller and Armin Segmüller. "Propagation of x rays in waveguides." *Applied Physics Letters* 24.2 (Jan. 1974), pp. 60–61. DOI: 10.1063/1.1655093.

[Tol99] Metin Tolan. *X-Ray Scattering from Soft-Matter Thin Films. Materials Science and Basic Research*. Springer Tracts in Modern Physics 148. Berlin: Springer, 1999. ISBN: 9783540495253.

[Tom95] M. S. Tomaš. "Green function for multilayers: Light scattering in planar cavities." *Physical Review A* 51.3 (Mar. 1995), pp. 2545–2559. DOI: 10.1103/physreva.51.2545.

[TPP13] K. J. Tsanaktsidis, D. M. Paganin, and D. Pelliccia. "Analytical description of partially coherent propagation and absorption losses in x-ray planar waveguides." *Optics Letters* 38.11 (June 2013), pp. 1808–1810. DOI: 10.1364/OL.38.001808.

[Vas79] C. Vassallo. "Radiating normal modes of lossy planar waveguides." *Journal of the Optical Society of America* 69.2 (Feb. 1979), p. 311. DOI: 10.1364/josa.69.000311.

[VS21] Malte Vassholz and Tim Salditt. "Observation of electron-induced characteristic x-ray and bremsstrahlung radiation from a waveguide cavity." *Science Advances* 7.4 (Jan. 2021). DOI: 10.1126/sciadv.abd5677.

[Zet12] Anton Zettl. *Sturm-Liouville Theory*. American Mathematical Society, 2012. ISBN: 9780821852675.

[Zho+17] Q. Zhong, M. Osterhoff, M. W. Wen, Z. S. Wang, and T. Salditt. "X-ray waveguide arrays: tailored near fields by multi-beam interference." *X-Ray Spectrometry* 46.2 (Jan. 2017), pp. 107–115. DOI: 10.1002/xrs.2740.

[Zwa+99] M. J. Zwanenburg, J. F. Peters, J. H. H. Bongaerts, S. A. de Vries, D. L. Abernathy, and J. F. van der Veen. "Coherent Propagation of X Rays in a Planar Waveguide with a Tunable Air Gap." *Physical Review Letters* 82.8 (Feb. 1999), pp. 1696–1699. DOI: 10.1103/physrevlett.82.1696.

4. Collective nuclear excitation and pulse propagation in single-mode x-ray waveguides

This chapter and the following one are recompiled[1] under the terms of the *Creative Commons BY-SA 4.0* license from the preprint:
Leon M. Lohse, Petar Andrejić, Sven Velten, Malte Vassholz, Charlotte Neuhaus, Ankita Negi, Anjali Panchwanee, Ilya Sergeev, Adriana Pálffy, Tim Salditt, and Ralf Röhlsberger. *Collective nuclear excitation and pulse propagation in single-mode x-ray waveguides*. 2024. DOI: `10.48550/ARXIV.2403.06508`

Author Contributions
LML, MV, TS, and RR conceived of and planned the experiments. LML authored the proposals for the synchrotron experiments with help from TS and RR. LML and SV fabricated the samples. LML, SV, AN, APan, CN, IS, and TS performed the two experiments. LML, PA, and APal developed the theory. LML analyzed the experimental data. LML wrote the manuscript with significant contributions from RR, APal, and PA. All authors discussed the results and contributed to the final manuscript.

Abstract
Waveguides offer a means to controllably couple atomic ensembles to the electromagnetic field therein. Here, we demonstrate x-ray propagation in planar thin-film waveguides coupled to Mössbauer nuclei under collective resonant excitation by short pulses of synchrotron radiation. We record x-ray photons that have been emitted into resonant modes of the waveguide. Depending on the geometry and mode of excitation, two fundamentally different signatures of the collective emission are observed, for which we present a unifying theoretical model. Our results form a new platform for waveguide quantum electrodynamics in the hard x-ray regime with the potential to provide a coherent narrowband source of x-rays on the nanometer scale.

When interacting with radiation, ensembles of identical quantum optical systems exhibit collective dynamics which is fundamentally different from that of the individual constituents [Dic54]. Collective effects such as directed emission [Scu+06; Ebe06],

[1] Subject to slight adjustments of the notation and minor corrections.

collective frequency shifts, superradiant decay [Scu09], and collective oscillations emerge already in the regime of weak excitation from as little as a single photon [SS09]. Furthermore, in spatially extended ensembles, the geometry and spatial distribution distinctively affects the dynamics [SCS10; Man12]. These effects have been observed over various platforms, including one-dimensional chains of atoms coupled to optical waveguides [Ase+17; Sol+17; Kum+20; Pen+22; Car+23; Su+23] and Mössbauer nuclei in solid-state systems driven by hard x-rays [AK65; Ger+85; Bür+87; SS89; HT99; Smi99; Bür99; Röh+05; Röh+10; Hab+17; Chu+17]. The latter are a particularly well-suited platform to observe and harness collective effects, since nuclear transitions resonant to hard x-ray frequencies have extremely narrow linewidths [Röh05], rendering exceptionally clean quantum-optical systems [RE21; Ada09], such that Mössbauer nuclei were among the earliest systems to investigate collective radiative phenoma (see Refs. [AK65; KAK79; HT99; Smi99] and the references therein).

The experimental platforms available so far for quantum optics with Mössbauer nuclei have been either nuclear forward scattering (NFS) from unstructured foils [Bür99], nuclear Bragg diffraction (NBD) from crystals [AK65; Ger+85; SS89; Chu+17], or grazing-incidence reflection from thin-film structures [RE21]. Depending on the experimental geometry, the collective nuclear excitation—also known as nuclear exciton [AK65; HT99; Smi99]—has a different temporal dynamics. In NFS, i.e., a thick slab or foil illuminated in normal incidence, the nuclear exciton exhibits so-called dynamical beats and emits into forward direction [Bür99; Smi+07]. In contrast, a thin film embedded in an x-ray waveguide (WG) and excited in grazing-incidence illumination decays exponentially and emits into the direction of specular reflection—which we call reflection geometry—with superradiant speedup and a shifted resonance frequency compared to the single atom [Röh+10], similar to NBD [AK65; KAK79; SS89]. Still unexplored is a waveguide geometry, where identical nuclei are coupled to photons that propagate confined in a waveguide. The waveguide allows some control over the modes of the photon field and their dispersion. Such systems have attracted a lot of attention recently in the emerging field of waveguide QED [She+23], yet so far restricted to longer photon wavelengths.

In this Letter, we demonstrate the excitation and collective dynamics of Mössbauer nuclei coupled in forward incidence to a single-mode nanometer-thin x-ray waveguide, resolved in both time and position. We present two experiments, in which we excite the sample either in front-coupling (FC) geometry [Fig. 4.1(a)] [Fuh+04] or resonant-beam-coupling (RBC) geometry [Fig. 4.1(b)] [Fen+93]. Our experimental technique combined with optimized WG designs and fabrication allows to observe the photons that have been emitted into resonant modes of the WG leaving its back end. Depending on the way of excitation, the decay of the nuclear exciton either exhibits dynamical beats as in NFS or it decays exponentially with superradiant speedup. We explain our observations by a unifying theoretical model based on a recently introduced approach based on a real-space Green's function formalism [ALP24]. Our results shed new light on earlier experiments in reflection geometry and open new ways to design spatio-temporal properties of the nuclear exciton based on hard x-ray waveguiding, thus benefiting the emerging field of waveguide QED [She+23].

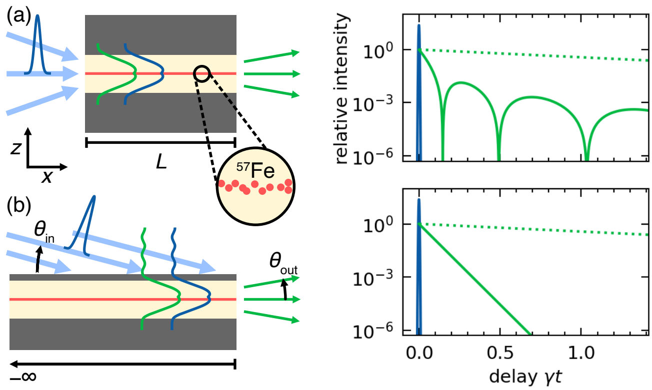

Figure 4.1.: A short excitation pulse (blue) couples into a planar WG and creates a nuclear exciton in the ^{57}Fe layer (red) that radiatively decays (green). (a) FC excitation creates an exciton that emits pronounced temporal beatings. (b) RBC excitation of a long WG: the exciton decays exponentially. Superradiant speedup and shifted resonance, compared to the natural exponential decay with rate γ (dotted green line), depend on the incidence angle θ_{in}. The plots on the right show exemplary theory calculations.

Hard x-rays are an extreme regime for waveguiding. In the energy regime above 10 keV, refractive indices are written as $n = 1 - \delta + i\beta$, where $\delta, \beta < 10^{-5}$. X-ray waveguiding manifests when lighter core materials are surrounded by denser cladding materials. Because of the small contrasts in n, x-ray WGs are weakly guiding (modes typically extend over a few 100 wavelengths in the transversal direction) and cause significant photo-electric absorption in the dense cladding. Consequently, the Purcell enhancement is negligible and coupling to resonant modes is small [LA24]. However, dense cladding strongly attenuates everything but the lowest few resonant modes [OS11], so that fields generated by emitters in the WG can be asymptotically approximated by only their resonant components [LA24].

We have prepared two planar x-ray WGs, both containing a few-atomic-layers-thin iron film, to 95 % enriched in ^{57}Fe, in the center of its guiding layer (see Supplemental Material on p. 127). The ^{57}Fe does not develop long-range magnetic order in this thin film and hence exhibits essentially a single resonance line. The experiments were performed at the dynamics beamline P01 at PETRA III (DESY, Hamburg). The samples were illuminated by 100 ps-long synchrotron pulses with photon energy 14.4 keV (monochromatized to 1 meV bandwidth) at a repetition period of 192 ns, creating nuclear excitons. The photons leaving the WG at its back end were detected with a stack of avalanche photo diodes (APDs). By temporal gating, the (delayed) emissions of the nuclear exciton are detected independently from the (prompt) synchrotron pulse.

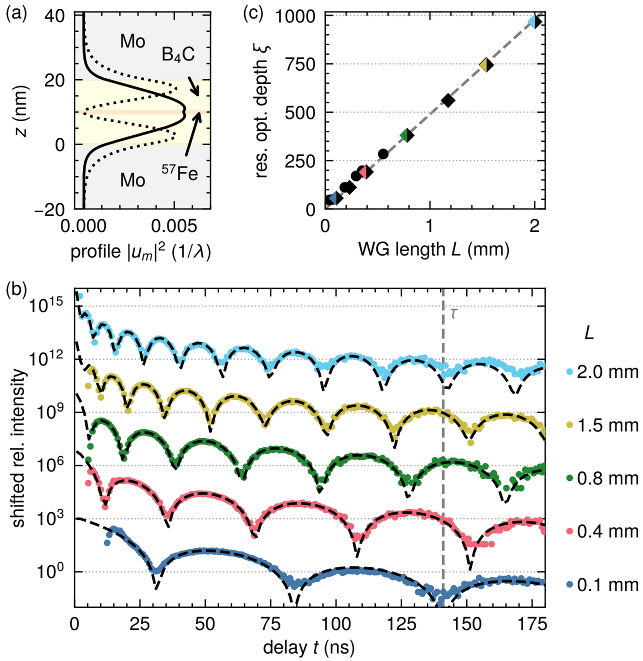

Figure 4.2.: Layer design and experimental data for FC excitation. (a) Transversal mode profiles $u_m(z)$ of the 2 guided modes supported by the WG. (b) Experimentally observed emissions as a function of delay t after excitation for different WG lengths L (colored points). The intensities are normalized and vertically shifted. The dashed lines show simulations of NFS through ^{57}Fe-foils, using hyperfine parameters and resonant optical depth ξ that were estimated from the experimental data. (c) Extracted resonant optical depth ξ for different L (diamonds and discs indicate 2 independent measurements).

First, we have prepared a layer system optimized for FC excitation, consisting of a 0.6 nm-thin layer of ^{57}Fe, embedded in a planar x-ray WG with 20 nm B_4C core, and symmetric 30 nm-thick Mo cladding as sketched in Fig. 4.2(a). The layer structure was deposited onto a 1 mm-thick Ge wafer and capped with a second Ge wafer after deposition as detailed in Ref. [Krü+12]. The synchrotron beam was focussed with two elliptical mirrors in Kirkpatrick-Baez geometry to a spot of about 7 μm diameter into the WG entrance at the focal position. The Ge wafers were used to absorb the tails of the focus to reduce background signal, but they do not affect the resonant mode structure due to the thick cladding [Sal+08]. The wafer sandwich was cut to triangular shape, allowing us to change the effective WG length L by translating it along y transversal to the beam (see Supplemental Material on p. 127). The WG length was calibrated by measuring the absorption in the wafer as a function of y-translation. Figure 4.2(b) shows the temporal evolution of the emitted x-rays for several WG lengths up to 2 mm (limited by off-resonant absorption). The emissions clearly exhibit dynamical beats resembling those known from NFS through a homogeneous single-line resonant absorber. The dashed lines show simulations of NFS through a thick foil of enriched ^{57}Fe including inhomogeneous hyperfine-splitting in the order of 6 natural linewidths, in a 4-parameter model (see Supplemental Material on p. 127), which accurately describes the data. The optimal parameters were found using a maximum-likelihood estimation assuming Poisson statistics. The magnitude of hyperfine splitting is expected from similar amorphous thin films [Röh+10; Sah+11]. The extracted optical depth ξ (also called "effective thickness" [Bür99]) [Fig. 4.2(c)] is strictly proportional to the WG length L.

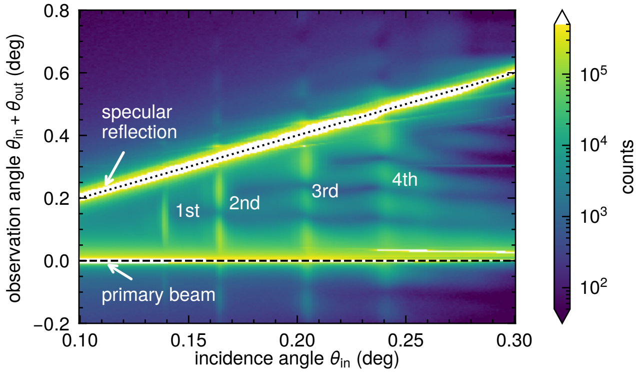

Figure 4.3.: Off-resonant intensity of the RBC sample, illuminated at an incidence angle of θ_{in} and recorded 3 m downstream of the sample with a pixel detector. Vertical cuts correspond to observed far-field patterns. The 4 resonant modes, which are supported by the layer structure, are clearly visible in the region between the primary beam ($\theta_{in} + \theta_{out} = 0$) and the specularly reflected beam ($\theta_{out} = \theta_{in}$). The modes are well separated in θ_{in}.

For the second experiment, we have prepared a layer system optimized for RBC excitation [Fig. 4.1(b)], having a 40 nm-thick B_4C core and, in contrast to the FC experiment, a top Mo cladding layer of only 8 nm to allow incident light to evanescently couple into the WG. We used a 10 mm long Si wafer as substrate, so that the WG is significantly longer than the attenuation length of the resonant modes and thus has effectively infinite extent. The back end of the sample was broken off after deposition to create a clean exit face. The sample was placed onto a goniometer stage for tuning the incidence angle θ_{in}. Figure 4.3 shows the off-resonant far-field intensity distribution, detected 3 m downstream of the sample by a time-insensitive pixel detector as a function of θ_{in}. We then aligned the APDs with the WG exit [$\theta_{out} \approx 0°$, see Fig. 4.1(b)] and collected the emitted photons for several values of θ_{in} in the vicinity of the third resonance $\theta_3 = 0.203°$. We selected the 3rd mode for practical reasons, because the divergence of the incident beam was 0.002°, which is wider than the resonance of the 1st mode. Figure 4.4(a) shows the emitted intensity as a function of time for three different θ_{in}. The intensity exhibits an initial superradiant decay and a slow-down for longer delays, which is caused by a residual hyperfine splitting of the nuclear levels. The initial decay is plotted in panel (b), showing a decay rate of 30γ at θ_3, which gradually diminishes as θ_{in} moves away from resonance. Similar behaviour was previously observed with NBD [SS89] and thin films in reflection geometry [Röh+10]. The solid line shows a simulation in reflection geometry [see SM] that considers divergence of the incoming beam and hyperfine splitting of the transitions. The hyperfine parameters for the simulation were extracted from measurements at $\theta_{in} = 0.5°$, far from the WG modes, and are consistent with the FC experiment [see SM].

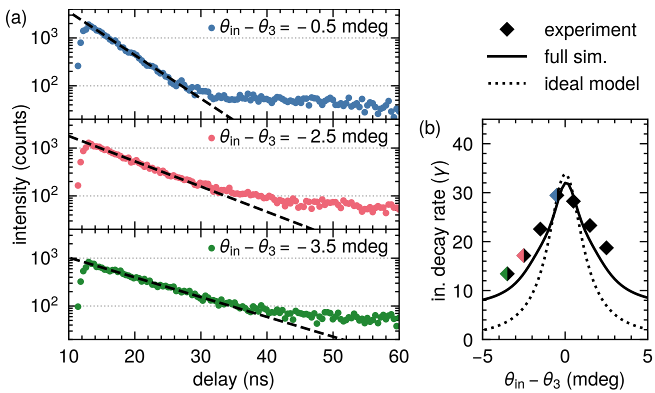

Figure 4.4.: Experimentally measured emissions of the nuclear exciton in RBC excitation. (a) Decay pattern for 3 angles in the vicinity of the 3rd resonant mode and initial exponential decay (black dashed line). (b) Initial decay rate as a function of angle detuning: extracted from the experimental data (black diamonds); calculated with the simplified ideal model (4.7) (dashed line); simulation including hyperfine splitting of the transition energies as well as the angular divergence of the experiment (solid line).

To qualitatively model the experimental observations, we employ the theory developed in Ref. [ALP24] based on macroscopic quantum electrodynamics, which describes the atom-light interaction using the classical electromagnetic Green's function. Importantly, it explicitly models the propagating field modes in the dispersive waveguide environment with spatial dependency, which has not been relevant for the existing theories of NFS [Smi+07; Shv99], NBD [HT99; KAK79], or the reflection geometry [HE13; Len+20; Len+23]. Here, we neglect the nearly degenerate sublevels of the ground ($I_g = 1/2$) and excited ($I_e = 3/2$) state of ^{57}Fe ($\hbar\omega_0 = 14.4\,\mathrm{keV}$, $\hbar\gamma = 4.7\,\mathrm{neV}$, M1-transition) and describe the nuclear state by a single nuclear transition operator for each atom $\hat{\sigma}^i_{ge} = |g\rangle\langle e|$. The excitation pulses have very small pulse areas so that the nuclear excited states remain unpopulated ($\langle\hat{\sigma}^i_{ee}\rangle \approx 0$) and the response is linear. The expectation values of the transition operators $\sigma^i_{ge} := \langle\hat{\sigma}^i_{ge}\rangle$ evolve, in the rotating frame of the nuclear transition frequency ω_0, according to [Ase+17]

$$\begin{aligned}-i\omega\sigma^i_{ge}(\omega) = -\frac{\gamma}{2}\sigma^i_{ge}(\omega) + i\Omega(\mathbf{r}_i,\omega) \\ + i\sum_{j\neq i} g_{ij}(\omega)\sigma^j_{ge}(\omega),\end{aligned} \tag{4.1}$$

where $\Omega(\mathbf{r},t) = \mathbf{m}_0^* \cdot \mathbf{B}_{\mathrm{in}}(\mathbf{r},t)/\hbar$ is the propagating excitation pulse expressed as a Rabi frequency, $\mathbf{m}_0$ the magnetic dipole moment of the transition and g_{ij} are dispersive coupling coefficients. The total single-atom spontaneous decay rate γ includes self-interaction and is equal to its value in a homogeneous environment (negligible Purcell factor). Note that $\mathbf{B}_{\mathrm{in}}$ is the free incident magnetic field and scattering from the nuclei is fully accounted for by g_{ij}. The coupling is mediated by the WG environment via

$$g_{ij}(\omega) := \frac{\mu_0 k_0^2}{\hbar}\,\mathbf{m}_0^* \cdot \underline{\mathbf{G}}_{\mathrm{m}}(\mathbf{r}_i,\mathbf{r}_j,\omega_0+\omega)\cdot\mathbf{m}_0, \tag{4.2}$$

where μ_0 is the vacuum permeability, $k_0 = \omega_0/c$, and $\underline{\mathbf{G}}_{\mathrm{m}}$ the Green's function for the magnetic field in the WG (see Supplemental Material on p. 127). While the σ^i_{ge} are defined in the rotating frame, this Green's function depends on the absolute frequency $\omega_0 + \omega$.

We convert (4.1) into a one-dimensional macroscopic equation. To that end, we assume homogeneously distributed nuclei in a single thin layer, insert the analytic expression for the Green's function, and assume interaction via a single resonant mode. We obtain

$$\dot{\sigma}_{ge}(x,t) = -\frac{\gamma}{2}\sigma_{ge}(x,t) + i\Omega(x,t) - \frac{\zeta_m\gamma}{4\Lambda_{\mathrm{res}}}\int_{-L}^{0} \mathrm{d}x' e^{ik_0\nu_m|x-x'|}\sigma_{ge}(x', t-|x-x'|\nu_m/c). \quad (4.3)$$

Here, Λ_{res} is the on-resonance attenuation length (61 nm for bulk ^{57}Fe), ν_m is the complex effective refractive index of the mode [LA24], and ζ_m the dimensionless coupling-coefficient of the WG mode. The latter effectively rescales Λ_{res} and is given by $\zeta_m = du_m(z_0)^2$, where d and z_0 are thickness and position of the ^{57}Fe-layer, respectively and $u_m(z)$ is the complex transversal mode profile, described in Ref. [LA24], which is bi-normalized to $\int[u_m(z)]^2\mathrm{d}z = 1$. The field radiated by the nuclear exciton is obtained via

$$\mathbf{B}^{+}_{\mathrm{nuc}}(\mathbf{r},\omega) = \mu_0 k_0^2 \sum_j \underline{\mathbf{G}}_{\mathrm{m}}(\mathbf{r},\mathbf{r}_j,\omega_0+\omega)\cdot\mathbf{m}_0\sigma^j_{ge}(\omega), \quad (4.4)$$

corresponding to the field radiated by the oscillating magnetization

$$\mathbf{M} = \mathbf{m}_0\rho\sigma_{ge}\exp(-i\omega_0 t) + \text{h.c.}.$$

Note that (4.3) not only describes planar WGs (after integrating out y) as discussed here, but also one-dimensional channel WGs, and furthermore homogeneous slabs (foils) with translational symmetry in y-z [FM08], with different values for ν_m ($= n$ for slab) and ζ_m ($= 1$ for slab).

Equation (4.1) is often treated as an eigenvalue problem, decomposing σ_{ge} into radiative eigenmodes [Ase+17; SCS10; Man12]. Instead, we employ a forward-scattering approximation that allows us to solve (4.3) analytically for the two experimental settings sketched in Fig. 4.1. The rapidly oscillating phase factor in (4.3) strongly suppresses the back-scattered field [ALP24]. Hence, we change the upper limit of integration in (4.3) to x.

In the FC geometry [Fig. 4.1(a)], the only surviving component of the excitation pulse is the fundamental guided mode, so that $\Omega(x,t) = \Omega_0\exp(ik_0\nu_m x)\Pi(t_{\mathrm{ret}})$, with some slowly varying envelope $\Pi(t)$ where $t_{\mathrm{ret}} = t - k_0\nu_m x/c$. Note that the excitation pulse decays with x, as $\mathrm{Im}\{\nu_m\} > 0$. For finite L, (4.3) becomes a Volterra integral equation due to the forward-scattering approximation and hence has no radiative eigenmodes. Its exact analytical solution for the given $\Omega(x,t)$ is

$$\sigma_{ge}(x,t) = iAe^{ik_0\nu_m x-\gamma t_{\mathrm{ret}}/2}J_0\left[\sqrt{\gamma t_{\mathrm{ret}}x\zeta_m\Lambda^{-1}_{\mathrm{res}}}\right], \quad (4.5)$$

for $t_{\mathrm{ret}} \geq 0$, where J_0 is a Bessel function of the first kind and $A = \Omega_0 \int \Pi(t)\mathrm{d}t$ the pulse area. This is the well known solution for NFS [Shv99; Smi+07] with Λ_{res} rescaled by ζ_m. Computing the emitted field from (4.5) is straight-forward (see Supplemental Material on p. 127). The exciton emits directionally and purely into the WG mode. The emission undergoes the dynamical beats, well known from coherent pulse propagation through resonant media [KAK79; Bür99]—and clearly observed in our experiment. From the experimental data, we obtain an estimate for the coupling coefficient $|\zeta_m| = \xi\Lambda_{\mathrm{res}}/L \approx 0.029$, slightly smaller than the theoretical value (from design parameters) of 0.038.

In the RBC geometry [Fig. 4.1(b)], the incidence angle θ_{in} fixes the in-plane wavevector to $k_{\mathrm{in}} = k_0 \cos\theta_{\mathrm{in}}$. The excitation pulse can be written as

$$\Omega(x,t) = \Omega_0 \exp(ik_{\mathrm{in}}x)\Pi(t_{\mathrm{ret}}),$$

with here $t_{\mathrm{ret}} = t - k_{\mathrm{in}}x/\omega_0$. Assuming that L is significantly larger than the off-resonance attenuation length of the mode, $\Lambda_m = (2k_0 \operatorname{Im}\{\nu_m\})^{-1}$, (typically a few 100 µm) we can extend the lower boundary of integration in (4.3) to $-\infty$. This eliminates the boundary effect in the forward direction. The linear spatial phase in $\Omega(x,t)$ corresponds to a radiative eigenmode of the exciton, so that the exciton evolves harmonically with shifted frequency and enhanced decay. We obtain (see Supplemental Material on p. 127)

$$\sigma_{ge}(x,t) = iA \exp\left[ik_0 x \cos\theta_{\mathrm{in}} - \left(\frac{\gamma}{2} - i\eta\right)t_{\mathrm{ret}}\right], \tag{4.6}$$

$$\eta(\theta_{\mathrm{in}}) = \frac{\zeta_m\Lambda_m}{\Lambda_{\mathrm{res}}} \frac{1}{2\Lambda_m q - i} \frac{\gamma}{2}, \tag{4.7}$$

with $q = k_0\cos\theta_{\mathrm{in}} - k_0 \operatorname{Re}\{\nu_m\} \approx -k_0(\theta_{\mathrm{in}} - \theta_m)\sin\theta_m$ and pulse area A as previously defined. The mode angle is defined via $\cos\theta_m = \operatorname{Re}\{\nu_m\}$. Similar to NBD [KAK79; SS89], the exciton decays superradiantly with peak speedup of $1 + \zeta_m\Lambda_m/\Lambda_{\mathrm{res}}$ depending on ratio between off- and on-resonant attenuation lengths, as well as the mode coupling coefficient ζ_m. Note that $\Lambda_m/\Lambda_{\mathrm{res}} = \rho\Lambda_m\sigma_{\mathrm{res}}$ (σ_{res}: resonant cross section, ρ: number density of nuclei) gives the number of nuclei within the off-resonant absorption length (compare Ref. [Ada09]), clearly demonstrating the collective superradiant nature of the speedup, contrasting earlier interpretations based on an increase of the photon density of states [Röh+05]. Figure 4.4(b) shows the speedup from calculations (dashed line) with (4.7) using the design parameters as well as the speedup from the experimental data (diamonds). This simple single-mode model already explains the observed peak speedup. It does not fully account for the increased angular resonance width, which can be attributed to the residual hyperfine splitting and angular divergence observed in the experiment [see SM]. Thus, we see that (4.3) qualitatively reproduces both experiments. Notably, similar eigenmodes (4.6) are observed in crystals [SS89] and waveguides in grazing-incidence reflection geometry [RE21].

In summary, we have demonstrated the excitation and collective dynamics of Mössbauer nuclei in x-ray waveguides for two different modes of excitation. In the FC geometry, we have observed dynamical beats emitted by WGs with a 20 nm-thick guiding core and varying lengths from about 0.1 mm to 2 mm into the fundamental WG mode. In the RBC geometry, we have observed exponential decay into the resonantly excited WG mode with tuneable superradiant speedup. Our theory consistently describes the observations of both experiments in a one-dimensional waveguide picture. When a single mode dominates, the equation of motion is formally identical to that of a homogeneous slab with length (thickness) rescaled by a nucleus-mode coupling constant ζ_m. Depending on the off-resonant optical thickness of the WG, two regimes are realized. For optically thin WGs, the finite integrated nuclear density gives rise to dynamical beats. The grazing-incidence geometry allows the study of optically thick WGs, where off-resonant absorption suppresses boundary effects, establishing translation invariance and permitting radiative eigenmodes, so that the exciton evolves harmonically with resonant dispersion relation.

Our results open up a number of promising future directions. We demonstrated how to "harvest" the propagating beam at the exit of the WG, forming an extremely coherent narrowband source of 20 nm cross section, albeit with low brightness. Both the spatial diffraction patterns and temporal dynamics can be readily resolved at these scales. The FC geometry allows to simultaneously and coherently couple into multiple guided modes in one or several WGs. A multi-mode WG could be used to implement effective two-beam control techniques for the x-ray frequency regime. The spatial coherence allows to spatially separate individual modes and permits new approaches for narrowband x-ray control via the engineering of collective radiation patterns. The source may be utilized for investigations at the nanoscale that leverage both spatial and temporal coherence.

Acknowledgments
We thank Mike Kanbach for preparing the WG assemblies, Olaf Leupold for his support and fruitful discussions during the first beamtime, and Dieter Lott and Helmholtz-Zentrum Hereon for providing and supporting the reflectometer to calibrate the thin film samples. We acknowledge DESY (Hamburg, Germany), a member of the Helmholtz Association HGF, for the provision of experimental facilities. Beamtime was allocated for proposals I-20211677; I-20221193. We acknowledge partial funding by Max Planck School of Photonics; Deutsche Forschungsgemeinschaft (DFG) (432680300 SFB 1456/C03, 429529648 TRR 306/C04, 390858490 EXC 2147, 390715994 EXC 2056). A. Pálffy acknowledges support from the DFG in the framework of the Heisenberg Program. LML, MV, TS, and RR are part of the Max Planck School of Photonics.

References

[Ada09] B. W. Adams. "Nuclear γ-ray superradiance." *Journal of Modern Optics* 56.18-19 (Oct. 2009), pp. 1974–1984. DOI: 10.1080/09500340903199921.

[AK65] A. M. Afanas'ev and Yu. Kagan. "Radiation of a system of excited nuclei in a crystal." *JETP Letters* 2.3 (1965), p. 130.

[ALP24] Petar Andrejić, Leon Merten Lohse, and Adriana Pálffy. "Waveguide QED with Mössbauer nuclei." *Physical Review A* 109.6 (June 2024), p. 063702. DOI: 10.1103/physreva.109.063702.

[Ase+17] A. Asenjo-Garcia, J. D. Hood, D. E. Chang, and H. J. Kimble. "Atom-light interactions in quasi-one-dimensional nanostructures: A Green's-function perspective." *Physical Review A* 95.3 (Mar. 2017), p. 033818. DOI: 10.1103/physreva.95.033818.

[Bür+87] U. van Bürck, R. L. Mössbauer, E. Gerdau, R. Rüffer, R. Hollatz, G. V. Smirnov, and J. P. Hannon. "Nuclear Bragg scattering of synchrotron radiation with strong speedup of coherent decay, measured on antiferromagnetic $^{57}FeBO_3$." *Physical Review Letters* 59.3 (July 1987), pp. 355–358. DOI: 10.1103/physrevlett.59.355.

[Bür99] U. van Bürck. "Coherent pulse propagation through resonant media." *Hyperfine Interactions* 123–124.1–4 (Mar. 1999), pp. 483–509. DOI: 10.1023/a:1017080008712.

[Car+23] S. Cardenas-Lopez, P. Solano, L. A. Orozco, and A. Asenjo-Garcia. "Optical precursors in waveguide quantum electrodynamics." *Physical Review Research* 5.1 (Feb. 2023), p. 013133. DOI: 10.1103/physrevresearch.5.013133.

[Chu+17] Aleksandr I. Chumakov, Alfred Q. R. Baron, Ilya Sergueev, Cornelius Strohm, Olaf Leupold, Yuri Shvyd'ko, Gennadi V. Smirnov, Rudolf Rüffer, Yuichi Inubushi, Makina Yabashi, Kensuke Tono, Togo Kudo, and Tetsuya Ishikawa. "Superradiance of an ensemble of nuclei excited by a free electron laser." *Nature Physics* 14.3 (Nov. 2017), pp. 261–264. DOI: 10.1038/s41567-017-0001-z.

[Dic54] R. H. Dicke. "Coherence in Spontaneous Radiation Processes." *Physical Review* 93.1 (Jan. 1954), pp. 99–110. DOI: 10.1103/physrev.93.99.

[Ebe06] J. H. Eberly. "Emission of one photon in an electric dipole transition of one among N atoms." *Journal of Physics B: Atomic, Molecular and Optical Physics* 39.15 (July 2006), S599–S604. DOI: 10.1088/0953-4075/39/15/s07.

[Fen+93] Y. P. Feng, S. K. Sinha, H. W. Deckman, J. B. Hastings, and D. P. Siddons. "X-ray flux enhancement in thin-film waveguides using resonant beam couplers." *Physical Review Letters* 71.4 (July 1993), pp. 537–540. DOI: 10.1103/physrevlett.71.537.

[FM08] Richard Friedberg and Jamal T. Manassah. "Eigenfunctions and eigenvalues in superradiance with x-y translational symmetry." *Physics Letters A* 372.16 (Apr. 2008), pp. 2787–2801. DOI: 10.1016/j.physleta.2007.12.056.

[Fuh+04] Christian Fuhse, Ansgar Jarre, Christoph Ollinger, Jens Seeger, Tim Salditt, and Remi Tucoulou. "Front-coupling of a prefocused x-ray beam into a monomodal planar waveguide." *Applied Physics Letters* 85.11 (Sept. 2004), pp. 1907–1909. DOI: 10.1063/1.1791736.

[Ger+85] E. Gerdau, R. Rüffer, H. Winkler, W. Tolksdorf, C. P. Klages, and J. P. Hannon. "Nuclear Bragg diffraction of synchrotron radiation in yttrium iron garnet." *Physical Review Letters* 54.8 (Feb. 1985), pp. 835–838. DOI: 10.1103/physrevlett.54.835.

[Hab+17] Johann Haber, Xiangjin Kong, Cornelius Strohm, Svenja Willing, Jakob Gollwitzer, Lars Bocklage, Rudolf Rüffer, Adriana Pálffy, and Ralf Röhlsberger. "Rabi oscillations of X-ray radiation between two nuclear ensembles." *Nature Photonics* 11.11 (Oct. 2017), pp. 720–725. DOI: 10.1038/s41566-017-0013-3.

[HE13] Kilian P. Heeg and Jörg Evers. "X-ray quantum optics with Mössbauer nuclei embedded in thin-film cavities." *Physical Review A* 88.4 (Oct. 2013). DOI: 10.1103/physreva.88.043828.

[HT99] J. P. Hannon and G. T. Trammell. "Coherent γ-ray optics." *Hyperfine Interactions* 123–124.1–4 (Mar. 1999), pp. 127–274. DOI: 10.1023/a:1017011621007.

[KAK79] Yu Kagan, A. M. Afanas'ev, and V. G. Kohn. "On excitation of isomeric nuclear states in a crystal by synchrotron radiation." *Journal of Physics C: Solid State Physics* 12.3 (Feb. 1979), pp. 615–631. DOI: 10.1088/0022-3719/12/3/027.

[Krü+12] S. P. Krüger, H. Neubauer, M. Bartels, S. Kalbfleisch, K. Giewekemeyer, P. J. Wilbrandt, M. Sprung, and T. Salditt. "Sub-10nm beam confinement by X-ray waveguides: design, fabrication and characterization of optical properties." *Journal of Synchrotron Radiation* 19.2 (Jan. 2012), pp. 227–236. DOI: 10.1107/s0909049511051983.

[Kum+20] Jan Kumlin, Kevin Kleinbeck, Nina Stiesdal, Hannes Busche, Sebastian Hofferberth, and Hans Peter Büchler. "Nonexponential decay of a collective excitation in an atomic ensemble coupled to a one-dimensional waveguide." *Physical Review A* 102.6 (Dec. 2020), p. 063703. DOI: 10.1103/physreva.102.063703.

[LA24] Leon M. Lohse and Petar Andrejić. "Nano-optical theory of planar x-ray waveguides." *Optics Express* 32.6 (Mar. 2024), p. 9518. DOI: 10.1364/oe.504206.

[Len+20] Dominik Lentrodt, Kilian P. Heeg, Christoph H. Keitel, and Jörg Evers. "Ab initio quantum models for thin-film x-ray cavity QED." *Physical Review Research* 2.2 (June 2020), p. 023396. DOI: 10.1103/physrevresearch.2.023396.

[Len+23] Dominik Lentrodt, Oliver Diekmann, Christoph H. Keitel, Stefan Rotter, and Jörg Evers. "Certifying Multimode Light-Matter Interaction in Lossy Resonators." *Physical Review Letters* 130.26 (June 2023), p. 263602. DOI: 10.1103/physrevlett.130.263602.

[Man12] Jamal T. Manassah. "Cooperative radiation from atoms in different geometries: decay rate and frequency shift." *Advances in Optics and Photonics* 4.2 (June 2012), p. 108. DOI: 10.1364/aop.4.000108.

[OS11] Markus Osterhoff and Tim Salditt. "Coherence filtering of x-ray waveguides: analytical and numerical approach." *New Journal of Physics* 13.10 (Oct. 2011), p. 103026. DOI: 10.1088/1367-2630/13/10/103026.

[Pen+22] Riccardo Pennetta, Martin Blaha, Aisling Johnson, Daniel Lechner, Philipp Schneeweiss, Jürgen Volz, and Arno Rauschenbeutel. "Collective Radiative Dynamics of an Ensemble of Cold Atoms Coupled to an Optical Waveguide." *Physical Review Letters* 128.7 (Feb. 2022), p. 073601. DOI: 10.1103/physrevlett.128.073601.

[RE21] Ralf Röhlsberger and Jörg Evers. "Quantum Optical Phenomena in Nuclear Resonant Scattering." In: *Modern Mössbauer Spectroscopy*. Ed. by Yutaka Yoshida and Guido Langouche. Topics in Applied Physics. Springer Singapore, 2021, pp. 105–171. DOI: 10.1007/978-981-15-9422-9_3.

[Röh+05] R. Röhlsberger, K. Schlage, T. Klein, and O. Leupold. "Accelerating the Spontaneous Emission of X Rays from Atoms in a Cavity." *Physical Review Letters* 95.9 (Aug. 2005). DOI: 10.1103/physrevlett.95.097601.

[Röh+10] R. Röhlsberger, K. Schlage, B. Sahoo, S. Couet, and R. Rüffer. "Collective Lamb Shift in Single-Photon Superradiance." *Science* 328.5983 (May 2010), pp. 1248–1251. DOI: 10.1126/science.1187770.

[Röh05] Ralf Röhlsberger. *Nuclear Condensed Matter Physics with Synchrotron Radiation*. Springer Tracts in Modern Physics. Springer Berlin Heidelberg, 2005. ISBN: 9783540446996. DOI: 10.1007/b86125.

[Sah+11] B. Sahoo, K. Schlage, J. Major, U. von Hörsten, W. Keune, H. Wende, R. Röhlsberger, Amitabha Ghoshray, Bilwadal Bandyopadhyay, and Chandan Mazumdar. "Preparation and Characterization of Ultrathin Stainless Steel Films." In: *AIP Conference Proceedings*. AIP, 2011, pp. 57–60. DOI: 10.1063/1.3601785.

[Sal+08] T. Salditt, S. P. Krüger, C. Fuhse, and C. Bähtz. "High-Transmission Planar X-Ray Waveguides." *Physical Review Letters* 100.18 (May 2008), p. 184801. DOI: 10.1103/physrevlett.100.184801.

[SCS10] Anatoly A. Svidzinsky, Jun-Tao Chang, and Marlan O. Scully. "Cooperative spontaneous emission of N atoms: Many-body eigenstates, the effect of virtual Lamb shift processes, and analogy with radiation of N classical oscillators." *Physical Review A* 81.5 (May 2010), p. 053821. DOI: 10.1103/physreva.81.053821.

[Scu+06] Marlan O. Scully, Edward S. Fry, C. H. Raymond Ooi, and Krzysztof Wódkiewicz. "Directed Spontaneous Emission from an Extended Ensemble of N Atoms: Timing Is Everything." *Physical Review Letters* 96.1 (Jan. 2006), p. 010501. DOI: 10.1103/physrevlett.96.010501.

[Scu09] Marlan O. Scully. "Collective Lamb Shift in Single Photon Dicke Superradiance." *Physical Review Letters* 102.14 (Apr. 2009), p. 143601. DOI: 10.1103/physrevlett.102.143601.

[She+23] Alexandra S. Sheremet, Mihail I. Petrov, Ivan V. Iorsh, Alexander V. Poshakinskiy, and Alexander N. Poddubny. "Waveguide quantum electrodynamics: Collective radiance and photon-photon correlations." *Reviews of Modern Physics* 95.1 (Mar. 2023), p. 015002. DOI: 10.1103/revmodphys.95.015002.

[Shv99] Yuri V. Shvyd'ko. "Nuclear resonant forward scattering of x rays: Time and space picture." *Physical Review B* 59.14 (Apr. 1999), pp. 9132–9143. DOI: 10.1103/physrevb.59.9132.

[Smi+07] G. V. Smirnov, U. van Bürck, J. Arthur, G. S. Brown, A. I. Chumakov, A. Q. R. Baron, W. Petry, and S. L. Ruby. "Currents and fields reveal the propagation of nuclear polaritons through a resonant target." *Physical Review A* 76.4 (Oct. 2007), p. 043811. DOI: 10.1103/physreva.76.043811.

[Smi99] G. V. Smirnov. "General properties of nuclear resonant scattering." *Hyperfine Interactions* 123–124.1–4 (Mar. 1999), pp. 31–77. DOI: 10.1023/a:1017007520099.

[Sol+17] P. Solano, P. Barberis-Blostein, F. K. Fatemi, L. A. Orozco, and S. L. Rolston. "Super-radiance reveals infinite-range dipole interactions through a nanofiber." *Nature Communications* 8.1 (Nov. 2017). DOI: 10.1038/s41467-017-01994-3.

[SS09] Marlan O. Scully and Anatoly A. Svidzinsky. "The Super of Superradiance." *Science* 325.5947 (Sept. 2009), pp. 1510–1511. DOI: 10.1126/science.1176695.

[SS89] Yu V. Shvyd'ko and G. V. Smirnov. "Experimental study of time and frequency properties of collective nuclear excitations in a single crystal (gamma-ray resonance)." *Journal of Physics: Condensed Matter* 1.51 (Dec. 1989), pp. 10563–10584. DOI: 10.1088/0953-8984/1/51/025.

[Su+23] Dianqiang Su, Yuan Jiang, Silvia Cardenas-Lopez, Ana Asenjo-Garcia, Pablo Solano, Luis A. Orozco, and Yanting Zhao. "Dynamical beats of short pulses in waveguide QED." *Physical Review Research* 5.4 (Dec. 2023), p. l042041. DOI: 10.1103/physrevresearch.5.l042041.

5. Supplemental Material to: Collective nuclear excitation and pulse propagation in single-mode x-ray waveguides

5.1. Theory

5.1.1. Detailed derivation of the equation of motion

We derive the equations of motion from the main manuscript using the approach detailed in Ref. [ALP24]. It is based on the Gruner-Welsch quantization of the macroscopic Maxwell's equations [GW96], which expresses the electromagnetic field in terms of the classical dyadic Green's function of the medium. We use an asymptotic expansion of the Green's function in terms of its resonant (guided and leaky) and non-resonant modes, derived in Ref. [LA24], to obtain tractable, yet quantitative, analytical expressions for the coupling terms. Refer to the references given in the introductions of Refs. [ALP24; LA24] for an extensive list of related works.

The 14.4 keV resonance of the ^{57}Fe nucleus corresponds to a magnetic dipole (M1) transition between one of the ground and excited states with nuclear spins $I_g = 1/2$ and $I_e = 3/2$, respectively. For the purpose of this letter, we neglect the $2I+1$ sublevels and consider only a single ground $|g\rangle$ and a single excited state $|e\rangle$, with a magnetic transition dipole moment that is aligned with the polarization of the excitation pulse. The full picture is discussed in Ref. [ALP24]. We write the nuclear transition operator, in the rotating frame of the nuclear transition frequency, as $\hat{\sigma}_{ge} := |g\rangle\langle e|$, so that the magnetic dipole moment operator is

$$\hat{\mathbf{m}}^i = \mathbf{m}_0\big(\hat{\sigma}^i_{ge}e^{-i\omega_0 t} + \hat{\sigma}^i_{eg}e^{i\omega_0 t}\big), \tag{5.1}$$

with magnetic dipole moment $\mathbf{m}_0$ and transition energy $\hbar\omega_0$. The diagonal operators for the excited and ground states are written accordingly. Similarly, we separate the magnetic field operators into components with positive and negative frequencies, such that

$$\hat{\mathbf{B}}(t) = \hat{\mathbf{B}}^+(t)e^{-i\omega_0 t} + \hat{\mathbf{B}}^-(t)e^{i\omega_0 t}. \tag{5.2}$$

The nuclear transition operators then fulfill [ALP24]

$$\frac{\mathrm{d}}{\mathrm{d}t}\hat{\sigma}^i_{ge}(t) = -\frac{\gamma}{2}\hat{\sigma}^i_{ge}(t) - \left[\hat{\sigma}^i_{ee}(t) - \hat{\sigma}^i_{gg}(t)\right]\frac{i}{\hbar}\mathbf{m}_0^* \cdot \hat{\mathbf{B}}^+(\mathbf{r}_i, t), \tag{5.3}$$

under the rotating wave approximation. Since the pulse areas of the synchrotron pulses are tiny, even under extreme focussing, the excited state populations will be very small and negligible in (5.3). We make the approximation $\left[\hat{\sigma}^i_{ee}(t) - \hat{\sigma}^i_{gg}(t)\right] \approx -1$. Taking the expectation values on both sides yields

$$\dot{\sigma}^i_{ge}(t) = -\frac{\gamma}{2}\sigma^i_{ge}(t) + \frac{i}{\hbar}\mathbf{m}_0^* \cdot \mathbf{B}^+(\mathbf{r}_i, t). \tag{5.4}$$

The field consists of the incoming field and the field emitted by the nuclei, $\mathbf{B} = \mathbf{B}_{\text{in}} + \mathbf{B}_{\text{nuc}}$. The nuclei emit the field [ALP24]

$$\begin{aligned} \mathbf{B}^+_{\text{nuc}}(\mathbf{r}, \omega) &= \mu_0\left(\frac{\omega + \omega_0}{c}\right)^2 \sum_i \underline{\mathbf{G}}_{\text{m}}(\mathbf{r}, \mathbf{r}_i, \omega + \omega_0) \cdot (\mathbf{m}^i)^+(\omega) \\ &= \mu_0\left(\frac{\omega + \omega_0}{c}\right)^2 \sum_i \underline{\mathbf{G}}_{\text{m}}(\mathbf{r}, \mathbf{r}_i, \omega + \omega_0) \cdot \mathbf{m}_0\, \sigma^i_{ge}(\omega), \end{aligned} \tag{5.5}$$

where

$$\left\{\epsilon(\mathbf{r})\nabla \times \frac{1}{\epsilon(\mathbf{r})}\nabla \times -[n(\mathbf{r})\omega/c]^2\right\}\underline{\mathbf{G}}_{\text{m}}(\mathbf{r}, \mathbf{r}') = \epsilon(\mathbf{r})\delta(\mathbf{r} - \mathbf{r}')\underline{\mathbf{1}} \tag{5.6}$$

defines the magnetic Green's function. Here ϵ is the relative electric permeability and n the refractive index of the layer system, excluding the nuclear interaction. Inserting (5.5) into the Fourier transform of (5.4), we obtain

$$-i\omega\sigma^i_{ge}(\omega) = -\frac{\gamma}{2}\sigma^i_{ge}(\omega) + i\Omega(\mathbf{r}_i, \omega) + i\sum_{j\neq i} g_{ij}(\omega + \omega_0)\sigma^j_{ge}(\omega), \tag{5.7}$$

where $\Omega(\mathbf{r}, \omega) = \mathbf{m}_0^* \cdot \mathbf{B}^+_{\text{in}}(\vec{r}, \omega)/\hbar$ is the time-dependent Rabi frequency produced by our propagating excitation pulse and coupling between the nuclei is mediated by

$$g_{ij}(\omega) = \frac{\mu_0\omega^2}{\hbar c^2}\,\mathbf{m}_0^* \cdot \underline{\mathbf{G}}_{\text{m}}(\mathbf{r}_i, \mathbf{r}_j, \omega) \cdot \mathbf{m}_0. \tag{5.8}$$

The waveguide contains a large number of nuclei that are homogeneously distributed in an amorphous thin layer at height $z = z_0$. Let d denote the layer thickness and ρ the nuclear number density within the layer. Going to continuous variables and integrating out the transversal dimensions y and z, we obtain

$$- i\omega\sigma_{ge}(x,\omega) = -\frac{\gamma}{2}\sigma_{ge}(x,\omega) + i\Omega(x,z_0,\omega) + i\rho d\,\text{P.V.}\int g(x-x',\omega+\omega_0)\sigma_{ge}(x',\omega)\,\mathrm{d}x', \quad (5.9)$$

with

$$g(x-x',\omega) = \frac{\mu_0\omega^2}{\hbar c^2}\,\mathbf{m}_0^* \cdot \underline{\mathbf{G}}_{\mathrm{m,2d}}(x-x',z_0,z_0,\omega)\cdot \mathbf{m}_0. \quad (5.10)$$

where $\underline{\mathbf{G}}_{\mathrm{m,2d}}$ is the Green's function corresponding to a line source extended along y (see Ref. [LA24] for a detailed discussion). For x-ray waveguides, it is approximately transversal and can be expanded into its resonant and non-resonant modes, giving

$$\underline{\mathbf{G}}_{\mathrm{m,2d}}(x-x',z,z',\omega) \approx \underline{\mathbf{1}}_{\perp}\frac{i}{\omega/c}\sum_m \frac{u_m(z)u_m(z')}{2\nu_m}e^{i\omega|x-x'|\nu_m/c} + \text{non-resonant}, \quad (5.11)$$

where ν_m are the (complex) effective refractive indices of the corresponding resosonant modes (in short: mode indices), $\underline{\mathbf{1}}_{\perp} = \hat{\mathbf{y}}\otimes\hat{\mathbf{y}} + \hat{\mathbf{z}}\otimes\hat{\mathbf{z}}$ the transversal unit tensor, and $u_m(z)$ are transversal mode profiles as defined in Ref. [LA24]. They are bi-normalized according to

$$\int \frac{[u_m(z)]^2}{\epsilon(z)}\,\mathrm{d}z = 1. \quad (5.12)$$

The expansion (5.11) in particular uses the fact that transverse magnetic and transverse electric modes are approximately degenerate in the hard x-ray regime due to the small refractive index contrasts, so that the polarization-dependence simplifies to the transversal unit tensor.

We make the crucial approximation to neglect the non-resonant modes, since they are strongly attenuated, and obtain

$$- i\omega\sigma_{ge}(x,\omega) = -\frac{\gamma}{2}\sigma_{ge}(x,\omega) + i\Omega(x,\omega) - \frac{\mu_0|\mathbf{m}_0|^2\rho}{2\hbar}\frac{\omega+\omega_0}{c}\sum_m \zeta_m \int_{-L}^{0}\mathrm{d}x'\, e^{i(\omega+\omega_0)|x-x'|\nu_m/c}\sigma_{ge}(x',\omega). \quad (5.13)$$

Since $\omega \ll \omega_0$, we neglect the frequency detuning in the prefactor. Fourier-transforming (5.13) finally yields

$$\dot{\sigma}_{ge}(x,t) = -\frac{\gamma}{2}\sigma_{ge}(x,t) + i\Omega(x,t) - \frac{\gamma}{4\Lambda_{\mathrm{res}}}\sum_m \zeta_m \int_{-L}^{0} \mathrm{d}x'\, e^{ik_0\nu_m|x-x'|}\sigma_{ge}(x', t-|x-x'|\nu_m/c), \quad (5.14)$$

where $k_0 = \omega_0/c$ and

$$\frac{1}{\Lambda_{\mathrm{res}}} = \rho\frac{k_0\mu_0|\mathbf{m}_0|^2}{\hbar}\frac{2}{\gamma} \equiv \rho\sigma_{\mathrm{res}} \quad (5.15)$$

is the reciprocal on-resonance attenuation length.

Making the forward-scattering approximation and assuming that only a single mode contributes gives

$$\dot{\sigma}_{ge}(x,t) = -\frac{\gamma}{2}\sigma_{ge}(x,t) + i\Omega(x,t) - \frac{\gamma\zeta_m}{4\Lambda_{\mathrm{res}}}\int_{-L}^{x} \mathrm{d}x'\, e^{ik_0\nu_m(x-x')}\sigma_{ge}\left(x', t-\nu_m\frac{x-x'}{c}\right). \quad (5.16)$$

5.1.2. Frequency shift and superradiant speedup

The resonant-beam-coupling geometry permits an analytical solution of (5.16), which we briefly discuss here. The incidence angle θ_{in} fixes the in-plane wavenumber to $k_{\mathrm{in}} = k_0\cos\theta_{\mathrm{in}}$. The excitation pulse can be written as $\Omega(x,t) = \Omega_0\exp(ik_{\mathrm{in}}x)\Pi(t_{\mathrm{ret}})$, with $t_{\mathrm{ret}} = t - k_{\mathrm{in}}x/\omega_0$. Note that such an excitation pulse is made possible by the RBC geometry, where the incident plane wave is propagating in air/vacuum and therefore not attenuated. Other geometries will unavoidably introduce an off-resonant attenuation due to material absorption.

Taking the Fourier transform gives

$$\Omega(x,\omega) = \Omega_0 e^{i\tilde{k}_{\mathrm{in}}x}\Pi(\omega), \quad (5.17)$$

with $\tilde{k}_{\mathrm{in}} = (\omega+\omega_0)/c\cdot\cos\theta_{\mathrm{in}}$ Fourier-transforming (5.16) and inserting (5.17), we obtain

$$-i(\omega + i\gamma/2)\sigma_{ge}(x,\omega) + \frac{\gamma\zeta_m}{4\Lambda_{\mathrm{res}}}\int_{-L}^{x}\mathrm{d}x'\, e^{i\tilde{k}_m(x-x')}\sigma_{ge}(x',\omega) = i\Omega_0\Pi(\omega)e^{i\tilde{k}_{\mathrm{in}}x}, \quad (5.18)$$

with $\tilde{k}_m = \nu_m(\omega+\omega_0)/c$.

The key to solve (5.18) is that, for $L \to \infty$, the right-hand side is an eigenfunction of the integral operator on the left-hand side. One readily obtains

$$\sigma_{ge}(x,\omega) = \frac{-\Omega_0 \Pi(\omega)}{\omega + i\gamma/2 - \tilde{\eta}(\omega)} \exp\big(i\tilde{k}_{\text{in}} x\big) \tag{5.19}$$

where

$$\tilde{\eta}(\omega) = \frac{\zeta_m \gamma}{4\Lambda_{\text{res}}} \frac{1}{(\omega_0 + \omega)/c} \frac{-1}{\nu_m - \cos\theta_{\text{in}}} \tag{5.20}$$

is the complex frequency shift. Since $\omega \ll \omega_0$, we can neglect the frequency-dependency, setting $\eta := \tilde{\eta}(\omega = 0)$. We write

$$\eta = \frac{\gamma}{2} \frac{\zeta_m \Lambda_m}{\Lambda_{\text{res}}} \frac{1}{2\Lambda_m q_\theta - i} \tag{5.21}$$

with $q_\theta = k_0(\cos\theta_{\text{in}} - \text{Re}\{\nu_m\})$. Fourier-transforming the solution gives

$$\begin{aligned} \sigma_{ge}(x,t) &= \int \frac{\mathrm{d}\omega}{2\pi} e^{-i\omega t} \sigma(x,\omega) \\ &= i\Omega_0 \Pi(\delta - i\gamma/2) \Theta(t_{\text{ret}}) \exp[ik_{\text{in}} x - (\gamma/2 - i\eta) t_{\text{ret}}]. \end{aligned} \tag{5.22}$$

Finally, we approximate $\Omega_0 \Pi(\eta - i\gamma/2) \approx A$ to be the pulse area, taking into account that the frequency detuning is small compared to the bandwidth of the excitation pulse.

5.1.3. The emitted field

To compute the field emitted by the nuclei, we use (5.5) and apply the same assumptions as before, in particular the asymptotic expansion of the Green's function. We obtain

$$\begin{aligned} \mathbf{B}^{+}_{\text{nuc}}(x,z,\omega) &= \mu_0 \rho d \Big(\frac{\omega + \omega_0}{c}\Big)^2 \int \underline{\mathbf{G}}_{\text{m,2d}}(x - x', z, z_0, \omega + \omega_0) \cdot \mathbf{m}_0 \, \sigma_{ge}(x',\omega) \, \mathrm{d}x' \\ &\approx ik\mu_0 \rho d \frac{u_m(z) u_m(z_0)}{2\nu_m} \mathbf{m}_0 \int_{-L}^{0} e^{i\tilde{k}_m |x - x'|} \sigma_{ge}(x',\omega) \, \mathrm{d}x' . \end{aligned} \tag{5.23}$$

The constant factor can be brought into a more expressive form, so that

$$\mathbf{B}^{+}_{\text{nuc}}(x,z,\omega) = -\mathbf{B}^{+}_0 \zeta_m \frac{u_m(z)}{u_m(z_0)} \frac{\gamma\tau}{4\Lambda_{\text{res}}} \frac{1}{iA} \int_{-L}^{0} e^{i\tilde{k}_m |x - x'|} \sigma_{ge}(x',\omega) \, \mathrm{d}x' , \tag{5.24}$$

where $\tau = \Pi(\omega = 0)$ is the length of the excitation pulse and the field amplitude is $\mathbf{B}_0^+ = \mathbf{m}_0 \Omega_0 \hbar / |\mathbf{m}_0|^2$. To compute the field inside the sample, we can again employ the forward scattering approximation or integrate (5.24) numerically. In the experiment, we measure the far-field pattern of the field at the back end of the waveguide ($x = 0$).

The integral can be readily evaluated analytically for the two cases discussed in the letter. For the FC geometry we obtain

$$\mathbf{B}_{\mathrm{nuc}}^+(0, z, t) = -\mathbf{B}_0^+ \frac{u_m(z)}{u_m(z_0)} \frac{\gamma\tau}{4} \left[\frac{\zeta_m L}{\Lambda_{\mathrm{res}}} \exp(i k_0 \nu_m L) \right] \exp(-\gamma t_{\mathrm{ret}}/2) \frac{2 J_1\left(\sqrt{\gamma t_{\mathrm{ret}} \zeta_m L / \Lambda_{\mathrm{res}}}\right)}{\sqrt{\gamma t_{\mathrm{ret}} \zeta_m L / \Lambda_{\mathrm{res}}}}. \tag{5.25}$$

For the RBC geometry, we obtain

$$\mathbf{B}_{\mathrm{nuc}}^+(0, z, t) = -\mathbf{B}_0^+ \frac{u_m(z)}{u_m(z_0)} \frac{\gamma\tau}{4} \left[\frac{2\zeta_m \Lambda_m}{\Lambda_{\mathrm{res}}} \frac{-i}{2 q_\theta \Lambda_m - i} \right] \exp\left[-(\gamma/2 - i\eta) t_{\mathrm{ret}}\right], \tag{5.26}$$

retaining the frequency shift and superradiant decay. Here, the overall intensity decreases when the θ_{in} is detuned from the mode resonance due to the wavelength mismatch.

5.2. Samples and experiment

5.2.1. Layer design

The waveguides were designed using the xwglib software described in Ref. [LA24]. The materials were chosen for minimal mode absorption while being suitable for sputter deposition. The cladding thickness was set to 30 nm, which is thick enough to fully contain the resonant modes (effectively infinite) but still relatively thin to minimize roughness build-up. Table 5.1 lists the model parameters computed for the two final layer designs, assuming perfectly sharp interfaces.

5.2.2. Sample preparation

The two samples were fabricated by magnetron sputter deposition, using an argon plasma at a pressure of 5×10^{-3} mbar at a target-to-substrate distance of about 7 cm with sputtering guns from the A300-XP series (AJA International, Massachusetts, USA). The residual base pressure prior to deposition was typically less than 4×10^{-7} mbar. Molybdenum and the ^{57}Fe-isotope-enriched iron (97 % enrichment) were deposited using targets with diameter 3.81 cm at 12 W DC, and B_4C using a target with diameter 5.08 cm at 53 W RF power. The deposition rates were calibrated based on x-ray reflectivity measurements.

m	ζ_m (10^{-2})	$1 - \mathrm{Re}\{\nu_m\}$	$\mathrm{Im}\{\nu_m\}$	Λ_m (mm)
FC				
1	3.8	3.8×10^{-6}	2.8×10^{-8}	0.25
2	0	6.8×10^{-6}	6.8×10^{-8}	0.11
RBC				
1	2.1	2.9×10^{-6}	1.3×10^{-8}	0.51
2	0	3.9×10^{-6}	2.2×10^{-8}	0.31
3	2.3	5.9×10^{-6}	7.5×10^{-8}	0.09
4	0	8.2×10^{-6}	1.6×10^{-7}	0.04

Table 5.1.: Model parameters for the resonant modes m of the two waveguide designs: coupling coefficient ζ_m, effective mode index ν_m, and (off-resonance) mode attenuation length Λ_m for the supported resonant modes.

To block the overilluminating part of the x-ray focus in the FC experiment, we bonded a second 1 mm-thick germanium wafer on top of the layer structure, as detailed in Ref. [Krü+12]. Figure 5.1(a,b) show photographs of the final FC sample after bonding and cutting it to shape. To verify the layer structure of the FC sample, we acquired high-resolution cross-sectional SEM images. To that end, the layer structure was exposed with a Helios G4 focussed ion beam system (Thermo Fisher Scientific, Massachusetts, USA). The SEM images were acquired with an eLiNE system (Raith GmbH, Germany). Panels (c) and (d) show such images at different magnification. At highest magnification, the individual films are clearly distinguishable.

5.2.3. Experimental setup

Figure 5.2 shows the setups of the two experiments performed at P01. The undulator radiation is monochromatized to about 1 meV by a high-resolution monochromator (HRM). In the front-coupling experiment, the beam was focussed by two mirrors in Kirkpatrick Baez geometry to about 7 µm in focus diameter. A pair of slits was used to cut off the outer tails of the focus that were not blocked by the 2 mm thick waveguide assembly. A stack of four avalanche photo diodes (APDs), mounted on a translation stage, approximately 1 m downstream of the waveguide was used to detect the photons exiting the waveguide. In the resonant-beam-coupling experiment, the beam was mildly focussed by a beryllium compound refractive lens (CRL) down to about 100 µm diameter. The CRL stack was placed immediately after the monochromator to maximize the focal distance and minimize angular divergence of the beam, which was about 0.002°. The beam was cut in vertical direction to about 20 µm using a slit placed immediately in front of the sample. The angular acceptance of the APDs

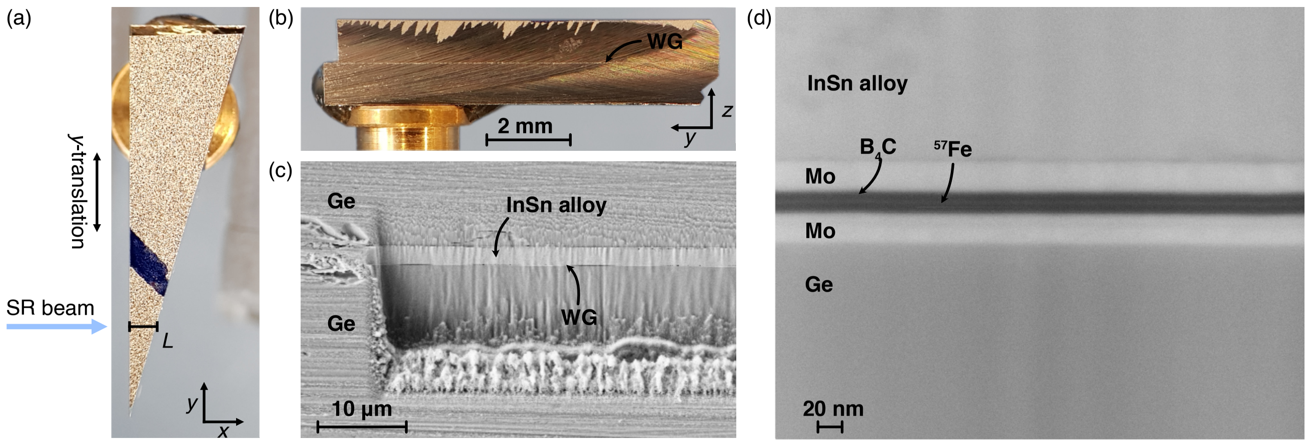

Figure 5.1.: The FC waveguide assembly: (a) top view, showing the sample along the y-direction to change the propagation length L of the x-rays in the WG; (b) Front-view; (c) the two wafers were bonded with an InSn alloy, visible as a horizontal stripe at medium magnification; (d) high-resolution view of the layer structure.

was adjusted with a pair of slits mounted in front of the APDs. In both experiments, a time-insensitive pixel detector, a LAMBDA 750k (X-Spectrum GmbH, Hamburg, Germany) with 55 μm pixel size, was placed about 3 m downstream of the sample to measure the off-resonant (prompt) photons exiting the waveguide.

Figure 5.3 shows far-field diffraction patterns, acquired with the LAMBDA 750k pixel detector in front-coupling geometry. Panels (a) and (b) illustrate how the primary beam is absorbed by the waveguide so that only the coherent guided mode is transmitted. The one-dimensional far-field pattern (c) is consistent with a fully transversally (in the vertical direction) coherent Gaussian mode with FWHM 19.8 nm at the end of the waveguide, as discussed in Ref. [OS11].

5.3. Data analysis

5.3.1. Approach

The theory presented in the Letter captures the central features of the exciton dynamics and spontaneous photon emission and illustrates the qualitative behaviour. To obtain analytical solutions, we neglected the energetic sublevels of the nuclei, which will be slightly perturbed in the presence of hyperfine interactions. Even very weak hyperfine interactions affect the observable time-dependence and need to be taken into account in the analysis. In principle, the theory can be readily extended to include the full hyperfine structure of the nuclei and then solved numerically [ALP24].

However, our theory shows that the time-dependence of the emitted fields is formally equivalent to that known from established experimental geometries. In FC geometry, if only a single guided mode contributes, the time-dependence resembles NFS through a foil with rescaled thickness. In RBC geometry, the time-dependence is the same for the emission into the mode and into the direction of specular reflection—the well-known grazing incidence reflection geometry [Röh99]. This allows us to use available and tested software for simulation and data analysis of nuclear resonant scattering to model the experimentally observed temporal emissions. We emphasize that only the time-dependence is equivalent, whereas the spatial emission structure is clearly different.

Hyperfine parameters

The iron films in the samples are too thin to develop magnetic order so that we can neglect magnetic hyperfine splitting. However, variations in the electric field at the positions of the nuclei may cause inhomogeneous line broadening. An electric field gradient couples with the non-vanishing quadrupole moment of the excited state and may cause a splitting into two lines. Since the thin iron layer is likely amorphous,

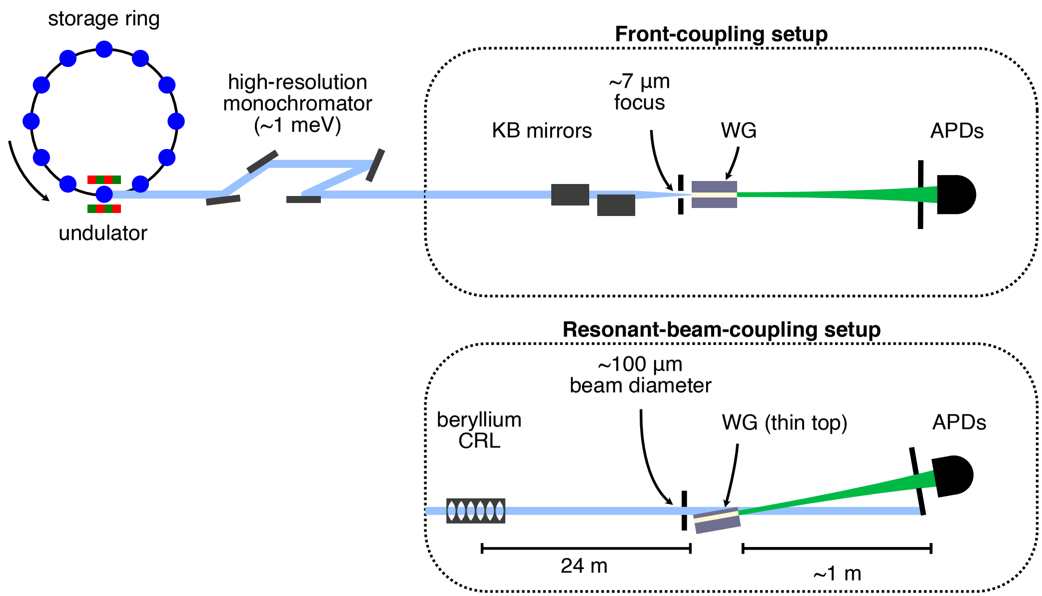

Figure 5.2.: Experimental setups at the high resolution dynamics beamline P01 for realization of the front-coupling and the grazing-incidence geometries. Only the relevant components are sketched. In both experiments, a time-insensitive pixel detector was mounted 3 m downstream of the WG (not shown). The APDs were moved out of the beam to acquire images with the pixel detector.

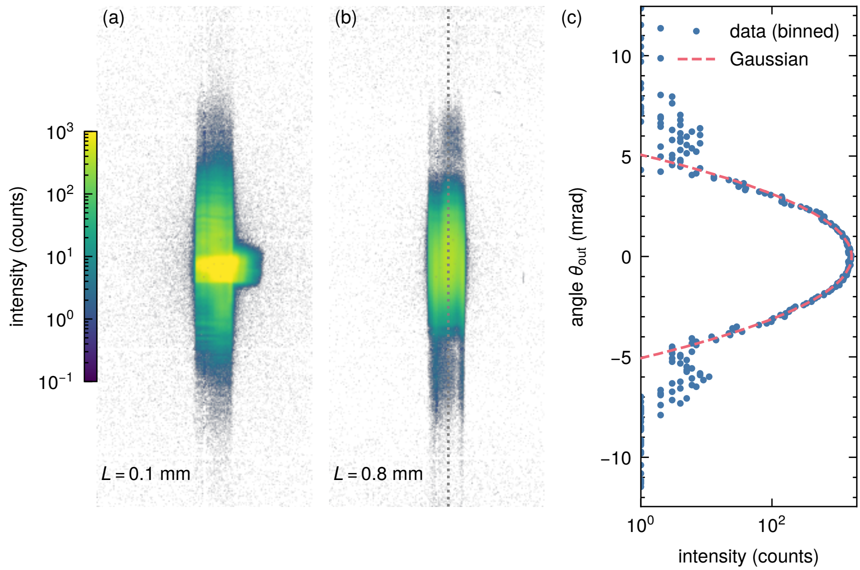

Figure 5.3.: Off-resonant far-field diffraction patterns in the front-coupling geometry, acquired with time-insensitive pixel detector. (a,b) diffraction pattern for waveguide lengths $L = 0.1$ mm and 0.8 mm, respectively. The primary beam is fully absorbed for the longer waveguide (b) but still visible in the shorter one (a). (c) Vertical profile [dotted line in (c)] through the diffraction pattern in logarithmic scale with a Gaussian fit that corresponds to a fully vertically coherent exit beam with FWHM 19.8 nm.

there is no overall directional dependence and we can take the isotropic average. We assumed a normal distribution for the line broadening, parameterized by its full width at half maximum w_{HF}. The quadrupole splitting is parameterized by the distance between the split lines s_{HF}.

Data regression approach

We used the Nexus [Boc23] library to implement the forward model for the delayed intensity $f(t, \vec{p})$ and inferred the model parameters $\vec{p}$ by numerically finding the maximum likelihood estimator (MLE), given the data (histogram of counts over time delay) and assuming Poisson statistics.

The log-likelihood for Poisson-distributed data $\vec{t} = (t_1, \dots, t_N)$ and $\vec{y} = (y_1, \dots, y_N)$ can be written as

$$l(\vec{p}) = -\sum_j \left[f(t_j, \vec{p}) - y_j \cdot \log f(t_j, \vec{p}) \right], \tag{5.27}$$

where here y_j denote the number of counts in bin corresponding to time t_j. We computed the MLE by numerically optimizing (5.27), $\vec{p}_{\mathrm{MLE}} = \mathrm{argmax}_{\vec{p}\in\mathcal{D}} \{-l(\vec{p})\}$ within a reasonable domain $\mathcal{D}$.

5.3.2. Front coupling

We modeled the FC waveguide as a thick slab/foil of ^{57}Fe (isotopically enriched to 95 %, density 7.874 g cm^{-3}) in a nuclear forward scattering geometry. The density and abundance are only relevant to relate the optical thickness ξ to the geometrical thickness d of the slab—they do not enter the model. With no magnetic hyperfine splitting and isotropically averaged hyperfine interactions, we optimized for the following 4 free parameters: intensity scale I_0, optical thickness ξ, line broadening FWHM w_{HF}, and quadrupole splitting s_{HF}. This was done for each each waveguide length independently. The results are listed in Tab. 5.2.

Parameter	FC	RBC
Broadening FWHM w_{HF} (γ)	6(2)	4
Quad. splitting s_{HF} (γ)	6(1)	7

Table 5.2.: Hyperfine parameters inferred from the experimental data, assuming normally distributed broadening and quadrupole splitting of the transition lines. For FC, the parameters were extracted from each WG length independently. The number in parentheses gives the standard deviation. For RBC, the parameters were extracted from a single measurement in reflection geometry at $\theta_{\mathrm{in}} = \theta_{\mathrm{out}} = 0.5°$.

5.3.3. Resonant beam coupling

Extraction of initial decay rate

To extract the initial speedup of the emissions in RBC geometry, we assumed a simple exponential decay $f(t, \vec{p}) = p_0 \exp(-p_1\gamma t)$ and inferred the optimal parameters (scale p_0 and speedup p_1) by numerically computing the MLE based on the data in the time interval 13 ns $\leq t \leq$ 30 ns.

Estimation of hyperfine parameters

To estimate the hyperfine parameters (w_{HF} and s_{HF}) of the RBC waveguide, we measured the delayed photons in reflection geometry at $\theta_{\mathrm{in}} = \theta_{\mathrm{out}} = 0.5°$. This angle is far from the waveguide resonances to ensure that the time-dependence (up to a global scaling) is to a good approximation unaffected by the waveguide structure, yet still sensitive to the hyperfine interactions.

We modeled the experiment numerically, using ideal geometrical parameters (design layer thicknesses and densities, perfectly sharp interfaces). Similar to the FC geometry, we optimized for the following 3 free parameters: intensity scale I_0, line broadening FWHM w_{HF}, and quadrupole splitting s_{HF}. The results are also listed in Tab. 5.2.

Full simulation of speedup

To explain the values of the speedup in the RBC geometry, we simulated the emission from the layer system as a function of time in reflection geometry, $\theta_{\mathrm{out}} = \theta_{\mathrm{in}}$. To that end, we exploit that the time-dependence is the same for the emissions out of the back end of the WG and for the field that evanescently couples through the top cladding and is emitted into the direction of specular reflection. We used Nexus [Boc23] to simulate the time-dependent field in reflection geometry, assuming an infinitely extended layer system. Note, however, that the angular dependence is different between the two geometries, so that the simulated intensity scale is meaningless. The results, without hyperfine interactions, with hyperfine interactions (extracted from independent data as detailed above), and including a uniform angular divergence of 2.1 mdeg (FWHM),

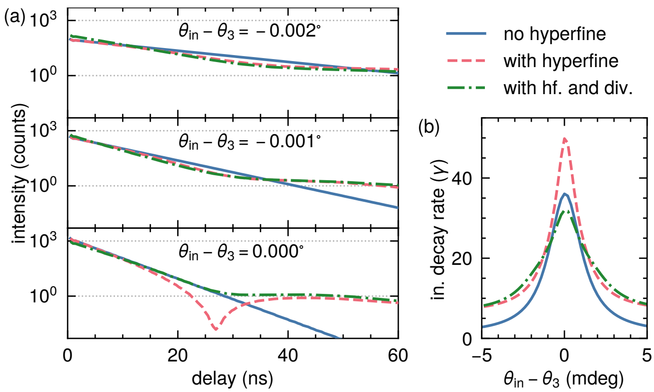

Figure 5.4.: Simulated emission in reflection geometry ($\theta_{\mathrm{in}} = \theta_{\mathrm{out}}$) to describe the time-dependence in RBC excitation. (a) Time-dependence and (b) speedup. Without hyperfine splitting (blue), the simulation is in perfect agreement (up to global scaling) with the predictions of the simple theory. The additional beating due to the hyperfine interactions (red) results in increased (apparent) speedup. Close to resonance, this effect is partially reversed by the angular divergence of 2.1 mdeg FWHM (green), which is assumed to be uniform and incoherent.

are presented in Fig. 5.4(a). The angular divergence is modeled as an incoherent average with uniformly distributed angles (arithmetic mean).

From these simulated curves, we extracted the initial decay rate, using the same procedure as for the experimental data. The results are shown and discussed in Fig. 5.4(b). The simulation without hyperfine splitting, on the one hand, accurately matches the simple single-mode model. The full simulation including hyperfine splitting and divergence, on the other hand, explains the experimental data (see main text). We conclude that the deviation from the simple model is indeed mainly caused by residual hyperfine splitting and beam divergence.

References

[ALP24] Petar Andrejić, Leon Merten Lohse, and Adriana Pálffy. "Waveguide QED with Mössbauer nuclei." *Physical Review A* 109.6 (June 2024), p. 063702. DOI: 10.1103/physreva.109.063702.

[Boc23] Lars Bocklage. *Nexus - Nuclear Elastic X-ray scattering Universal Software*. en. 2023. DOI: 10.5281/ZENODO.10074447.

[GW96] T. Gruner and D.-G. Welsch. "Green-function approach to the radiation-field quantization for homogeneous and inhomogeneous Kramers-Kronig dielectrics." *Physical Review A* 53.3 (Mar. 1996), pp. 1818–1829. DOI: 10.1103/physreva.53.1818.

[Krü+12] S. P. Krüger, H. Neubauer, M. Bartels, S. Kalbfleisch, K. Giewekemeyer, P. J. Wilbrandt, M. Sprung, and T. Salditt. "Sub-10nm beam confinement by X-ray waveguides: design, fabrication and characterization of optical properties." *Journal of Synchrotron Radiation* 19.2 (Jan. 2012), pp. 227–236. DOI: 10.1107/s0909049511051983.

[LA24] Leon M. Lohse and Petar Andrejić. "Nano-optical theory of planar x-ray waveguides." *Optics Express* 32.6 (Mar. 2024), p. 9518. DOI: 10.1364/oe.504206.

[OS11] Markus Osterhoff and Tim Salditt. "Coherence filtering of x-ray waveguides: analytical and numerical approach." *New Journal of Physics* 13.10 (Oct. 2011), p. 103026. DOI: 10.1088/1367-2630/13/10/103026.

[Röh99] R. Röhlsberger. "Theory of X-ray grazing incidence reflection in the presence of nuclear resonance excitation." *Hyperfine Interactions* 123–124.1–4 (Mar. 1999), pp. 301–325. DOI: 10.1023/a:1017063605078.

6. Interferometric measurement of nuclear resonant phase shift with a nanoscale Young double waveguide

This chapter is recompiled[1] under the terms of the *Creative Commons BY 4.0* license from the preprint:
Leon M. Lohse, Ankita Negi, Markus Osterhoff, Paul Meyer, Sergey Yaroslavtsev, Aleksandr I. Chumakov, Lars Bocklage, Ralf Röhlsberger, and Tim Salditt. *Interferometric measurement of nuclear resonant phase shift with a nanoscale Young double waveguide*. 2025. DOI: 10.48550/ARXIV.2506.05823

Author Contributions
LML conceived of the experiment. LML authored the proposals for the synchrotron experiment with help from TS and RR. LML, PM, MO, SY, AC, RR, and TS planned the experiment. LML, MO, PM, and LB tested and integrated the detection system. LML fabricated the samples. LML, AN, TS, LB, and SY performed the experiment. LML analyzed the data with help from AN and SY. LML wrote the manuscript with input from the other authors. All authors discussed the results and contributed to the final manuscript.

Abstract
The phase shift of an electromagnetic wave, imprinted by its interaction with atomic scatterers, is a central quantity in optics and photonics. In particular, it encodes information about optical resonances and photon-matter interaction. While being a routine task in the optical regime, interferometric measurements of phase shifts in the x-ray frequency regime are notoriously challenging due to the short wavelengths and associated stability requirements. As a result, the methods demonstrated to date are unsuitable for nanoscopic systems. Here, we demonstrate a nanoscale interferometer, inspired by Young's double-slit experiment, to measure the dispersive phase shift due to the 14.4 keV nuclear resonance of the Mössbauer isotope ^{57}Fe coupled to an x-ray waveguide. From the single-photon interference patterns, we precisely extract the

[1]Subject to slight adjustments of the notation and minor corrections.

phase shifts in the vicinity of the nuclear resonance resolved in photon energy by using Bayesian inference. We find that the combined information from phase shift and absorbance reveals microscopic coupling parameters, which are not accessible from the intensity data alone. The demonstrated principle lays a basis for integrated x-ray interferometric sensors.

6.1. Introduction

The phase of an electromagnetic wave is shifted upon scattering from an atom, a microscopic effect which adds up coherently and determines the macroscopic properties of wave propagation, as described by the index of refraction n. Near atomic transitions, resonant effects become particularly pronounced and a wealth of information about the photon-atom interactions and the involved atomic energy levels is encoded in the optical response. Both for the resonant and non-resonant case, wave propagation phenomena are relevant for nearly all methods for the manipulation of light. Examples are plenty: from passive shaping with lenses and phase plates, guiding of light in fiber optics and waveguides, all the way to the precise active control, for example in liquid crystal displays, electro-optical modulators, and integrated photonic devices. These optical properties and functionalities crucially rely on precisely known and controllable phase shifts. At the same time, when a wave propagates through an object with a spatially dependent index of refraction $n(\mathbf{r})$, the local variations in the accumulated phase shifts reflect its internal structure, offering a contrast mechanism for phase-sensitive imaging. Note that phase contrast can not only be significantly more prominent than attenuation contrast [HS19], for example in X-ray imaging of biological matter, but also more dose-efficient [Spi+23], because the underlying elastic scattering process does not deposit any energy in the specimen.

Guided modes offer a particular benefit to control light propagation and phase effects. In optical waveguides, photons can be coupled to individual quantum emitters such as resonant atoms, in a controllable manner. This is exploited in the emerging field of waveguide quantum electrodynamics in order to investigate quantum many-body physics and to develop integrated functional quantum technologies, see [Tür+19; She+23] for a review. The resulting quantum-optical systems are often non-linear [Tür+19], and can become increasingly complex so that refractive index models are no longer valid. Yet the phase shift imposed by individual emitters remains a central quantity, which can even become a function of the number of photons [Sta+24]. Further, the phase shift can be manipulated, for example, in quantum phase switches with single atoms [Tie+14; Vol+14], a building block that may pave the way to photon-photon quantum gates. To observe any of this experimentally, one crucially relies on methods for precise and accurate measurements of phase shifts.

In the optical regime, instruments such as the Mach-Zehnder interferometer are readily available to measure phase shifts. They can be assembled on optical tables from discrete components, but are also routinely realized in integrated photonic devices. In the x-ray regime on the other hand, the situation is quite different, because the short wavelengths require extreme stability and translation precision in the order of picometers. Bonse and Hart realized the first interferometer for hard x-rays [BH65], a Mach-Zehnder-type setup, achieving the necessary stability by cutting the entire interferometer from one solid single crystal. This principle based on crystal reflections [Col96; Bow96; Lid14] has enabled the design of interferometers that have been used to measure refractive indices and dispersion corrections to the atomic form factors close to absorption edges [BH69; Tem+80]. In most cases, however, refractive indices in the hard x-ray regime are obtained indirectly from absorption spectra based on Kramers-Kronig relation [HGD93; Len94], a method which relies on precisely measured absorption spectra over a wide frequency range. Unfortunately, neither bulky crystal interferometers nor any of the other methods [Len94] are suitable to measure phase shifts at the nanometer scale.

This limitation is particularly regrettable, since x-ray photon-matter interaction within nanostructures exhibits many interesting phenomena [Shi+24]. These include x-ray generation in nanostructures [VS21], Purcell-enhanced x-ray scintillation, and enhanced interaction in waveguide-cavities [LKE24]. Nanometer-sized x-ray waveguides have been realized for double-waveguide phase-contrast imaging [FOS06], curved x-ray waveguides [Sal+15], and integrated x-ray beam splitters [HS16], representing first steps towards “x-ray optics on a chip”. Recently, ensembles of Mössbauer nuclei coupled to an x-ray waveguide were experimentally investigated with synchrotron radiation, demonstrating a platform for waveguide quantum electrodynamics in the hard x-ray regime [ALP24; Loh+24]. Such Mössbauer isotopes constitute exceptionally clean quantum systems due to their extremely narrow resonances [RE21], making them a particularly successful experimental platform for quantum-optics in the hard x-ray frequency regime [Röh+10; Hee+21; Kha+21; Boc+21; Shv+23; Vel+24]. Despite the tremendous importance of the phase shift in these examples, however, it has been elusive to direct measurement.

In this work, we interferometrically measure the phase shift that an ultrathin layer of ^{57}Fe Mössbauer nuclei coherently imprints onto photons propagating through a single-mode x-ray waveguide. To that end, we have devised a nanoscale double-waveguide interferometer, reminiscent of Young’s celebrated double-slit experiment [You02]. It coherently superimposes the exit fields of the signal waveguide (SWG) and a reference waveguide (RWG) which is free of resonant nuclei, and directly converts the resonant phase shift in the SWG into a measurable lateral shift of the far-field interference pattern (see Fig. 6.1**b**). This allows to extract the nuclear phase shift from just a small number of detected photons. The isotope ^{57}Fe has a low-lying nuclear resonance at $\hbar\omega_0 = 14.41\,\mathrm{keV}$ with a linewidth of only $\hbar\Gamma = 4.7\,\mathrm{neV}$ (Fig. 6.1**a**). While several methods to measure the phase shift induced by macroscopic samples

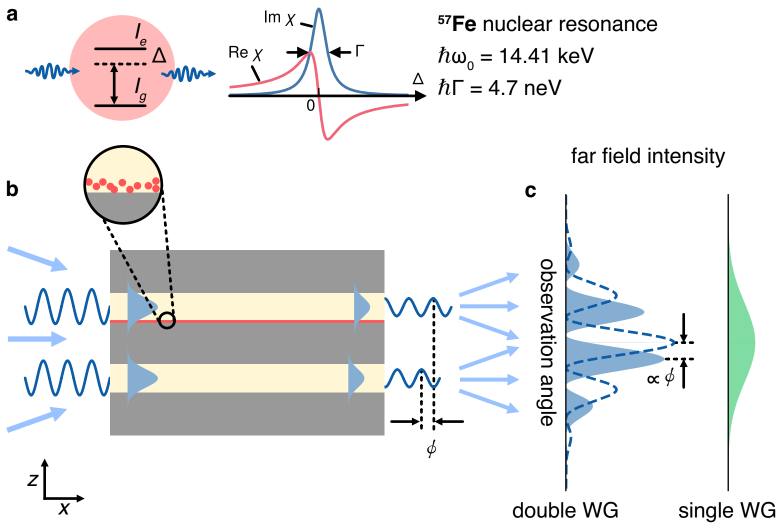

Figure 6.1.: Principle of the double-waveguide interferometer. a A resonant atom (here, the nuclear resonance of ^{57}Fe between states with nuclear spin $I_g = 1/2$ and $I_e = 3/2$) causes a phase shift depending on the detuning $\Delta = \omega - \omega_0$ of the light frequency ω to the resonance ω_0. This is described by the real part of the complex susceptibility χ. **b** An ensemble of resonant atoms (red) in a nanoscopic waveguide coherently shifts the phase of photons propagating through this "signal waveguide" (SWG) compared to a reference waveguide (RWG) without the atoms. **c** The phase shift results in a shift of the far-field double-slit interference pattern (filled blue curve) of the two exit waves compared to the unshifted pattern (dashed line). Blocking the reference waveguide results in a single-slit diffraction pattern (green filled curve) that is unaffected by the phase shift.

containing resonant nuclei have been proposed [Stu01] and demonstrated [SLT04; Cal+05; Hee+15; Goe+19; WE23; Yua+25; Neg+25], they are all indirect methods that rely on computational reconstruction of the spectral phase shift from measured time-domain response functions, which requires a large number of detected photons. To that end, the sample and a resonant reference absorber are usually illuminated with short broad-band pulses and temporal interference patterns are recorded. By contrast, here we directly measure the spectral phase shift $\phi(\Delta)$ resolved in detuning from the resonance $\Delta = \omega - \omega_0$ using monochromatic narrowband illumination by coherently interfering individual photons. The measured phase shifts unambigously reveal the value of hyperfine broadening and the coupling strength between the nuclei and photons propagating in the waveguide, beyond the information that is accessible from absorption measurements alone.

6.2. Results

To implement the nano-interferometer, we have fabricated a pair of 0.5 mm long planar x-ray waveguides, stacked on top of each other, one of which (the signal waveguide) contains a 0.6 nm-thin film (about two atomic layers) of isotope-enriched ^{57}Fe (see Fig. 6.1). The waveguides consist of a 20 nm-thick boron carbide (B_4C) guiding core surrounded by 30 nm of molybdenum cladding, resulting in the interferometer baseline of 50 nm. The design ensures that only a single guided mode of the electromagnetic field is transmitted by each waveguide. The waveguides are enclosed in 1 mm thick germanium wafers to block the tails of the illuminating focus [Krü+12]. In addition, as control experiments, we have prepared a double-waveguide without the resonant nuclei, as well as a single waveguide containing resonant nuclei. The latter conceptually corresponds to blocking the reference "slit".

The experiment requires a beam of hard x-rays at photon energy $\hbar\omega_0 = 14.4\,\mathrm{keV}$ which is both highly monochromatic, on the order of the natural linewidth of ^{57}Fe, and tightly focused, to couple efficiently into the front face of the two single-mode waveguides [Fuh+04]. To this end, the experiments were performed at the nuclear resonance beamline ID18 [RC96] of the European Synchrotron Radiation Facility (ESRF), utilizing the "Synchrotron Mössbauer Source" (SMS) [Pot+12] to provide a monochromatic beam, which is subsequently focused to a spot of about 0.5 µm in diameter by a pair of elliptical focusing mirrors in Kirkpatrick-Baez geometry [Kup+24]. A sketch of the experimental setup is shown in Fig. 6.2. The SMS employs an electronically forbidden but nuclear allowed Bragg reflection of an isotopically enriched iron borate ($^{57}FeBO_3$) crystal to extract a bandwidth of a few neV with practically zero background [Smi+11]. To tune the photon energy over the target resonance, the iron borate is mounted on a Doppler velocity transducer, which is harmonically oscillating (the motion is harmonic for optimal stability), thus periodically shifting the energy via the Doppler effect. The photons transmitted by the waveguides are detected by a time-resolving pixel array detector based on Timepix3 [TJS16]. The detector is synchronized to the velocity transducer so that the photon time-of-arrival encodes the transducer oscillation phase and thereby the detuning of the photon energy. The detector is installed 1 m downstream of the waveguides, where the 55 µm pixel pitch provides an angular resolution of the interference pattern of about 0.003°, with a total photon detection rate on the order of $10\,\mathrm{s}^{-1}$.

Figure 6.3 shows the measured far-field interference patterns as a function of photon energy detuning (see Methods for a detailed account of the data pre-processing) for the three interferometer configurations: **a** *with* resonant nuclei in the signal waveguide, **b** with nuclei in the signal waveguide but reference waveguide blocked (no reference), and **c** both waveguides *without* resonant nuclei. Hence, **b** and **c** can be considered "control" experiments to the case of interest **a**. The lower panels show the corresponding absorption spectra, obtained by summing the interference pattern

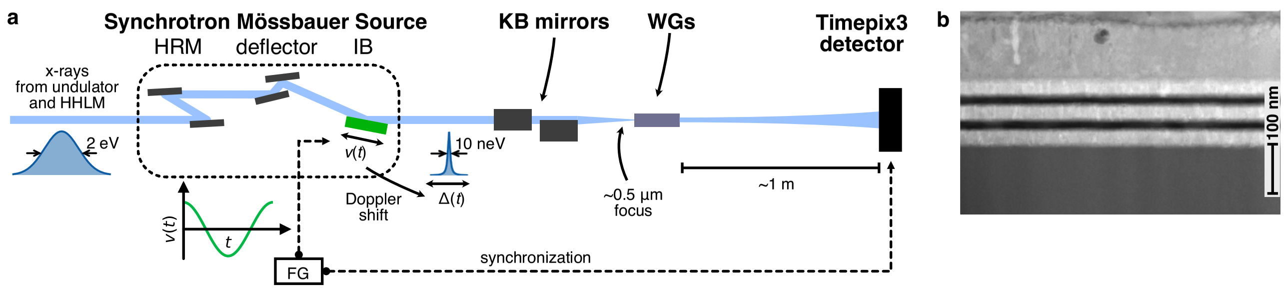

Figure 6.2.: Experimental scheme of the waveguide nano-interferometer. **a** The broadband undulator radiation, pre-monochromatized to about 2 eV with a high heat load monochromator (HHLM), is further monochromatized to the nuclear linewidth by the Synchrotron Mössbauer source, then focussed by elliptical mirrors in Kirkpatrick-Baez (KB) geometry and front-coupled into the double-waveguide (WGs). The far-field pattern of the double-waveguide is observed by a time-resolving pixel detector (Timepix3). Internally, the SMS consists of a high-resolution monochromator (HRM), a deflector and the iron borate (IB) crystal. The IB is mounted on a velocity transducer, which periodically Doppler-shifts the photon energy, controlled by a function generator (FG). The detector is synchronized to the IB oscillation so that the photon time of arrival encodes the instantaneous frequency detuning. **b** Cross-sectional scanning transmission electron microscopy image of the double-waveguide.

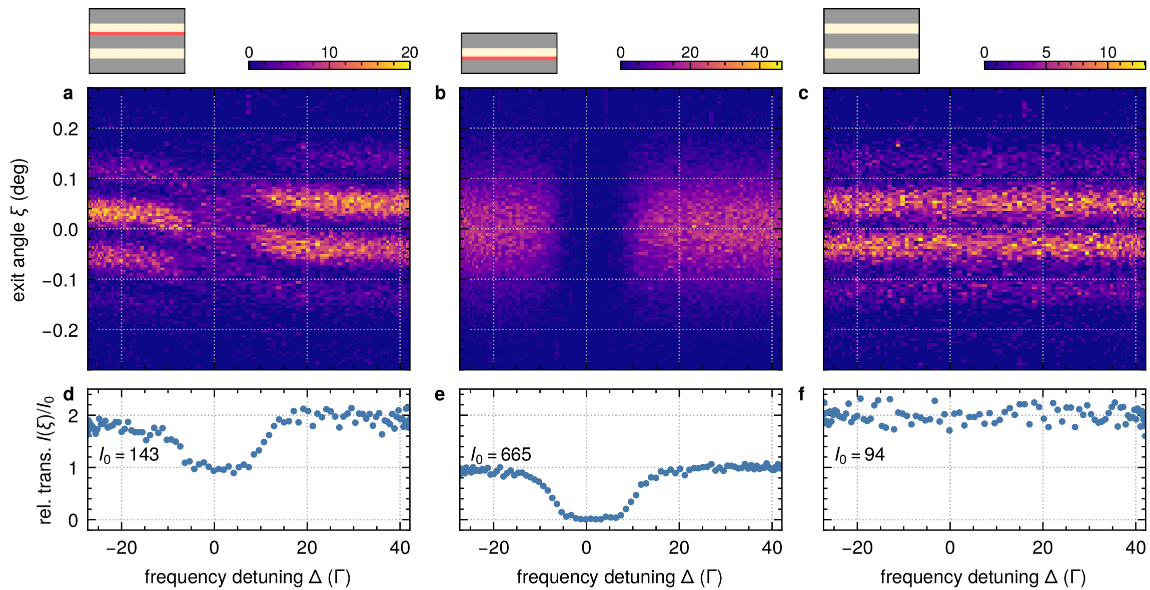

Figure 6.3.: Measured energy-resolved interference patterns and corresponding absorption spectra. The sketches illustrate the 3 different cases, within which the red line indicates the layer of Mössbauer nuclei. **a**-**c** Far-field interference pattern in terms of exit angle ξ and detuning $\Delta = \omega - \omega_0$ for the three cases: **a** signal and reference waveguide, **b** signal waveguide only, **c** two reference waveguides (no Mössbauer nuclei). The color encodes the total number of detected photons per bin. **d**-**f** Waveguide transmission coefficients ("Mössbauer absorption spectra") for the 3 cases, respectively (column-wise sum of the interference patterns). I_0 indicates the total number of detected photons per interference pattern.

column-wise. The single waveguide **e** exhibits a broadened resonant absorption dip, which is reproduced by the interferometer **d** with a unit offset due to the reference waveguide. Note that the interference patterns encode the phase difference between the fields at the exits of the two waveguides, including shifts accumulated within the waveguides as well as phase differences already present at the waveguide entrances. In particular, a slightly tilted wave front results in a frequency-independent shift of the interference pattern, a global offset. This effectively limited the maximum acquisition time and consequently the total number of detected photons in the interference patterns, because of gradual drifts of the wave front of the illuminating focus, likely due to the ambient temperature (see Methods).

The far-field interference pattern can be modeled by (see Methods)

$$I(\xi) = I_0(\xi)\left[1 + T + V_0\sqrt{T}\cos(\phi + kb\xi)\right], \tag{6.1}$$

where $I_0(\xi)$ is the far-field diffraction pattern of a single waveguide mode, ξ is the observation angle, b the baseline (waveguide separation in z), ϕ the phase shift between the two waveguides, $k = \omega_0/c$ the on-resonance wavenumber, and T the intensity transmission coefficient of the SWG. The parameter $V_0 \leq 1$ accounts for a global loss of fringe visibility. On resonance, the nuclei fully absorb the photons ($T = 0$) which results in 0 % and 50 % transmission in the single and double waveguide, respectively. Further away from resonance, the interference pattern is clearly visible and continuously shifts with varying detuning.

From the measured interference pattern, we have extracted the phase shifts $\phi(\Delta)$ induced by the nuclear resonance, using Bayesian inference [Gel+04] taking the Poissonian probability distribution of the data into account. To that end, we have computed the full *posterior probability density* of the phase shift $p(\phi \mid \text{data})$, conditional on the respective observed interference pattern, using a Markov Chain Monte Carlo ensemble sampler [For+13], independently for each frequency detuning Δ. This approach gives us not only the most likely value of the phase shift but its entire probability distribution and hence a robust estimate of the uncertainty.

Figure 6.4 shows the resulting probability densities for the phase shift. For larger detunings, the phase shift is precisely localized (standard deviation of 0.13 rad) and exhibits the expected resonance. On the other hand, within $\pm 6\,\Gamma$ of the resonance, the visibility is practically zero (compare Fig. 6.3**a**) so that the interference pattern contains no information on the phase shift. As can be seen by the values of I_0 in Fig. 6.3**d**, the phases were extracted from interference patterns with less than 300 photons each.

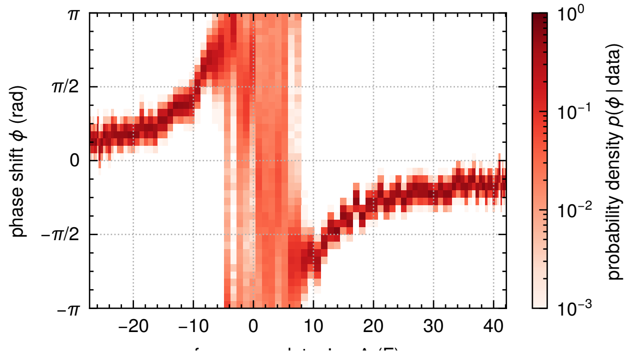

Figure 6.4.: Extracted phase shifts. Phase shift ϕ extracted from the data shown in Fig. 6.3**a** by the Bayesian phase retrieval procedure. The color encodes the posterior probability density for $\phi(\Delta)$ given the measured interference patterns at a certain detuning Δ. Due to the strong absorption, the phase is undetermined in a frequency band of $\pm 6\,\Gamma$ around the resonance frequency. Outside of that band, the phase is well determined.

Connecting the phase shifts to photon-matter interaction

The phase shift contains information about the photon-nuclei coupling and helps to disambiguate parameters that lead to similar absorption spectra. Based on a recently developed theoretical model [ALP24], the harmonic components of the field which is propagating (along x) through the waveguide while coherently interacting with the nuclei can be written as

$$E(\omega, x) = E_0(\omega, x) \exp\left[ik\zeta_m \chi(\omega) x/2\right], \tag{6.2}$$

where E_0 is the reference field without nuclei and ζ_m quantifies the coupling between the single guided mode and the nuclear layer (see Methods). The bare nuclear resonance corresponds to the magnetic susceptibility

$$\chi_0(\omega) = -\rho_\mathrm{n} \frac{\sigma_\mathrm{rad}}{k} \frac{\Gamma/2}{\omega - \omega_0 + i\Gamma/2} \tag{6.3}$$

(σ_rad: radiative cross section, $k = \omega_0/c$: wavenumber, ρ_n: number density of resonant nuclei) as shown in Fig. 6.1**a**. The nuclear levels are generally split due to electric and magnetic hyperfine interactions, leading to a modified susceptibility χ. Since the thin iron layer, which is only about two atomic layers thick, does not develop long range magnetic order at room temperature, we do not expect magnetic hyperfine splitting here. Yet, even small differences of the environment and electric field gradients of the nuclei in the thin iron film lead to inhomogeneous line broadening and possibly a quadrupole splitting of the resonance line. We assume a Gaussian broadened susceptibility χ governed by two effective hyperfine parameters—net central shift and line broadening (see methods).

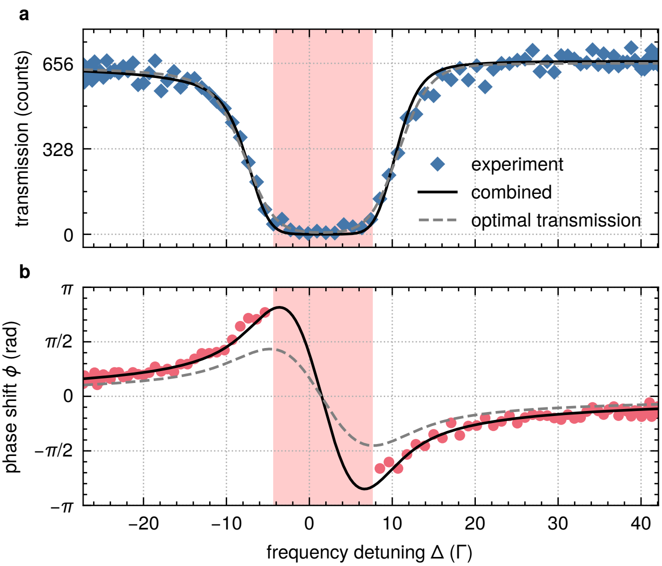

Figure 6.5.: Absorption spectra and phase shifts. a Measured intensity transmission as a function of detuning $\Delta = \omega - \omega_0$ together with two model curves (see main text). **b** Extracted phase shifts (first moment of the posterior probability density) together with the corresponding model curves from **a**. The red area indicates the $\pm 6\,\Gamma$ band of nearly full absorption, for which the data does not contain any phase information.

Figure 6.5**a** shows the measured absorption spectrum and two theory curves based on (6.2), for which the hyperfine parameters and coupling strength $|\zeta_m|$ were found with maximum likelihood estimations with respect to either the absorption spectrum alone (dashed line), or the absorption spectrum combined with the phase shifts (solid line). More precisely, the former shows the model for which the measured absorption spectrum is most likely, with no regard for the phase shift. For the latter, on the other hand, the two hyperfine parameters were optimized with respect to the absorption spectrum and the coupling strength with respect to the phase shift. In both cases, only the modulus $|\zeta_m|$ of the complex coupling coefficient $\zeta_m = |\zeta_m| \exp[i \arg \zeta_m]$ was varied and the complex argument was fixed at the value $\arg \zeta_m^\dagger = 0.03$, which was obtained from simulations using the design parameters of the layer structure.

Table 6.1.: Hyperfine parameters and coupling strength extracted from the data. The parameters ($|\zeta_m|$: coupling strength, w_{HF}: line broadening (FWHM), and δ_{HF}: central shift with respect to α-iron) were found numerically via maximum likelihood estimation from the absorption spectrum alone, or the absorption spectrum combined with the phase shifts (see main text).

model	$\lvert\zeta_m\rvert$	w_{HF}	δ_{HF}
absorption	4.5×10^{-3}	$11\,\Gamma$	$1.6\,\Gamma$
combined	7.1×10^{-3}	$9\,\Gamma$	$1.6\,\Gamma$

The parameters extracted in this way are listed in Tab. 6.1. The coupling strength of the combined model closely matches the design value from theory calculations of $\left|\zeta_m^\dagger\right| = 7.1 \times 10^{-3}$ (see methods), while the absorption model corresponds to substantially smaller coupling of 4.5×10^{-3}. Both models describe the absorption spectrum (Fig. 6.5**a**) well, which is the result of line broadening and the coupling strength being anticorrelated with respect to the absorption spectra. In the phase shifts (Fig. 6.5**b**), however, we can clearly disambiguate the two models. It is evident that the first model does not reproduce the phase shifts at all, while the second model does. Thus, only the combination of the two observables allows us to uniquely extract the model parameters and in particular quantify the coupling parameter.

The higher sensitivity and information content of the phase compared to the absorption signal can be attributed to the fact that the phase shift asymptotically decays like $\phi \propto \Delta^{-1}$, whereas the absorbance decays like $\mu \propto \Delta^{-2}$. Consequently, even noisy measurements of the phase shift reveal quantitative information over a frequency range much wider than the width of the absorption line.

6.3. Discussion

In summary, we have directly measured the resonant phase shift imprinted onto photons that propagate through an x-ray waveguide, while coherently interacting with an ensemble of nuclear resonances, using a nano-interferometer operated in the single photon regime. The method is based on two-path interference of individual photons and has allowed us to accurately extract the phase shifts from only on the order of 100 detected photons (for each energy detuning value) by employing Bayesian inference. Using the extracted phase shift, we were able to quantify the coupling strength between waveguide mode and the nuclei, which was not possible from the absorption spectrum alone, since line broadening and optical thickness lead to ambiguous signatures (see Fig. 6.5). The observed phase-shift and absorption spectra are consistently described by a recently derived theoretical model [ALP24; LA24].

Our results demonstrate the interferometric measurement of phase shifts in the x-ray regime on the nanometer scale, using a few individual photons. The technique is not restricted to nuclear resonances but can analogously be applied to electronic resonances. This paves the way for a new generation of "x-ray photonics on a chip", combining curved waveguides [Sal+15], beamsplitters [HS16], and x-ray sources [VS21] with integrated interferometric sensors.

Having accurately measured the phase shift, one can envision its control. A thicker layer of resonant iron nuclei will develop long range magnetic order so that the degenerate resonance splits into a sextet. The phase shift for a fixed photon energy could then be tuned by controlling the magnetic hyperfine spectrum, either by applying a static magnetic field or transiently with RF pulses as demonstrated in Ref. [Boc+21]. This would enable active control of the phase for narrowband pulses in a nanophotonic device in the hard x-ray frequency range.

6.4. Methods

Waveguide design

The waveguides were designed using the xwglib software from Ref. [LA24]. Materials, layer thicknesses, and length was chosen to effectively absorb everything but a single guided mode of the electromagnetic field. The iron layer was dimensioned to produce a resonant phase shift in the order of $\pm\pi$.

Waveguide fabrication

The waveguide samples were fabricated via magnetron sputter deposition, using an argon plasma at a pressure of 5×10^{-3} mbar at a target-to-substrate distance of about 7 cm with sputtering guns from the A300-XP series (AJA Inter- national, Massachusetts, USA). The residual base pressure prior to deposition was typically less than 4×10^{-7} mbar. Molybdenum and the ^{57}Fe-isotope-enriched iron (97 %) were deposited using targets with diameter 3.81 cm at 12 W DC, and B_4C using a target with diameter 5.08 cm at 53 W RF power. The deposition rates were calibrated based on x-ray reflectivity measurements. The waveguides were deposited onto 1 mm thick polished germanium wafers. To block the over-illuminating part of the x-ray focus. A second 1 mm-thick germanium wafer was bonded on top of the layer structure, using soft alloy bonding as detailed in Ref. [Krü+12].

High-angle annular dark-field (HAADF-STEM) imaging was performed in an FEI Titan 80-300 E-TEM using an acceleration voltage of 300 kV and a convergence semi-angle of 10 mrad yielding a probe size of approximately 0.14 nm.

Event-based detection

To detect the photons in the far-field, we used an AdvaPIX TPX3 (ADVACAM s.r.o., Czech Republic) with a 500 μm-thick silicon sensor (70 % efficiency at 14.4 keV photon energy). We operated this Timepix3-based [TJS16; Poi+14] detector in event-based mode, so that it produces a list of detection events with pixel coordinates, time-of-arrival (ToA), and time-over-threshold data. The velocity transducer of the SMS was controlled by a DFG-1200 digital function generator (Wissenschaftliche Elektronik GmbH, Germany) set to sinusoidal mode. We fed the TTL output of the DFG through a custom-built signal converter into the external synchronization interface of the AdvaPIX. In this way, we set the detector to reset its ToA counter in each oscillation period of the velocity transducer. The temporal resolution of the synchronization was limited by the detector clock frequency of 40 MHz—significantly exceeding the resolution required for the 10 Hz oscillation of the velocity transducer. As a result, the

ToA data of the detected photons encodes the velocity of the transducer and thereby the energy detuning.

The total number of detected photons is limited by the fact that the interference pattern is highly sensitive to small relative changes in the wave front (phase) of the illuminating focus. It could only be kept stable for about 1 h because the beamline optics had to be periodically realigned due to temperature drifts in the building, which slightly altered the wave front in the focus and shifted the interference patterns. We remark that this instability has been substantially reduced shortly after our experiment, as the beamline has been moved into temperature-controlled hutches.

Photon energy calibration

The photon energy detuning was calibrated based on the absorption spectrum of a natural α-iron reference absorber foil used for synchrotron and conventional Mössbauer spectroscopy. Zero detuning ($\Delta = 0$) corresponds to the center of the α-iron absorption spectrum.

Data preprocessing

Several preprocessing steps were applied to the data to generate the interference patterns.

1. Apply a photon-energy filter to reduce spurious events due to environmental and cosmic radiation as well as charge-sharing events. For this, events outside a time-over-threshold range were discarded.

2. Select data from a time window during which the beam was most stable by visual inspection.

3. Select a horizontal range of the data that is as homogeneous as possible by visual inspection. This was necessary because the illuminating wave field had a visibly tilted phase gradient.

4. Project the detection position onto the vertical axis.

5. Convert ToA data to energy detuning based on the calibration and vertical pixel position z to raw observation angle, i.e. $\xi_{\mathrm{raw}} = \arctan(z/D)$ where $D = 1.18\,\mathrm{m}$ is the distance between waveguide and detector and z the vertical position on the detector.

Interference pattern

Two (partially) coherent wave fields $E_1(x_0, z) = A_0(z + b/2)$ and $E_2(x_0, z) = A_0(z - b/2)\sqrt{T}e^{i\phi}$ with wavelength λ centered at $z = \pm b/2$, where $A_0(z)$ describes a complex amplitude with finite width w, produce a far-field Fraunhofer diffraction pattern that can be described by equation (6.1) (see Ref. [Sal19], for example). The fringe visibility parameter $V_0 \in [0, 1]$ accounts for the partial coherence [BW19] and $I_0(\xi)$ is the Fraunhofer diffraction pattern of $A_0(z)$. Setting $T_{\text{eff}} = 1 + T$ and $V_{\text{eff}} = \sqrt{T}V_0$ yields

$$I(\xi; \vec{\theta}) = I_0(\xi) T_{\text{eff}} \left[1 + V_{\text{eff}} \cos(\phi + kb\xi)\right], \tag{6.4}$$

with model parameters $\vec{\theta} = (\phi, T_{\text{eff}}, V_{\text{eff}})$ and global (constant) parameters: wave number $k = 2\pi/\lambda$, mode width w, waveguide separation b, central angle ξ_0, total intensity I_{tot}. We approximate the exit field of the waveguide to be Gaussian, so that its far-field intensity distribution is

$$I_0(\xi) = \frac{I_{\text{tot}}}{\sigma\sqrt{\pi}} \exp\left[-(\xi - \xi_0)^2/\sigma^2\right] \tag{6.5}$$

where $\sigma = 2.355/(kw)$.

Statistical model

We employ a statistical model to implement phase retrieval from the sparse interference patterns. The model parameters $\vec{\theta}$ will be extracted for each detuning Δ independently. The probability to measure y_j counts at angle ξ_j conditional on certain values of $\vec{\theta}$ is $p(y_j \mid \vec{\theta}) = \Pr(Y_j = y_j \mid \lambda)\big|_{\lambda = I(\xi_j; \vec{\theta})}$, where

$$\Pr(Y_j = y_j \mid \lambda) = \frac{\lambda_j^y e^{-\lambda}}{y_j!} \tag{6.6}$$

is the Poisson distribution. Since measurements for different angles are independent, we have $p(\vec{y} \mid \vec{\theta}) = \prod_j p(y_j \mid \vec{\theta})$. Bayes theorem implies for the *posterior* distribution

$$p(\vec{\theta} \mid \vec{y}) \propto p(\vec{\theta}) \cdot p(\vec{y} \mid \vec{\theta}), \tag{6.7}$$

where the proportionality constant only depends on the data $\vec{y}$ and is independent of the parameters $\vec{\theta}$ [Gel+04]. We use the "emcee" Markov Chain Monte Carlo (MCMC) ensemble sampler [For+13] to compute the posterior as detailed below.

The MCMC sampler is based on the logarithm of the right hand side of (6.7), which can be computed as follows. The log-likelihood for a given angle ξ is

$$\begin{aligned} \ell_1(\vec{\theta}; y) &\equiv \log p(y \mid \vec{\theta}) \\ &= -I(\xi; \vec{\theta}) + y \log I(\xi; \vec{\theta}) - \log(y!). \end{aligned} \tag{6.8}$$

The total log-likelihood is therefore

$$\ell(\vec{\theta}; \vec{y}) = \sum_j \left[-I(\xi_j; \vec{\theta}) + y_j \log I(\xi_j; \vec{\theta}) \right] + \text{const.} \tag{6.9}$$

We assume uniform prior distributions as follows: $\phi \sim U(-\pi, \pi)$, $V_{\text{eff}} \sim U(0, 1)$, and $T_{\text{eff}} \sim U(0.3, 1.3)$. While the real part of the exponent in (6.2) can take any value, the interferometer signal is 2π periodic and hence, the phase is only uniquely retrievable within an interval of length 2π.

Phase retrieval

Phase retrieval proceeds as follows.

1. Estimate ξ_0, w and I_{tot} from the interference patterns on resonance with $V_{\text{eff}} = 0$ and $T_{\text{eff}} = 1$.
2. Estimate b from a narrow range of off-resonance interference patterns, using the parameters from step 1.
3. Compute a sample ensemble of $\vec{\theta}$ given the data $\vec{y}$ with "emcee", using the global parameters of step 1 and 2.
4. Estimate the probability density of the phase shift parameter ϕ from a marginal histogram of the ensemble.
5. Shift the phase shift globally such that $\mathrm{E}[\phi(+\Delta)] = -\,\mathrm{E}[\phi(-\Delta)]$ for $\Delta = 20\,\Gamma$.

Coupling constant

The coupling constant ζ_m in (6.2) is defined as

$$\zeta_m = \frac{[u_m(z_0)]^2}{\nu_m} d, \tag{6.10}$$

where ν_m is the (complex) effective refractive index of the mode, d the thickness of the iron layer, z_0 the position of the iron layer, and $u_m(z)$ is the transversal profile of the guided mode, which is bi-normalized to $\int [u_m(z)]^2/\epsilon(z)\mathrm{d}z = 1$ ($\epsilon(z)$ being the relative electric permeability at height z in the layer system) [LA24]. It can be computed numerically, for example with the xwglib library (see Ref. [LA24]).

Hyperfine splitting

The 0.6 nm-thin iron layer is amorphous and too thin to develop long range-magnetic order. Thus, it does not exhibit magnetic hyperfine splitting. However, the individual nuclei can generally experience different isomeric shifts and possibly quadrupole splittings, due to their inhomogeneous environments in the film, which is only about two atomic layers thick. We account for this by introducing an effective Gaussian line broadening and a net central shift,

$$\chi(\omega;\delta_{\mathrm{HF}},\sigma_{\mathrm{HF}}) = f(\omega;\sigma_{\mathrm{HF}}) * \chi_0(\omega-\delta_{\mathrm{HF}}) \tag{6.11}$$

with

$$f(\omega;\sigma_{\mathrm{HF}}) = \frac{1}{\sigma_{\mathrm{HF}}\sqrt{2\pi}} \exp\left\{-\frac{1}{2}\left(\frac{\omega}{\sigma_{\mathrm{HF}}}\right)^2\right\}. \tag{6.12}$$

Acknowledgements
We thank Mike Kanbach for preparing the waveguide assemblies, Matthias Hahn and Tobias Meyer for providing and supporting the electron microscope, Ilya Kupenko for supporting the nanoscope at ID18, and Dieter Lott and Helmholtz-Zentrum Hereon for providing and supporting the reflectometer to calibrate the thin film samples. We acknowledge the European Synchrotron Radiation Facility (ESRF) for provision of synchrotron radiation facilities at ID18 under proposal number MI-1454. We acknowledge partial funding by Max Planck School of Photonics and Deutsche Forschungsgemeinschaft (DFG) (432680300 SFB 1456/C03; 390715994 EXC 2056). LML, PM, RR, and TS are part of the Max Planck School of Photonics.

References

[ALP24] Petar Andrejić, Leon Merten Lohse, and Adriana Pálffy. “Waveguide QED with Mössbauer nuclei.” *Physical Review A* 109.6 (June 2024), p. 063702. DOI: `10.1103/physreva.109.063702`.

[BH65] U. Bonse and M. Hart. “An X-ray Interferometer.” *Applied Physics Letters* 6.8 (Apr. 1965), pp. 155–156. DOI: `10.1063/1.1754212`.

[BH69] U. Bonse and H. Hellkötter. “Interferometrische Messung des Brechungsindex für Röntgenstrahlen.” *Zeitschrift für Physik A Hadrons and nuclei* 223.4 (Aug. 1969), pp. 345–352. DOI: `10.1007/bf01392864`.

[Boc+21] Lars Bocklage, Jakob Gollwitzer, Cornelius Strohm, Christian F. Adolff, Kai Schlage, Ilya Sergeev, Olaf Leupold, Hans-Christian Wille, Guido Meier, and Ralf Röhlsberger. "Coherent control of collective nuclear quantum states via transient magnons." *Science Advances* 7.5 (Jan. 2021). DOI: 10.1126/sciadv.abc3991.

[Bow96] D. K. Bowen. "Applications of X-Ray Interferometry." In: *X-Ray and Neutron Dynamical Diffraction: Theory and Applications*. Ed. by André Authier, Stefano Lagomarsino, and Brian K. Tanner. Vol. 357. NATO Science Series B. Springer US, 1996, pp. 381–410. ISBN: 9781461558798. DOI: 10.1007/978-1-4615-5879-8_26.

[BW19] Max Born and Emil Wolf. *Principles of optics*. Seventh anniversary edition, 60th anniversary of first edition, 20th anniversary of seventh edition. Cambridge: Cambridge University Press, 2019. ISBN: 9781108769914.

[Cal+05] R. Callens, C. L'abbé, J. Meersschaut, I. Serdons, W. Sturhahn, and T. S. Toellner. "Phase determination in nuclear resonant scattering using a velocity drive as an interferometer and phase shifter." *Physical Review B* 72.8 (Aug. 2005), p. 081402. DOI: 10.1103/physrevb.72.081402.

[Col96] R. Colella. "X-Ray and Neutron Interferometry: Basic Principles and Applications." In: *X-Ray and Neutron Dynamical Diffraction: Theory and Applications*. Ed. by André Authier, Stefano Lagomarsino, and Brian K. Tanner. Vol. 357. NATO Science Series B. Springer US, 1996, pp. 369–380. ISBN: 9781461558798. DOI: 10.1007/978-1-4615-5879-8_25.

[For+13] Daniel Foreman-Mackey, David W. Hogg, Dustin Lang, and Jonathan Goodman. "emcee: The MCMC Hammer." *Publications of the Astronomical Society of the Pacific* 125.925 (Mar. 2013), pp. 306–312. DOI: 10.1086/670067.

[FOS06] C. Fuhse, C. Ollinger, and T. Salditt. "Waveguide-Based Off-Axis Holography with Hard X Rays." *Physical Review Letters* 97.25 (Dec. 2006), p. 254801. DOI: 10.1103/physrevlett.97.254801.

[Fuh+04] Christian Fuhse, Ansgar Jarre, Christoph Ollinger, Jens Seeger, Tim Salditt, and Remi Tucoulou. "Front-coupling of a prefocused x-ray beam into a monomodal planar waveguide." *Applied Physics Letters* 85.11 (Sept. 2004), pp. 1907–1909. DOI: 10.1063/1.1791736.

[Gel+04] Andrew Gelman, John B. Carlin, Hal S. Stern, and Donald B. Rubin, eds. *Bayesian data analysis*. 2nd ed. Texts in statistical science. Boca Raton, Fla. [u.a.]: Chapman & Hall/CRC, 2004. ISBN: 158488388X.

[Goe+19] Stephan Goerttler, Kilian Heeg, Andreas Kaldun, Patrick Reiser, Cornelius Strohm, Johann Haber, Christian Ott, Rajagopalan Subramanian, Ralf Röhlsberger, Jörg Evers, and Thomas Pfeifer. "Time-Resolved sub-Ångström Metrology by Temporal Phase Interferometry near X-Ray Resonances of Nuclei." *Physical Review Letters* 123.15 (Oct. 2019). DOI: 10.1103/physrevlett.123.153902.

[Hee+15] K. P. Heeg, C. Ott, D. Schumacher, H.-C. Wille, R. Röhlsberger, T. Pfeifer, and J. Evers. "Interferometric phase detection at x-ray energies via Fano resonance control." *Physical Review Letters* 114.20 (May 2015). DOI: 10.1103/physrevlett.114.207401.

[Hee+21] Kilian P. Heeg, Andreas Kaldun, Cornelius Strohm, Christian Ott, Rajagopalan Subramanian, Dominik Lentrodt, Johann Haber, Hans-Christian Wille, Stephan Goerttler, Rudolf Rüffer, Christoph H. Keitel, Ralf Röhlsberger, Thomas Pfeifer, and Jörg Evers. "Coherent X-ray-optical control of nuclear excitons." *Nature* 590.7846 (Feb. 2021), pp. 401–404. DOI: 10.1038/s41586-021-03276-x.

[HGD93] B. L. Henke, E. M. Gullikson, and J. C. Davis. "X-Ray Interactions: Photoabsorption, Scattering, Transmission, and Reflection at E = 50-30,000 eV, Z = 1-92." *Atomic Data and Nuclear Data Tables* 54.2 (July 1993), pp. 181–342. DOI: 10.1006/adnd.1993.1013.

[HS16] Sarah Hoffmann-Urlaub and Tim Salditt. "Miniaturized beamsplitters realized by X-ray waveguides." *Acta Crystallographica Section A* 72.5 (Aug. 2016), pp. 515–522. DOI: 10.1107/s205327331601144x.

[HS19] Peter W. Hawkes and John C. H. Spence, eds. *Springer Handbook of Microscopy*. Springer International Publishing, 2019. ISBN: 9783030000691. DOI: 10.1007/978-3-030-00069-1.

[Kha+21] I. R. Khairulin, Y. V. Radeonychev, V. A. Antonov, and Olga Kocharovskaya. "Acoustically induced transparency for synchrotron hard x-ray photons." *Scientific Reports* 11.1 (Apr. 2021). DOI: 10.1038/s41598-021-86555-x.

[Krü+12] S. P. Krüger, H. Neubauer, M. Bartels, S. Kalbfleisch, K. Giewekemeyer, P. J. Wilbrandt, M. Sprung, and T. Salditt. "Sub-10nm beam confinement by X-ray waveguides: design, fabrication and characterization of optical properties." *Journal of Synchrotron Radiation* 19.2 (Jan. 2012), pp. 227–236. DOI: 10.1107/s0909049511051983.

[Kup+24] I. Kupenko, X. Li, S. C. Müller, D. Bessas, S. Yaroslavtsev, G. Aprilis, A. I. Chumakov, J.-P. Celse, and R. Rüffer. "Nuclear resonance techniques for high-pressure research: example of the ID18 beamline of the European Synchrotron Radiation Facility." *High Pressure Research* 44.3 (July 2024), pp. 310–336. DOI: 10.1080/08957959.2024.2371023.

[LA24] Leon M. Lohse and Petar Andrejić. "Nano-optical theory of planar x-ray waveguides." *Optics Express* 32.6 (Mar. 2024), p. 9518. DOI: 10.1364/oe.504206.

[Len94] B. Lengeler. "Experimental Determination of the Dispersion Correction f'(E) to the Atomic Scattering Factor." In: *Resonant Anomalous X-ray Scattering: Theory and Applications*. Ed. by G. Materlik, C. J. Sparks, and K. Fischer. Amsterdam [u.a.]: North-Holland, 1994, pp. 35–60. ISBN: 0444820256.

[Lid14] V. V. Lider. "X-ray crystal interferometers." *Physics-Uspekhi* 57.11 (Nov. 2014), pp. 1099–1117. DOI: 10.3367/ufne.0184.201411e.1217.

[LKE24] Dominik Lentrodt, Christoph H. Keitel, and Jörg Evers. *Towards nonlinear optics with Mössbauer nuclei using x-ray cavities*. 2024. DOI: 10.48550/ARXIV.2405.12773.

[Loh+24] Leon M. Lohse, Petar Andrejić, Sven Velten, Malte Vassholz, Charlotte Neuhaus, Ankita Negi, Anjali Panchwanee, Ilya Sergeev, Adriana Pálffy, Tim Salditt, and Ralf Röhlsberger. *Collective nuclear excitation and pulse propagation in single-mode x-ray waveguides*. 2024. DOI: 10.48550/ARXIV.2403.06508.

[Neg+25] Ankita Negi, Leon Merten Lohse, Sven Velten, Ilya Sergeev, Olaf Leupold, Sakshath Sadashivaiah, Dimitrios Bessas, Aleksandr Chumakhov, Christina Brandt, Lars Bocklage, Guido Meier, and Ralf Röhlsberger. *Energy Time Ptychography for one-dimensional phase retrieval*. 2025. DOI: 10.48550/ARXIV.2506.00492.

[Poi+14] T. Poikela, J. Plosila, T. Westerlund, M. Campbell, M. De Gaspari, X. Llopart, V. Gromov, R. Kluit, M. van Beuzekom, F. Zappon, V. Zivkovic, C. Brezina, K. Desch, Y. Fu, and A. Kruth. "Timepix3: a 65K channel hybrid pixel readout chip with simultaneous ToA/ToT and sparse readout." *Journal of Instrumentation* 9.05 (May 2014), pp. C05013–C05013. DOI: 10.1088/1748-0221/9/05/c05013.

[Pot+12] Vasily Potapkin, Aleksandr I. Chumakov, Gennadii V. Smirnov, Jean-Philippe Celse, Rudolf Rüffer, Catherine McCammon, and Leonid Dubrovinsky. "The ^{57}Fe Synchrotron Mössbauer Source at the ESRF." *Journal of Synchrotron Radiation* 19.4 (May 2012), pp. 559–569. DOI: 10.1107/s0909049512015579.

[RC96] Rudolf Rüffer and Aleksandr I. Chumakov. "Nuclear Resonance Beamline at ESRF." *Hyperfine Interactions* 97–98.1 (Dec. 1996), pp. 589–604. DOI: 10.1007/bf02150199.

[RE21] Ralf Röhlsberger and Jörg Evers. "Quantum Optical Phenomena in Nuclear Resonant Scattering." In: *Modern Mössbauer Spectroscopy*. Ed. by Yutaka Yoshida and Guido Langouche. Topics in Applied Physics. Springer Singapore, 2021, pp. 105–171. DOI: 10.1007/978-981-15-9422-9_3.

[Röh+10] R. Röhlsberger, K. Schlage, B. Sahoo, S. Couet, and R. Rüffer. "Collective Lamb Shift in Single-Photon Superradiance." *Science* 328.5983 (May 2010), pp. 1248–1251. DOI: 10.1126/science.1187770.

[Sal+15] T. Salditt, S. Hoffmann, M. Vassholz, J. Haber, M. Osterhoff, and J. Hilhorst. "X-Ray Optics on a Chip: Guiding X Rays in Curved Channels." *Physical Review Letters* 115.20 (Nov. 2015), p. 203902. DOI: 10.1103/physrevlett.115.203902.

[Sal19] Bahaa E. A. Saleh. *Fundamentals of photonics*. Ed. by Malvin Carl Teich. Third edition. Hoboken, NJ: Wiley, 2019. ISBN: 9781119506874.

[She+23] Alexandra S. Sheremet, Mihail I. Petrov, Ivan V. Iorsh, Alexander V. Poshakinskiy, and Alexander N. Poddubny. "Waveguide quantum electrodynamics: Collective radiance and photon-photon correlations." *Reviews of Modern Physics* 95.1 (Mar. 2023), p. 015002. DOI: 10.1103/revmodphys.95.015002.

[Shi+24] Xihang Shi, Wen Wei Lee, Aviv Karnieli, Leon Merten Lohse, Alexey Gorlach, Lee Wei Wesley Wong, Tim Salditt, Shanhui Fan, Ido Kaminer, and Liang Jie Wong. "Quantum Nanophotonics with Energetic Particles: X-rays and Free Electrons." *Progress in Quantum Electronics* (2024).

[Shv+23] Yuri Shvyd'ko et al. "Resonant X-ray excitation of the nuclear clock isomer ^{45}Sc." *Nature* 622.7983 (Sept. 2023), pp. 471–475. DOI: 10.1038/s41586-023-06491-w.

[SLT04] W. Sturhahn, C. L'abbé, and T. S. Toellner. "Exo-interferometric phase determination in nuclear resonant scattering." *Europhysics Letters (EPL)* 66.4 (May 2004), pp. 506–512. DOI: 10.1209/epl/i2003-10235-7.

[Smi+11] G. V. Smirnov, A. I. Chumakov, V. B. Potapkin, R. Rüffer, and S. L. Popov. "Multispace quantum interference in a ^{57}Fe synchrotron Mössbauer source." *Physical Review A* 84.5 (Nov. 2011), p. 053851. DOI: 10.1103/physreva.84.053851.

[Spi+23] Rebecca Spiecker, Pauline Pfeiffer, Adyasha Biswal, Mykola Shcherbinin, Martin Spiecker, Holger Hessdorfer, Mathias Hurst, Yaroslav Zharov, Valerio Bellucci, Tomáš Faragó, Marcus Zuber, Annette Herz, Angelica Cecilia, Mateusz Czyzycki, Carlos Sato Baraldi Dias, Dmitri Novikov, Lars Krogmann, Elias Hamann, Thomas van de Kamp, and Tilo Baumbach. "Dose-efficient in vivo X-ray phase contrast imaging at micrometer resolution by Bragg magnifiers." *Optica* 10.12 (Dec. 2023), p. 1633. DOI: 10.1364/optica.500978.

[Sta+24] Mathias J. R. Staunstrup, Alexey Tiranov, Ying Wang, Sven Scholz, Andreas D. Wieck, Arne Ludwig, Leonardo Midolo, Nir Rotenberg, Peter Lodahl, and Hanna Le Jeannic. "Direct observation of a few-photon phase shift induced by a single quantum emitter in a waveguide." *Nature Communications* 15.1 (Aug. 2024). DOI: 10.1038/s41467-024-51805-9.

[Stu01] W. Sturhahn. "Phase problem in synchrotron Mössbauer spectroscopy." *Physical Review B* 63.9 (Jan. 2001), p. 094105. DOI: 10.1103/physrevb.63.094105.

[Tem+80] D. H. Templeton, L. K. Templeton, J. C. Phillips, and K. O. Hodgson. "Anomalous scattering of X-rays by cesium and cobalt measured with synchrotron radiation." *Acta Crystallographica Section A* 36.3 (May 1980), pp. 436–442. DOI: 10.1107/s0567739480000940.

[Tie+14] T. G. Tiecke, J. D. Thompson, N. P. de Leon, L. R. Liu, V. Vuletić, and M. D. Lukin. "Nanophotonic quantum phase switch with a single atom." *Nature* 508.7495 (Apr. 2014), pp. 241–244. DOI: 10.1038/nature13188.

[TJS16] D. Turecek, J. Jakubek, and P. Soukup. "USB 3.0 readout and time-walk correction method for Timepix3 detector." *Journal of Instrumentation* 11.12 (Dec. 2016), pp. C12065–C12065. DOI: 10.1088/1748-0221/11/12/c12065.

[Tür+19] Pierre Türschmann, Hanna Le Jeannic, Signe F. Simonsen, Harald R. Haakh, Stephan Götzinger, Vahid Sandoghdar, Peter Lodahl, and Nir Rotenberg. "Coherent nonlinear optics of quantum emitters in nanophotonic waveguides." *Nanophotonics* 8.10 (Aug. 2019), pp. 1641–1657. DOI: 10.1515/nanoph-2019-0126.

[Vel+24] Sven Velten, Lars Bocklage, Xiwen Zhang, Kai Schlage, Anjali Panchwanee, Sakshath Sadashivaiah, Ilya Sergeev, Olaf Leupold, Aleksandr I. Chumakov, Olga Kocharovskaya, and Ralf Röhlsberger. "Nuclear quantum memory for hard x-ray photon wave packets." *Science Advances* 10.26 (June 2024). DOI: 10.1126/sciadv.adn9825.

[Vol+14] Jürgen Volz, Michael Scheucher, Christian Junge, and Arno Rauschenbeutel. "Nonlinear π phase shift for single fibre-guided photons interacting with a single resonator-enhanced atom." *Nature Photonics* 8.12 (Nov. 2014), pp. 965–970. DOI: 10.1038/nphoton.2014.253.

[VS21] Malte Vassholz and Tim Salditt. "Observation of electron-induced characteristic x-ray and bremsstrahlung radiation from a waveguide cavity." *Science Advances* 7.4 (Jan. 2021). DOI: 10.1126/sciadv.abd5677.

[WE23] Lukas Wolff and Jörg Evers. "Unraveling time- and frequency-resolved nuclear resonant scattering spectra." *Physical Review Research* 5.1 (Feb. 2023), p. 013071. DOI: 10.1103/physrevresearch.5.013071.

[You02] Thomas Young. "On the theory of light and colours." *Philosophical Transactions of the Royal Society of London* 92 (Dec. 1802), pp. 12–48. DOI: 10.1098/rstl.1802.0004.

[Yua+25] Ziyang Yuan, Hongxia Wang, Zhiwei Li, Tao Wang, Hui Wang, Xinchao Huang, Tianjun Li, Ziru Ma, Linfan Zhu, Wei Xu, Yujun Zhang, Yu Chen, Ryo Masuda, Yoshitaka Yoda, Jianmin Yuan, Adriana Pálffy, and Xiangjin Kong. "Nuclear phase retrieval spectroscopy using resonant x-ray scattering." *Nature Communications* 16.1 (Mar. 2025). DOI: 10.1038/s41467-025-58396-z.

7. Summary and outlook

This work has explored the physics of Mössbauer nuclei in x-ray waveguides experimentally and theoretically. In the following, we will briefly recapitulate what we have *done* and what we have *learned* – to then suggest what could be done next.

Spatial modes in x-ray waveguides

In Chapter 3, we have derived a theory to describe the *resonant modes* of the electromagnetic field in arbitrary planar waveguide structures. After defining and classifying the resonant modes, we have presented a recipe (and implementation) to find these modes and to compute the numerical value of all relevant coefficients. This *mode finder* works reliably in the x-ray regime. We have shown how the modes emerge in the fields generated by oscillating dipoles embedded in the layer structure and have derived asymptotic expansions of the electromagnetic Green's functions (for large spatial distances) in terms of the resonant modes. We have also discussed dispersion and that it can be neglected in most cases. The theory is based on the full vector wave equations and omits approximations specific to the x-ray regime, which makes it applicable to a wide range of the electromagnetic spectrum.

One important application is the computer-aided design of waveguide structures. The theory gives explicit analytical expressions for key figures of merit, such as attenuation lengths, propagation constants, transverse spatial confinement, and coupling coefficients, all in terms of the effective refractive indices of the modes – which can be readily computed with the mode finder. We have made heavy use of this to design the waveguide structures for the experiments that are featured in chapters 4 and 6.

The Green's functions allow to quantify the coupling strength between emitters that are embedded in a waveguide structure and the field modes. The partial spontaneous decay rates correspond to the relative power that an oscillating dipole (embedded in the waveguide) radiatively emits into each of the resonant modes (see Chapter 8 in Ref. [NH12]). Our calculations clearly show that the partial emission into the modes is neither Purcell-enhanced nor particularly strong. On the contrary, the partial decay rates into the resonant modes are relatively weak due to their weak spatial confinement: the decay rates are in the order of $\lambda/l \lesssim 10^{-2}$ where l is the linear spatial confinement. Their exact values depend on the normalized transversal mode profiles $u_m(z)$ and the emitter position.

The *total* decay rate in an x-ray waveguide is also not significantly different from its value in free space, as can be seen rather intuitively. The Purcell effect can be classically understood as an interference phenomenon [Ryb+16]. In a high-finesse resonator, the field radiated by an oscillating dipole is back-reflected by the resonator mirrors and thereby modifies the field at the dipole position, which alters the emission rate. In this case, the Green's function evaluated at the emitter position, $\underline{\mathbf{G}}(\mathbf{r}_0, \mathbf{r}_0, \omega)$, can differ substantially from its value in free space $\underline{\mathbf{G}}^{(0)}(\mathbf{r}_0, \mathbf{r}_0, \omega)$. In the x-ray regime, however, reflectivities are appreciably different from zero only for very small incidence angles (with respect to the interface), $\theta \lesssim \sqrt{2\delta}$, and normal-incidence back-reflection is practically non-existent (apart from Bragg reflections). As a consequence, the field generated by an emitter within the waveguide is, to a very good approximation, purely outward-propagating so that the field *at the emitter position* is essentially the same with or without the waveguide environment, $\underline{\mathbf{G}}(\mathbf{r}_0, \mathbf{r}_0, \omega) \approx \underline{\mathbf{G}}^{(0)}(\mathbf{r}_0, \mathbf{r}_0, \omega)$. In this sense, x-ray waveguides are no actual cavity resonators! While they can act *like* a cavity resonator for translation-invariant collective spin-wave states (see Refs. [RE21; Len21]), this does not apply to localized atoms.

Yet, x-ray waveguides *do* alter the fields substantially for large spatial distances, so that $\underline{\mathbf{G}}(\mathbf{r}, \mathbf{r}_0, \omega)$ can be expanded into the resonant modes and the non-resonant components for large $|\mathbf{r} - \mathbf{r}_0|$. This asymptotic expansion is not restricted to the x-ray regime but particularly useful there, because strong absorption in the cladding efficiently attenuates the non-resonant components of the field. Substituting this mode expansion into the formalism presented in chapter 2, has allowed to derive analytical solutions for pulse propagation in x-ray waveguides containing Mössbauer nuclei [ALP24], and similarly for the nuclear exciton dynamics after impulsive driving (see chapter 4).

Several interesting questions are still open and provide promising avenues to generalize and advance the theory.

Bragg-multilayer waveguides: Waveguides with Bragg-reflecting multilayers instead of homogeneous cladding layers have been considered in the past [Pru03; Pru05; Hab17]. They promise tighter mode confinement and thereby stronger coupling, from which experiments with Mössbauer nuclei could benefit in particular [Hab17]. The present theory assumes homogeneous and semi-infinite outermost layers, but could in principle be adapted for periodic multilayers.

Channel waveguides: One can expect similar asymptotic mode expansion in channel waveguides (or more generally, any structures with two-dimensional confinement). The main challenge is to develop or identify a suitable two-dimensional mode-finding algorithm, either in a suitable finite-element approach or assuming, for example, cylindrical symmetry. To that end, it is particularly important to find appropriate boundary conditions that work well with the extremely small refractive index contrast.

Planar x-ray waveguides for nuclear resonant scattering experiments

In chapter 4, we have presented two nuclear resonant scattering experiments with x-ray waveguides that contained thin layers of the Mössbauer isotope ^{57}Fe. We have demonstrated for the first time (i) front-coupling into thin film x-ray waveguides with Mössbauer nuclei and (ii) detecting the delayed photons that leave the waveguide at its back end. In particular, we observed the delayed photons after propagating through a 2 mm-long and 20 nm-thick waveguide (10^5 aspect ratio) containing a 0.6 nm-thin layer of ^{57}Fe.

The experiments represent the culmination of our quest for suitable waveguide designs and experimental parameters. While the chapter only features the data from one specific sample for each of the two experiments, we have fabricated and screened a significant number of different sample designs. In the end, the best were a combination of the planar waveguide designs and fabrication protocols that had been developed by the group of Tim Salditt in Göttingen (see Ref. [Sal+08; Krü+12]) and the thin-film cavity designs [Röh+10; Hab17] and sputter-deposition protocols (see for example Ref. [Wil20]) that had been developed by the group of Ralf Röhlsberger in Hamburg. Material-wise, the combination of boron carbide (B_4C) for the waveguide core and molybdenum for the cladding performed best. Molybdenum leads to substantially increased mode attenuation lengths compared to a platinum cladding, as it is popular for experiments in reflection geometry. Using germanium wafers to block the overilluminating beam in the front-coupling geometry as detailed in Ref. [Krü+12] was vital to detect the weak signal.

The layer systems are still not ideal, though. This leaves potential for improvement.

Stress: The B_4C layers develop appreciable stress so that thicker layers would regularly peel off the substrate. This could potentially be mitigated by annealing the layer system after deposition [BB11]. Alternative light materials such as pure boron or carbon could also be reconsidered.

Hyperfine parameters: The resonance line of the ultra-thin ^{57}Fe layers in the B_4C core repeatedly displayed inhomogeneous broadening and quadrupole splitting in the order of 5 to 10 natural linewidths. This effect is well-known [Röh+10; Sah+11] but its microscopic origin is still unclear. In our case, it is generally undesireable since it results in a “less clean” quantum system and introduces additional parameters that need to be taken into account during data analysis. In the future, we wish to either significantly reduce this effect or to precisely characterize it – for example via conversion electron Mössbauer spectroscopy. One promising option to reduce this effect would be using ^{119}Sn as an alternative Mössbauer isotope, in particular in form of a thin layer of $^{119}SnO_2$ embedded between magnesium oxide (MgO) layers [Vel22].

Nuclear excitation dynamics

In Chapter 4, we have investigated how the collective excitation of a nuclear ensemble in an x-ray waveguide evolves in time after impulsive driving – in the two geometries front-coupling and grazing-incidence (resonant-beam-coupling). In other words, the nuclear ensemble was coherently excited by a short synchrotron pulse and we observed its subsequent collective spontaneous emission. The two cases generate fundamentally different dynamics of the delayed collectively emitted photons that leave the waveguide at its back end. In front-coupling, they clearly exhibit dynamical beats, identical to those emerging in nuclear forward scattering from a homogeneous foil (see chapter 2). In grazing-incidence, however, they exhibit a simple "superradiant" exponential decay with a "speed-up" that depends on the angle of incidence of the driving pulse.

We have modeled these observations using a theoretical approach based on Ref. [ALP24], which was developed in close collaboration with the group of Adriana Pálffy in Erlangen (at the time). The observations in both geometries are well reproduced by a single equation of motion for one temporal and one spatial dimension. They are well described assuming that the nuclei are coupled only through a single resonant mode of the fields – even though the coupling between an individual atom and the mode is very weak. The two geometries realize different regimes of the (off-resonant) optical thickness of the waveguide L/Λ_m, which is quantified by the waveguide length in units of the attenuation length of the resonant mode. In optically thin waveguides, the boundary causes the dynamical beats, while optically thick waveguides are effectively semi-infinite and free of this boundary effect.

The dynamics in the single-mode waveguide is formally identical to the dynamics in a homogeneous slab, which we have discussed extensively in section 2.3. This is evident since the Green's functions of the two systems are identical up to rescaled coefficients. The equation of motion is commonly treated as an eigenvalue problem, which leads to radiative eigenmodes (certain spatial distributions of the excitation amplitude that decay exponentially). Instead, we have solved the dynamics by exploiting a forward-scattering approximation, which enables an analytical solution (see section 2.3).

The theoretical model suggests that the delayed response is temporally coherent in the order of the nuclear lifetime ($\tau \sim 100\,\mathrm{ns}$) – even though the driving pulses are highly incoherent with coherence times of $\lesssim 1\,\mathrm{ps}$ (see for example Ref. [Kun+97] and Appendix A). This is because the driving pulse is quasi-instantaneous on the time scale of the nuclear decay so that the collective excitation depends only on its integral (the pulse area A). The "randomness" of the driving pulse is thus transformed into a *global* complex prefactor that merely fluctuates from pulse to pulse. Consequently, the delayed radiation from the waveguide has near perfect coherence both longitudinally and transversally [OS11].

Nuclear phase shift interferometry

In chapter 6, we have measured the phase shift imprinted onto a resonant quasi-monochromatic field that propagates through an x-ray waveguide containing Mössbauer nuclei. To that end, we have devised and implemented a nanoscopic double-waveguide interferometer consisting of one waveguide *with* and one waveguide *without* resonant nuclei. It translates the relative phase-shift between the waveguides into a spatial displacement of the far-field interference pattern – which we have observed.

We have formulated a statistical model for the sparsely sampled interference pattern and have employed Bayesian inference to extract the phase shifts. In this way, we have obtained precise measurements of the resonant phase shift from only in the order of 100 photons per photon energy. In principle, even the first measured photon contains some *usable* information about the phase shift and every additional photon improves the precision.

The phase information is not resolved in typical experiments, but it carries additional quantitative information, particularly for resonant scattering. While the absorption contrast falls of with $1/\Delta^2$, (where $\Delta = \omega - \omega_0$) the phase shift only falls of with $1/\Delta$. This has allowed us to quantitatively discriminate between sample thickness and resonance broadening, even though the two parameters are anticorrelated in the absorption contrast.

We have experimentally measured the resonant phase shifts and transmission coefficients as a function of photon energy. The experimental data is consistent with our theoretical models derived in chapters 2, 3, and 4, which further verifies them.

The experimental technique is not restricted to *nuclear* resonances but can be used with electronic resonances just as well. In fact, we have already carriedout an experiment to measure the resonant phase shift of "white line" close to the L3 absorption edge of tantalum ($\hbar\omega_0 = 9.88\,\mathrm{keV}$), inspired by the seminal work of Haber and colleagues [Hab+19]. Given the much broader width of electronic resonances in the order of 1 eV, they can be resolved with regular silicon crystal monochromators, which considerably simplifies the setup. However, the evaluation is still ongoing at the time of writing.

The main experimental challenge is the extreme sensitivity of the interferometer to phase shifts at its entrance. The two waveguid entrances are illuminated by a focussed beam with diameter of less than 1 μm. Small changes of the wave front, for example small displacements of the focal position, lead to relative phase shifts. In the experiment at ID18, small temperature drifts made it necessary to regularly realign parts of the beamline optics. The interference patterns before and after alignment have an uncontrolled global phase difference and hence can not be combined without substantial effort. For that reason, datasets had to be acquired within about 1 h. Since then, the beamline has been moved to ID14 which has much better temperature stabilization and could allow for longer acquisition times. A single-mode waveguide with an integrated beamsplitter (see Ref. [HS16] for a multi-mode demonstration) could overcome this limitation entirely. Here, the illuminating beam would couple into the only available mode, so that phase and amplitude changes affect both of the interferometer legs equally.

Event-based pixel detectors at the synchrotron Mössbauer source

The overall photon count rate in the double-waveguide experiment has been very low due to the highly monochromatic illumination and the low front-coupling efficiency. This, combined with the limited acquisition time and the required spatial resolution prohibits the use of the APD detectors that are normally used at the beamline (see Section 2.2.2). Scanning the detector position with a narrow aperture to spatially resolve the interference pattern wastes the majority of photons and takes too long. For that reason, we have used an event-based pixel detector using the Timepix3 chip in place of the APDs.

Once in place, we took the opportunity to test the potential of the detector for full-field imaging applications. We placed different samples slightly downstream of the focus, thus implementing a full-field spectral x-ray microscope with nano-eV energy resolution for spectral imaging and spectroscopy with spatial sensitivity. We acquired full-field images of microstructures in ultra-thin iron films as well as magnetic domain structures of iron foils. This approach could in particular benefit Mössbauer spectroscopy in high-pressure applications. The experimental data is not fully evaluated at the time of writing, though. Both experiments, the interferometer and the microscope, crucially rely on the event-based detection mode of Timepix3 and synchronization to the oscillating synchrotron Mössbauer source.

Outlook

We have demonstrated nuclear resonant x-ray propagation in planar x-ray waveguides in several complementary experiments. We have also provided a unifying theoretical model that reproduces the experimental results and allows for their interpretation. This opens up promising new avenues for future experiments.

Conceptually, “Mössbauer nuclei in x-ray waveguides” realize a very large number of very clean quantum emitters that are weakly coupled to one or more waveguide modes. As such, they constitute an experimental platform for the emerging field of waveguide QED. It realizes the regime of very low coupling efficiency and extremely high number of emitters compared to other platforms (see the review [She+23]). It also allows for very large optical depths in comparison (see Ref. [Cha+18]). However, realizing a wider range of phenomena requires one to go beyond the single-mode designs that we have investigated here. For example, waveguides supporting two resonant modes and containing a longitudinally microstructured layer of resonant nuclei could give rise to a phenomenon similar to selective sub-radiance [ALP24].

With planar waveguides, one could already realize some of the more elaborate ideas that were mentioned in the introduction. Coupling a *magnetic* layer of Mössbauer nuclei to a waveguide mode, one could *control* the coherent radiation from the waveguide by changing the magnetization. Another proposal aims to *measure* the gravitational redshift on the millimeter scale [LAL25]. While this is undoubtedly ambitious, the idea is more general: interference between waveguide modes can translate miniscule changes of the hyperfine structure into macroscopic changes of the far-field diffraction pattern.

In the future, waveguides with two-dimensional confinement hold the prospect to integrate such functionality onto a chip – *integrated x-ray photonics*. The biggest challenge is the fabrication, however. State-of-the-art x-ray channel waveguides (see Ref. [Hof+16]) consist of air cores surrounded by a single homogeneous material. This hampers embedding of resonant nuclei and leads to unfavourable performance for $\hbar\omega \gtrsim 10\,\mathrm{keV}$. Hence, new fabrication techniques are required that allow to combine different materials.

In any case, current technological developments will greatly facilitate future experiments with x-ray waveguides. Future detectors such as the Timepix4-based *TEMPUS* [Cor+24] will provide nanosecond temporal resolution as well as spatial sensitivity and therefore allow to record time-resolved far-field diffraction patterns without scanning. Finally, the advent of 4th generation (diffraction-limited) synchrotron light sources such as Petra IV (see Ref. [Sch+22]) promises greatly increased focusing capabilities – and hence superior front-coupling efficiency.

To conclude, we have demonstrated that x-ray waveguides with Mössbauer nuclei are a versatile experimental platform. Yet, we have only scratched the surface of what might be possible, and more elaborate designs paired with current technological developments promise to push the boundaries in metrology, the investigation of collective dynamics, and coherent control of narrowband radiation on the nanoscale.

References

[ALP24] Petar Andrejić, Leon Merten Lohse, and Adriana Pálffy. "Waveguide QED with Mössbauer nuclei." *Physical Review A* 109.6 (June 2024), p. 063702. DOI: `10.1103/physreva.109.063702`.

[BB11] Miriam Barthelmess and Saša Bajt. "Thermal and stress studies of normal incidence Mo/B_4C multilayers for a 67 nm wavelength." *Applied Optics* 50.11 (Apr. 2011), p. 1610. DOI: `10.1364/ao.50.001610`.

[Cha+18] D. E. Chang, J. S. Douglas, A. González-Tudela, C.-L. Hung, and H. J. Kimble. "Colloquium: Quantum matter built from nanoscopic lattices of atoms and photons." *Reviews of Modern Physics* 90.3 (Aug. 2018), p. 031002. DOI: `10.1103/revmodphys.90.031002`.

[Cor+24] Jonathan Correa, Alexandr Ignatenko, David Pennicard, Sabine Lange, Sergei Fridman, Sebastian Karl, Leon Lohse, Björn Senfftleben, Ilya Sergeev, Sven Velten, Deepak Prajapat, Lars Bocklage, Hubertus Bromberger, Andrey Samartsev, Aleksandr Chumakov, Rudolf Rüffer, Joachim von Zanthier, Ralf Röhlsberger, and Heinz Graafsma. "TEMPUS, a Timepix4-based system for the event-based detection of X-rays." *Journal of Synchrotron Radiation* 31.5 (July 2024). DOI: 10.1107/s1600577524005319.

[Hab+19] Johann Haber, Jakob Gollwitzer, Sonia Francoual, Martin Tolkiehn, Jörg Strempfer, and Ralf Röhlsberger. "Spectral Control of an X-Ray L-Edge Transition via a Thin-Film Cavity." *Physical Review Letters* 122.12 (Mar. 2019), p. 123608. DOI: 10.1103/physrevlett.122.123608.

[Hab17] Johann Haber. "Hard X-ray quantum optics in thin-film nanostructures." PhD thesis. Universität Hamburg, 2017. DOI: 10.3204/PUBDB-2017-02595.

[Hof+16] Sarah Hoffmann-Urlaub, Philipp Höhne, Mike Kanbach, and Tim Salditt. "Advances in fabrication of X-ray waveguides." *Microelectronic Engineering* 164 (Oct. 2016), pp. 135–138. DOI: 10.1016/j.mee.2016.07.010.

[HS16] Sarah Hoffmann-Urlaub and Tim Salditt. "Miniaturized beamsplitters realized by X-ray waveguides." *Acta Crystallographica Section A* 72.5 (Aug. 2016), pp. 515–522. DOI: 10.1107/s205327331601144x.

[Krü+12] S. P. Krüger, H. Neubauer, M. Bartels, S. Kalbfleisch, K. Giewekemeyer, P. J. Wilbrandt, M. Sprung, and T. Salditt. "Sub-10nm beam confinement by X-ray waveguides: design, fabrication and characterization of optical properties." *Journal of Synchrotron Radiation* 19.2 (Jan. 2012), pp. 227–236. DOI: 10.1107/s0909049511051983.

[Kun+97] Y. Kunimune, Y. Yoda, K. Izumi, M. Yabashi, X.-W. Zhang, T. Harami, M. Ando, and S. Kikuta. "Two-Photon Correlations in X-rays from a Synchrotron Radiation Source." *Journal of Synchrotron Radiation* 4.4 (July 1997), pp. 199–203. DOI: 10.1107/s0909049597006912.

[LAL25] Shin-Yu Lee, Sven Ahrens, and Wen-Te Liao. "Gravitationally sensitive structured x-ray optics using nuclear resonances." *Physical Review Research* 7.1 (Feb. 2025), p. 013158. DOI: 10.1103/physrevresearch.7.013158.

[Len21] Dominik Lentrodt. "Ab initio approaches to x-ray cavity QED - From multi-mode theory to nonlinear dynamics of Mössbauer nuclei." PhD thesis. Universität Heidelberg, 2021. DOI: 10.11588/HEIDOK.00030671.

[NH12] Lukas Novotny and Bert Hecht. *Principles of Nano-Optics*. Cambridge University Press, 2012. ISBN: 9780511794193.

[OS11] Markus Osterhoff and Tim Salditt. "Coherence filtering of x-ray waveguides: analytical and numerical approach." *New Journal of Physics* 13.10 (Oct. 2011), p. 103026. DOI: 10.1088/1367-2630/13/10/103026.

[Pru03] I. R. Prudnikov. "X-ray waveguides based on Bragg scattering of multilayers." *Physical Review B* 67.23 (June 2003), p. 233303. DOI: 10.1103/physrevb.67.233303.

[Pru05] I. R. Prudnikov. "X-ray guided modes produced by Bragg reflections of multilayers: an analytical treatment." *Journal of Applied Crystallography* 38.4 (July 2005), pp. 595–602. DOI: 10.1107/s0021889805011830.

[RE21] Ralf Röhlsberger and Jörg Evers. "Quantum Optical Phenomena in Nuclear Resonant Scattering." In: *Modern Mössbauer Spectroscopy*. Ed. by Yutaka Yoshida and Guido Langouche. Topics in Applied Physics. Springer Singapore, 2021, pp. 105–171. DOI: 10.1007/978-981-15-9422-9_3.

[Röh+10] R. Röhlsberger, K. Schlage, B. Sahoo, S. Couet, and R. Rüffer. "Collective Lamb Shift in Single-Photon Superradiance." *Science* 328.5983 (May 2010), pp. 1248–1251. DOI: 10.1126/science.1187770.

[Ryb+16] Mikhail V. Rybin, Sergei F. Mingaleev, Mikhail F. Limonov, and Yuri S. Kivshar. "Purcell effect and Lamb shift as interference phenomena." *Scientific Reports* 6.1 (Feb. 2016). DOI: 10.1038/srep20599.

[Sah+11] B. Sahoo, K. Schlage, J. Major, U. von Hörsten, W. Keune, H. Wende, R. Röhlsberger, Amitabha Ghoshray, Bilwadal Bandyopadhyay, and Chandan Mazumdar. "Preparation and Characterization of Ultrathin Stainless Steel Films." In: *AIP Conference Proceedings*. AIP, 2011, pp. 57–60. DOI: 10.1063/1.3601785.

[Sal+08] T. Salditt, S. P. Krüger, C. Fuhse, and C. Bähtz. "High-Transmission Planar X-Ray Waveguides." *Physical Review Letters* 100.18 (May 2008), p. 184801. DOI: 10.1103/physrevlett.100.184801.

[Sch+22] Christian G. Schroer, Hans-Christian Wille, Oliver H. Seeck, Kai Bagschik, Horst Schulte-Schrepping, Markus Tischer, Heinz Graafsma, Wiebke Laasch, Karolin Baev, Stephan Klumpp, Riccardo Bartolini, Harald Reichert, Wim Leemans, and Edgar Weckert. "The synchrotron radiation source PETRA III and its future ultra-low-emittance upgrade PETRA IV." *The European Physical Journal Plus* 137.12 (Dec. 2022). DOI: 10.1140/epjp/s13360-022-03517-6.

[She+23] Alexandra S. Sheremet, Mihail I. Petrov, Ivan V. Iorsh, Alexander V. Poshakinskiy, and Alexander N. Poddubny. "Waveguide quantum electrodynamics: Collective radiance and photon-photon correlations." *Reviews of Modern Physics* 95.1 (Mar. 2023), p. 015002. DOI: 10.1103/revmodphys.95.015002.

[Vel22] Sven Velten. *Phonon engineering in thin tin films for tuning photon-nuclei interaction*. Physik. München: Verlag Dr. Hut, 2022. ISBN: 3843949689.

[Wil20] Svenja Willing. "Oblique-incidence deposition of ferromagnetic thin films and their application in magnetoresistive sensors." PhD thesis. Universität Hamburg, 2020. DOI: 10.3204/PUBDB-2020-02479.

A. Figures of merit

A.1. Synchrotron radiation and pulse area

We calculate and discuss some figures of merit of pulsed synchrotron radiation and how they quantitatively translate to driving of the nuclear excitation state.

Synchrotron radiation is typically characterized by its photon energy E, photon bandwidth ΔE, photon flux R_{ph}, pulse repetition rate R_{pulse}, pulse duration τ_{pulse} and focus size a. Parameters for the P01 beamline are listed in Tab. A.1. These parameters can readily be converted to the more useful quantities, photons per pulse N_{ph}, pulse power P, and pulse intensity I, via

$$N_{\mathrm{ph}} \sim R_{\mathrm{ph}}/R_{\mathrm{pulse}}, \tag{A.1}$$

$$P \sim E N_{\mathrm{ph}}/\tau_{\mathrm{pulse}}, \tag{A.2}$$

$$I \sim P/a. \tag{A.3}$$

Table A.1.: Typical operating parameters (upper section) and derived estimates for some figures of merit (lower section) of a focussed synchrotron beam at the P01 beamline.

Photon energy E	14.4 keV
Bandwidth ΔE	1 meV
Photon flux R_{ph}	$0.5 \times 10^{10}\,\mathrm{s}^{-1}$
Pulse repetition rate R_{pulse}	1/192.125 ns
Pulse duration τ_{pulse}	100 ps
Focus size a	$(1\,\mu\mathrm{m})^2$
Photons per pulse N_{ph}	960
Pulse power P	22 mW
Pulse intensity I	$2.2 \times 10^6\,\mathrm{W\,cm}^{-2}$
Temporal mode number M_{c}	152
Peak magnetic field amplitude (coherent) B	1 mT
Peak electric field amplitude (coherent) $\mathcal{E}$	$3\,\mathrm{kV\,cm}^{-1}$

Synchrotron pulses have a low temporal coherence, evident from the fact that $\tau_{\mathrm{pulse}} \gg \hbar/\Delta E$. This can be quantified by the temporal coherence mode number M_{c}, defined as

$$M_\mathrm{c} \sim \frac{\tau_\mathrm{pulse}}{\hbar/\Delta E}. \tag{A.4}$$

Equation (A.4) is to be understood as an order of magnitude, as the actual mode number depends on the exact spectrum. The intensity is related to the magnetic field amplitudes via

$$I \sim \frac{1}{2} Z_0 M_\mathrm{c} |H|^2, \tag{A.5}$$

(Z_0: impedance of free space) so that

$$B \sim \mu_0 \frac{\sqrt{2I}}{\sqrt{Z_0 M_\mathrm{c}}}. \tag{A.6}$$

Table A.1 lists numerical values for these derived estimates.

The interaction of the synchrotron radiation with the nuclei is quantified by the Rabi frequency

$$\Omega = m_0 B/\hbar, \tag{A.7}$$

where the dipole amplitude was defined in (2.50) to be

$$m_0^2 = f_\mathrm{LM} \frac{\sigma_\mathrm{rad}\hbar}{\mu_0 k_0} \frac{\Gamma}{2}(2I_g + 1) \sim f_\mathrm{LM} \frac{\sigma_\mathrm{rad}\hbar}{\mu_0 k_0} \frac{\Gamma}{2}. \tag{A.8}$$

The pulse area is approximately $A = \Omega\tau_\mathrm{pulse}$. Substituting our explicit expressions yields the estimate

$$\begin{aligned} A &\sim \left[\frac{\hbar\Gamma}{\Delta E} \times N_\mathrm{ph} \times \frac{\sigma_\mathrm{rad}}{a} \right]^{\frac{1}{2}} \\ &\sim \left[\frac{1}{Q} \times \frac{E_\mathrm{pulse}}{\Delta E} \times \frac{\sigma_\mathrm{rad}}{a} \right]^{\frac{1}{2}}, \end{aligned} \tag{A.9}$$

where $Q = \omega_0/\Gamma$ is the quality factor of the nuclear resonance and $E_\mathrm{pulse} = \hbar\omega N_\mathrm{ph}$ the pulse energy. The estimate (A.9) should be quantitative up to a factor in the order of 1 due to the exact spectrum of the driving pulses. For the given parameters and Q of the ^{57}Fe resonance, we have $A \sim 1 \times 10^{-6}$.

Table A.2 lists parameters of the Mössbauer transition of ^{57}Fe in pure enriched bcc-iron. The on-resonance attenuation length is defined as

$$\Lambda_\mathrm{res} = \frac{1}{f_\mathrm{LM}\sigma_\mathrm{rad}\rho}. \tag{A.10}$$

Table A.2.: Parameters of the Mössbauer transition of pure ^{57}Fe (upper section) and derived figures of merit (lower section). The resonance attenuation length assumes 100 % enrichment of ^{57}Fe. Data from Refs. [Bha98; Röh05].

Nuclear transition energy E_0	14.41 keV
Effective resonant cross-section σ_{rad}	2.465 Mb
Total nuclear spont. decay rate Γ	1/141 ns $\approx$ 7 MHz
Number density of nuclei ρ	$8.3 \times 10^{22}\,\mathrm{cm}^{-3}$
Lamb-Mössbauer factor f_{LM}	0.8
Magnetic dipole moment $m_0/\hbar$	$8.5\,\mathrm{MHz}\,\mathrm{T}^{-1}$
Resonance attenuation length Λ_{res}	61 nm

References

[Bha98] M. R. Bhat. "Nuclear Data Sheets for A = 57." *Nuclear Data Sheets* 85.3 (Nov. 1998), pp. 415–536. DOI: 10.1006/ndsh.1998.0021.

[Röh05] Ralf Röhlsberger. *Nuclear Condensed Matter Physics with Synchrotron Radiation*. Springer Tracts in Modern Physics. Springer Berlin Heidelberg, 2005. ISBN: 9783540446996. DOI: 10.1007/b86125.

B. Detailed derivations

B.1. Nuclear magnetic dipole operator

The magnetic dipole operator $\hat{\mathbf{m}}$ is an *irreducible spherical tensor operator* of rank 1. We expand it in the basis of the nuclear states, eigenvalues of the perturbed nuclear Hamiltonian, only using symmetry considerations. A derivation for the unperturbed case can be found in textbooks such as Ref. [Ste23].

B.1.1. Basic definitions

We are using the conventions of Steck [Ste23]. A detailed discussion (using slightly different conventions) can also be found in Rose [Ros95]. The dipole operator $\hat{\mathbf{m}}$ is actually a set of 3 operators that requires two definitions of basis: for the quantum states and for the spatial dimensions.

The *spherical basis* is defined as

$$\hat{\xi}_0 = \hat{\mathbf{z}}, \qquad \hat{\xi}_{\pm 1} = \mp \frac{1}{\sqrt{2}} \left(\hat{\mathbf{x}} \pm i \hat{\mathbf{y}} \right). \tag{B.1}$$

We analyze the dipole operator by its action on the angular-momentum states $|I\, m\rangle$. These states transform under rotations as

$$R(\theta)\, |I\, m\rangle = \sum_{m'=-I}^{I} |I\, m'\rangle\, D^{I}_{m'm}(\theta), \tag{B.2}$$

where

$$D^{I}_{m'm}(\theta) = \langle I\, m' | R(\theta) | I\, m\rangle \tag{B.3}$$

are *Wigner D-matrices* and θ parameterizes a rotation (for example in terms of Euler angles).

An *irreducible spherical tensor operator* of rank k, $\hat{\mathbf{T}}^{(k)}$, is defined as a set of $2k+1$ operators, $\{\hat{T}^{(k)}_q \mid -k \leq q \leq k\}$, that transform among themselves under rotations in the same way as the angular-momentum states $|I, m\rangle$, where $I = k$,

$$R(\theta)\hat{\mathbf{T}}^{(k)}R^{\dagger}(\theta) = \sum_{m'=-k}^{k} \hat{T}_{q'}^{(k)} D_{q'q}^{k}(\theta). \tag{B.4}$$

Finally, we will need the *Wigner-Eckart theorem* (WET). For the qth spherical component of an irreducible spherical tensor of rank k, it says that a complex number $\langle I\|\hat{T}^{(k)}\|I'\rangle$ exists such that

$$\langle I\, m|\hat{T}_q^{(k)}|I'\, m'\rangle = \langle I\, m|I'\, m'\, k\, q\rangle\, \langle I\|\hat{T}^{(k)}\|I'\rangle, \tag{B.5}$$

where the other term on the right hand side are Clebsch-Gordan coefficients. The number $\langle I\|\hat{T}^{(k)}\|I'\rangle$ is called the *reduced matrix element* $\langle I\|\hat{T}^{(k)}\|I'\rangle$. In other words, the WET states that the dependence on the angular momentum orientation is entirely captured by Clebsch-Gordan coefficients.

Note that $\langle I\, m|I'\, m'\, k\, q\rangle = \langle I'\, m'\, k\, q|I\, m\rangle$. Replacing the Clebsch-Gordan coefficients with Wigner's 3j-symbols yields

$$\begin{aligned}\langle I, m|\hat{T}_q^{(k)}|I', m'\rangle &= \sqrt{2I+1}(-1)^{I-I'-m}\begin{pmatrix} I' & k & I \\ m' & q & -m\end{pmatrix}\langle I\|\hat{T}^{(k)}\|I'\rangle \\ &= \sqrt{2I+1}(-1)^{2I+k-m}\begin{pmatrix} I' & I & k \\ m' & -m & q\end{pmatrix}\langle I\|\hat{T}^{(k)}\|I'\rangle.\end{aligned} \tag{B.6}$$

B.1.2. Matrix elements of the nuclear magnetic dipole operator

In the following, we will be concerned with the operator mediating the coupling between ground an excited state, $\hat{\mathbf{m}}^{+} = P_g\hat{\mathbf{m}}P_e$. We expand it into the spherical basis

$$\hat{\mathbf{m}}^{+} = \sum_{q=-1}^{1} \hat{m}_q \hat{\boldsymbol{\xi}}_q^{*}. \tag{B.7}$$

Expanding the matrix element in the angular momentum basis yields

$$\langle j|\hat{m}_q|\mu\rangle = \sum_{m_g, m_e} \langle I_e, m_e|\mu\rangle \left\langle j|I_g, m_g\right\rangle \left\langle I_g, m_g|\hat{m}_q|I_e, m_e\right\rangle. \tag{B.8}$$

Using the Wigner-Eckart Theorem with $k = 1$, we write

$$\langle j|\hat{m}_q|\mu\rangle = C(1q, j \leftarrow \mu)\sqrt{2I_g+1}\langle I_g\|\hat{m}\|I_e\rangle, \tag{B.9}$$

where

$$C(1q, j \leftarrow \mu) = \sum_{m_g, m_e} \langle I_e, m_e | \mu \rangle \langle j | I_g, m_g \rangle (-1)^{-m_g} \begin{pmatrix} I_e & I_g & 1 \\ m_e & -m_g & q \end{pmatrix}. \tag{B.10}$$

Here we have used that $2I_g + 1$ is always even for half-integer spin. Plugging the result into (B.7) yields

$$\hat{\mathbf{m}}^+ = \sum_{q=-1}^{1} \sum_{\mu, j} \langle j | \hat{m}_q | \mu \rangle \, |j\rangle\langle\mu| \, \hat{\boldsymbol{\xi}}_q^* = m_0 \sum_{\mu, j} |j\rangle\langle\mu| \, \mathbf{d}_{j\mu}, \tag{B.11}$$

with

$$\mathbf{d}_{j\mu} = \sqrt{3} \sum_q C(1q, j \leftarrow \mu) \hat{\boldsymbol{\xi}}_q^*, \tag{B.12}$$

$$m_0 = \frac{1}{\sqrt{3}} \sqrt{2I_g + 1} \langle I_g \| \hat{m} \| I_e \rangle. \tag{B.13}$$

Importantly, the angular dependence is fully contained in the transition dipole vectors $\mathbf{d}_{j\mu}$.

B.1.3. Orthogonality and normalization

We show the normalization identities (2.41) and (2.42).

To that end, we write

$$\mathbf{d}_{j\mu} \otimes \mathbf{d}_{j\mu}^* = 3 \sum_{q, q'} C(1q, j \leftarrow \mu)^* C(1q', j \leftarrow \mu) \hat{\boldsymbol{\xi}}_q \otimes \hat{\boldsymbol{\xi}}_{q'}^*. \tag{B.14}$$

Summing over initial and final states yields

$$\begin{aligned} &\sum_{\mu, j} C(1q, j \leftarrow \mu)^* C(1q', j \leftarrow \mu) \\ &= \sum_{m_g, m_e, m_g', m_e'} \begin{pmatrix} I_e & I_g & 1 \\ m_e & -m_g & q \end{pmatrix} \begin{pmatrix} I_e & I_g & 1 \\ m_e' & -m_g' & q' \end{pmatrix} A(m_g, m_e, m_g', m_e') B(m_g, m_g'), \end{aligned} \tag{B.15}$$

where

$$\begin{aligned}A(m_g, m_e, m_g', m_e') &= \sum_{\mu,j} \langle I_e, m_e|\mu\rangle \langle j|I_g, m_g'\rangle \langle I_e, m_e'|\mu\rangle^* \langle j|I_g, m_g\rangle^* \\ &= \sum_j \langle I_g, m_g|j\rangle \langle j|I_g, m_g'\rangle \times \sum_\mu \langle I_e, m_e|\mu\rangle \langle \mu|I_e, m_e'\rangle \\ &= \delta_{m_g,m_g'}\delta_{m_e,m_e'}\end{aligned} \tag{B.16}$$

and

$$B(m_g, m_g') = ((-1)^{-m_g})^* (-1)^{-m_g'}. \tag{B.17}$$

It follows that

$$\sum_{\mu,j} C(1q, j \leftarrow \mu)^* C(1q', j \leftarrow \mu) = \sum_{m_g,m_e} \begin{pmatrix} I_e & I_g & 1 \\ m_e & -m_g & q \end{pmatrix} \begin{pmatrix} I_e & I_g & 1 \\ m_e & -m_g & q' \end{pmatrix}. \tag{B.18}$$

We use the following orthogonality relation of the 3j symbols,

$$\sum_{m_1,m_2} \begin{pmatrix} j_1 & j_2 & j_3 \\ m_1 & m_2 & m_3 \end{pmatrix} \begin{pmatrix} j_1 & j_2 & j_3 \\ m_1 & m_2 & m_3' \end{pmatrix} = \frac{1}{2j_3+1}\delta_{m_3,m_3'}, \tag{B.19}$$

for when j_1, j_2, j_3 are physical. We arrive at the orthogonality relation

$$\sum_{\mu,j} C(1q, j \leftarrow \mu)^* C(1q', j \leftarrow \mu) = \frac{1}{3}\delta_{q,q'}. \tag{B.20}$$

It immediately follows that

$$\begin{aligned}\sum_{\mu,j} \mathbf{d}_{j\mu} \otimes \mathbf{d}_{j\mu}^* &= \sum_{q,q'} 3\left(\sum_{\mu,j} C(1q, j \leftarrow \mu)^* C(1q', j \leftarrow \mu)\right) \hat{\xi}_q \otimes \hat{\xi}_{q'}^* \\ &= \sum_{q,q'} \delta_{q,q'} \hat{\xi}_q \otimes \hat{\xi}_{q'}^* = \underline{\mathbf{1}},\end{aligned} \tag{B.21}$$

proving (2.42). Moreover

$$\sum_{\mu,j} |\mathbf{d}_{j\mu}|^2 = \sum_{q,q'} 3 \sum_{\mu,j} C(1q, j \leftarrow \mu)^* C(1q', j \leftarrow \mu) = \sum_{q,q'} \delta_{q,q'} = 3, \tag{B.22}$$

proving (2.41).

B.1.4. Rotational averaging

We use the shorthand

$$T_{qq'} \equiv 3C(1q, j \leftarrow \mu)^* C(1q', j \leftarrow \mu). \tag{B.23}$$

Rotation acts like

$$R(\theta)\mathbf{d}_{j\mu} \otimes \mathbf{d}^*_{j\mu} R^\dagger(\theta) = \sum_{r,r'} \left\{ \sum_{q,q'} D^1_{rq}(\theta) D^1_{r'q'}(\theta)^* T_{qq'} \right\} \vec{\,}^*_r \otimes \vec{\,}_{r'}. \tag{B.24}$$

Taking the rotational average thus evaluates to

$$\begin{aligned}
\left\langle \mathbf{d}_{j\mu} \otimes \mathbf{d}^*_{j\mu} \right\rangle &= \sum_{r,r'} \left\{ \sum_{q,q'} \left\langle D^1_{rq}(\theta) D^1_{r'q'}(\theta)^* \right\rangle T_{qq'} \right\} \vec{\,}^*_r \otimes \vec{\,}_{r'} \\
&= \sum_{r,r'} \left\{ \sum_{q,q'} \frac{1}{2+1} \delta_{qq'} \delta_{rr'} T_{qq'} \right\} \vec{\,}^*_r \otimes \vec{\,}_{r'} \\
&= \frac{1}{3} \left\{ \sum_q T_{qq} \right\} \sum_r \vec{\,}^*_r \otimes \vec{\,}_r \\
&= \frac{1}{3} \operatorname{Tr}_q \left\{ \mathbf{d}_{j\mu} \otimes \mathbf{d}^*_{j\mu} \right\} \underline{\mathbf{1}}
\end{aligned} \tag{B.25}$$

with

$$\operatorname{Tr}\left\{ \mathbf{d}_{\mu j} \otimes \mathbf{d}^*_{\mu j} \right\} = \left| \mathbf{d}_{\mu j} \right|^2. \tag{B.26}$$

B.2. Green's functions

B.2.1. Homogeneous environment

In a homogeneous environment ($\mu \equiv$ const. and $\epsilon \equiv$ const.), the defining equations (2.10a) and (2.10b) simplify to

$$\nabla \times \nabla \times \underline{\mathbf{G}}_{\mathrm{e}}(\mathbf{r}, \mathbf{r}') - \frac{\omega^2}{c^2} n^2 \underline{\mathbf{G}}_{\mathrm{e}}(\mathbf{r}, \mathbf{r}') = \mu \delta(\mathbf{r} - \mathbf{r}') \underline{\mathbf{1}}, \tag{B.27}$$

$$\nabla \times \nabla \times \underline{\mathbf{G}}_{\mathrm{m}}(\mathbf{r}, \mathbf{r}') - \frac{\omega^2}{c^2} n^2 \underline{\mathbf{G}}_{\mathrm{m}}(\mathbf{r}, \mathbf{r}') = \epsilon \delta(\mathbf{r} - \mathbf{r}') \underline{\mathbf{1}}, \tag{B.28}$$

so that the two Green's functions become proportional to one another (for $\mathbf{r} \neq \mathbf{r}'$), $\underline{\mathbf{G}}_{\mathrm{m}}(\mathbf{r}, \mathbf{r}') = (\epsilon/\mu) \underline{\mathbf{G}}_{\mathrm{e}}(\mathbf{r}, \mathbf{r}')$. We just drop the subscript for brevity.

B.2.2. Planar sources

A particularly simple solution exists for planar sources. Consider a source at x' that is coherently extended along y' and z'. The corresponding Green's function can be defined as

$$\underline{\mathbf{G}}^{\mathrm{ps}}(x, x') := \int \mathrm{d}y' \int \mathrm{d}z' \underline{\mathbf{G}}(x, x', y, y', z, z'). \tag{B.29}$$

The left hand side of (B.27) simplifies to (integrating both sides by parts and dropping the boundary terms)

$$-(\partial_x^2 \underline{\mathbf{1}}_{\perp}) \underline{\mathbf{G}}^{\mathrm{ps}}(x, x') - \frac{\omega^2}{c^2} n^2 \underline{\mathbf{G}}^{\mathrm{ps}}(x, x') = \mu \delta(x - x') \underline{\mathbf{1}}, \tag{B.30}$$

where $\underline{\mathbf{1}}_{\perp} = \hat{\mathbf{y}} \otimes \hat{\mathbf{y}} + \hat{\mathbf{z}} \otimes \hat{\mathbf{z}}$, from which we can immediately read off the polarization

$$\underline{\mathbf{G}}^{\mathrm{ps}}(x, x') = G^{\mathrm{ps}}(x - x') \underline{\mathbf{1}}_{\perp} \tag{B.31}$$

and the scalar equation

$$\left(\partial_x^2 + \frac{\omega^2}{c^2} n^2 \right) G^{\mathrm{ps}}(x) = -\mu \delta(x). \tag{B.32}$$

Its solution is easily found to be

$$G^{\mathrm{ps}}(x - x') = \frac{i\mu}{2kn} e^{ikn|x - x'|}, \tag{B.33}$$

where $k = \omega/c$. We finally obtain

$$\underline{\mathbf{G}}_{\mathrm{e}}^{\mathrm{ps}}(x - x'; \omega) = \frac{i\mu}{2kn} e^{ikn|x - x'|} \underline{\mathbf{1}}_{\perp}, \tag{B.34}$$

$$\underline{\mathbf{G}}_{\mathrm{m}}^{\mathrm{ps}}(x - x'; \omega) = \frac{i\epsilon}{2kn} e^{ikn|x - x'|} \underline{\mathbf{1}}_{\perp}. \tag{B.35}$$

B.3. Correspondence between transition-operators and timed Dicke states

The excitation-dynamics approach described in section 2.3 leads to identical dynamical equations as the theories for collective spontaneous emission. This becomes more clear when we establish a correspondence between the two formalisms.

The mentioned theories for collective spontaneous emission consider the time-evolution of the atomic excitation *state* (see Refs. [Scu07; SCS10; FM08b] and the references therein). In contrast to that, here we consider the time-evolution of the transition *operators* $\hat{\sigma}_{ge} = |g\rangle\langle e|$. The two representations are related through expectation values. The following observations can be made. For the timed Dicke state, the expectation value of $\hat{\sigma}_{ge}^j$ vanishes,

$$\langle \psi(\mathbf{k}_0)|\hat{\sigma}_{ge}^j|\psi(\mathbf{k}_0)\rangle = 0, \tag{B.36}$$

reflecting the vanishing dipole moment. Consequently, the linearized transition-operator approach is not applicable to describe the evolution of timed Dicke states. For the timed dipole state (2.99), on the other hand,

$$\langle \psi_\epsilon(\mathbf{k}_0)|\hat{\sigma}_{ge}^j|\psi_\epsilon(\mathbf{k}_0)\rangle \approx \frac{\epsilon}{\sqrt{N}} e^{i\mathbf{k}_0\cdot\mathbf{r}_j}, \tag{B.37}$$

which is proportional to the nuclear exciton in nuclear forward scattering (2.90). The timed dipole states thus correspond to

$$\sigma_{ge}^j \propto e^{i\mathbf{k}_0\cdot\mathbf{r}_j} \tag{B.38}$$

in the discrete, and

$$\sigma_{ge}(x) \propto e^{ik_0 x} \tag{B.39}$$

in the continuous case.

Equation (2.79) is formulated for vector fields and general Green's functions. Inserting the vacuum Green's function leads to relatively complicated coupling terms, which are given in Ref. [FM08b]. Other papers consider scalar fields which leads to very similar equations but considerably simpler coupling terms [SC08; FM08a]. Going to the continuous formulation with full y-z symmetry simplifies the coupling terms significantly and lead us to (2.89), which is identical to the corresponding equation (3.8) in Ref. [FM08b]. The latter was derived in a quantum electrodynamics formalism. This shows that both approaches lead to *identical dynamics* of the expectation values and further underlines the analogy [SCS10; Ebe06; SZS15] between quantum and classical description (if we recall that the theory is equivalent to a classical oscillator model).

References

[Ebe06] J. H. Eberly. "Emission of one photon in an electric dipole transition of one among N atoms." *Journal of Physics B: Atomic, Molecular and Optical Physics* 39.15 (July 2006), S599–S604. DOI: 10.1088/0953-4075/39/15/s07.

[FM08a] Richard Friedberg and Jamal T. Manassah. “Effects of including the counterrotating term and virtual photons on the eigenfunctions and eigenvalues of a scalar photon collective emission theory.” *Physics Letters A* 372.14 (Mar. 2008), pp. 2514–2521. DOI: 10.1016/j.physleta.2007.11.064.

[FM08b] Richard Friedberg and Jamal T. Manassah. “Eigenfunctions and eigenvalues in superradiance with x-y translational symmetry.” *Physics Letters A* 372.16 (Apr. 2008), pp. 2787–2801. DOI: 10.1016/j.physleta.2007.12.056.

[Ros95] Morris Edgar Rose. *Elementary theory of angular momentum*. New York: Dover Publications, Inc., 1995. ISBN: 0486684806.

[SC08] Anatoly Svidzinsky and Jun-Tao Chang. “Cooperative spontaneous emission as a many-body eigenvalue problem.” *Physical Review A* 77.4 (Apr. 2008), p. 043833. DOI: 10.1103/physreva.77.043833.

[SCS10] Anatoly A. Svidzinsky, Jun-Tao Chang, and Marlan O. Scully. “Cooperative spontaneous emission of N atoms: Many-body eigenstates, the effect of virtual Lamb shift processes, and analogy with radiation of N classical oscillators.” *Physical Review A* 81.5 (May 2010), p. 053821. DOI: 10.1103/physreva.81.053821.

[Scu07] M. O. Scully. “Correlated spontaneous emission on the Volga.” *Laser Physics* 17.5 (May 2007), pp. 635–646. DOI: 10.1134/s1054660x07050064.

[Ste23] Daniel A. Steck. *Quantum and Atom Optics*. available online at http://steck.us/teaching. Aug. 2023. URL: http://steck.us/teaching.

[SZS15] Anatoly A. Svidzinsky, Xiwen Zhang, and Marlan O. Scully. “Quantum versus semiclassical description of light interaction with atomic ensembles: Revision of the Maxwell-Bloch equations and single-photon superradiance.” *Physical Review A* 92.1 (July 2015), p. 013801. DOI: 10.1103/physreva.92.013801.

List of publications

[LVS17] L. M. Lohse, M. Vassholz, and T. Salditt. "Tomography with extended sources: Theory, error estimates, and a reconstruction algorithm." *Physical Review A* 96.6 (Dec. 2017), p. 063804. DOI: 10.1103/physreva.96.063804.

[Loh+20a] L. M. Lohse, M. Vassholz, M. Töpperwien, T. Jentschke, A. Bergamaschi, S. Chiriotti, and T. Salditt. "Spectral μCT with an energy resolving and interpolating pixel detector." *Optics Express* 28.7 (Mar. 2020), p. 9842. DOI: 10.1364/oe.385389.

[Loh+20b] Leon M. Lohse, Anna-Lena Robisch, Mareike Töpperwien, Simon Maretzke, Martin Krenkel, Johannes Hagemann, and Tim Salditt. "A phase-retrieval toolbox for X-ray holography and tomography." *Journal of Synchrotron Radiation* 27.3 (Apr. 2020), pp. 852–859. DOI: 10.1107/s1600577520002398.

[LVS21] Leon M. Lohse, Malte Vassholz, and Tim Salditt. "On incoherent diffractive imaging." *Acta Crystallographica Section A Foundations and Advances* 77.5 (Aug. 2021), pp. 480–496. DOI: 10.1107/s2053273321007300.

[Sol+21] Jakob Soltau, Leon Merten Lohse, Markus Osterhoff, and Tim Salditt. "Finite-difference propagation for the simulation of x-ray multilayer optics." *Optics Express* 29.25 (Dec. 2021), p. 41932. DOI: 10.1364/oe.445300.

[Ves+21] Martin Veselý, Roozbeh Valadian, Leon Merten Lohse, Mareike Toepperwien, Kathryn Spiers, Jan Garrevoet, Eelco T. C. Vogt, Tim Salditt, Bert M. Weckhuysen, and Florian Meirer. "3-D X-ray Nanotomography Reveals Different Carbon Deposition Mechanisms in a Single Catalyst Particle." *ChemCatChem* 13.10 (Mar. 2021), pp. 2494–2507. DOI: 10.1002/cctc.202100276.

[Wer+21] Maximilian J. Werny, Roozbeh Valadian, Leon M. Lohse, Anna-Lena Robisch, Silvia Zanoni, Coen Hendriksen, Bert M. Weckhuysen, and Florian Meirer. "X-ray nanotomography uncovers morphological heterogeneity in a polymerization catalyst at multiple reaction stages." *Chem Catalysis* 1.7 (Dec. 2021), pp. 1413–1426. DOI: 10.1016/j.checat.2021.10.008.

[Huh+22] Simon Huhn, Leon Merten Lohse, Jens Lucht, and Tim Salditt. "Fast algorithms for nonlinear and constrained phase retrieval in near-field X-ray holography based on Tikhonov regularization." *Optics Express* 30.18 (Aug. 2022), p. 32871. DOI: 10.1364/oe.462368.

[ALP24] Petar Andrejić, Leon Merten Lohse, and Adriana Pálffy. "Waveguide QED with Mössbauer nuclei." *Physical Review A* 109.6 (June 2024), p. 063702. DOI: 10.1103/physreva.109.063702.

[Cor+24] Jonathan Correa, Alexandr Ignatenko, David Pennicard, Sabine Lange, Sergei Fridman, Sebastian Karl, Leon Lohse, Björn Senfftleben, Ilya Sergeev, Sven Velten, Deepak Prajapat, Lars Bocklage, Hubertus Bromberger, Andrey Samartsev, Aleksandr Chumakov, Rudolf Rüffer, Joachim von Zanthier, Ralf Röhlsberger, and Heinz Graafsma. "TEMPUS, a Timepix4-based system for the event-based detection of X-rays." *Journal of Synchrotron Radiation* 31.5 (July 2024), pp. 1209–1216. DOI: 10.1107/s1600577524005319.

[Loh+24] Leon M. Lohse, Petar Andrejić, Sven Velten, Malte Vassholz, Charlotte Neuhaus, Ankita Negi, Anjali Panchwanee, Ilya Sergeev, Adriana Pálffy, Tim Salditt, and Ralf Röhlsberger. *Collective nuclear excitation and pulse propagation in single-mode x-ray waveguides*. 2024. DOI: 10.48550/ARXIV.2403.06508.

[LA24] Leon Merten Lohse and Petar Andrejic. "Nano-optical theory of planar x-ray waveguides." *Optics Express* 32.6 (Mar. 2024), p. 9518. DOI: 10.1364/oe.504206.

[Luc+24] Jens Lucht, Leon M. Lohse, Thorsten Hohage, and Tim Salditt. *Phase retrieval beyond the homogeneous object assumption for X-ray in-line holographic imaging*. 2024. DOI: 10.48550/ARXIV.2403.00461.

[Loh+25] Leon M. Lohse, Ankita Negi, Markus Osterhoff, Paul Meyer, Sergey Yaroslavtsev, Aleksandr I. Chumakov, Lars Bocklage, Ralf Röhlsberger, and Tim Salditt. *Interferometric measurement of nuclear resonant phase shift with a nanoscale Young double waveguide*. 2025. DOI: 10.48550/ARXIV.2506.05823.

[Neg+25] Ankita Negi, Leon Merten Lohse, Sven Velten, Ilya Sergeev, Olaf Leupold, Sakshath Sadashivaiah, Dimitrios Bessas, Aleksandr Chumakhov, Christina Brandt, Lars Bocklage, Guido Meier, and Ralf Röhlsberger. *Energy Time Ptychography for one-dimensional phase retrieval*. 2025. DOI: 10.48550/ARXIV.2506.00492.

[Shi+] Xihang Shi, Wen Wei Lee, Aviv Karnieli, Leon Merten Lohse, Alexey Gorlach, Lee Wei Wesley Wong, Tim Salditt, Shanhui Fan, Ido Kaminer, and Liang Jie Wong. "Quantum Nanophotonics with Energetic Particles: X-rays and Free Electrons." *Progress in Quantum Electronics*.

Danksagung

Diese Arbeit wurde nur dank der Unterstützung einiger großartiger Wissenschaftler *und Menschen* möglich. Die Zusammenarbeit zwischen Göttingen und Hamburg hat einzigartige Möglichkeiten geboten ohne dabei für mich zu spürbaren Komplikationen zu führen – was in erster Linie an den beteiligten Personen lag.

An erster Stelle möchte ich mich sehr herzlich bei Tim Salditt bedanken, der mich immer wieder mit seiner Begeisterung für die Wissenschaft angesteckt und mich stets unterstützt, gefördert, und beraten hat. Gleichzeitig gilt mein ganz besonderer Dank Ralf Röhlsberger, der mich herzlich in seine Hamburger Gruppe aufgenommen und durchgängig unterstützt und gefördert hat. Auch bei Claus Ropers möchte ich mich herzlich bedanken, insbesondere für die hilfreichen Diskussionen und das Stellen genau der richtigen Fragen im Betreuungsausschuss. Ich hatte alle Freiheit die ich wollte aber konnte mich stets auf die nötige Unterstützung verlassen.

Vielen Dank auch an die anderen Mitglieder der Prüfungskommission: Thorsten Hohage, Hans Hofsäss und Matthias Krüger.

Dann möchte ich mich ganz herzlich bei Adriana Pálffy-Buß und Petar Andrejić bedanken, für die fruchtvolle Kollaboration, die wunderbare Zusammenarbeit, und auch die außerordentlich engagierte Unterstützung.

Mein großer Dank gilt meinen Hamburger Kollegen, die mich in die Gruppe aufgenommen und immer vielfältig unterstützt haben: Lars Bocklage, Sven Velten, Ankita Negi, Anjali Panchwanee, Kai Schlage, Tanya Guryeva, Janne Lütjens, und Andrey Siemens – aber auch Christina Bömer, Dietrich Krebs, und den anderen "Mixies".

Gleichermaßen gilt mein Dank meinen Göttinger Kollegen im IRP, insbesondere Malte Vassholz, Paul Meyer, Charlotte Neuhaus, Mike Kanbach, Jakob Soltau, Markus Osterhoff, Hannes Hoeppe, Jette Alfken, Jens "Der Lurch" Lucht, Jan Goeman, Peter Luley, Bastian Hartmann, und Susanne Hengst. All das aufzuzählen wobei sie mir geholfen haben, würde den Rahmen bei Weitem sprengen.

Ich möchte mich auch für die hervorragende Betreuung bei den Messzeiten durch die engagierten Beamline-Wissenschaftler bedanken: Fabian Westermeier und Michael Sprung an der P10; Ilya Sergueev und Olaf Leupold an der P01; Sergey Yaroslavtsev, Dimitrios Bessas und Sasha Chumakov an der ID18.

Vielen Dank an Yutaka Yoshida für die spannenden Diskussionen und Mössbauer-Messungen in Jena. Ich danke Jörg Evers für die interessanten Diskussionen am Rande so einiger Konferenzen. Lieben Dank auch an Thomas Staudt, für die Hilfe und spannende Diskussionen zu Statistik.

Ganz herzlichen Dank an alle, die Teile der Arbeit Korrektur gelesen und so einige Kanten geglättet haben: Sven Velten, Ankita Negi, Sonka Reimers, Jakob Soltau, Charlotte Neuhaus, Lars Bocklage, und Dietrich Krebs.

Meinen regelmäßige Besuche in Göttingen waren nur möglich weil mich einige meiner lieben Kollegen und ihre Partner und Mitbewohner stets herzlich beherbergt haben. Dafür möchte ich ganz besonders bedanken bei Sonia und Jakob, bei Lotte, Eva, und Fine, bei Paul und Nico, bei Marina, bei Hannes, und bei Lina und Jasper.

Die vielen Fahrten zwischen Hamburg und Göttingen und zu diversen Messzeiten und Konferenzen waren auch ein erheblicher Verwaltungsaufwand. Dank der zuvorkommenden Unterstützung im Sekretariat habe ich davon kaum etwas gemerkt. Herzlichen Dank dafür an Kerstin Pluschke und Michaela Ständer im Sekretariat des IRP, aber auch an das Team des SFB 1456: Eva Hetzel und Norma Rahlfs-Rittmeier. Vielen Dank auch an das Koordinationsteam der Max Planck School of Photonics: Reinhard Geiß, Barbora Marsikova, Adrienn Takacs, und Anna Späthe.